CURRENT-DRIVE AND PLASMA-FORMATION EXPERIMENTS ON THE VERSATOR-II TOKAMAK USING LOWER-HYBRID AND ELECTRON-CYCLOTRON WAVES

by

Jeffrey Alan Colborn

B. S., University of California, Berkeley, 1983

S. M. and E. E., Massachusetts Institute of Technology, 1988

Submitted to the

DEPARTMENT OF ELECTRICAL ENGINEERING AND COMPUTER SCIENCE

in Partial Fulfillment of the Requirements

for the Degree of

DOCTOR OF PHILOSOPHY

at the

MASSACHUSETTS INSTITUTE OF TECHNOLOGY

August 14, 1992

Signature of Author_____

Department of Electrical Engineering
and Computer Science
August 14, 1992

Certified by_____

Professor Ronald R. Parker
Thesis Supervisor

Accepted by_____

Professor Campbell L. Searle
Chairman, Departmental Committee
on Graduate Students

CURRENT-DRIVE AND PLASMA-FORMATION EXPERIMENTS ON THE VERSATOR-II TOKAMAK USING LOWER-HYBRID AND ELECTRON-CYCLOTRON WAVES

by

Jeffrey Alan Colborn

Submitted to the Department of Electrical Engineering
and Computer Science, August 14, 1992,
in partial fulfillment of the requirements for the degree of
Doctor of Philosophy in Electrical Engineering and Computer Science

ABSTRACT

During lower-hybrid current-driven (LHCD) tokamak discharges with thermal electron temperature $T_e \approx 150$ eV, a two-parallel-temperature tail is observed in the electron distribution function. The cold tail extends to parallel energy $E_{\|} \approx 4.5$ keV with temperature $T_{tail}^{cold} \approx 1.5$ keV, and the hot tail extends to $E_{\|} > 150$ keV with $T_{tail}^{hot} > 40$ keV. Fokker-Planck computer simulations suggest the cold tail is created by low power, high-$N_{\|}$ sidelobes in the lower-hybrid antenna spectrum, and that these sidelobes bridge the "spectral gap," enabling current drive on small tokamaks such as Versator.

During plasma-formation experiments using 28 GHz electron-cyclotron (EC) waves, the plasma is born near the EC layer, then moves toward the upper-hybrid (UH) layer within 100-200μs. Wave power is detected in the plasma with frequency $f = 300$ MHz, indicating the EC waves decay into ion modes and electron Bernstein waves during plasma formation. Measured turbulent plasma fluctuations are correlated with decay-wave amplitude. Toroidal currents up to $I_p \approx 1$ kA are generated, consistent with theory, which predicts asymmetric electron confinement. Electron confinement measurements agree with theory. Soft X-rays are emitted with energies up to 6 keV and emission temperatures up to 1.75 keV.

Electron-cyclotron current-drive (ECCD) is observed with loop voltage $V_{loop} \leq 0$ and fully sustained plasma current $I_p \lesssim 15$ kA at densities up to $\langle n_e \rangle = 2 \times 10^{12}$ cm^{-3}. The ECCD efficiency $\eta \equiv \langle n_e \rangle I_p R_0 / P_{rf}$=0.003, which is 30%-40% of the maximum achievable LHCD efficiency on Versator. The efficiency falls rapidly to zero as the density is raised above $\langle n_e \rangle = 3 \times 10^{12}$ cm^{-3}, suggesting the ECCD depends on low collisionality. X-ray measurements indicate the current is carried primarily by electrons with energies 1 keV $\lesssim E \lesssim$ 10 keV. The efficiency is maximum when the EC layer is 5–6 cm to the high-field side of the plasma center. The efficiency is independent of launch angle and polarization.

The EC waves enhance magnetic turbulence in the frequency range 50 kHz $\lesssim f \lesssim$400 kHz by up to an order of magnitude. Assuming the poloidal mode number $m = 15$, it is esti-

mated that this reduces the confinement time of electrons with $E_{\|} = 80$ keV by a factor of two to six in the outer two-thirds of the plasma, while the effect on electrons with 1 keV $\lesssim E_{\|} \lesssim$ 10 keV is small. The time-of-arrival of the turbulence to probes at the plasma boundary is longer when the EC layer is farther from the probes, suggesting the turbulence is driven by wave damping in the plasma interior.

The theoretically-predicted current-drive synergism between EC and LH waves is not observed. This is at least in part because the EC waves enhance the losses of the fast, current-carrying electrons generated by the LH waves, as indicated by increased X-ray flux from the limiter during EC wave injection. These losses may be caused by the observed EC-enhanced magnetic turbulence. The enhanced turbulence and losses decrease with increasing plasma density, and thus may not reduce the EC/LH current-drive efficiency in a high-density, reactor-grade plasma.

Thesis Supervisor: Dr. Ronald R. Parker
Title: Professor of Electrical Engineering

ACKNOWLEDGEMENTS

I sincerely thank the other members of the Versator team, especially Ed Fitzgerald, Professor Miklos Porkolab, Jared Squire, and Joel Villaseñor. Ed, the senior staff technician on Versator, taught me a great deal over the years, and put in an enormous amount of unpaid overtime helping me and the other students in the lab. Professor Porkolab strongly supported me during my experiments on Versator, and he contributed numerous helpful suggestions and criticisms. My fellow graduate students Jared and Joel contributed a great deal toward maintaining the tokamak and developing diagnostics and the data acquisition system, both of which were crucial to my experiments.

I sincerely thank the members of my thesis committee, Professors Ron Parker, Miklos Porkolab, and Abe Bers. It has been a great privilege to receive guidance and advice from this outstanding group of scientists. I especially thank my thesis advisor, Professor Ron Parker, for his excellent advice and encouragement during my stay at MIT.

I thank my parents for their love, support, and encouragment throughout my life. I thank my wife's mother and grandparents, Suhan, Feride, and Sungur, for their love and support, in effect giving me a second family. Especially I thank my wife, Ash, who has loved me and patiently waited for me through this long and trying period.

In the name of God, Most Gracious, Most Merciful.

CONTENTS

FIGURES

CHAPTER 1
BACKGROUND AND THEORY

1.1 MAGNETIC FUSION AND THE TOKAMAK

Nuclear Fusion supplies energy to the sun and stars, making them shine and preventing their collapse. In an effort to harness this energy source, physicists and engineers have been trying to develop a fusion power plant since the early 1950s. The easiest fusion reaction is that of deuterium nuclei (or ions), which consist of one proton and one neutron, with tritium nuclei, which consist of one proton and two neutrons:

$$D^+ + T^+ \longrightarrow He^{2+} + n + 17.6\ \text{MeV} \qquad (1)$$

where He^{2+} is a helium nucleus, n is a neutron, 17.6 MeV is the energy released per reaction, and the superscripts indicate charge. This reaction requires some energy input. For the nuclei to fuse, the Coulomb repulsive force must be overcome and the ions brought together to within $\sim 10^{-15}$ meters. At this distance the nuclear strong force, an attractive force, can overcome the Coulomb repulsion and pull the nuclei together.

In magnetic fusion, the repulsive force is overcome by confining the ions with a magnetic field and heating them to extremely high temperatures, forming a plasma. The quality of a fusion plasma is measured by its ion temperature and Lawson parameter [1], which is the product of the plasma density n, and energy confinement time τ. The energy confinement time is defined in equilibrium as the total plasma energy divided by the total power input to (or loss from) the plasma. For an

economically feasible fusion reactor, the Lawson parameter must be greater than about $10^{14}\text{cm}^{-3}\cdot\text{s}$, and the ion temperature must be about 200,000,000 K.

The most successful magnetic confinement scheme to date has been the tokamak, which was invented by Russian physicists [2] in the 1950s and is continually being refined and improved. As shown in Figure 1-1, the tokamak has two components of the magnetic field—a toroidal component directed the long way around the torus, and a poloidal component circulating the short way around. These components add to give field lines that twist helically around the tokamak. Both field components are needed for the equilibrium and stability of the plasma.

The toroidal magnetic field is produced by a set of coils that are outside the plasma, as shown in Figure 1-1. The poloidal field is produced by a *toroidal* plasma current (often several megaampères in contemporary tokamaks). Traditionally, this current has been generated via induction, the plasma being a one-turn secondary coil of a transformer. Current generated by induction cannot be steady-state, because it is proportional to the time-rate-of-change of the poloidal magnetic flux linked by the plasma (see Figure 1-2). That is, the tokamak must be pulsed and the transformer reset between pulses. Pulsing a reactor fatigues its structure and lowers its average power output. If current could be economically driven noninductively in reactor-grade plasmas, a steady-state reactor may be realized. Perhaps the most promising methods of steady-state current-drive are the injection of high-power microwaves into the plasma in the "lower-hybrid" and "electron cyclotron" ranges of frequencies. These two methods are known as "lower-hybrid current-drive" (LHCD) and "electron-cyclotron current-drive" (ECCD), respectively. Lower-hybrid current-drive has been demonstrated up to megaampère levels in large tokamaks, but is predicted to be less effective in reactor-grade plasmas. Electron-cyclotron current-drive is predicted to be more effective and flexible than LHCD in reactor-grade plasmas, but it has not yet been demonstrated on a large scale. Another promising method is to combine electron-cyclotron waves and lower-hybrid waves. This method has

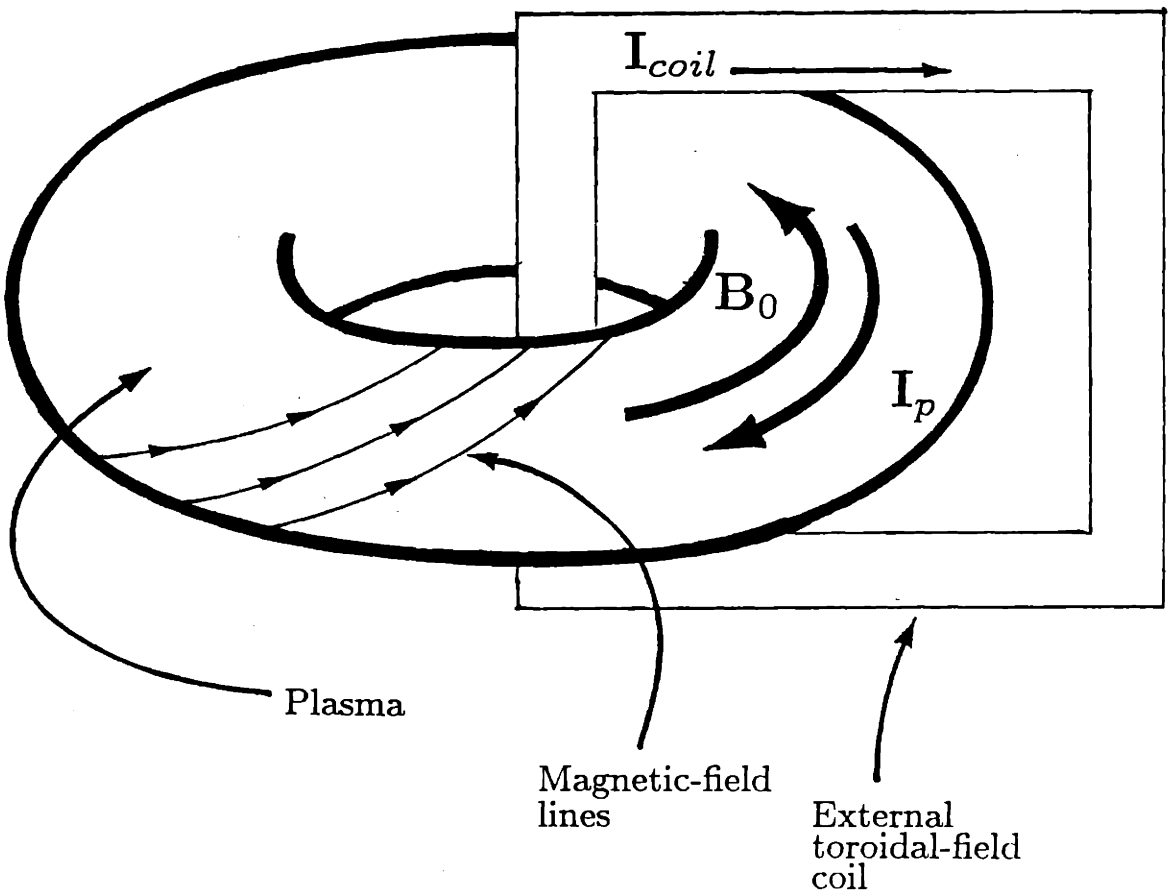

Figure 1-1 Schematic Diagram of a Tokamak. The toroidal-field coils are spaced uniformly around the torus; only one is shown for clarity.

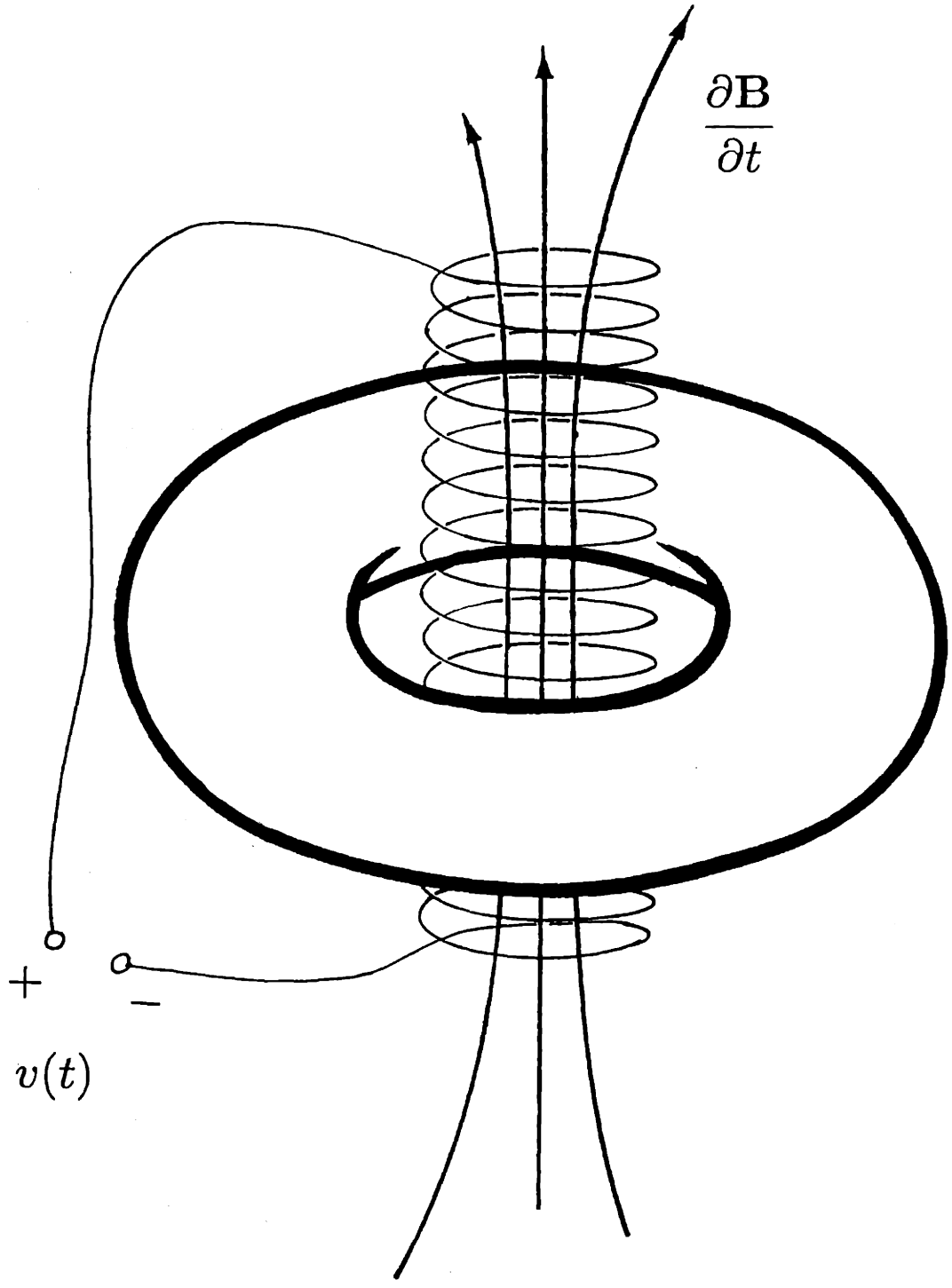

Figure 1-2 The transformer circuit of a tokamak.

not been significantly studied experimentally, but it is theoretically predicted to be more efficient than either ECCD or LHCD.

The toroidal electric field induced in the tokamak by the transformer primary has another purpose: it breaks down the initial gas contained in the tokamak vacuum chamber, forming the plasma from it and heating the plasma ohmically. If a noninductive method could be found for breaking down the initial gas and ramping up and sustaining the plasma current, the expensive and space-consuming transformer could be eliminated. A promising method for doing this is to break down the initial gas with electron-cyclotron waves and subsequently initiate and sustain the toroidal plasma current using LHCD.

The experiments described in this thesis were designed to explore some of the above current-drive methods, including LHCD, ECCD, combined LHCD/ECCD, and transformerless startup. The organization of this thesis is as follows. The remainder of Chapter 1 describes the basic dispersion, polarization, and absorption theory of lower-hybrid (LH) and electron-cyclotron (EC) waves, mode conversion of EC waves, simple current-drive theory, and the past work of other experimenters on the topics covered in this thesis. The experimental apparatus is described in Chapter 2. Chapters 3, 4, and 5 present the experimental results and include analysis and theory specific to the phenomena under study. Chapter 3 describes experiments in which a "two-parallel-temperature" electron tail was observed during LHCD. Chapter 4 presents results and analysis of experiments on EC plasma formation, EC-induced turbulence, and ECCD. Chapter 5 describes transformerless startup and combined ECCD/LHCD experiments. Conclusions are given in Chapter 6, and details of the theory of LH and EC wave propagation, EC wave absorption, current drive, and the anomalous Doppler instability are given in Appendices A through D, respectively.

1.2 THEORY OF LOWER-HYBRID AND ELECTRON-CYCLOTRON WAVES

The polarization and dispersion of lower-hybrid (LH) and electron-cyclotron (EC) waves can be obtained for a cold plasma from Maxwell's equations and the fluid or kinetic equations. The cold plasma approximation accurately describes the wave dispersion away from resonance layers, where the wavenumber becomes very large, and wave damping usually occurs. In the cold-plasma approximation, $k_\perp \rightarrow \infty$ at resonance layers, where $k_\perp$ is the wavenumber perpendicular to the static magnetic field $\mathbf{B}_0$. In the current-drive regime relevant for the experiments described in this thesis, there are no resonance layers in the plasma for LH waves, but resonance layers do exist for EC waves.

Starting with Maxwell's equations, assuming wave fields varying as $\exp(i\mathbf{k}\cdot\mathbf{r} - i\omega t)$, using the WKB approximation, and assuming a linear, dispersive medium, we obtain the wave equation:

$$\mathbf{k}\times(\mathbf{k}\times\mathbf{E}) + \frac{\omega^2}{c^2}\overline{\overline{\mathbf{K}}}\cdot\mathbf{E} = 0. \tag{2}$$

Under the WKB approximation $|\mathbf{k}| \gg |\partial/\partial\mathbf{r}|$, which means the wavelength of the perturbations is much shorter than the scale length of gradients in equilibrium quantities such as plasma density or static magnetic field strength. Equation 2 has been transformed in time and space, $\mathbf{k}$ is the wave vector, $\mathbf{E}$ is the wave electric-field, ω is the wave frequency, c is the speed of light, and $\overline{\overline{\mathbf{K}}}$ is the dielectric tensor, incorporating free-current effects. The dielectric tensor is defined as follows:

$$\overline{\overline{\mathbf{K}}}\cdot\mathbf{E} = \mathbf{E} + \frac{i}{\omega\epsilon_0}\mathbf{J} \tag{3}$$

where $\mathbf{J} = \sum_j n_{j0} Z_j e v_{j1}$ is the plasma current (summed over species), n_0 is the zeroth-order density, Z is the charge state of the species, e is the magnitude of the charge of the electron, and v_1 is the first-order (wave-induced) particle velocity. Applying cold-plasma theory, i. e. , using the fluid equations or the reduced kinetic equations, the dielectric tensor for $\mathbf{B} = \hat{\mathbf{z}} B(\mathbf{r})$ becomes

$$\overline{\overline{\mathbf{K}}} = \begin{pmatrix} K_{xx} & K_{xy} & 0 \\ -K_{xy} & K_{xx} & 0 \\ 0 & 0 & K_{zz} \end{pmatrix} \tag{4}$$

where

$$K_{xx} = 1 - \frac{\omega_{pe}^2}{\omega^2 - \omega_{ce}^2} - \frac{\omega_{pi}^2}{\omega^2 - \omega_{ci}^2} \tag{5}$$

$$K_{xy} = \frac{i\omega_{ce}}{\omega} \frac{\omega_{pe}^2}{\omega^2 - \omega_{ce}^2} - \frac{i\omega_{ci}}{\omega} \frac{\omega_{pi}^2}{\omega^2 - \omega_{ci}^2} \tag{6}$$

$$K_{zz} = 1 - \frac{\omega_{pe}^2}{\omega^2} - \frac{\omega_{pi}^2}{\omega^2}, \tag{7}$$

$\omega_{pj} = \sqrt{n_j e^2 Z_j^2 / m_j \epsilon_0}$ is the plasma frequency of the jth species (e. g. electrons or hydrogen ions), and $\omega_{cj} = Z_j e B / m_j$ is the cyclotron frequency of the jth species. For the plasma interior (i. e. , *not* in the coupling region), the situation shown in Figure 1-3 can be assumed without loss of generality, so that $N_\parallel = ck_\parallel/\omega = (ck/\omega)\cos\theta$ and $N_\perp = ck_\perp/\omega = (ck/\omega)\sin\theta$. Substituting into the wave equation gives

$$\begin{pmatrix} K_{xx} - N_\parallel^2 & K_{xy} & N_\parallel N_\perp \\ -K_{xy} & K_{xx} - N^2 & 0 \\ N_\parallel N_\perp & 0 & K_{zz} - N_\perp^2 \end{pmatrix} \begin{pmatrix} E_x \\ E_y \\ E_z \end{pmatrix} = 0. \tag{8}$$

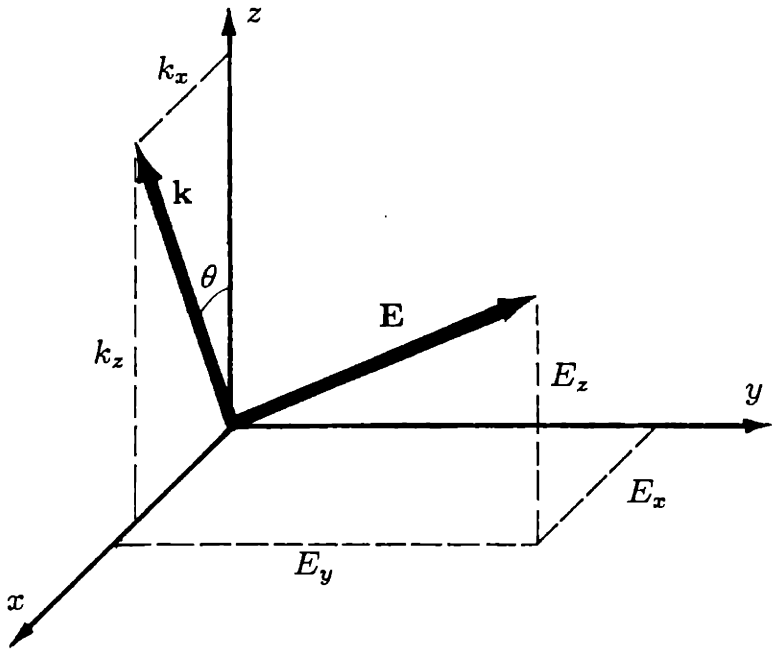

Figure 1-3 Coordinate system for accessibility calculation in slab geometry.

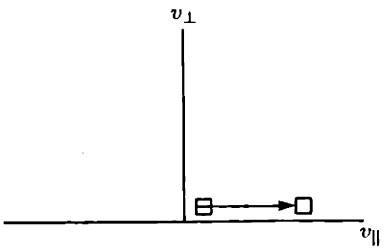

Figure 1-4a Displacement in velocity-space by LH waves.

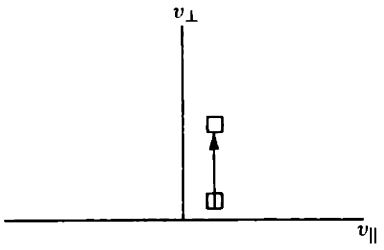

Figure 1-4b Displacement by EC waves.

The dispersion relation is obtained by setting the determinant of this system of equations to zero. This yields the following quadratic equation for $N_\perp^2$:

$$K_{xx}N_\perp^4 + N_\perp^2[(K_{xx}+K_{zz})N_\parallel^2 - (K_{xy}^2 + K_{xx}^2 + K_{xx}K_{zz})] + K_{zz}[(N_\parallel^2 - K_{xx})^2 + K_{xy}^2] = 0. \quad (9)$$

This equation can be used to describe the dispersion of LH waves and EC waves in a cold plasma, as shown in Appendix A.

Calculating the absorption of electron-cyclotron waves is complicated, and analytical expressions are not available for the general case. However, using suitable assumptions the absorption on Versator can be estimated for a Maxwellian plasma. This is done in Appendix B. It is shown that the single-pass absorption by the thermal electron population on Versator for the O-mode is expected to be about 13% for propagation perpendicular to **B** and 6% for propagation at 45° to **B**. For the X-mode, 0.02% and 23% are expected for perpendicular and 45° propagation, respectively.

Although the absorption of the X-mode by thermal electrons in Versator-II is generally very weak, this mode can linearly convert [3] or parametrically decay [4] into the Electron Bernstein wave [5] at the upper-hybrid layer, as described in Appendix C. The electron Bernstein (EB) wave is strongly damped by the thermal electrons, and can thereby heat the bulk plasma. During parametric decay the EC "pump" wave at frequency f_0 decays into a low-frequency lower-hybrid wave at frequency $f_1 \approx f_{lh}$ and an EB wave at frequency $f_2 = f_0 - f_1$. f_{lh} is the lower hybrid frequency. As will be seen in Chapter 4, parametric decay can occur in Versator EC-formed plasmas, as indicated by the detection of the low-frequency mode at f_1.

1.3 THEORY OF CURRENT DRIVE

To gain a realistic qualitative picture of how current-drive works, and to obtain accurate quantitative predictions of current-drive efficiency, kinetic theory must be used. The interaction of the waves and the electron distribution function must be examined, taking into account two-dimensional effects. Following the analysis of Fisch and Boozer, [6] the current-drive efficiency J/P_d may be calculated using an "impulse response" method, where J is the driven current density and P_d is the power dissipated per unit volume.

Consider the displacement in velocity space of a small number of electrons δf from velocity $\mathbf{v}_1$ to $\mathbf{v}_2$. The energy required for this displacement is

$$\Delta E = (E_2 - E_1)\delta f, \tag{10}$$

where $E_1 = \frac{1}{2}m_e v_1^2$ and $E_2 = \frac{1}{2}m_e v_2^2$. The collisional drag on an electron is dependent on its velocity. Assigning a velocity decay rate $\nu_i(v)$ to each velocity v_i gives the following transient current:

$$\mathcal{J}(t) \;=\; -e\delta f\left[v_{\|2}e^{-\nu_2 t} - v_{\|1}e^{-\nu_1 t}\right], \tag{11}$$

where the $\|$ subscript indicates the component of v_i parallel to the confining magnetic field. The first term on the right results from the new electron at velocity v_2, and the second term results from the missing electron at v_1. These currents decay at different rates ν_1 and ν_2, which depend only on v_1 and v_2 [6].

The average of $\mathcal{J}(t)$ over a time Δt that is large compared to $1/\nu_1$ and $1/\nu_2$ is defined as J:

$$J \equiv \frac{1}{\Delta t}\int_0^{\Delta t}\mathcal{J}(t)dt = \frac{e\delta f}{\Delta t}\left(\frac{v_{\|1}}{\nu_1} - \frac{v_{\|2}}{\nu_2}\right), \tag{12}$$

where J can be interpreted as the current generated in a time Δt by an amount of energy ΔE. Substituting from Equation 10 for δf and identifying $\Delta E/\Delta t$ as P_d yields the following:

$$\frac{J}{P_d} = -e\left(\frac{v_{\parallel 1}/\nu_1 - v_{\parallel 2}/\nu_2}{E_1 - E_2}\right). \tag{13}$$

Taking the limit as $\mathbf{v}_2 \rightarrow \mathbf{v}_1$ yields [6]

$$\frac{J}{P_d} = \frac{-e\hat{\mathbf{s}} \cdot \nabla_v (v_\parallel/\nu)}{\hat{\mathbf{s}} \cdot \nabla_v E} \tag{14}$$

where $\hat{\mathbf{s}}$ is the unit vector (in velocity space) in the direction of $\Delta\mathbf{v}$, ∇_v is the gradient operator in velocity space, and the subscripts have been dropped.

This equation shows that the current-drive efficiency depends on the velocity of the electrons absorbing the power, *and* on the direction in velocity space in which these electrons are accelerated. This can be seen by taking the limit $\mathbf{v}_1 \rightarrow \mathbf{v}_2$ of Equation 12 [7]:

$$\mathbf{J} = -e\frac{\Delta\mathbf{v}}{\Delta t} \cdot \nabla_v \left(\frac{v_\parallel}{\nu(v)}\right) \tag{15}$$

where $\Delta\mathbf{v} = \mathbf{v}_2 - \mathbf{v}_1$ and $v = |\mathbf{v}|$. Differentiating,

$$\mathbf{J} = -e\frac{\Delta\mathbf{v}}{\Delta t} \cdot \left(\frac{\hat{\mathbf{z}}}{\nu} + \frac{v_\parallel}{\nu^2}\nabla_v \nu\right). \tag{16}$$

The first term represents the contribution to the current via direct parallel momentum transfer from the rf to the electrons and is proportional to the parallel component of $\Delta\mathbf{v}$. The second term, present even if no parallel momentum is imparted to the electrons, is due to the velocity dependence of the collision frequency. If electrons traveling in one toroidal direction are preferentially heated, even if this heating is purely perpendicular, they will become less collisional, resulting in an

asymmetric resistivity and a net toroidal current. Lower-hybrid waves can carry significant net parallel momentum and thus can drive current via both terms in Equation 16. Electron cyclotron waves carry little parallel momentum, but they can drive current via the second term in Equation 63 by imparting perpendicular energy to electrons traveling in a particular parallel direction. Figure 1-4 shows displacements in velocity space typical of current-drive with LH-waves (a) and EC-waves (b).

Now $\Delta \mathbf{v}$ is related to the characteristics of the rf wave that produces it. Energy and momentum are absorbed by the electron when it is in "resonance" with the wave, that is, when the Doppler-shifted wave frequency (as seen by the electron streaming parallel to the confining magnetic field) is an integer multiple of the cyclotron frequency:

$$\omega - k_{\|} v_{\|} = n\omega_{ce} \tag{17}$$

where $n = 0, \pm 1, \pm 2, \ldots$ and relativity has been neglected. The parallel velocity at which an electron will strongly absorb energy from the wave is then

$$v_{\|} = \frac{\omega - n\omega_{ce}}{k_{\|}}. \tag{18}$$

For waves in the lower-hybrid range of frequencies (LHRF), $\omega \ll \omega_{ce}$ and resonance occurs for $n = 0$, yielding $v_{\|} = \omega/k_{\|} = v_{phase}$. This is the Landau resonance. Because we want electrons with a particular sign of $v_{\|}$ to be preferentially heated, we must launch LH waves with a phase velocity in a particular parallel direction and, most importantly, some electrons should have pre-existing parallel velocities near the phase velocity of the launched wave. Otherwise, at least in theory, no wave-particle interaction should occur. One aspect of LHCD that is not well understood is the so-called "spectral gap" problem, i.e., the problem of determining how current drive is achieved in many experiments even though this condition is not satisfied:

in most current-drive experiments on small tokamaks, the launched waves have parallel phase velocities $v_{ph} > c/4$ and the target plasmas have electron thermal velocities of $v_{th} < c/25$. Waves with high phase velocities are easier to launch and give higher experimental current-drive efficiencies, but these waves do not resonate with a significant number of electrons, according to simple theory, and hence should not drive current.

For electron cyclotron waves near the fundamental harmonic frequency, $n = 1$ and resonance occurs for $v_{\|} = (\omega - \omega_{ce})/k_{\|}$. This shows that, for electron cyclotron waves, the direction of the parallel velocity of the electrons interacting with the waves, and hence the direction of the driven current, depends on the sign of $\omega - \omega_{ce}$. On a tokamak, this is equivalent to a dependence on which side of the resonance layer the absorption region lies.

The basic idea of current drive by LH waves through parallel momentum transfer can best be understood by considering the original paper on the subject by Fisch [8]. The one-dimensional treatment presented there shows how the first term in Equation 16 contributes to the current-drive efficiency of a broad spectrum of LH waves interacting with a distribution of electrons. In the parallel direction, the LH waves diffuse electrons toward higher $v_{\|}$, competing with the collisional relaxation of the plasma, which attempts to restore itself to a Maxwellian. This derivation is given in Appendix E, where the following expression for the LHCD figure of merit is derived:

$$\eta \equiv \frac{\langle n_e \rangle I_p R_0}{P_{lh}} \approx \frac{1.4}{2 + Z_i} \frac{1/N_{\|1}^2 - 1/N_{\|2}^2}{2 \ln(N_{\|1}/N_{\|2})}, \tag{19}$$

where $\langle n_e \rangle$ is the line-averaged density, I_p is the plasma current, R_0 is the major radius, P_{lh} is the wave power, Z_i is the ion charge state, and the LH wave spectrum extends from $N_{\|1}$ to $N_{\|2}$. An effect neglected in Equation 19 is the two-dimensional structure of the collision operator. When this structure is retained, the calculated

current-drive efficiency is improved by a factor of two to three [9]. This is because when fast electrons are pitch-angle scattered out of the resonance region by thermal electrons, resulting in a loss of parallel momentum, they gain (on the average) perpendicular energy. This decreases their collisionality relative to what one would expect if the increase in perpendicular energy were ignored. Because these electrons are on the average traveling in the same direction as before they were scattered, the calculated current-drive efficiency is higher than one would expect taking into account only the parallel dynamics.

A fully relativistic calculation of the current-drive efficiency of a narrow spectrum of low-$N_{\|}$ lower-hybrid waves has been given by Karney and Fisch [10]. They found that two relativistic effects set an upper limit on the efficiency. First, the relativistic electrons slow down faster because they are heavier. Second, the current carried by the electrons is proportional to their velocity, which approaches a constant (equal to the speed of light) as momentum is imparted to them and they become heavier. Each of these effects reduces the efficiency by a factor of γ, so combined they reduce η by a factor of $\gamma^2 \sim p^2$, where p is momentum, cancelling the nonrelativistic v^2 dependence and forcing η to approach a constant at high velocities.

Electron-Cyclotron waves drive current by selectively heating electrons perpendicularly, thereby creating an asymmetric resistivity. The frequency, magnetic field, and launch angle are chosen such that electrons traveling in one toroidal direction are preferentially heated. This reduces their collisionality so that, on average, they deposit less of their momentum into the ions than electrons traveling in the opposite direction. This results in a net toroidal current. For conventional EC current-drive, electrons with parallel velocities $v_{\|} \gtrsim v_{te}$ are targeted. The efficiency of this type of current drive is very poor for electron temperatures typical of Versator (150-300 eV). If a superthermal tail is present, however, the efficiency can be greatly improved. This tail can be created, for example, by a parallel electric field, or by LH waves. These two cases are studied experimentally in Chapters 4 and 5, respectively.

1.4 RELATED EXPERIMENTAL WORK OF OTHERS

1.4.1 Lower-Hybrid Current Drive

Soon after it was first proposed [8]that current may be driven by LH waves, successful LHCD experimental results were reported on the JFT-2M tokamak in Japan [11] and on Versator-II [12]. In these experiments, the current was sustained mostly by the ohmic-heating transformer, and current-drive of $\sim$ 15 kA was inferred from a drop in the loop voltage (the parallel electric field) relative to similar discharges without LH wave injection. On Versator-II, it was observed for the first time that the drop in V_{loop} was not due to electron heating, because the electron temperature (as measured by Thomson scattering) was observed to drop during LH wave injection, thereby increasing the plasma resistance. Also, a "density limit" was seen, above which no current-drive was observed. On the Versator experiment, the source frequency was 800 MHz, and the density limit was about 6×10^{12} cm^{-3}, for which the lower-hybrid frequency is about 400 MHz. The "spectral gap" was large for these experiments, with $v_{ph}/v_{te} \sim$ 10-20. No explanation was given for how it could have been bridged during the experiments.

Fully lower-hybrid current-driven (LHCD) discharges were first reported on the Princeton Large Torus (PLT), where a steady plasma current of 165 kA was maintained for 3.5 s with V_{loop} near zero. [13] The OH transformer primary was open-circuited after plasma startup, and the subsequent L/R decay of the plasma current was arrested by the LH waves, so that a steady plasma current was maintained. Reasonably good agreement with Fisch's theory was observed for the efficiency, and a density limit was observed. The spectral gap was smaller, with $v_{ph}/v_{te} \sim$ 8-10.

Lower-hybrid current-drive has since been demonstrated up to megaampère levels on a number of large tokamaks, including Alcator C [14], the Joint European

Torus (JET) [15], the Japanese Tokamak 60 (JT-60) [16], the ASDEX tokamak (Germany) [17] and Tore Supra (France) [15]. Also, LHCD has been demonstrated for plasma discharge times of over one hour on the TRIAM tokamak in Japan [18].

1.4.2 EC-formed Toroidal Plasmas

In the early 1970's, Anisimov and co-workers [19-22] studied plasmas formed by electron-cyclotron heating (ECH) in a toroidal magnetic field. They made three important observations. First, in the first several microseconds of the high-power ECH discharge, the plasma density peak (and hence its formation region) moved from the electron cyclotron (EC) layer toward the upper-hybrid (UH) layer. Thus it appeared that the launched electromagnetic X-mode was mode-converting to electron Bernstein waves at the UH layer, and these EB waves were strongly damping and building up the plasma density and temperature locally. Such a mode-conversion was predicted by linear theory much earlier [3]. Second, they found that at low gas-fill pressures, the rf absorption was an order of magnitude higher than predicted, indicated by plasma formation only near the UH layer even when the calculated linear collisional damping length was greater than the size of the torus. Third, they showed that breakdown did not occur below a certain gas fill pressure that was dependent on the ECH power. This third point was shown to be consistent with the idea that breakdown can only occur when the confinement time of the ECH-heated electrons exceeded the ionization time. This is becuase the ionization time is given by $\tau_i = (N\sigma v_e)^{-1}$, where N is the neutral particle density, σ is the ionization cross-section, and v_e is the electron speed.

These experiments were followed in the late 1970's and early 1980's by experiments on many tokamaks (FT-1, TOSCA, ISX-B, CLEO, JFT-2, WT-1, WT-2, Tokapol-II, and JIPPT-II) [23-33]. These experiments generally corroborated those

of Anisimov, et. al., and extended the parameter range to much higher EC-wave power and pulse length. Generally, the EC-formed plasmas were found to peak in density between the cyclotron and upper-hybrid layers, and to have temperatures of about $T_e \approx 20$ eV, with T_e as high as 50 eV near the UH layer. It was found in all of the experiments that the EC preionization significantly reduced the loop voltage (toroidal electric field) required for successful startup of the tokamak, and slightly reduced the overall flux consumption of the ohmic heating (OH) coil.

The first report on the systematic variation of many experimental parameters in order to determine the effect on an EC-formed plasma was made by Kulchar et. al. in 1984 [26]. They launched up to 70 kW at 28 GHz for up to 40 ms from the high-field side of ISX-B in a mixture of the X-mode and O-mode directed at an angle of 60° from the magnetic field. Many parameters were systematically varied and some were optimized, the main figure of merit being the reduction of peak loop voltage required for plasma breakdown, and the transformer flux consumed. The optimum toroidal field was such that the UH layer was at the outer limiter. There was no effect on loop voltage reduction of changing the ECH power from 70 kW to 35 kW, indicating a lower power threshold for preionization, in agreement with previous experiments. The loop-voltage drop was also independent of gas fill pressure over the range used. Remarkably, the volt-second savings was roughly independent of the delay time between ECH turn-off and the firing of the ohmic-heating coils for delay times between 5 and 30 ms. The authors considered this to be evidence of a long-lived ($\gtrsim 30$ ms) very low density plasma component created by the ECH. The decay time of the density after rf turn-off was about 10 ms.

1.4.3 Electron-Cyclotron Current-Drive

The first ECCD experiments were performed on TOSCA, a very small tokamak at Culham Laboratory in the United Kingdom [34]. The EC driven current

was detected by launching EC waves in opposite toroidal directions in turn and comparing the drops in the loop voltage. The observed ECCD was very weak. Similar experiments were performed on CLEO [35] and DIII-D [36]. The DIII-D experiments produced 50-100 kA of EC driven current, but this was still only a fraction of the plasma current, and a significant loop voltage was present. The first ECCD experiments with zero loop voltage were on the WT-2 Tokamak in Japan [37], in which up to 3 kA was sustained by EC waves launched from the low-field side into a very low-density plasma ($\langle n_e \rangle < 10^{12}$ cm^{-3}). More recently, ECCD has been achieved on WT-3 using EC waves at the second harmonic [38-39]. In these experiments, up to 20 kA was sustained and ramped up for over 30 ms with the loop voltage zero or negative. The ECCD efficiency was an order of magnitude smaller than the LHCD efficiency on the same tokamak, and decreased rapidly to zero as the density was raised above about 4×10^{12} cm^{-3}. The authors hypothesized that a slideaway target electron tail, pre-formed by the parallel electric field, was necessary for efficient ECCD. They did not explain, however, how the ECCD was sustained well beyond the time when the loop voltage became negative.

A decrease in electron particle confinement has been observed on several small tokamaks [40-42] during EC heating or current-drive. This has been shown to be consistent with the predicted loss of confinement due to ECH-enhanced electrostatic turbulence [43], but the mechanism by which the ECH enhances turbulent fluctuations is not known. Magnetic turbulence that accompanies electrostatic turbulence also is enhanced by ECH [43,44] , and this may adversely affect fast electron particle confinement. However, this has not been demonstrated.

1.4.4 Transformerless ECH/LHCD Startup

In 1983, Kubo and co-workers [45] reported experiments on WT-2 where the tokamak toroidal current was started and ramped up to $\sim$ 5 kA by lower-hybrid

(LH) waves from an EC-formed plasma. The ohmic-heating transformer primary was never energized, and the secondary was shorted. Up to 30 kW of EC waves were launched at 35.6 GHz for up to 10 ms and up to 100 kW of LH waves at 915 MHz for up to 21 ms were launched from a four-waveguide grill on the outside. The ECH produced a preionized plasma with $\overline{n}_e = 2 \times 10^{12}$ cm^{-3} and $I_p \approx 0.5$ kA. Upon application of the LH power, the plasma current rose to ≈ 5 kA with no change in the density. The loop voltage was zero or negative during the current-rise phase. Soft X-rays were emitted from the EC-formed plasma and became very much more intense in the lower-hybrid current driven (LHCD) plasma. Intense hard X-rays were emitted from the LHCD plasma. It was estimated that the bulk electron temperature of the LHCD plasma was about the same as that of the preionized plasma (about 20 eV), and that a fast-electron population was present in both stages that was heated from 0.5–1 keV in the EC-formed plasma to 30–50 keV in the LHCD plasma. It was discovered that the success rate of plasma start-up was sensitively dependent on the vertical magnetic field. The plasma current was maximum for $B_V/B_{tor} = 0.0025$. An initial hydrogen fill pressure of less than 10^{-4} torr was required for successful startup with ECH power of 20 kW, and this boundary increased with increasing ECH power. The authors suggested that the spectral gap was filled by electrons heated perpendicularly by the ECH and then pitch-angle scattered, forming a low-density tail in velocity-space that could damp the high-velocity LH waves. This process was modeled using a two-dimensional Fokker-Planck code [46]. The X-ray emission from the tail as a function of time and radial location was measured [47], and the data was fit by a two-temperature Maxwellian with $T_{low} = 15$ keV and $T_{high} = 55$ keV.

Considerably longer (170 ms) start-up discharges were reported in 1984 by Toi, et. al. on JIPPT-IIU [48]. About 20 kW of EC waves at 35.5 GHz for up to 15 ms was launched in the O-mode from the low-field side, and about 60 kW average of 800 MHz LH was launched from a pair of C-shaped waveguides phased at 180° (no directivity). In these experiments, EC-formed plasmas similar in some

respects to those on WT-2 were formed, and LH waves were used to ramp the plasma current up to $\sim$ 20 kA. It was observed that in the density range 1×10^{12} to 3×10^{12} cm^{-3}, the ramp-up rate, but not the final value, of the plasma current depended on the electron density. Current-drive efficiency at the end of the discharge was about 0.01 $\overline{n}_e(10^{20}$ m$^{-3})$ R(m) Amps/Watt. The following year, Ohkubo, Toi, and co-workers [49] attempted to explain the bridging of the spectral gap in the JIPPT-IIU start-up experiments by parametric decay of the injected 800 MHz waves. They noted that they observed little evidence of suprathermal electrons in the ECH preionized plasma, in sharp constrast to the observations reported on WT-2. In addition, they were ocasionally able to start-up the plasma current with LH wave power alone, without ohmic or ECH power. They concluded, by comparing the observed spectrum with calculated damping rates of parametric-decay waves, that the lower-hybrid decay waves at the lower sideband of the injected pump wave frequency are capable of bridging the spectral gap. A movable limiter placed on the low-field side stopped the current start-up when moved to within $a/2$ of the minor axis, which the authors take as indication that the "seed current" necessary to bridge the spectral gap is generated near $R = R_0 + a/2$. Also, measurements from a pair of magnetic probes indicate a large outward shift of the plasma during the current-initiation phase. Bulk electron heating up to about 150 eV was clearly observed, but the bulk ion temperature was estimated to be no more than 10 eV, although an ion tail in the range 1-2 keV was generated early in the discharge, possibly by the parametric decay waves. No definite explanations were given for the bulk electron heating.

1.4.5 Combined Steady-State ECCD/LHCD

There have been relatively few experimental results published on the efficiency of steady-state combined EC/LH current drive. Experimental results have been

presented by the WT-2 group [37,50], the JFT2-M group [51,52], and the T-7 group in Russia [53].

In 1986 Ando and coworkers [50]reported results from an experiment in which they injected 80 kW of ECH at 35.6 GHz for 5 ms into a LH-current-sustained plasma (with LH power of 48 kW at 915 MHz for about 32 ms). The ECH was launched from the top at $R - R_0 = -4.5$ cm in an equal mixture of the X-mode and O-mode, and the LH waves were launched from a phased array of four waveguides on the outside with $4 \leq |N_{\|}| \leq 10$. No ohmic power was applied to these discharges. The current was ramped only by LHCD and the loop voltage induced by the vertical field, with the initial seed current created by ECH. The tokamak transformer primary was shorted, as with the startup experiments discussed previously. The toroidal field was high ($B_t = 1.5$ T) so as to position the EC resonance layer near the outside of the plasma ($R - R_0 = +0.8a$). The ECH source was pulsed twice during each discharge, once at the beginning for plasma formation, and once later during the LHCD phase. The second pulse increased dI_p/dt and resulted in a higher plasma current at the end of the LHCD discharge than without the second application of ECH. Data from soft X-ray detectors, a pyroelectric detector, and a vacuum ultraviolet spectrometer indicated that the hot electron population (≥ 1 keV) grew or was heated during the ECH but that the bulk electrons ($\sim$20 eV) were not. On the other hand, when the ECR layer was placed toward the inside of the torus, at $R - R_0 = -0.3a$, the plasma current was reduced. In this case, the radiation measurements collectively indicated that the bulk electrons were heated by between 20 eV and 70 eV, and the suprathermal electrons were not. The authors were unable to explain this result. The slowing-down time of the suprathermal electrons was estimated to be about 60 ms, much longer than their confinement time and the ECH pulse length.

Later in 1986, Ando, et. al. [37]reported these results again, this time in conjunction with results from ECCD of an ohmically-heated (OH) plasma. In the ECCD experiments, EC waves were launched from the low-field side in the X-mode

at at angle of 48° from the toroidal field. The authors suggested that the ECH was heating the suprathermal electron tail created by the loop voltage applied earlier in the discharge. The dependence of dI_p/dt during ECCD on the location of the EC layer for these discharges was opposite of that for the ECH/LHCD discharges with top-launch. No explanation for this behavior was given. The electron density in these experiments was 1×10^{12} cm^{-3}.

In 1991, Kawashima, et. al. [52]reported results of second-harmonic EC heating of LHCD plasmas on the JFT-2M tokamak. They achieved a 65 kA/s ramp-up of the LH-driven current with 70 kW of EC waves in the X-mode polarization. They observed evidence of selective perpendicular heating obeying the relativistic resonance condition, and they deduced a 15% absorption efficiency at $\omega/2\omega_{ce} = 0.76$. However, no significant increases in steady-state driven current were observed during ECH.

CHAPTER 2
EXPERIMENTAL APPARATUS

2.1 THE TOKAMAK AND MICROWAVE SYSTEMS

The parameters of the Versator-II tokamak are shown in Figure 2-1, together with a top view of the tokamak and the locations of its major systems and diagnostics. The focus of research at this facility has primarily been on current drive and heating with radiofrequency waves. Versator was the first tokamak for which a lower-hybrid system was designed specifically for current drive, and it was one of the first on which current-drive results were reported [12]. These early results were obtained using an 800 MHz 150 kW radiofrequency (rf) system with a klystron source and a waveguide "grill" launcher, as is now conventional. Later, a 2.45 GHz system was installed by Mayberry [54], who tested the frequency scaling of the LHCD density limit. This system was used for the experiments described in this thesis. A schematic of this apparatus is shown in Figure 2-2. This system included two klystrons, which supplied rf power to a 4-waveguide side-launcher that was designed to launch slow lower-hybrid waves from the outer midplane of the tokamak. The waveguides could be phased independently so that, for example, a toroidally asymmetric wave spectrum could be launched. The calculated $N_{\|}$-spectrum of this grill is shown in Figure 2-3 for relative waveguide phasings $\Delta\phi$ of 90° and 180°. For $\Delta\phi = 90°$, net toroidal wave momentum is launched into the plasma, making this phasing more efficient for driving current than $\Delta\phi = 180°$. The Varian klystrons that provided the rf were powered by a high-voltage power supply consisting of a capacitor bank and modulator fed by a high-voltage charging supply. The system could produce up to 100 kW at 2.45 GHz for 40 ms, although power delivered to the

Versator-II Parameters

Major Radius	0.405 m
Minor Radius	0.13 m
Toroidal B-Field	$\leq$1.25 Tesla
Plasma Current	$\leq$50 kA
Central Electron Temperature	<500 eV
Central Ion Temperature	<150 eV
Electron Line-Averaged Density	$\leq 2.5\times10^{13}$ cm^{-3}
Discharge Duration	<75 ms
Electron Particle Confinement Time	0.5–2 ms
Z_{eff}	2–4

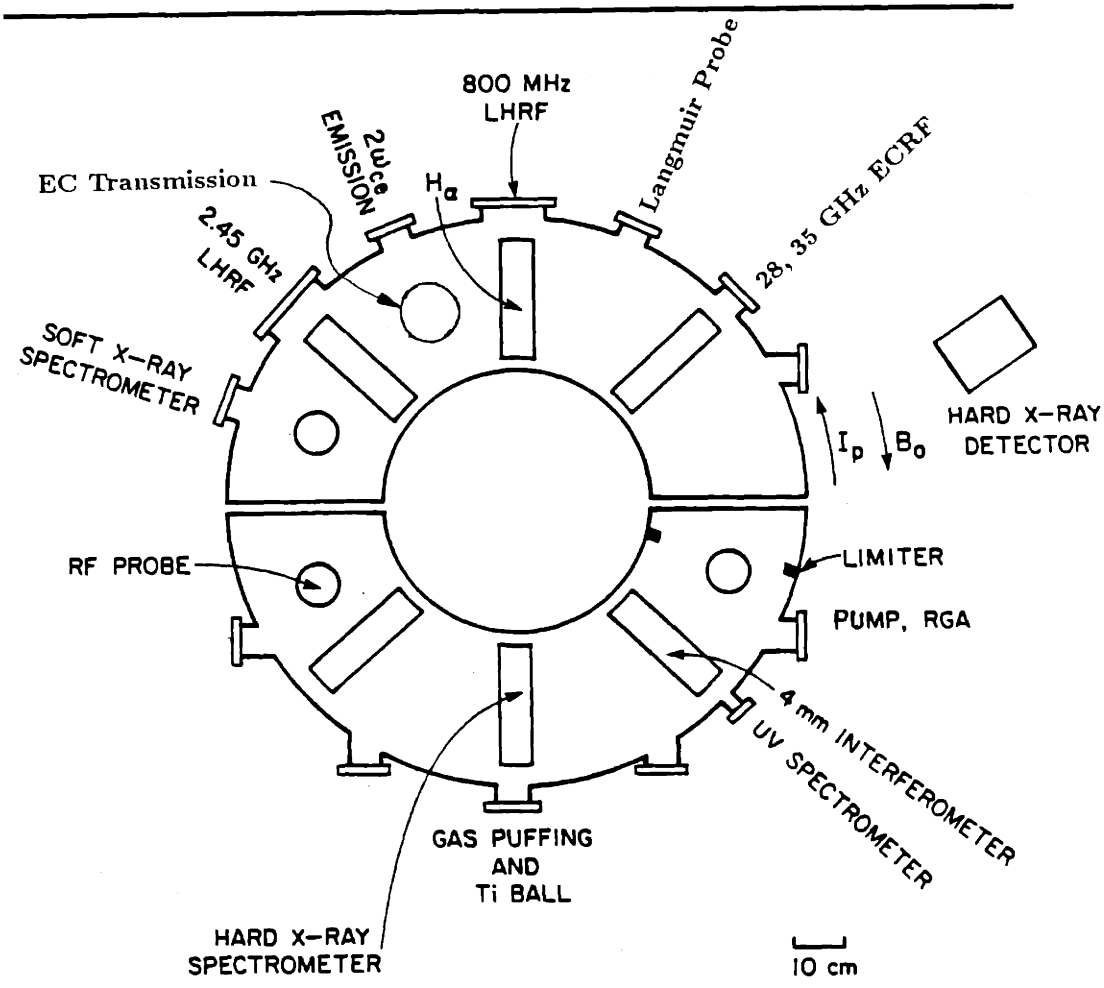

Figure 2-1 Top View of Versator-II.

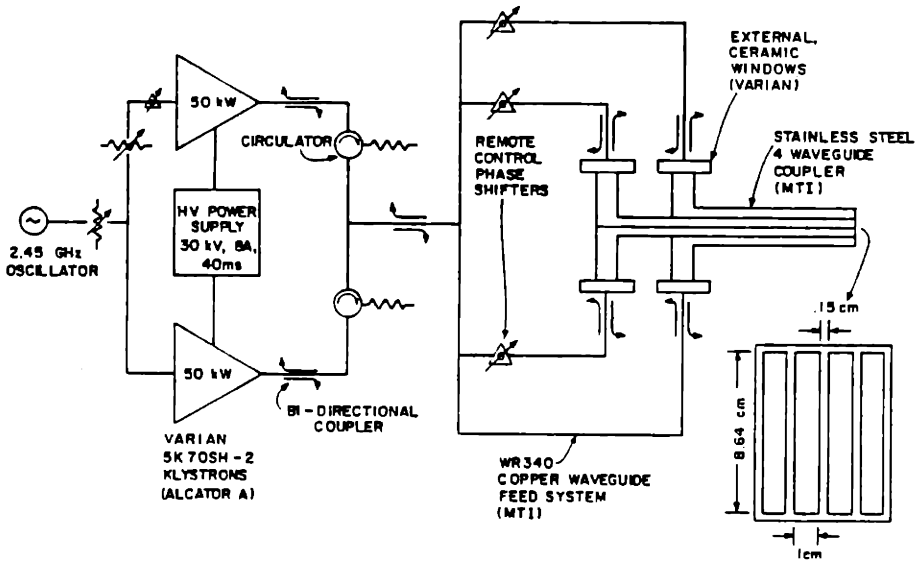

Figure 2-2 Schematic diagram of the Versator 2.45 GHz LH system. (from ref. [54])

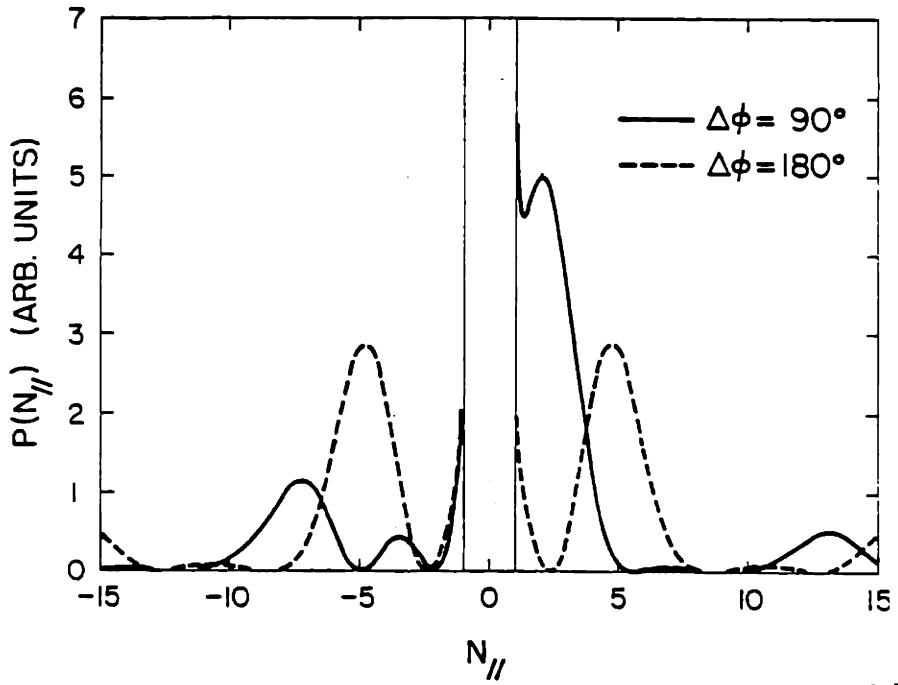

Figure 2-3 Launched spectrum of the 2.45 GHz antenna (from ref. [54])

plasma was typically somewhat lower. More detailed information on the 2.45 GHz lower hybrid system can be found in reference [54].

The major apparatus constructed specifically for the experiments described in this thesis were the Versator ECH systems, schematic diagrams of which are shown in Figures 2-4 and 2-5. Experiments were first carried out using a 35.07 GHz gyrotron manufactured by the Naval Research Laboratory, and the bulk of the experiments were later performed with a 28 GHz gyrotron manufactured by Varian. Both gyrotrons used the same 8 A, 90 kV power supply, and the same fault-detection and interlock circuitry was employed. The 35 GHz gyrotron used a superconducting magnet to produce the axial guide field for the electron beam. The transmission line was custom built and consisted of mode converters and filters that convert the TE_{01}-mode circular output of the gyrotron into the HE_{11}-mode, which is a linearly polarized mode. The HE_{11}-mode was launched from the high-magnetic-field side of the plasma via a rotatable mirror, which allowed launch angles $20° < \theta < 160°$, where θ is the angle between $\mathbf{k}$ and $\mathbf{B}_0$. The mode converters were rotatable so that any polarization angle could be launched.

The charging supply was controlled via a personal computer, and could charge the capacitor bank up to 90 kV. The high-voltage (HV) modulator was triggered externally by the Versator sequencer or a pulse generator, allowing a HV pulse to propagate from the bank to the voltage divider junction via RG-218/U HV cable. The magnitude of this pulse was determined by a request setting, via a regulation circuit, ensuring a flat-topped pulse of the desired magnitude. The divider junction passed the full regulated voltage to the gyrotron gun cathode via an oil-tank terminal hookup. Similarly, 50% of the voltage was fed to the modulation anode of the gyrotron gun. These high voltages were negative, so that an electron beam could be emitted from the gun. An interlock and fault detection system crowbarred the bank within 15μs of one of the following events: an arc in the gyrotron, on the gyrotron window, or elswhere in the system sufficient to cause more than about 20A to be drawn from the bank; failure of the gyrotron oil cooling system; depression of

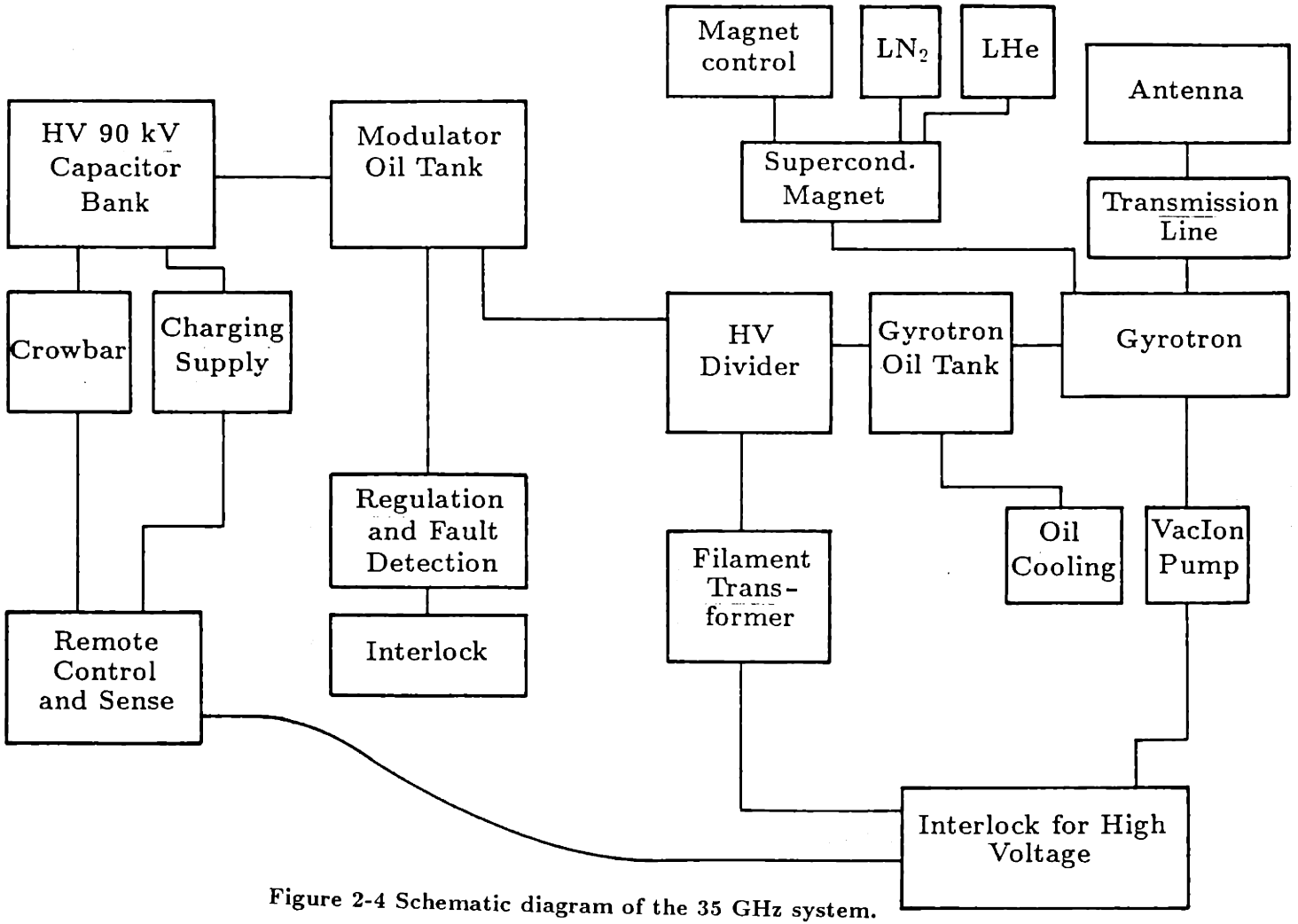

Figure 2-4 Schematic diagram of the 35 GHz system.

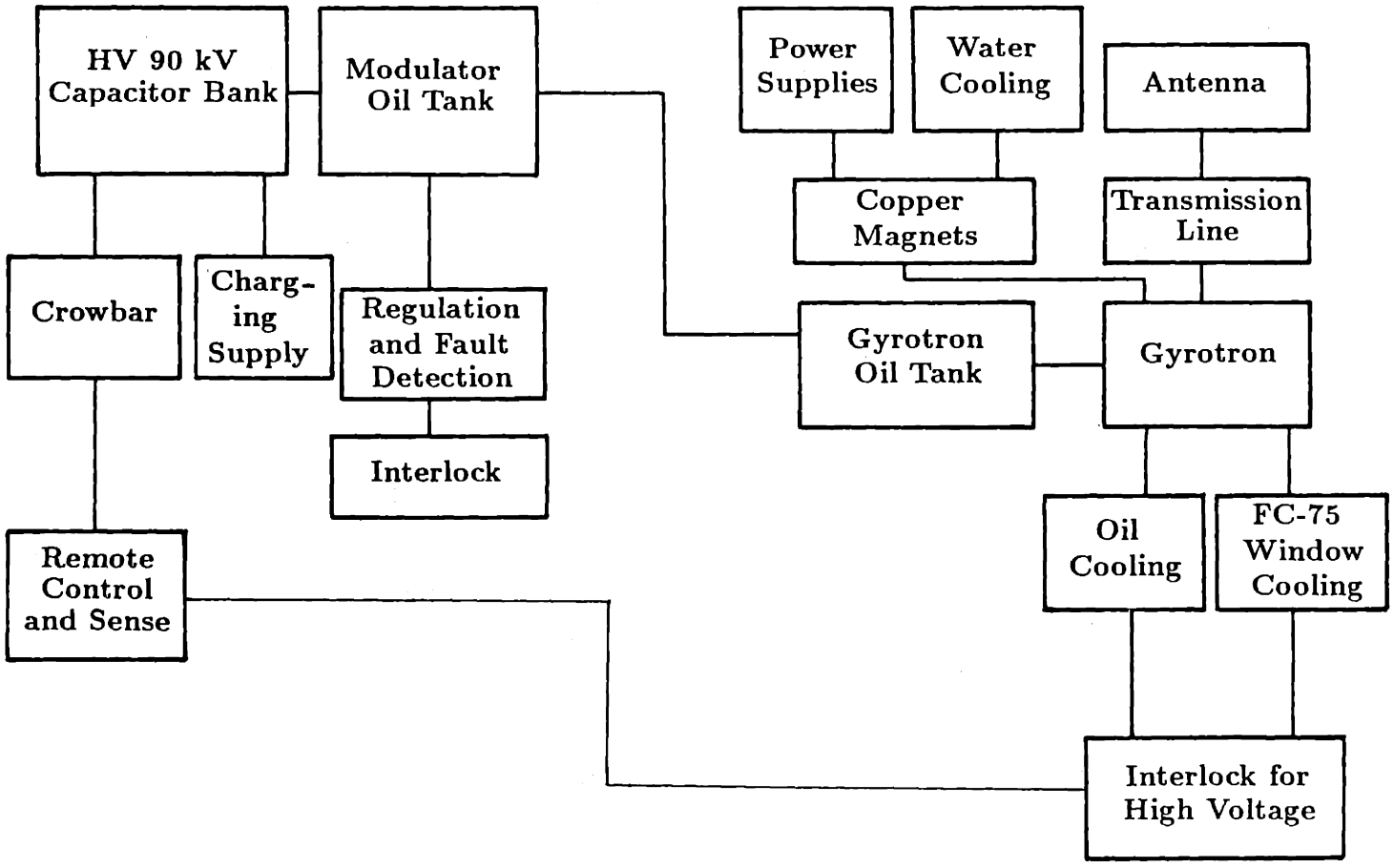

Figure 2-5 Schematic diagram of the 28 GHz system.

the panic button; opening of the door to the capacitor bank area; or failure of the fault-generator capacitor or of one of the modulator power supplies.

A schematic diagram of the 35 GHz gyrotron [55], transmission line, and antenna is shown in Figure 2-6. The main components of the gyrotron are the gun, the interaction region (or cavity), and the collector. The gun and interaction region were immersed in an axial magnetic field, which for the 35 GHz gyrotron was produced by a superconducting magnet. The principal components of the gun include the cathode, which was heated by an internal filament, and the modulation anode. A commercial high-voltage isolation transformer supplied 10 VAC to the gun cathode filament, which floated at the full gun potential. The 35 GHz gyrotron produced radiation in the TE_{01} mode, traveling in circular waveguide axially out of the tube away from the gun. Some short-pulse preionization and startup experiments were performed with the 35 GHz system, but the gyrotron failed to perform as advertised, and pulse lengths were limited (by arcing in the gun region) to 2-3 ms at up to 75 kW, even after extensive conditioning, rebuilds, and modifications. I attribute this poor performance to two fundamental design flaws: the gun is too small, making the electric fields very strong between the gun cathode and the nearby anodes (Varian, the manufacturer of the gun, recommends that it be used for pulse lengths not exceeding a few microseconds); second, the rubber O-ring seal and teflon electrical break between the cavity and the collector prevented the tube from being properly baked at high temperature (to outgas impurities from the walls) and may have continuously leaked small amounts of air. This made it impossible to achieve the ultra-clean vacuum environment necessary to sustain gun operation for longer than 2-3 ms. An experimental short ceramic electrical break and seal was built and tried, but its vacuum seal failed during cooldown from bakeout, presumably due to differential contraction between the ceramic and its copper seal.

The second ECH system was completely installed in three months, using the existing HVPS and control system. A Varian 28 GHz gyrotron was brought over

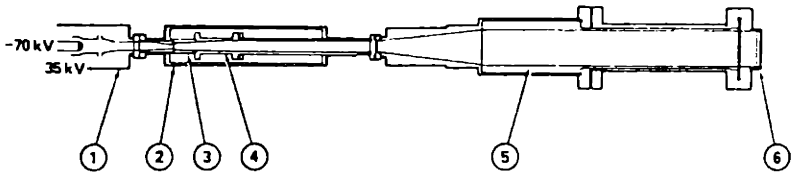

Schematic of the long pulse 35-GHz oscillator (1) electron gun, (2) vacuum envelope, (3) cavity, (4) output guide, (5) collector, and (6) output window.

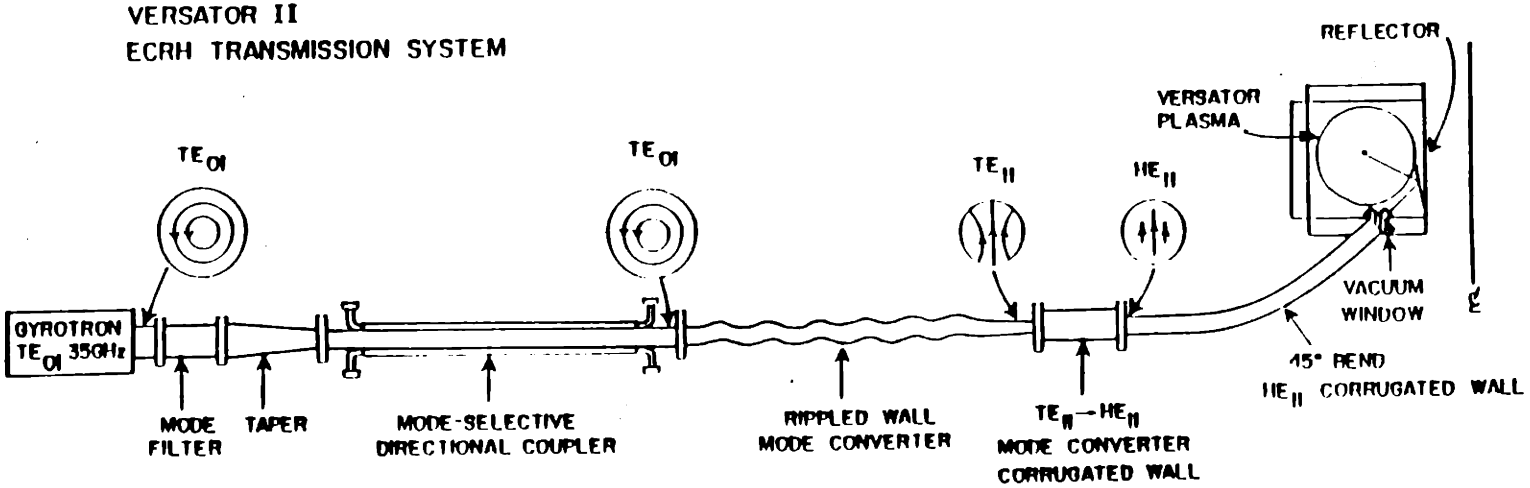

Figure 2-6 Schematic diagram of 35 GHz gyrotron and transmission line.

from a retired fusion experiment (TARA) on another part of campus, and it subsequently performed reliably, generating pulse lengths of up to 20 ms (limited by the power supply) at powers of up to 100 kW. A block diagram of the 28 GHz system is shown in Figure 2-5. This gyrotron used conventional copper magnets that dissipated about 60 kW continuously during an experimental run. This required substantial water cooling. The beam collector also required water cooling, but the tube was run at very low duty cycles ($\lesssim 10^{-4}$), so the beam was not a significant fraction of the heat load. Adequate cooling was achieved with about 30 gallons per minute of distilled water circulated through a heat exchanger with 55 degree plant water. The water cooling system was built from scratch, and it is shown in Figure 2-7. It included a primary loop, in which chilled plant water was circulated through a high-efficiency heat-exchanger by a 1/2 hp bronze pump. Distilled water was circulated through the secondary of the heat exchanger and through the gyrotron magnet coils and beam collector by a 3 hp bronze pump. Included in this loop were an air scoop with expansion tank, pressure gauges, thermometers, several air bleed valves, flow indicators, and traps. A cleansing loop ran in parallel to the secondary of the heat exchanger. This loop was valved off during main pump operation, but between runs could be activated to refresh the purity of the secondary water. It included a small 1/25 hp cirulator pump, a filter, and a deionizer. All components coming in contact with the secondary water were copper, bronze, brass, or plastic, to avoid contamination.

The output microwave window of the gyrotron required cooling with FC-75, a common solvent. This cooling system was in place when I received the tube. The filament power supply, filament oil-cooling system, and all high-voltage components feeding the gun were supplied and in place, as were the magnet coils. Additional interlock switches were added for the magnet and collector water flows, the currents in the main, gun, and collector magnet coils, the FC-75 flow through the output window, the door to the room, and nitrogen pressure in the transmission line (used to supress waveguide arcs). Arc detectors were added at the gyrotron window and

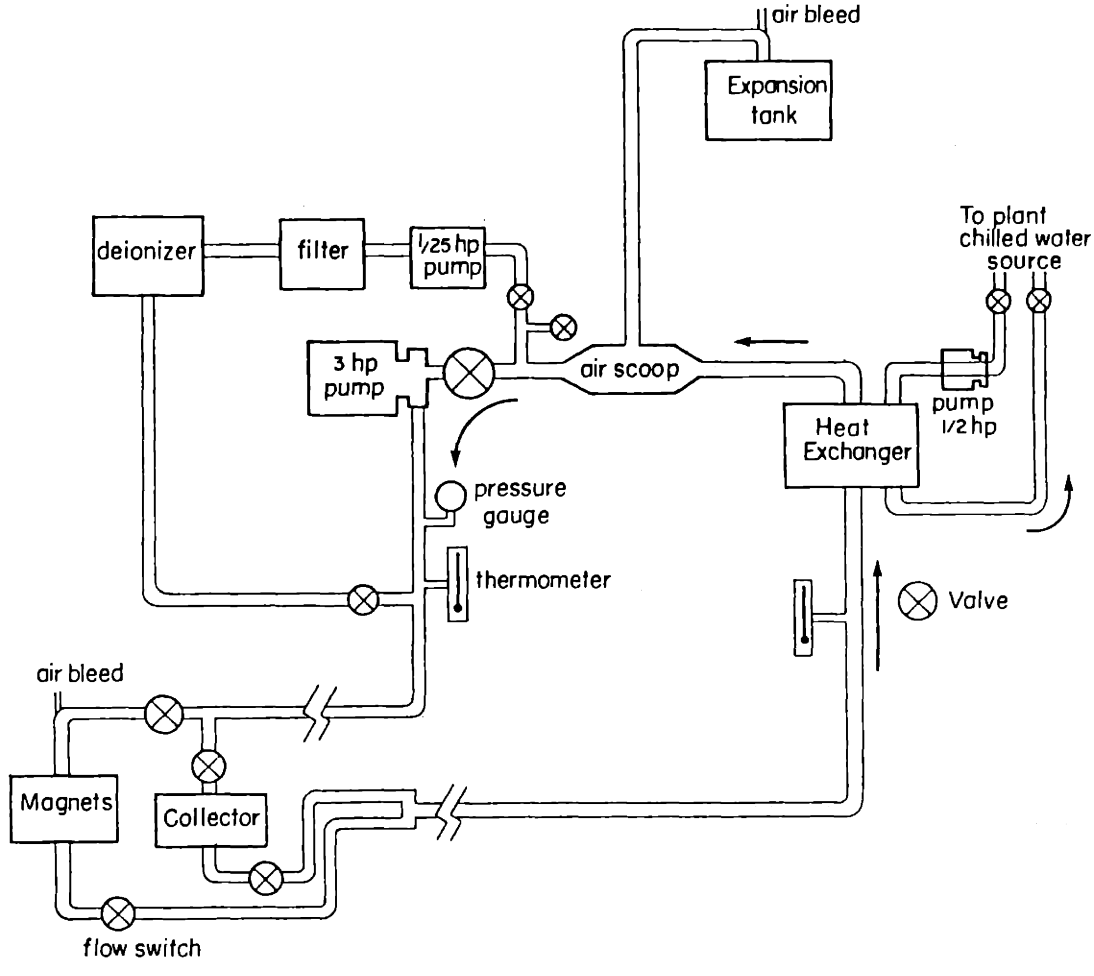

Figure 2-7 Water cooling system for 28 GHz gyrotron.

the outside tokamak waveguide window. The interlock and fault detection input circuits are shown in Figure 2-8.

Because of the change in gyrotron frequency, an entirely new transmission line was required. All of the expensive components were borrowed from sources on campus and from Culham Laboratory in the United Kingdom, and the few remaining components were built in-house. A schematic diagram of the 28 GHz trasmission line is shown in Figure 2-9. The output power of the Varian gyrotron is about 80% in the TE_{02}-mode, with about 10% in the TE_{01}-mode and 10% in other modes [56]. The transmission line was optimized for the TE_{02}-mode as the output from the gyrotron. A new antenna was built for outside midplane perpendicular launch, primarily for the O-mode, and the old 35 GHz inside launch antenna and rotatable mirror were rebuilt to accomodate 28 GHz waveguide. The final mode launched into the plasma by this tranmission line is the TE_{11}-mode, which is mostly linear in polarization, but not quite as linear as the HE_{11}-mode launched by the 35 GHz transmission line. The 45° bend under the tokamak required for the inside launch was accomplished by building a mitre-bend in smooth-walled waveguide to replace the gradual bend in corrugated guide used for the 35 GHz system. Microwave breakdown in this mitre bend limited inside-launched power to about 35 kW for the 28 GHz experiments with X-mode polarization, and about 50 kW for O-mode launching. This power was sufficient to match the ECH power densities of larger tokamaks, and was adequate for all the experiments described in this thesis.

2.2 THE DIAGNOSTICS

The primary Versator-II diagnostic set available during these experiments was as follows. The plasma current, toroidal field coil current, vertical field coil current,

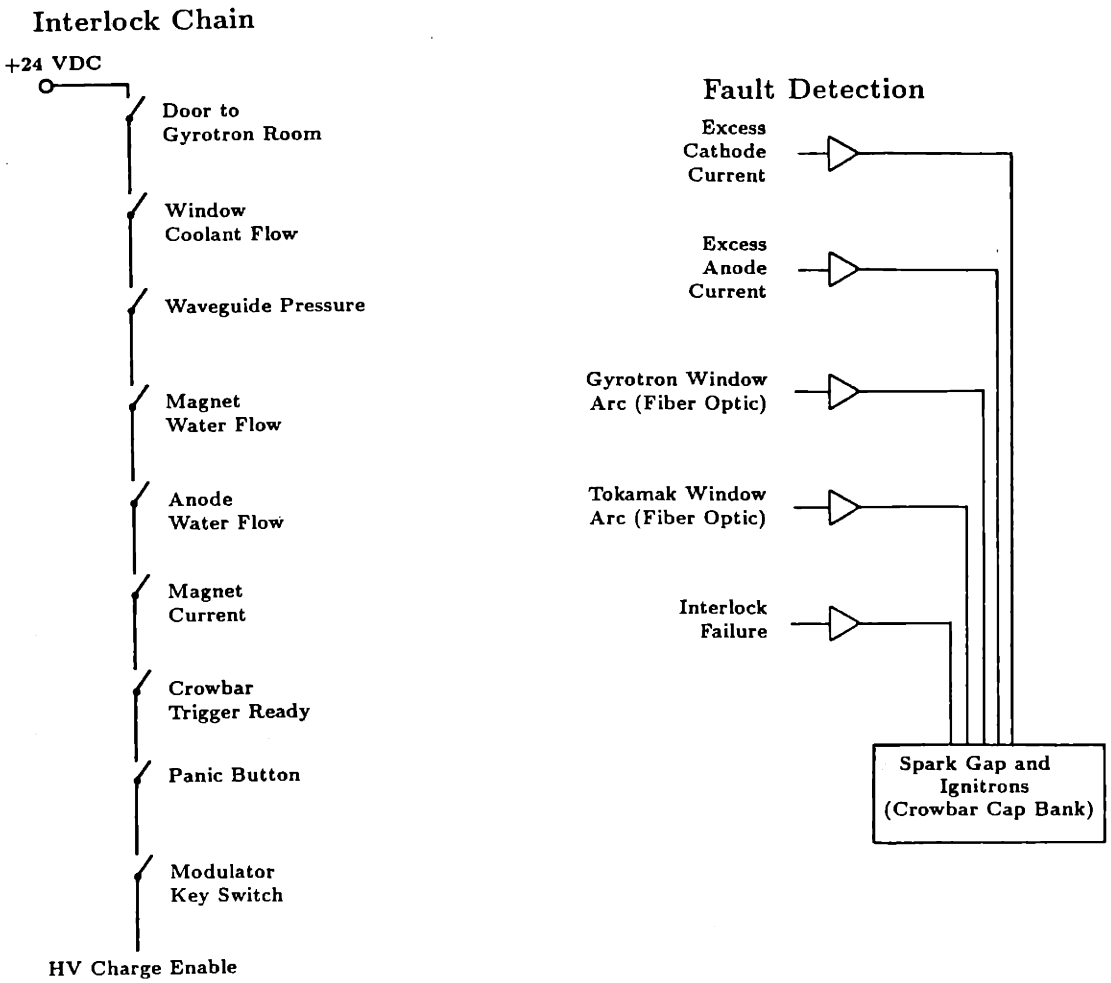

Figure 2-8 Interlock chain and fault-detection tree for the 28 GHz system.

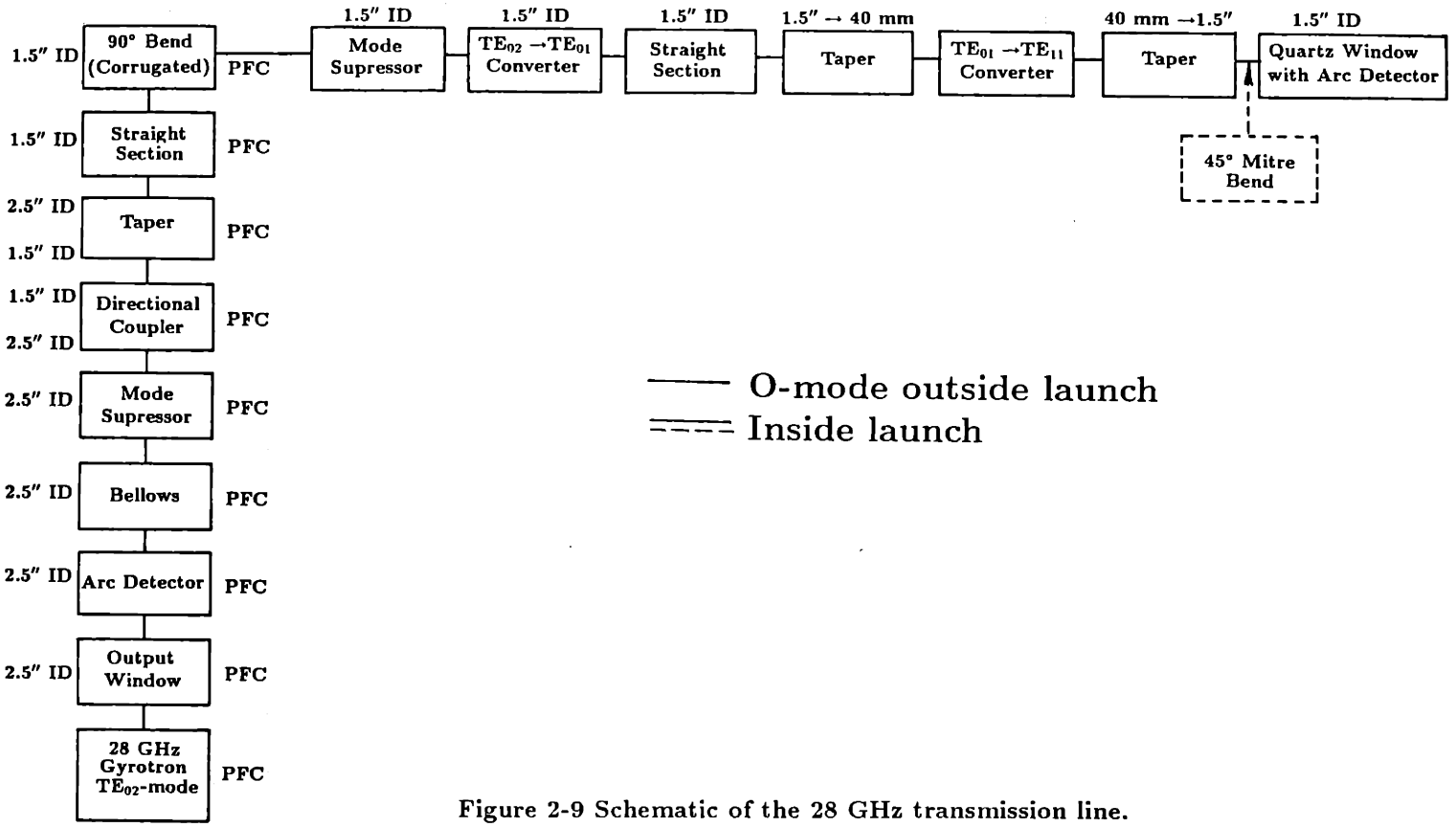

Figure 2-9 Schematic of the 28 GHz transmission line.

and ohmic heating coil current were monitored with Rogowski coils. The loop voltage was monitored by averaging the voltage across one-turn toroidal coils placed at the four corners of the vacuum-vessel poloidal cross-section. Energy-integrated hard X-rays with $E \gtrsim 100$ keV emitted from the limiter were monitored using a sodium-iodide scintillation detector, and 70 GHz microwave emission was monitored using a heterodyne receiver with receiving horn mounted on the side of the tokamak, viewing inward across the midplane. The vertically-averaged electron density was measured by a microwave interferometer (f=75 GHz) with movable transmitting and receiving horns. These horns could be moved via computer in the control room to any desired major radius from R =32 cm to R =53 cm, in 1 cm increments, enabling density profiles to be obtained on a shot-to-shot basis. The position of the plasma current channel in major radius was monitored with magnetic pickup coils outside the vacuum chamber and calculated by modeling the current channel as a toroidal wire. The vertical position of the plasma current channel could also be monitored in this way, although it was not monitored for most of these experiments. The H_α emission was measured with a diode detector placed on a movable carriage beneath the tokamak or on a fixed mount viewing the plasma from the outer midplane. Noise from the LH system was often a problem for this detector, and this prevented its use for the majority of the LHCD experiments. All rf powers were measured using calibrated directional couplers and crystal detectors. The electromagnetic wave spectrum at the plasma edge was monitored with an rf probe placed at the top of the tokamak, connected via low-loss coaxial cable to a 0-2.5 GHz spectrum analyzer. This could be used to observe the amplitudes and frequencies of decay waves from the lower-hybrid and electron-cyclotron waves, as well as the 2.45 GHz pump wave.

In addition to the standard set of diagnostics, the follwoing specialized diagnostics were used to study the fast electron distribution function and turbulence during these experiments. The radial hard X-ray detector array, designed and built

primarily by another graduate student, Jared Squire, was used to measure brehmstrahlung emitted from the plasma at various major radii [57]. A radial array of seven detectors, viewing upwards, were placed in a large lead enclosure beneath the tokamak. The detectors were spaced 4 cm apart. The X-rays emitted from the plasma were collimated by two tungsten plates and by lead shielding, and the entire apparatus was on wheels so that it could be moved radially between shots. Signal from the detectors was fed to a pulse counter and a pulse-height analyzer. The pulse counter measured the energy-integrated photon flux to each detector, giving a radial profile of hard X-ray emission for each shot, and the pulse height analyzer recorded the energy of each incoming photon, yielding an energy spectrum for each radial position when summed over many shots. The detectors are sensitive to photon energies in the range 30 keV to about 500 keV, which covers well the range of interest for the Versator experiments. Measurements were also taken using an angular array of hard X-ray detectors. For this array, the detectors from the radial array were housed in lead boxes with a wall thickness of about four inches. The detectors were placed at various locations around two side ports of the vacuum chamber so as to view the plasma from different angles. This gives information about the dependence of the fast electron distribution function versus pitch angle from the toroidal magnetic field. More detailed information on the hard X-ray detector arrays can be found in reference [57]. A Silicon-Lithium (SiLi) crystal was used to measure the soft X-ray flux in the 1–25 keV energy range. This detector viewed the plasma horizontally from the outer midplane, and was used to collect energy-integrated and spectral data.

An electron cyclotron transmission diagnostic was developed and built for these experiments. This diagnostic measured the asymmetric part of the superthermal electron distribution function. It was based on the diagnostic developed by Kirkwood [58], with improvements in the hardware, the mode of operation, and the data analysis. A schematic diagram of the system is shown in Figure 2-10. A microwave source tunable in the range 26.0 GHz$< f <$ 40.0 GHz was used to send about

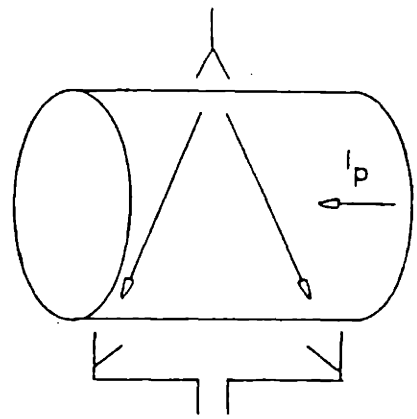

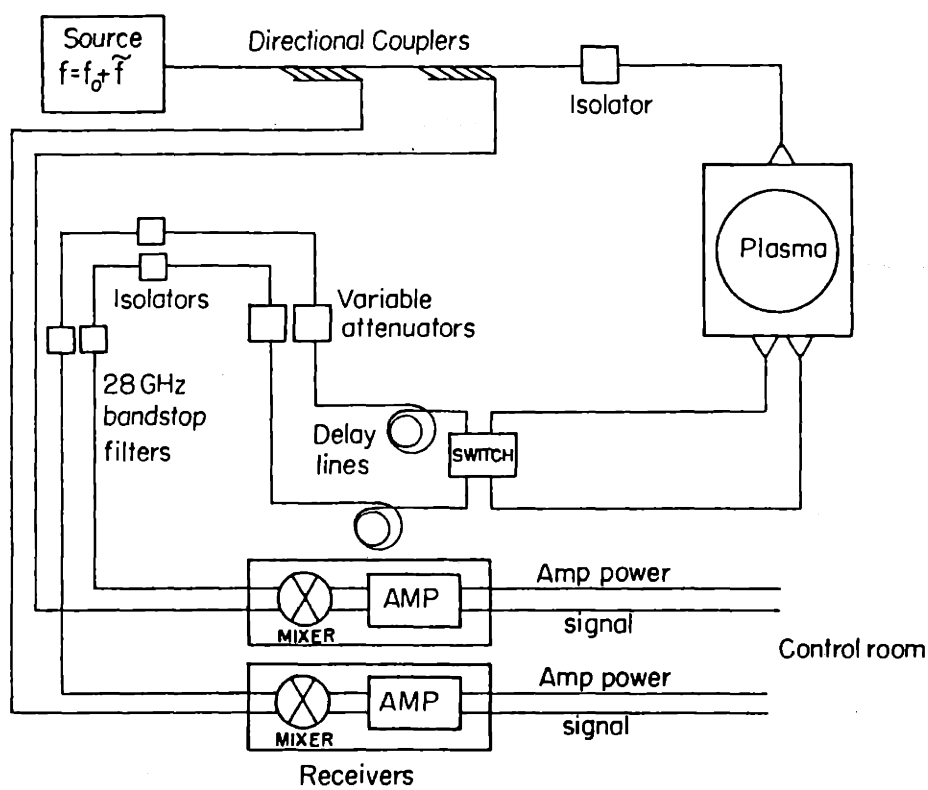

Figure 2-10 Schematic diagram of the upgraded ECT diagnostic.

10 mW to a directional coupler, which sent about 10% of this rf power to the local oscillator port of each of two balanced mixers. The remainder of the power was evenly divided between two horns at the top of the tokamak. These horns launched beam patterns centered at $N_{\|} = \pm 0.4$ toward two receiving horns as shown. Recall from section 1.4 that the absorption of electromagnetic waves in this frequency range is governed by the cyclotron resonance condition $\omega - \omega_{ce} = k_{\|} v_{\|}$, where ω is the source frequency, $\omega_{ce} = eB/\gamma m_e$ is the local relativistic cyclotron frequency, $k_{\|} = \omega N_{\|}/c$ is the wave number parallel to the magnetic field, and $v_{\|}$ is the parallel velocity of the absorbing electron. If more electrons are traveling in one parallel direction than the other, the absorption of the two beams will be unequal, but other wave loss mechanisms such as refraction or scattering will tend to be the same for the two beams. Therefore the asymmetric part of the electron distribution function at a particular parallel energy can be measured by comparing the relative attenuation of the two beams for a given frequency. The two received signals were sent to a waveguide switch, and then each was passed through a delay line and ferrite isolator before being sent to the rf port of each of the mixers. Each mixer was enclosed in an rf-tight copper capsule lined with echosorb, together with a small amplifier for amplifying the intermediate frequency output (DC in this case) of the mixer. Each capsule and its contents is referred to as a receiver. The output from each receiver was passed to the control room via double-shielded twisted-pair cable encased in steel conduit. The waveguide switch allowed each receiving horn to be connected to either receiver, so that differences between the two receivers could be accounted for. The extensive shielding was required to keep out noise from power supplies and rf from the 2.45 GHz LH system and the 28 GHz system, while measuring about 1 μW of transmitted signal. Each mixer produces an output proportional to $A_{rf} A_{lo} \sin\phi$ where A_{rf} is the amplitude of the wave received by the receiving horn, A_{lo} is the amplitude of the local oscillator signal, and ϕ is the phase angle between the two signals at the mixer ports. Because only the ratio of A_{rf} during the plasma discharge to A_{rf} in the absence of plasma is the desired quantity, A_{lo}

divides out. Its value is only dependent on the source output, not on the presence of plasma. The phase angle ϕ is affected by the presence of plasma, and can change considerably during a discharge. Therefore, I averaged over ϕ by rapidly modulating the source frequency in a narrow band about the desired center frequency. The delay lines on each receiving leg reduced the band required to average over a full period in ϕ to about 100 MHz. This enabled one period of modulation in less than one-tenth of a millisecond with the microwave source available. This gave a time-resolution of about one-tenth of a millisecond and a frequency-of-interaction resolution of 100 MHz, significantly improved over prior values for this diagnostic.

Edge magnetic, density, and potential fluctuations were monitored with a set of magnetic pickup probes and Langmuir probes. The magnetic fluctuations were measured in the frequency range 0-400 kHz. The turbulent fluctuations in the range 50-500 kHz are thought to be related to the transport of thermal particles and energy in tokamak plasmas. They may also enhance fast electron losses, decreasing the current-drive efficiency. The magnetic probes used for most of the measurements were part of a toroidal array, constructed by Jared Squire [57]. A drawing of the probe array, as it appears inside the vacuum chamber, is shown in Figure 2-11. The probes were calibrated, so that the fluctuating magnetic field in the direction of the probe (coil) axis could be determined. The voltage induced across the terminals of each coil by plasma effects was sent to the control room via a multi-shielded cable. This signal was then amplified and low-pass-filtered at 450 kHz (3 dB point). The filtered signal was digitized at a 1 MHz sampling rate and stored on the computer disk. The toroidal array consisted of ten coils, with their axes oriented vertically. This nearly corresponds to the poloidal direction at the array location. The coils were spaced at varying toroidal intervals from $2\pi R/8$ to $2\pi R/256$, so that toroidal harmonics could be isolated by correlating signals from different probes. The data acquisition system could only digitize data from four probes at a time, so when data from more than four probes were desired, the cables were swapped between plasma discharges.

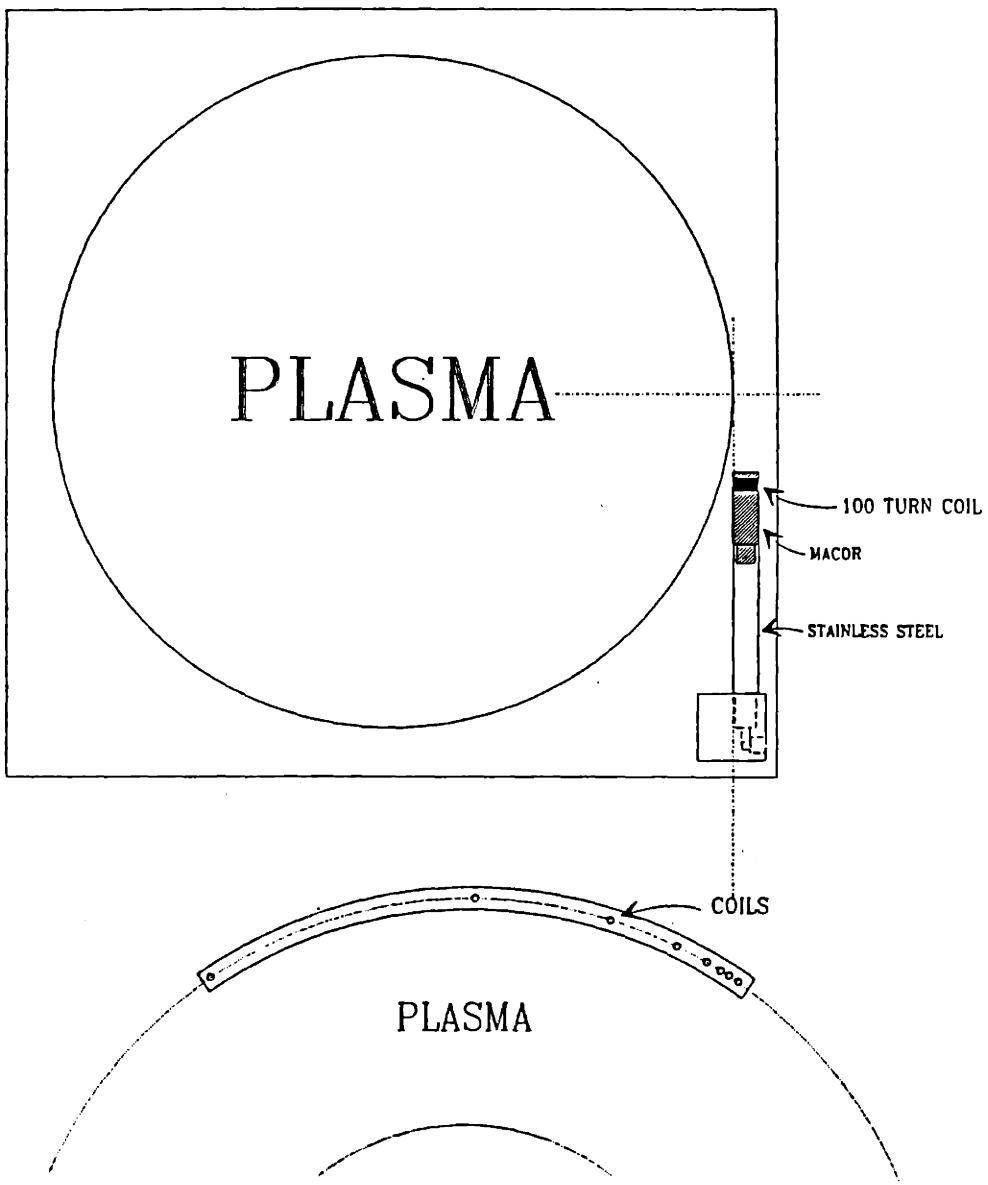

Figure 2-11 Poloidal and bottom views of the magnetic probe toroidal array.

Fluctuations in the edge plasma potential were monitored with a Langmuir probe and, to a limited degree, by an eight-piece isolated limiter. The probe was not biased, and it was connected directly to the amplifier and filter system. The signal was digitized at 1 MHz and stored on computer disk. Only low-frequency fluctuations could be observed with the eight-piece limiter, because its signal was digitized at 50 kHz.

CHAPTER 3
LOWER HYBRID CURRENT DRIVE EXPERIMENTS

In this chapter, measurements of the suprathermal electron distribution function during LHCD are described, along with supporting theory and analysis. These measurements were taken using the electron cyclotron transmission (ECT) diagnostic [59,60] and the perpendicular array of hard X-ray detectors described in the previous chapter. The observation and analysis of a "two parallel-temperature" feature of the fast electron distribution function during LHCD is described. This feature was not observed during ohmic discharges. Computational modeling suggests that the cold tail is initiated by low-power, high-$N_{||}$ waves from the sidelobes of the antenna $N_{||}$-spectrum, and that these waves bridge the "spectral gap," enabling current drive even though the wave phase velocity greatly exceeds the electron thermal velocity for the majority of the wave power [61]. This chapter is organized as follows. First, the theory of LH-wave-induced diffusion of electrons, ray tracing, and the spectral gap is described. Second, the ECT data is presented and analyzed, including modeling with the collisional quasilinear code CQL3D. Finally, the hard X-ray and density data are described, including the observation of an anomalous peak in the hard X-ray emission on the high-field side of the Versator plasma.

3.1 QUASILINEAR THEORY, RAY TRACING, AND THE SPECTRAL GAP

The diffusion of electrons in momentum-space by waves is described by the relativistic Fokker-Planck equation, which is derived [62,63] starting with the relativistic Vlasov equation:

$$\frac{\partial f}{\partial t} + \frac{\mathbf{p}}{\gamma m_0} \cdot \nabla f - e\left[\mathbf{E} + \frac{\mathbf{p}}{\gamma m_0} \times (\mathbf{B_0} + \mathbf{B})\right] \cdot \nabla_p f = \left.\frac{\partial f}{\partial t}\right|_{coll} \tag{20}$$

where $f = f(\mathbf{r}, \mathbf{p}, t)$ is the distribution function for electrons, $\mathbf{p}$ is the electron momentum, $\mathbf{B_0}$ is the applied DC magnetic field, $\mathbf{E}(\mathbf{r}, t)$ and $\mathbf{B}(\mathbf{r}, t)$ are the wave fields, $\gamma^2 = 1 + \hat{p}^2$, $\hat{p} \equiv p/m_0 c$, and $\left.\frac{\partial f}{\partial t}\right|_{coll}$ is the change in f due to collisions. The distribution function f is assumed to be composed of an average f_0 and a small, fluctuating f_1 such that $f = f_0 + f_1$, with f_0 averaged over gyro-angle. After some algebra, Equation 20 can be cast in the form of a diffusion equation for f_0:

$$\frac{\partial f_0}{\partial t} = \frac{\partial}{\partial \mathbf{p}} \cdot \overline{\overline{\mathbf{D}}} \cdot \frac{\partial f_0}{\partial \mathbf{p}} + \left.\frac{\partial f_0}{\partial t}\right|_{coll} \tag{21}$$

where $\mathbf{D}$ is the flux-surface-averaged diffusion tensor, which has a resonant and a nonresonant part. Equation 21 is the Fokker-Planck equation. It is generally a very good approximation to assume that the electrons are diffused only by resonant interaction with the waves. Thus the relevant part of the diffusion tensor is the resonant part, given by

$$\mathbf{D}_R = \frac{1}{V} \sum_{n=-\infty}^{\infty} \pi e^2 \int \frac{d^3 k}{(2\pi)^3} \delta\left(\omega - k_\parallel v_\parallel - n\omega_{ce}\right) \alpha^*_{\mathbf{kn}} \alpha_{\mathbf{kn}} \tag{22}$$

where $v_\parallel = p_\parallel / m_0 c$, $\omega_{ce} = eB/\gamma m$, and

$$\alpha_{kn} = \frac{1}{\omega}\left(\varepsilon_{kn} + \frac{p_\parallel}{p_\perp} J_n E_{kz}\right)\left(n\omega_{ce}\hat{e}_\perp + k_\parallel v_\perp \hat{e}_\parallel\right). \tag{23}$$

The unit vectors $\hat{e}_\perp$ and $\hat{e}_\parallel$ are in the directions perpendicular and parallel, respectively, to $\mathbf{B}_0$, $\varepsilon_{kn} = [(E_{kx} + iE_{ky})\, J_{n+1} + (E_{kx} - iE_{ky})]$, and J_n is the nth-order Bessel function of the first kind. The argument of the Bessel function is $k_\perp v_\perp / \omega_{ce}$.

Thus $\alpha^*_{kn}\alpha_{kn}$ incorporates the effects of the wave electric field strength and polarization on the diffusion coefficient.

For the case of lower hybrid waves, only the $n = 0$ term contributes significantly, and the diffusion tensor becomes a scalar, relating parallel diffusion by parallel gradients:

$$\frac{\partial f_0}{\partial t} = \frac{\partial}{\partial p_\parallel} D_{LH} \frac{\partial f_0}{\partial p_\parallel} + \left.\frac{\partial f_0}{\partial t}\right|_{coll} \tag{24}$$

where

$$D_{LH} = \frac{\pi e^2}{V} \int \frac{d^3k}{(2\pi)^3} \delta\left(k_\parallel - \omega/v_\parallel\right) \Lambda |E_{kz}|^2 \tag{25}$$

and

$$\Lambda = \frac{1}{|v_\parallel|} \left[\left[J_0 - \frac{v_\perp}{v_\parallel} J_1 \mathrm{Im}\left(\frac{E_{ky}}{E_{kx}}\right)\right]^2 + \left[J_0 \mathrm{Re}\left(\frac{E_{kz}}{E_{ky}}\right)\right]^2 \right]. \tag{26}$$

The function Λ incorporates the effects of the wave polarization on the diffusion coefficient. The field amplitude $|E_{kz}|$ is determined by solving the coupling problem for the antenna, and Λ is then determined by the local dispersion relation. The J_0 term describes diffusion by Landau damping, and the J_1 terms result from transit-time magnetic pumping. For lower hybrid waves, $|E_{kz}| \gg |E_{ky}|$ and $|E_{kx}| \gg |E_{ky}|$ so that $\Lambda \approx J_0^2/|v_\parallel|$ and Landau damping is the dominant diffusion mechanism.

The propagation of lower-hybrid waves in a tokamak can be modeled using the cold-plasma dispersion relation (Equation 9) together with the ray approximation, in which it is assumed that the scale length of variations in the plasma equilibrium quantities is much longer than the wavelength of the propagating wave [64]. The ray equations appropriate for toroidal geometry are Hamiltonian in nature, and can be written in terms of the toroidal coordinates r, θ, ϕ and their conjugates k_r, m, n, where k_r is the radial wavenumber, and m and n are the poloidal and toroidal mode numbers, respectively:

$$\frac{dr}{dt} = -\frac{\partial D/\partial k_r}{\partial D/\partial \omega} \tag{27}$$

$$\frac{d\theta}{dt} = -\frac{\partial D/\partial m}{\partial D/\partial \omega} \tag{28}$$

$$\frac{d\phi}{dt} = -\frac{\partial D/\partial n}{\partial D/\partial \omega} \tag{29}$$

$$\frac{dk_r}{dt} = -\frac{\partial D/\partial r}{\partial D/\partial \omega} \tag{30}$$

$$\frac{dm}{dt} = -\frac{\partial D/\partial \theta}{\partial D/\partial \omega} \tag{31}$$

$$\frac{dn}{dt} = -\frac{\partial D/\partial \phi}{\partial D/\partial \omega} = 0. \tag{32}$$

Equations 27-32 are the ray equations. Note that the axisymmetry ($\partial/\partial\phi = 0$) of a torus implies that the toroidal mode number n is a constant of the motion. Unlike a straight cylinder, however, a torus is not poloidally symmetric ($\partial/\partial\theta \neq 0$) so that the poloidal mode number m is *not* a constant of the motion. Equations 27-29 can be numerically integrated to give the ray trajectories in a tokamak, and Equations 30-31 can be simultaneously integrated along the ray path to give the evolution of k_r, m, and $k_{\|} \equiv \mathbf{k} \cdot \mathbf{B_0}/|\mathbf{B_0}| = [k_r B_r + (m/r)B_\theta + (n/R)B_\phi]/|\mathbf{B_0}|$. It can be seen that $k_{\|}$ will in general vary along the ray trajectory due to the combination

of m-variation (toroidicity) and B_θ-variation (shear). Note from Equation 25 that this will change the resonant parallel velocity of electrons that the LH-wave diffuses in velocity space.

Recall from Chapter 1 that high current-drive efficiency is predicted theoretically and observed experimentally only when the launched wave parallel phase velocity greatly exceeds the electron thermal velocity $\omega/k_\parallel \gg v_{te}$. One aspect of LHCD that is not well understood is the so-called "spectral-gap" problem, i.e., the problem of determining how waves launched with parallel velocities $\omega/k_\parallel \gg v_{te}$ Landau damp when the number of electrons resonant with such a wave in a Maxwellian plasma is exponentially small. For a small tokamak such as Versator with $25 \lesssim c/v_{te} \lesssim 50$, the damping and current drive is predicted to be very small for most of the wave spectrum launched by an LHCD antenna (Figure 3-1), yet successful current drive is observed experimentally [12, 54, 65-67] . Several mechanisms have been proposed to bridge the spectral gap [64, 68-70]. Perhaps the most universally accepted among these is the concept of toroidal upshift, in which the spectral gap is bridged by waves that upshift in $N_\parallel$ due to toroidicity [64]. This has been shown to be effective even for $v_{te} \approx c/45$ if the first forward sidelobe of the antenna spectrum (lobe #3 in Figure 3-1) is included in the modeled spectrum [72, 73] . It was predicted in references [72]and [73]that the low-energy part of the superthermal tail is elevated by this sidelobe. A similar elevation has been predicted for the outer, cooler regions of a hot plasma typical of larger tokamaks such as JT-60 [74]. This prediction followed work in which an ad-hoc "two-parallel-temperature" model for the superthermal tail, without direct experimental or computational verification, was proposed to explain the increase in the volume-averaged thermal electron temperature observed on the JT-60 tokamak [75].

Here the observation of a two-parallel-temperature superthermal tail on the electron distribution function during LHCD experiments on the Versator-II tokamak is described. In addition, results of modeling the steady-state solution to the Fokker-Planck equation are presented for conditions closely resembling those

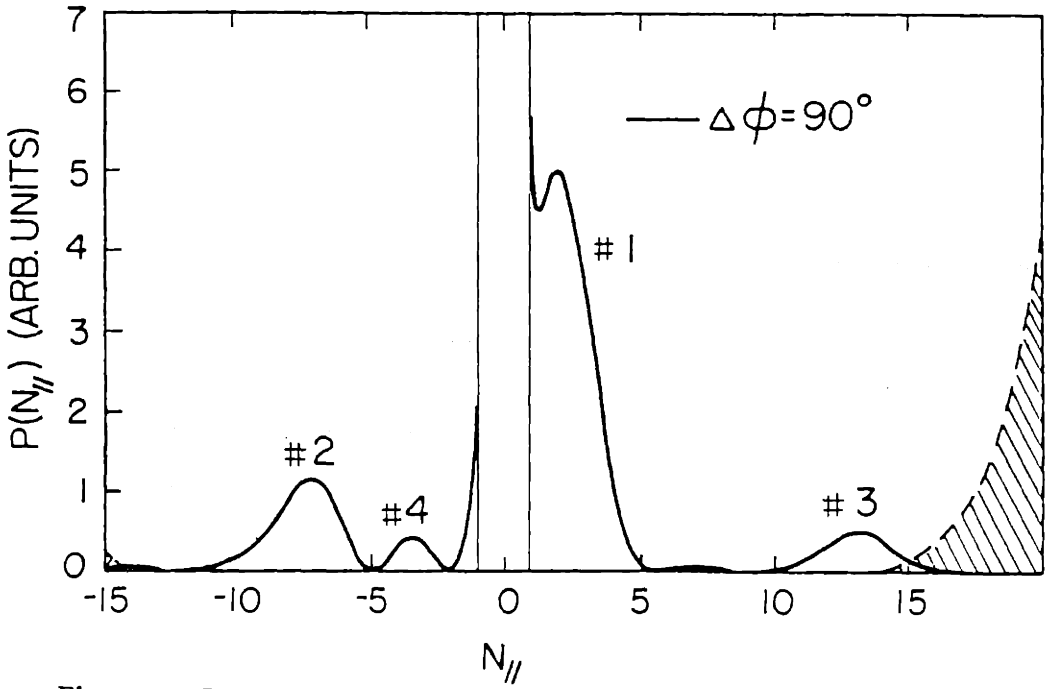

Figure 3-1 Launched LHCD power spectrum(from ref. [54]). Shaded region is thermal electron distribution function with $v_{te} = c/41$ ($T_e = 150$ eV).

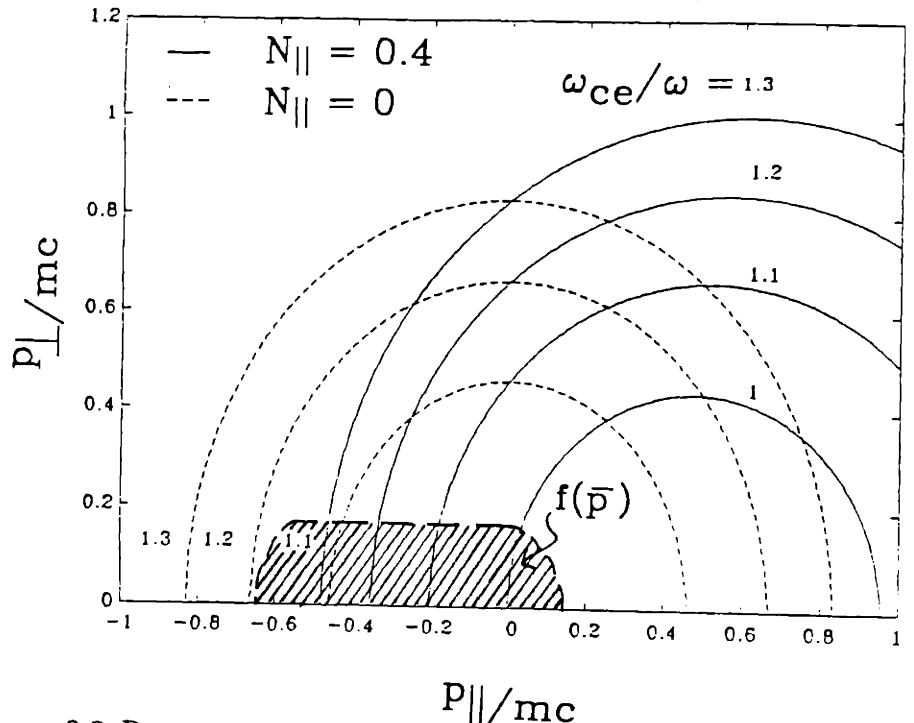

Figure 3-2 Resonance contours for perpendicular and oblique propagation (from ref. [59]). Superthermal electrons are expected in the shaded region.

of the experiment. These results suggest the cold superthermal tail is initiated by low-power, high-$N_{\|}$ waves from the first sidelobe of the antenna power spectrum ($10 < N_{\|} < 15$). Owing to toroidal effects, these waves upshift in $N_{\|}$, thus bridging the spectral gap and enabling the main power spectrum to damp and drive current. The cold tail and the net current are further enhanced by upshifted waves from the main power lobe (#1 in Figure 3-1), and by electrons that have been scattered $\sim 180°$ by ions after acceleration by waves with $N_{\|} < 0$ (lobe #2 in Figure 3-1).

3.2 ELECTRON-CYCLOTRON-TRANSMISSION MEASUREMENTS DURING LHCD

The fast electron distribution function was measured using the electron cyclotron transmission (ECT) technique [59, 76] . The physical principle of the technique is described in detail in reference [59]. Recent improvements in the apparatus, mode of operation, and data analysis are reported in reference [60], and the hardware is described in Chapter 2 of this thesis. The diagnostic uses the electron-cyclotron resonance condition $\omega - \omega_{ce} = k_{\|} v_{\|}$, where ω is the wave frequency, $\omega_{ce} = eB/\gamma m_e$ is the relativistic electron cyclotron frequency in the applied magnetic field B, and $k_{\|}$ and $v_{\|}$ are the wavenumber and resonant electron velocity, respectively, parallel to B. Strong absorption of electron-cyclotron-wave energy by electrons can occur along each "resonant semi-ellipse" described in velocity space by the above condition, as shown in Figure 3-2. If this absorption is measured, the number of electrons on or near a given semi-ellipse in velocity space can be deduced. For fast current-carrying electrons in a tokamak LHCD discharge, generally $v_{\|} \gg v_{\perp}$, so the absorbing electrons are clustered near the $v_{\|}$-axis at the ends of each semi-ellipse, so that to a good approximation, resonance occurs in only a narrow band of $v_{\|}$'s for a given semi-ellipse. The absorption, and hence the fast-electron distribution function f_e^{fast}, can be measured at different parallel velocities

by launching a low-power electron-cyclotron-wave across the plasma and varying ω or $k_{\|}$. The wave is launched top-to-bottom in a tokamak, so that $B \approx$ constant for the entire wave trajectory, and the extraordinary mode is used so that higher densities can be accessed. In practice, other mechanisms attenuate the wave besides resonant absorption, so two waves are launched with opposite parallel phase velocities. It is assumed that resonant absorption is the only attenuation mechanism dependent on the sign of $k_{\|}$, so that dividing the transmitted fractions of the two waves cancels the effects of the non-resonant mechanisms, yielding a measure of $\langle f_e^+ - f_e^- \rangle$, which is the asymmetric, or current-carrying, portion of f_e^{fast}, averaged over the plasma diameter. This results from the fact that the transmitted fractions of the two rays are proportional to $\exp(-\alpha_1 - \beta)$ and $\exp(-\alpha_2 - \beta)$, respectively, where the α's are the attenuation coefficients due to resonant absorption, and β is the attenuation factor due to non-resonant mechanisms. Corrections must be made to $N_{\|}$ and ω_{ce} in the assumed region of absorption due to refraction. Here these refractive effects were modeled using the electron-cyclotron ray-tracing code TORCH. [77]

Output plots for some of these runs are shown in Figure 3-3. The two primary effects of ray bending are to increase the effective ω_{ce} and the $N_{\|}$ of the received wave as the wave frequency approaches the cyclotron frequency in the plane of the transmitting and receiving horns. The first effect is a result of the ray bending toward lower magnetic field near the plasma edges, requiring the rays reaching the receiving horn to pass through a higher magnetic field region mid-chord, as shown in Figure 3-3. Thus the local cyclotron frequency is higher along the ray (especially in the central region of the plasma where the superthermal electrons are primarily located) than would be the case if the ray paths were along constant major radius R. The second effect results from the fact that the group velocity and the phase velocity diverge in direction as ω approaches ω_{ce}. The ray (and the wave energy) travels in the direction of the group velocity. This direction is fixed by the horn geometry, because the wave energy must pass from the transmitting horn to the receiving horn.

However, waves with the same group velocity directions but different frequencies will have different phase velocity directions (hence $N_{\|}$'s).

Because the transmitting and receiving horns are not infinitely separated, the received $N_{\|}$ is not perfectly resolved. Hence a beam of fixed frequency is absorbed by electrons with a finite distribution of energies [60]rather than of a single energy, as would be suggested by the electron-cyclotron resonance condition. This effect can be incorporated into the cyclotron absoption coefficient by substituting the following function [60]for the delta-function integrand (the resonance factor) into the expressions for the dielectric tensor elements:

$$\Delta = \frac{1}{\sqrt{\pi}} \exp\left[-\left(\gamma - \frac{n\omega_{ce}}{\omega} - N_{\|}\hat{p}_{\|} \right)^2 \left(\frac{k_{\|}d}{\hat{p}_{\|}} \right)^2 \right] \frac{\hat{p}_{\|}}{k_{\|}d} \tag{33}$$

where d is the beam width. This makes the measured distribution function appear flatter and smoother than the true function $\langle f_e^+ - f_e^- \rangle$. To get the true $\langle f_e^+ - f_e^- \rangle$, a test function for $\langle f_e^+ - f_e^- \rangle$ can be convolved with the absorption sensitivity function and the result compared with the data. This process can be iterated, or the output of a modeling code can be used as the test function, as is the case here. The convolved function, which is compared with the measurement, is denoted $\langle f_e^+ - f_e^- \rangle^*$.

Two series of discharges were analyzed from the Versator-II Tokamak with major radius $R_0 = 0.405$ m, minor radius $a = 0.13$ m, and toroidal magnetic field $B \leq 1.2$ T on axis. The plasma current, loop voltage, electron density, and toroidal magnetic field are shown in Figure 3-4. The discharges of the first series (shown by the solid curves in Figure 3-4) were sustained by LH waves with $V_{loop} < 0.05$ V and nearly constant $I_p \approx 15$ kA. The discharges of the second series (shown by the dashed curves) were driven ohmically with $V_{loop} \approx 1.0$ V, and I_p decreased from 23 kA to 10 kA at 1 kA/ms. The line-averaged electron density, central bulk electron temperature, and edge electron temperature were $\langle n_e \rangle = 8 \times 10^{12}$

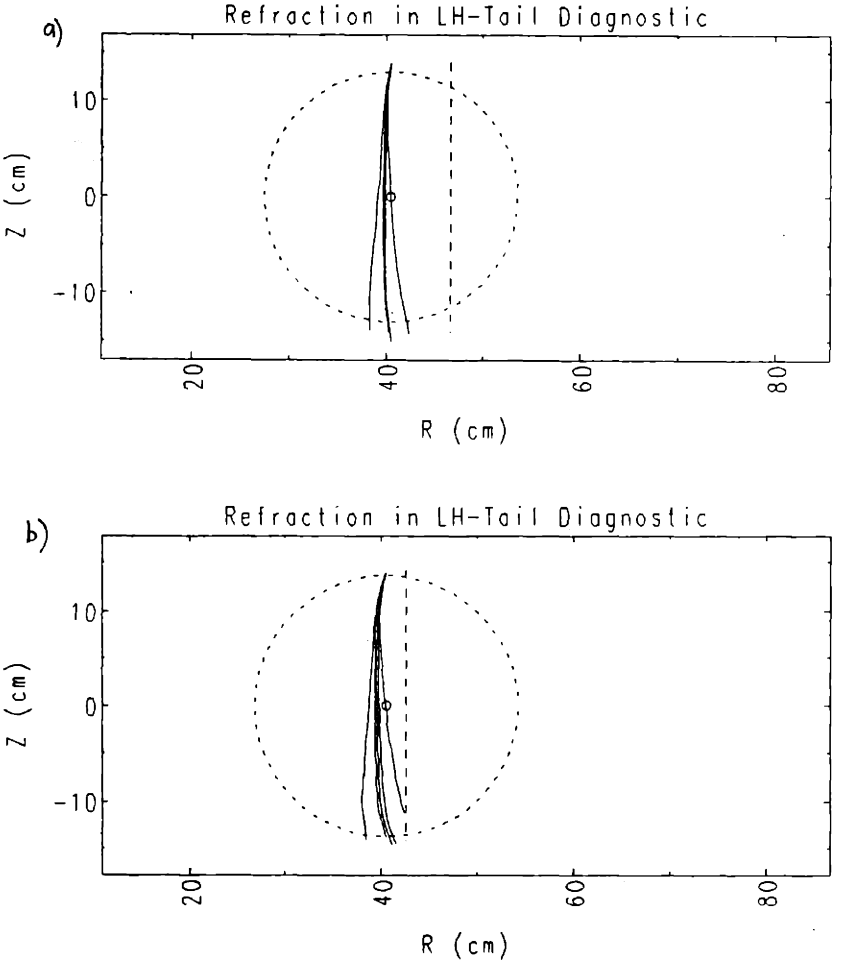

Figure 3-3 Ray trajectories from TORCH for $B_{tor} = 1.15$ T, $n_e(r) = 1.2 \times 10^{13}(1 - r^2/a^2)$ with a) $\omega_{ce}/\omega = 1.18$ and b) $\omega_{ce}/\omega = 1.06$.

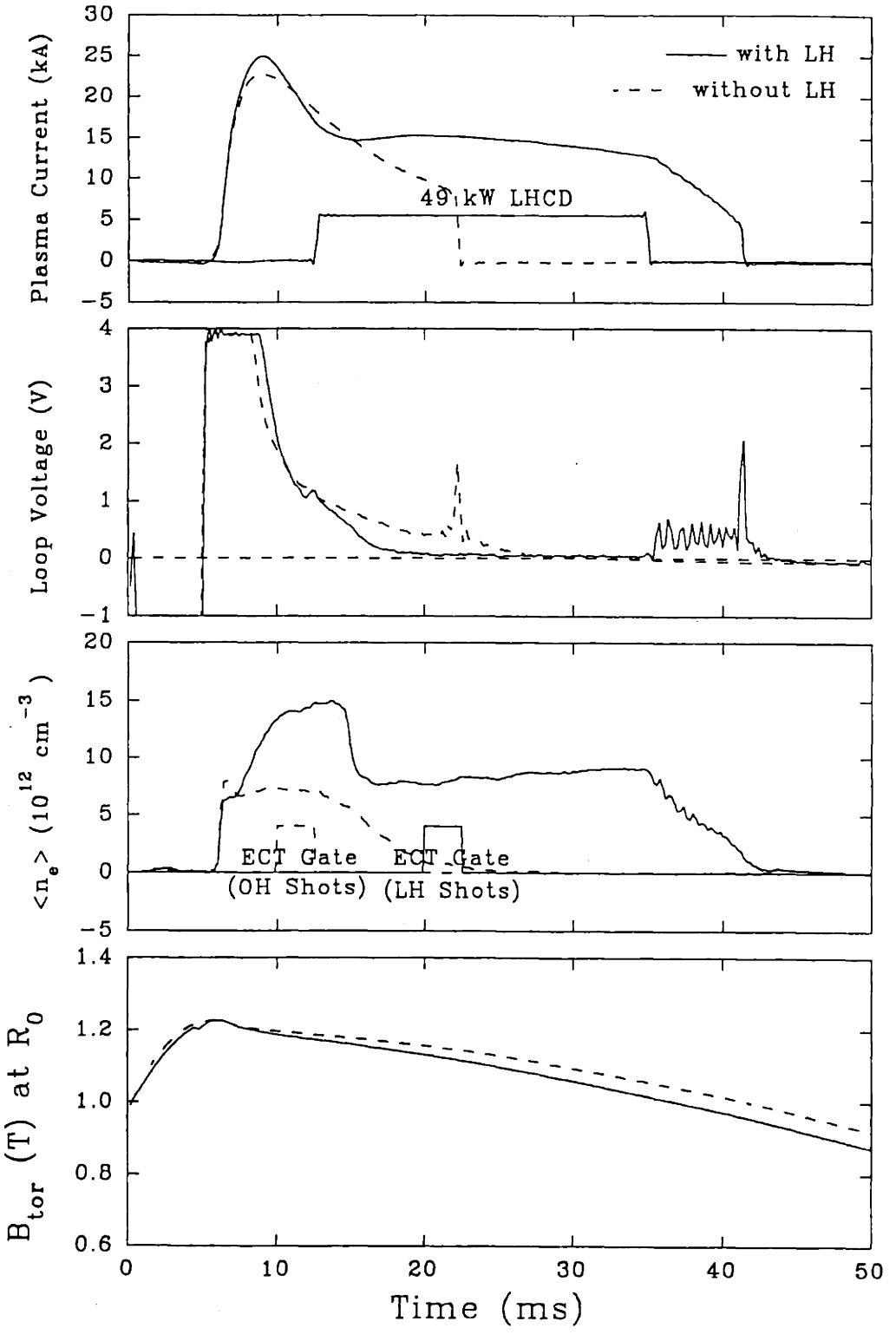

Figure 3-4 Plasma parameters for the LHCD and OH discharges.

cm^{-3}, $T_{e0} = 150 \pm 50$ eV, and $T_e^{edge} = 25 \pm 5$ eV, respectively, for the LHCD discharges. For the ohmic discharges $\langle n_e \rangle = 7.5 \times 10^{12}$ cm^{-3}, $T_{e0} = 250 \pm 50$ eV, and $T_e^{edge} = 10 \pm 5$ eV. The densities were measured by microwave interferometry, the edge temperatures were measured using a gridded energy probe, and the central temperatures were estimated from Thomson scattering measurements during previous Versator experimental runs [12]. Discharges within a series were highly similar, so that ECT measurements at different EC-wave frequencies could be made on a shot-to-shot basis. The ECT data for these two cases are shown in Figure 3-5. For the LHCD discharges (Figure 3-5a), two tails were observed in $\langle f_e^+ - f_e^- \rangle^*$, a cold tail extending from the lower limit of the measurement (about 2 keV) up to about 15 keV with a temperature $T_{\|}^{tail1}$ =3 keV, and a hot tail extending from about 15 keV to the upper limit of the measurement (about 50 keV) with a temperature $T_{\|}^{tail2}$ >40 keV. For the ohmic discharges (Figure 3-5b), a single tail in $\langle f_e^+ - f_e^- \rangle^*$ with $T_{\|}^{tailOH} = 7$ keV was seen from the lower limit of the measurement (2 keV) out to 25 keV, and no electrons with $E_{\|} > 25$ keV were detected. The data of Figure 3-5 were averaged over the gates shown in Figure 3-4. The vertical error bars in Figure 3-5 represent the local standard deviation, and the horizontal error bars are given by the uncertainty in ω_{ce} due to horn geometry and refraction. The experimental data were taken approximately one skin time after the measured loop voltage had fallen to near zero. It is unlikely that toroidal electric fields are responsible for sustaining the colder tail during the LHCD discharges, because the cold tail is observed until the end of the LH pulse, nearly three skin times after the external V_{loop} falls to near zero. Data from 20 ms< t < 22.5 ms are presented here because the higher toroidal magnetic field at this time enabled ECT measurements out to higher parallel energies.

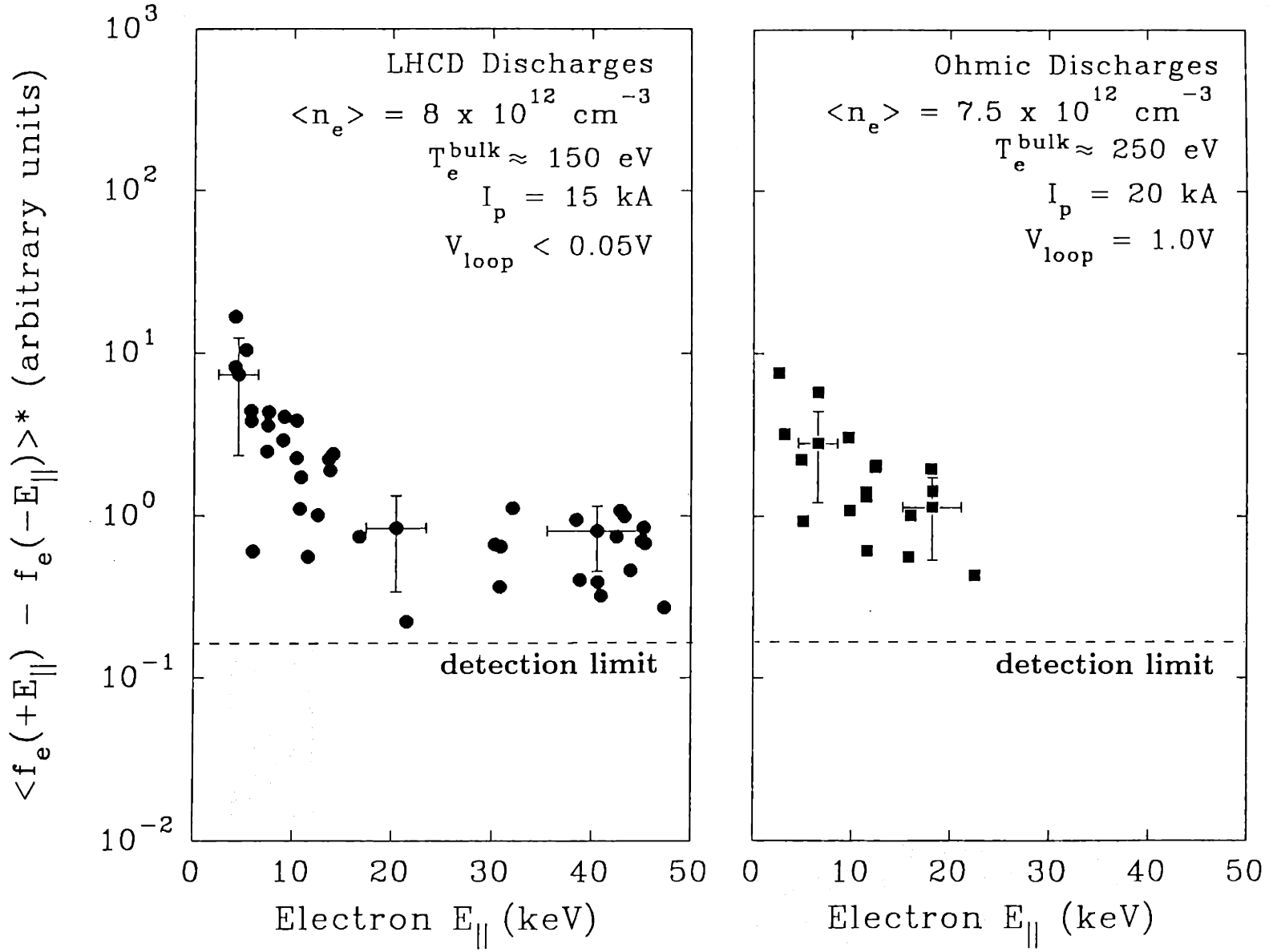

Figure 3-5 Unscaled ECT data for the LHCD and OH discharges.

3.3 COMPUTATIONAL MODELING USING CQL3D

The evolution of the electron distribution function, f_e, during the LHCD discharges was modeled using the three-dimensional, collisional quasilinear code, CQL3D [78], which solves the Fokker-Planck equation in $v_\parallel$,$v_\perp$-space on each flux surface in toroidal geometry during LHCD, including the effects of ray propagation, particle trapping, relativity, and particle losses and sources. Parameters were used that closely match the experimental conditions: 49 kW of LH wave power is launched from a 4-waveguide grill at 2.45 GHz with the power spectrum shown in Figure 3-1; a circular cross-section, low β target plasma with Shafranov equilibrium was assumed with $n_e = n_{e0}(1 - r^2/a_n^2)$, $T_e = T_{e0}(1 - r^2/a_T^2)^2$ where $n_{e0} = 1.2 \times 10^{13}$ cm^{-3}, $a_n = 0.1317$ m, $T_{e0} = 150$ eV, and $a_T = 0.169$ m. Also taken $Z_{eff} = 2$, $V_{loop} = 0.05$ V, and an electron particle confinement time of 1.5 ms, independent of velocity and position have been used.

When all four lobes shown in Figure 3-1 are included in the model antenna spectrum, we find good agreement between the experimentally observed electron distribution function and that predicted by the code, as shown in Figure 3-6 for the LHCD discharges. The most pronounced effect of the ECT absorption sensitivity function is to make the cold tail appear hotter and to remove the dip in $\langle f_e^+ - f_e^- \rangle$ near $p_\parallel/m_0c = 0.175$ predicted by the code. The dip is a result of the reverse tail, which is created by lobes #2 and #4 of the wave spectrum. In Figure 3-6, the convolved function $\langle f_e^+ - f_e^- \rangle^*$ has been normalized to match $\langle f_e^+ - f_e^- \rangle$ in the middle of the hotter tail. The ECT data scale factor has been found by fitting to $\langle f_e^+ - f_e^- \rangle^*$ from CQL3D, using the radial profile of the superthermal electron density as a free parameter. The resulting profile is consistent with measured radial hard X-ray profiles on Versator within experimental uncertainty. The uncertainty in the absolute level of the measured tail is much less than the magnitude of the two-temperature feature. The code predicts a total plasma current of 14.1 kA, with

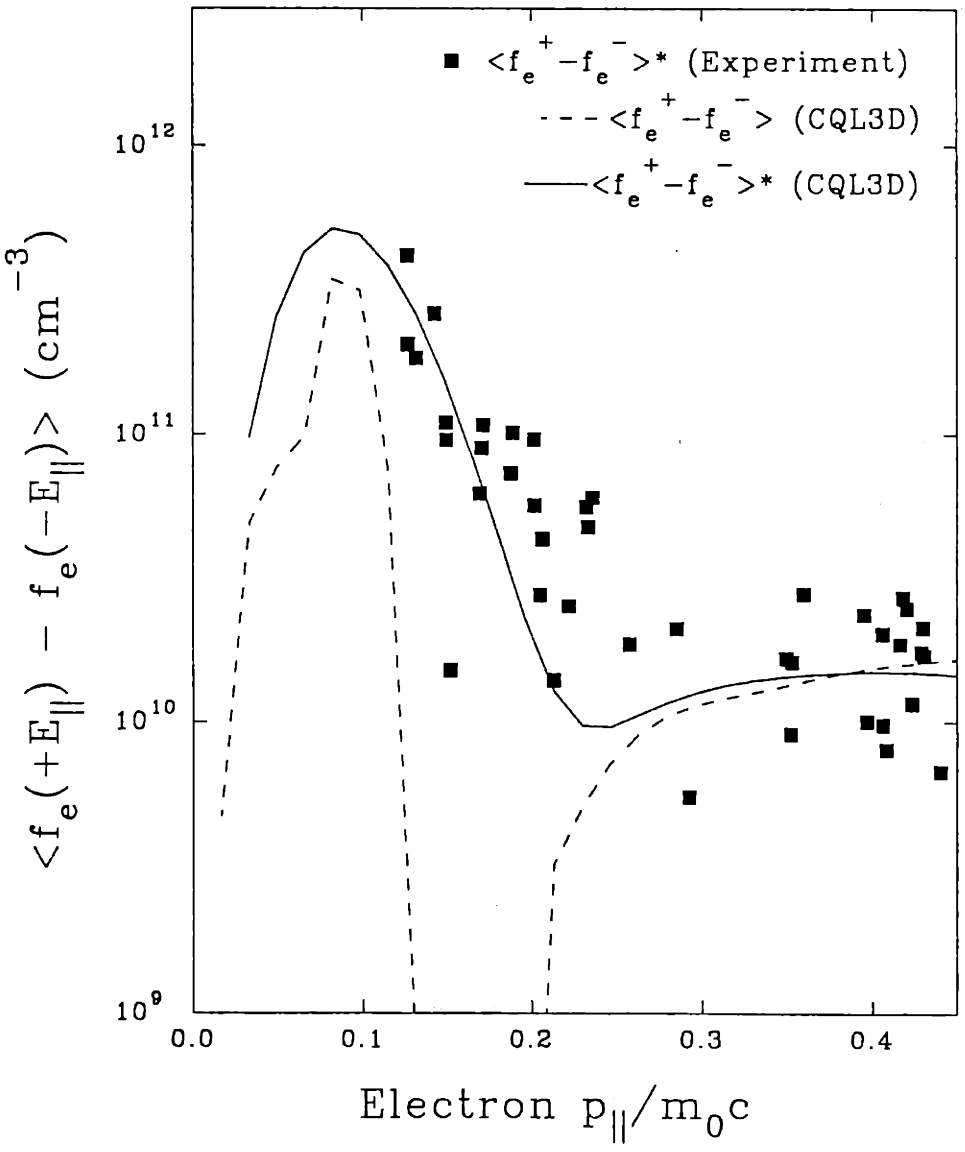

Figure 3-6 Comparison of ECT data with CQL3D results.

the cold forward tail carrying 2.6 kA in the range $0.082 < p_{\|}/m_0c < 0.15$ (1.7 keV< $E_{\|}$ <5.5 keV), the hot forward tail carrying 16.3 kA in the range $p_{\|}/m_0c > 0.15$ ($E_{\|} > 5.5$ keV), and the reverse tail carrying -4.8 kA in the range $p_{\|}/m_0c < 0.11$ ($E_{\|} > 3.1$ keV).

When lobes #2,3, and 4 are removed from the model antenna spectrum, the plasma current is predicted to be reduced to 223 A, and agreement with experiment becomes very poor. The electron distribution function predicted by CQL3D versus p/p_{norm}, averaged over the vertical plasma minor diameter, is shown in Figures 3-7a and 3-7b for the cases with and without sidelobes, respectively. In the figures, $p_{norm} = 0.82m_0c$ for clarity of the sidelobes, but for the plasma current calculations the numerical grid was extended to $p_{norm} = 1.10m_0c$. Negative $p_{\|}$ corresponds to the direction of the plasma current. When only lobes #1, 2 and 4 are included, the net plasma current is +4.6 kA. This is because a number of superthermal electrons created by lobe #2 are scattered from negative $p_{\|}$ to positive $p_{\|}$ by ions and are subsequently accelerated by upshifted waves from lobe #1. The current created in this way exceeds by 4.4 kA the reverse current generated by lobes #2 and #4. This effect is more pronounced at higher Z_{eff}. The elimination of the toroidal electric field in the model decreases the plasma current from 14.1 kA to 13.2 kA for the case with sidelobes and from 223 A to 0.1 A without the sidelobes. This results mostly from a decrease in $\langle f_e^+ - f_e^- \rangle$ in the range $E_{\|} < 1$ keV.

3.4 HARD X-RAY AND DENSITY MEASUREMENTS

In addition to the ECT measurements, hard X-ray emission was measured from the same plasmas using the seven-detector perpendicular array described in Chapter 2. The time evolution of the emission for these discharges is shown in Figure 3-8. Note that the emission is very low prior to LH-wave injection, implying that

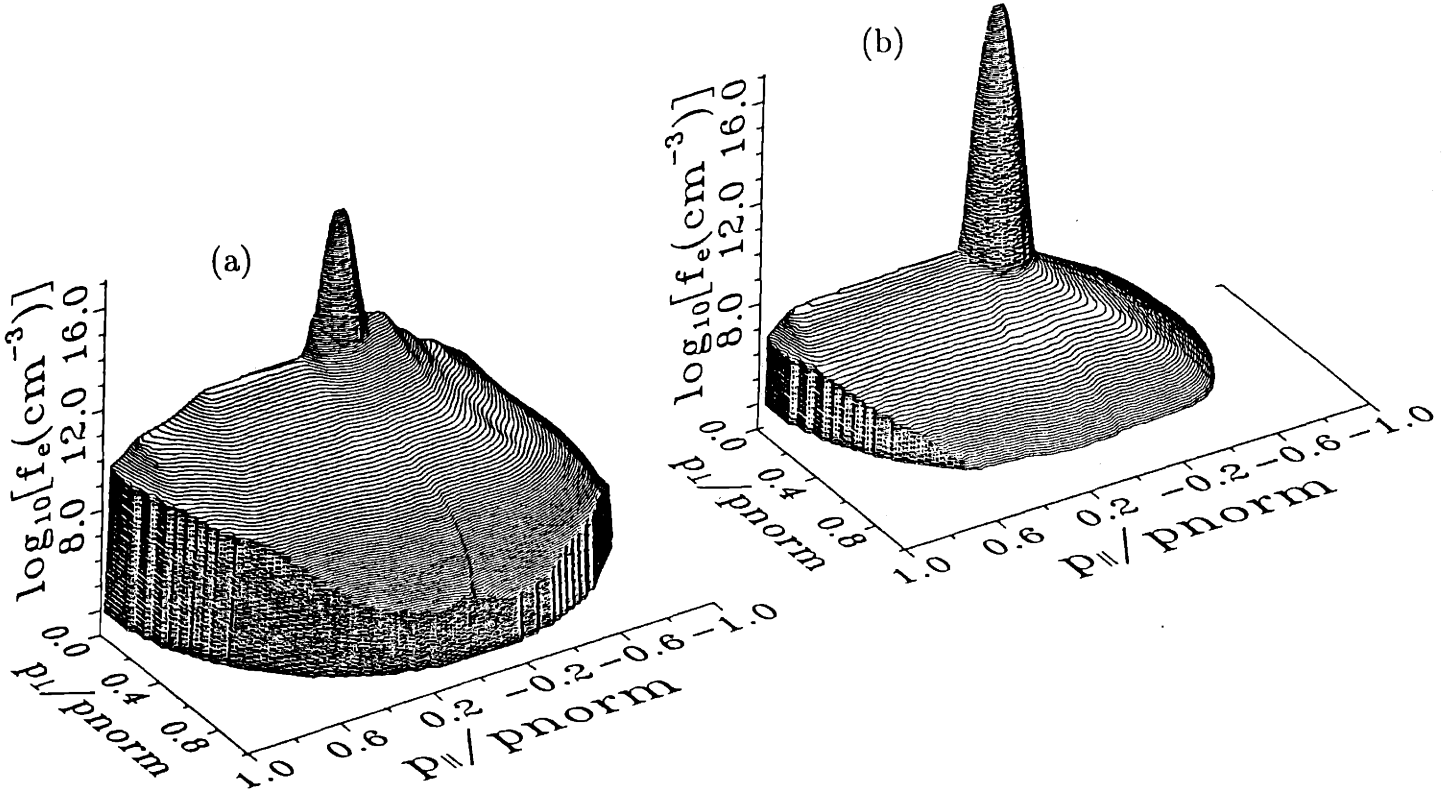

Figure 3-7 f_e **from CQL3D for a) with and b) without the spectral sidelobes.**
$p_{norm} = 0.82 m_0 c$.

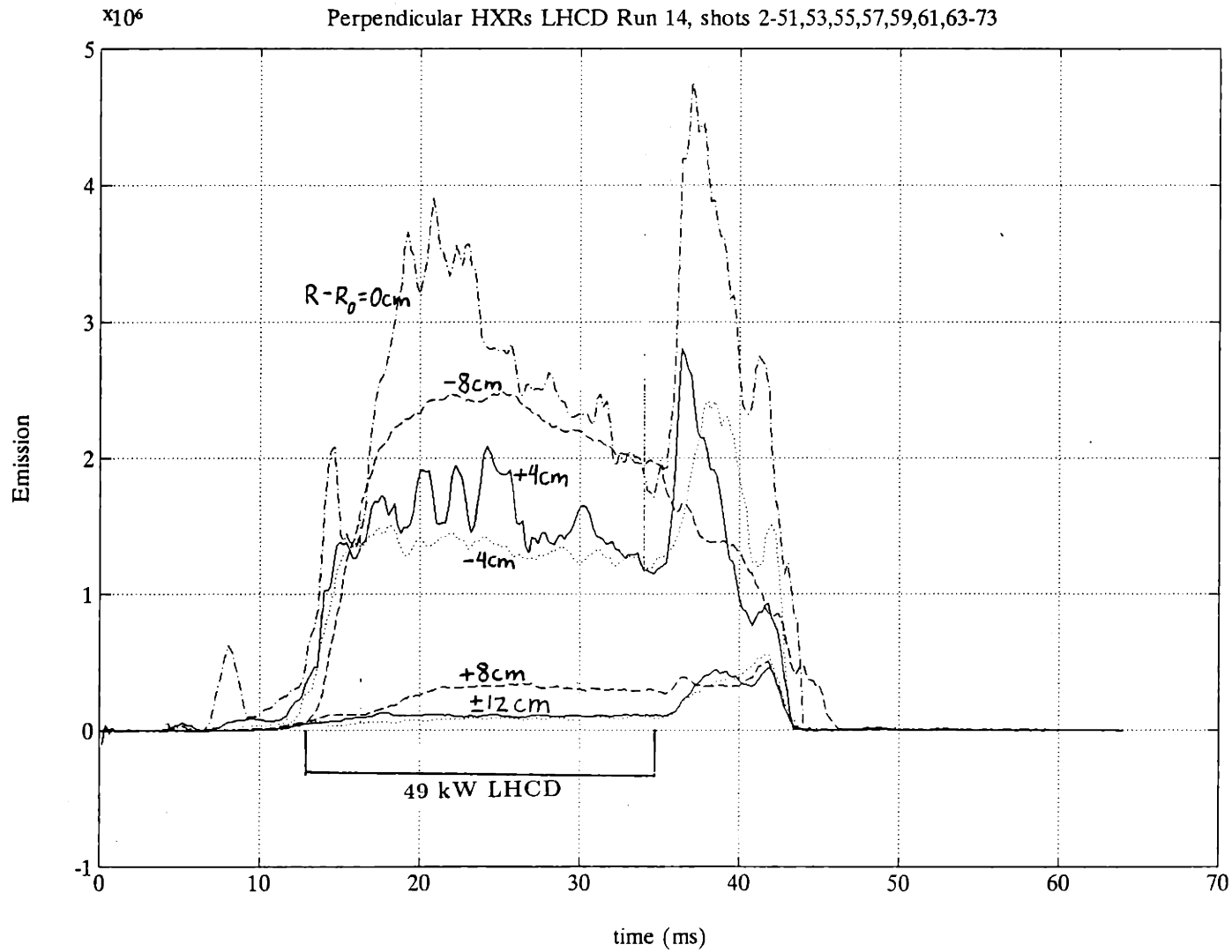

Figure 3-8 Hard X-rays averaged over 66 ECT discharges.

few runaway electrons were produced. Hence the superthermal electrons producing the hard X-rays were created by the LH waves. Radial profiles of the X-ray temperature and energy-integrated emission for discharges similar to these are shown in Figure 5-17 (the LH alone case). Except for the anomalously large emission at $R - R_0 = -8$ cm, the full width at half maximum (FWHM) of the emission profile is 8 cm. When the LH pulse is shut off at $t = 35$ ms, the X-ray emission at all radii increases, at most locations substantially, *except* at $R - R_0 = -8$ cm. This increase is approximately proportional to the emission at each location, and is probably caused by the rapid acceleration of the electron tail (formed by the LH waves) by the suddenly increased loop voltage. The relative increase in the emission at $R - R_0 = -8$ cm to the sudden increase in V_{loop} is of the same magnitude as the response at $R - R_0 = +8$ cm, about 1×10^5 photons/cm^2, which is only 5% of the total emission at $R - R_0 = -8$ cm at the time of termination of the LH pulse.

The density profile is parabolic, as shown in Figure 3-9, and exhibits no unusual features near $R - R_0 = -8$ cm, although the density at this radius was not measured for these discharges due to a limitation of the density interferometer. The interferometer was later improved to allow measurements at $R - R_0 = -8$ cm, and the density at this position followed the parabolic dependence of the profile during discharges similar to those examined here. The anomalous peak is localized to within ± 2 cm of $R - R_0 = -8$ cm. It moves to larger major radii as the plasma current is reduced (e.g., to $R - R_0 = -6$ cm for $I_p = 9$ kA), and it is not observed in high-β_p discharges with $I_p \leq 6$ kA [79]. One possibility is that the anomalously large hard X-ray peak is emitted by trapped electrons as they reach their turning points at the tips of their banana orbits. At this point the trapped electron has only perpendicular energy, and it emits more bremstrahlung in the perpendicular direction.

The problem with this explanation is that it does not explain the high degree of radial localization of the emission, because for energies less than 50 keV the brehmstrahlung is nearly isotropic, and trapped electrons with various pitch angles

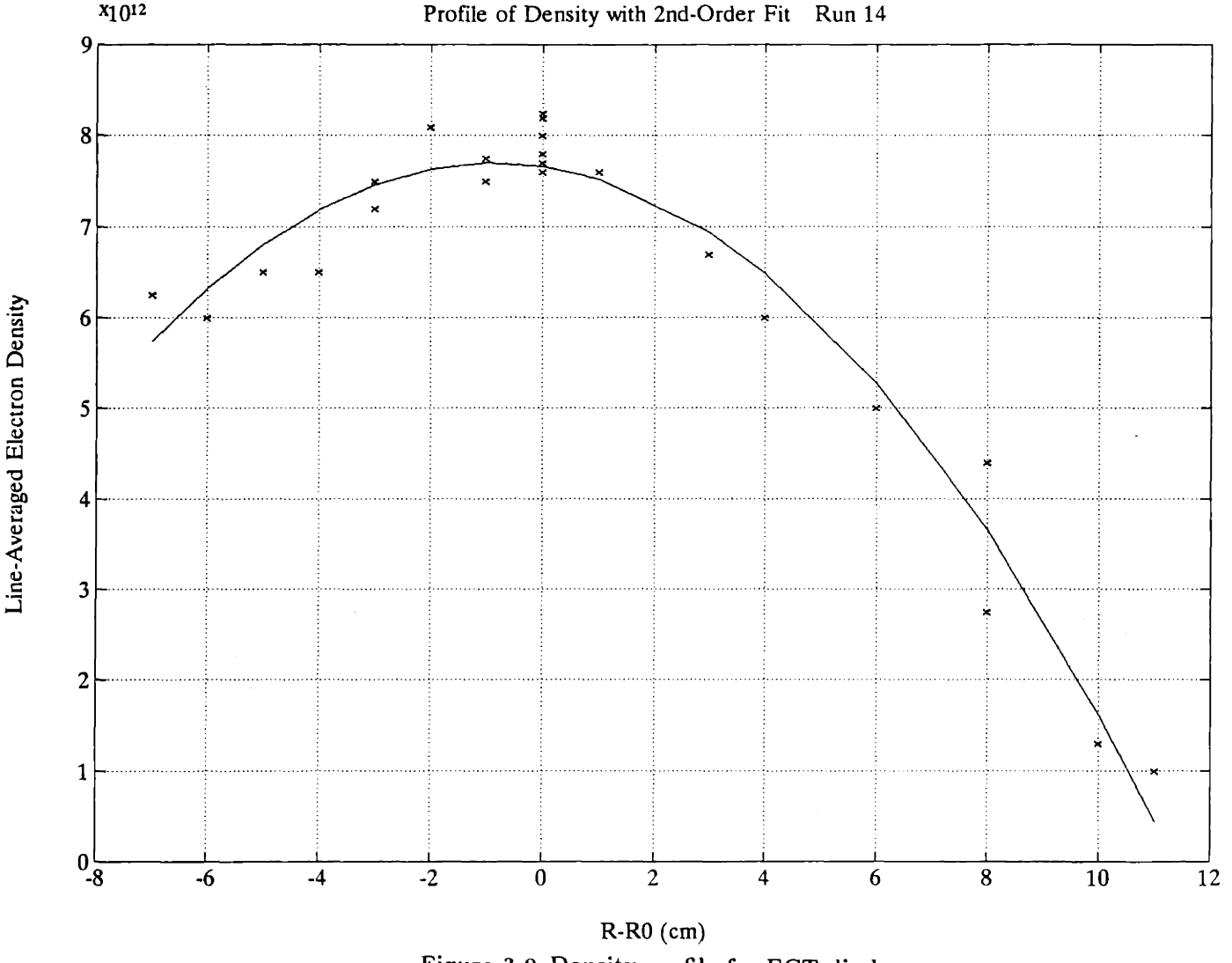

Figure 3-9 Density profile for ECT discharges.

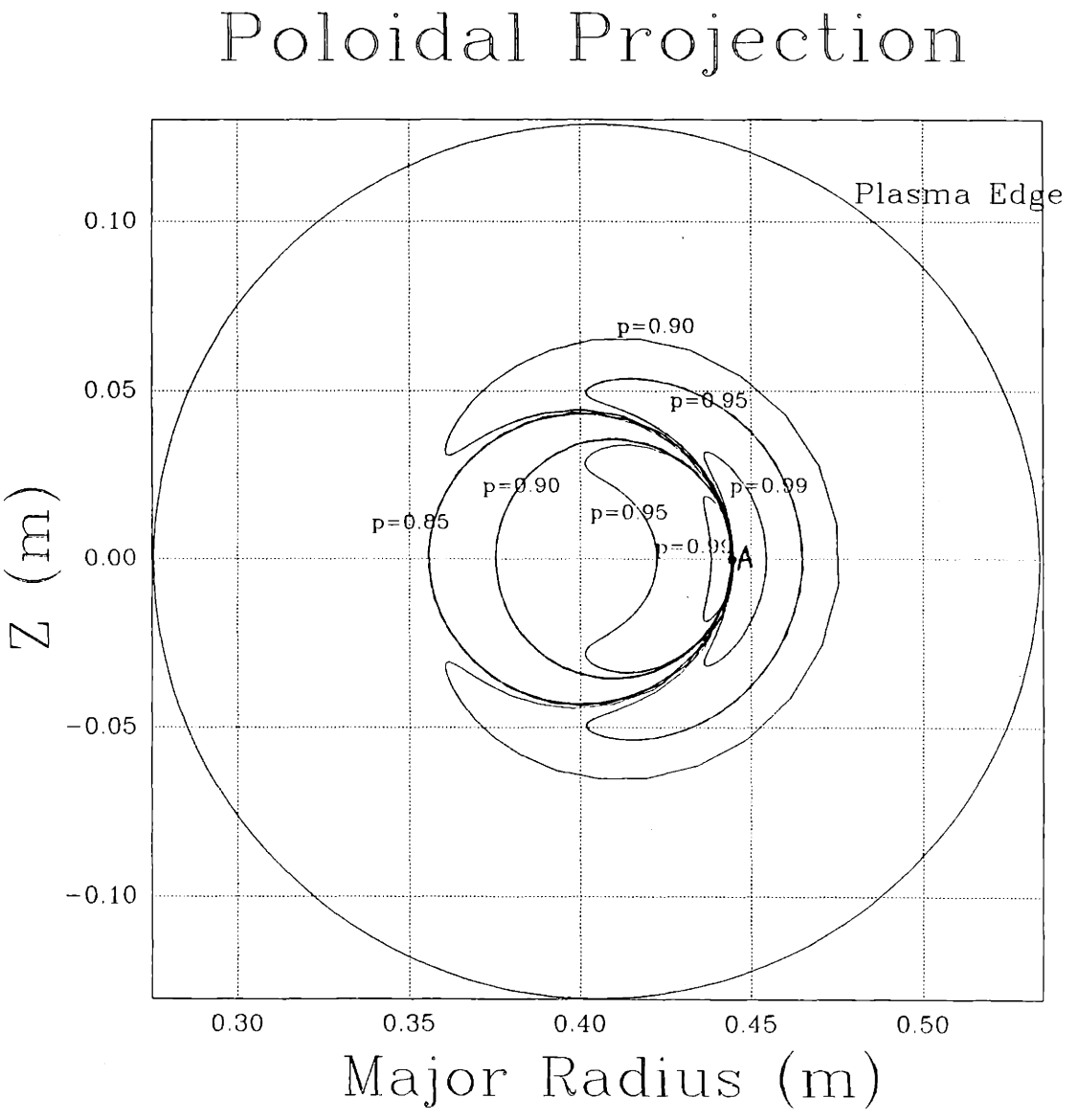

Figure 3-10

Orbits for 100keV electron born at R=0.445m, Z=0 on Versator. Inner orbits are for current−contributing electrons, outer for countercurrent electrons. Pitch is vperp/v.

have their banana tips at different major radii, as shown in Figure 3-10. This figure shows output from a computer code, ORBIT, [80] which follows the orbits of fast electrons in Versator. Figure 3-10 shows that, unless a large class of superthermal electrons exists with a well-defined pitch angle, it is difficult to imagine how the anomalous emission peak at $R - R_0 = -8$ cm could be caused by trapped electrons.

Another possibility is that the emission is caused by a hollow cylinder of circulating electrons, as shown in Figure 3-11. When the outward shift of the magnetic axis for these discharges and the drift off of the flux surfaces is taken into account, fast circulating electrons passing through $R - R_0 = -8$ cm also pass through $R - R_0 \approx$ 12–13 cm. Figure 3-11 shows a plot of the LH wave energy density in the tokamak [81], overlayed with the orbits of fast electrons with $pitch \equiv v_\perp/v = 0.1$ and energies of $E_\parallel = 20$, 50, 100, and 200 keV. This figure suggests that a hot cylinder of circulating electrons may be created by some form of electron heating at the mouth of the antenna or by ray focusing near $R - R_0 = -8$ cm. The LH energy density plot is for $f = 800$ MHz, so it may differ moderately from the 2.45 GHz case, but the major features are expected to be similar. The hard X-ray spectra for the anomalous emission peak indicate that most of the emission is from electrons with energy less than 50 keV. The large ratio ($\gtrsim 15$) of target ion densities at $R - R_0 = -8$ cm and $R - R_0 = +$12–13 cm could explain the large difference in bremstrahlung emission level, given the uncertainty in the location of the cylinder's outer major radius and the ion density at the mouth of the antenna. It is unlikely that the hypothesized hot electron ring significantly affects the ECT measurements of the two-parallel-temperature electron tail because the measured anomalous X-ray emission is highly localized in minor radius and is emitted by electrons with energies greater than 20 keV. This anomalous X-ray emission feature is analyzed in more detail in reference [57].

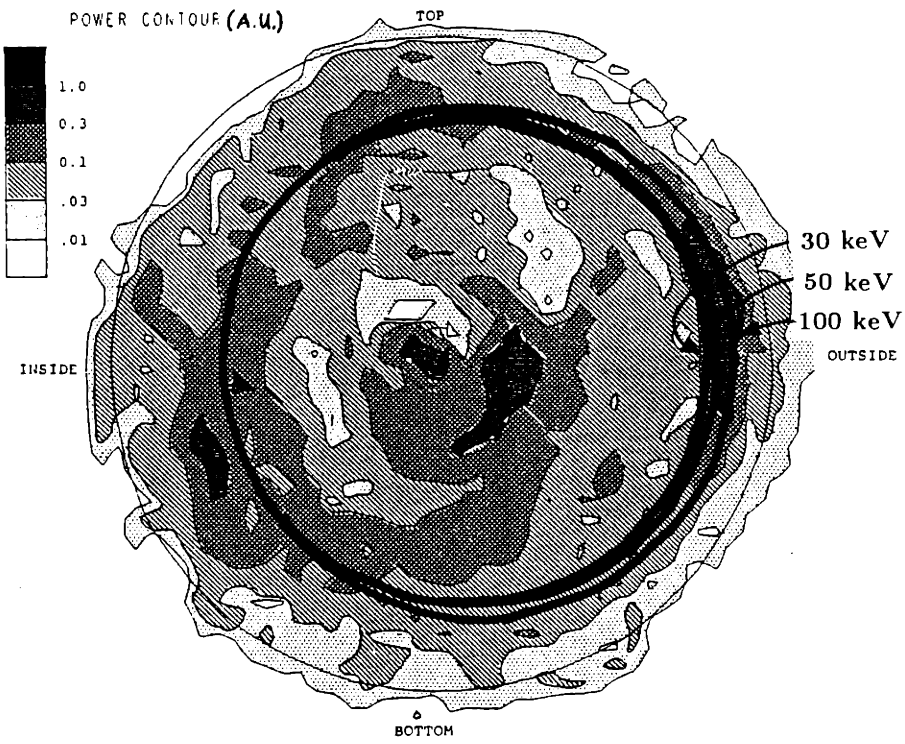

Figure 3-11 Orbits of fast electrons with pitch=0.1 overlayed on LH-wave power map (from ref. [81]).

3.5 CONCLUSIONS

A two-parallel-temperature tail in $\langle f_e^+ - f_e^- \rangle^*$ has been observed during LHCD discharges on the Versator-II tokamak. Code modeling suggests that the cold tail is initiated by high-$N_\parallel$ low-power waves from the first forward sidelobe of the antenna spectrum. The main power lobe, which is launched in the range $1 < N_\parallel < 5$, creates and sustains the hot tail and helps to sustain the cold tail, via $N_\parallel$-upshift to $7 \leq N_\parallel \leq 10$. The reverse power lobe with $-10 < N_\parallel < -5$ creates most of the reverse tail, part of which is reverse-scattered by ions, adding to the cold forward tail and enhancing the net plasma current. In agreement with earlier code modeling [72], the CQL3D code predicts that the $N_\parallel$-upshift of the main power lobe is insufficient to bridge the spectral gap during LHCD experiments on the Versator Tokamak. Inclusion of the sidelobes in the model is essential for correctly predicting the experimentally observed plasma current. A similar explanation may apply to LHCD results on other small tokamaks [65, 66]. In addition, this may be of importance in explaining the increase in current-drive efficiency with increase in volume-averaged electron temperature observed on the JT-60 Tokamak [75].

Radial profiles of the hard X-ray emission, X-ray temperature, and plasma density have been measured, and except for an anomalous peak in the emission at $R - R_0 = -8$ cm, the emission profile is sharply peaked near the magnetic axis, and the X-ray temperature is hotter near the plasma edge than at the center. The anomalous X-ray emission peak near $R - R_0 = -8$ cm does not appear to be caused by trapped electrons emitting as they turn at their banana tips, due to the sharp localization of the peak. The emission may be from a circulating hollow cyclinder of hot electrons, but in this case stronger-than-observed emission near the outside edge of the plasma would be expected. However, the large ratio ($\gtrsim 15$) of target ion densities at $R - R_0 = -8$ cm and $R - R_0 = +12$–13 cm could explain the large difference in bremstrahlung emission level, given the uncertainty in the location of

the cylinder's outer major radius and the ion density at the mouth of the antenna. Due to the high energy and sharp localization in minor radius of the anomalous emission, it is unlikely to affect the ECT measurements or the conclusions regarding the two-parallel-temperature tail.

Chapter 4
Experiments with Electron-Cyclotron (EC) Waves

4.1 EC-FORMED TOROIDAL PLASMAS

In this section, the characteristics of EC-formed plasmas on Versator are described. The confinement theory for these plasmas is presented and compared to the experimental results. Results from both 35 GHz and 28 GHz ECRH systems are presented.

Figure 4-1 shows the geometry of the 35 GHz antenna, along with the locations of the EC and upper-hybrid (UH) layers in the plasma for $\mathbf{B}_0 = 1.25$ T and $\langle n_e \rangle \approx 5 \times 10^{12}$ cm^{-3}. As in past experiments on other experimental devices, a cold plasma is formed and confined on Versator when EC waves are launched into the vacuum chamber with a toroidal magnetic field and hydrogen gas present. As described in Chapter 1, these plasmas have been formed on other tokamaks by mode conversion or nonlinear decay of the X-mode into the electron Bernstein (EB) wave near the UH layer. These EB waves propagate toward higher magnetic field from the UH layer towards the EC layer, and are heavily damped. When the O-mode is launched, it is believed that a large fraction of the power is converted to the X-mode due to low single-pass absorption and wall reflections, and the plasma is formed. No dependence on launched polarization has been observed, except for a moderate broadening of the density profile in some O-mode experiments [82], which may be beneficial for preionization. The present understanding of the early stages of the formation of these plasmas is that initial breakdown occurs at the EC layer and a very low-density plasma is formed in the first tens of microseconds of the discharge. This creates a UH resonance layer near the EC layer, and conversion to

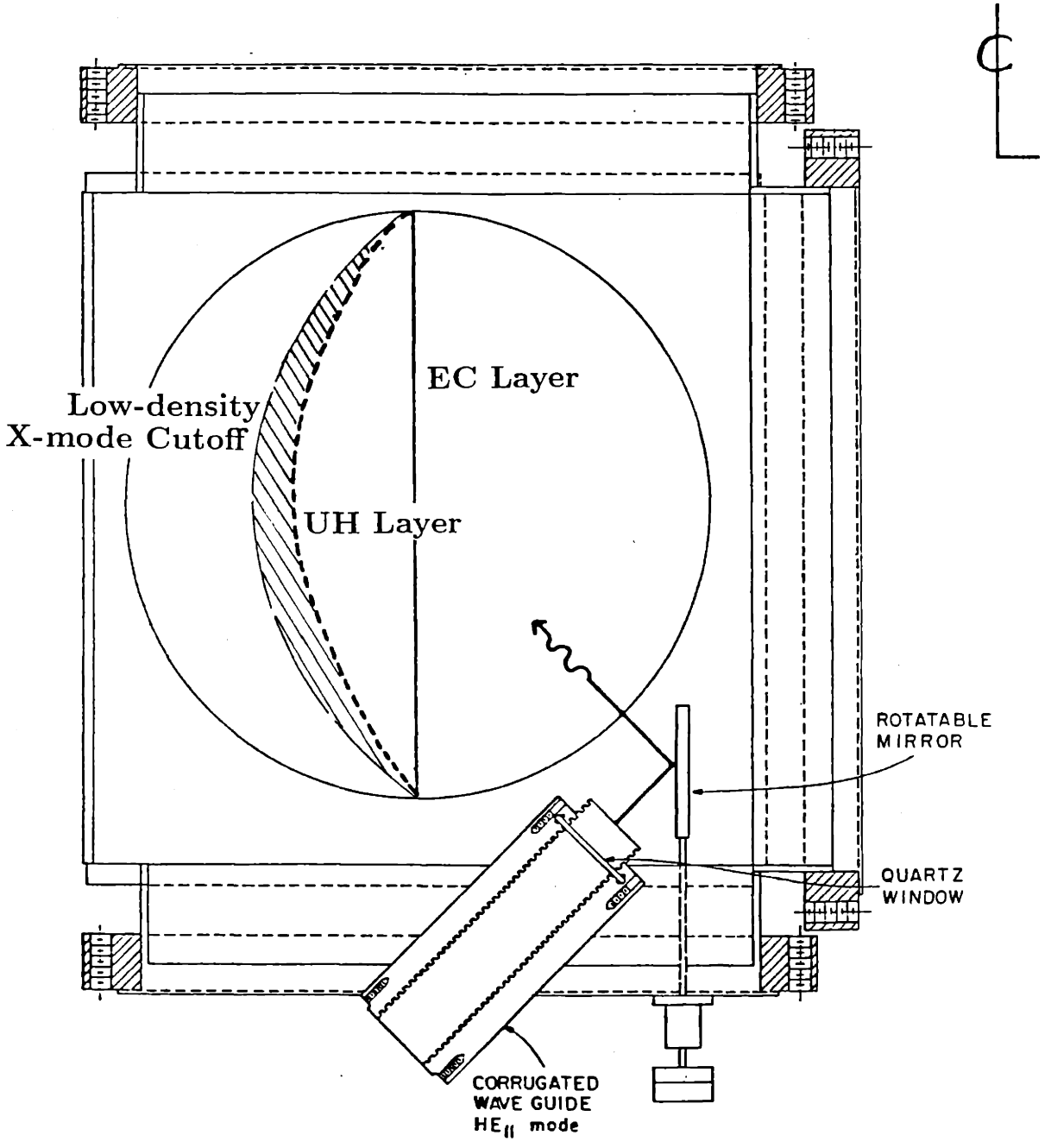

Figure 4-1 Schematic of the 35 GHz launcher and Versator plasma.

EB waves begins. The EB waves damp rapidly and build up the plasma density and temperature. This scenario is supported by the results of experiments on Versator. Figure 4-2 shows the wave spectrum detected by a radiofrequency (rf) probe inserted approximately 4 cm beyond the limiter from the top of the Versator vacuum chamber during EC plasma formation. A distinct spectral peak is observed in the range of 200-400 MHz with an amplitude 8 dB above noise. During the time this spectrum was taken, the plasma density was rapidly falling from 3×10^{12} cm^{-3}to 1×10^{12} cm^{-3}. The average ion plasma frequency was therefore 300 MHz, and the lower-hybrid frequency was 270 MHz. It would thus appear that parametric decay takes place during the formation of these discharges. The detected wave is most likely the ion-mode identified in Appendix D as the low-frequency decay wave. The frequency of this wave, according to the theory described in Appendix D [4]is given by Equation 103. For parameters typical of Versator EC-formed plasmas, $k_\perp r_{ce} \approx 0.04$ and $k_\parallel \approx 0$, where r_{ce} is the electron gyro-radius. This yields $f \approx 1.06 f_{lh} = 286$ MHz, which corresponds very well to the frequency of the observed spectral peak. It is not possible to determine from this measurement the absolute power of the decay wave in the plasma, however. Therefore it is still unclear to what extent nonlinear decay, as opposed to linear mode conversion, is responsible for the plasma formation.

Figure 4-3 shows a surface plot of vertically-line-averaged electron density versus radius and time on Versator. These data were collected using the 28 GHz system with O-mode outside launch. The 2.45 GHz LH system was also used to inject waves after time $t = 5$ ms, but this stage of the discharge is not considered here. The radial profile was obtained by moving the density interferomter between discharges. The plot represents about twenty-five near-identical discharges. These data were taken prior to the rebuild of the tokamak toroidal field system, and hence the field errors were relatively high. The toroidal field at $R = R_0$ was 1 T. The early stages of the discharge are clearly revealed by the density contours during the steep initial rise in the density. Disregarding the peak at $R - R_0 = -5$ cm for the moment, note that the density first forms near $R = R_0$ (the EC layer). The radial profiles

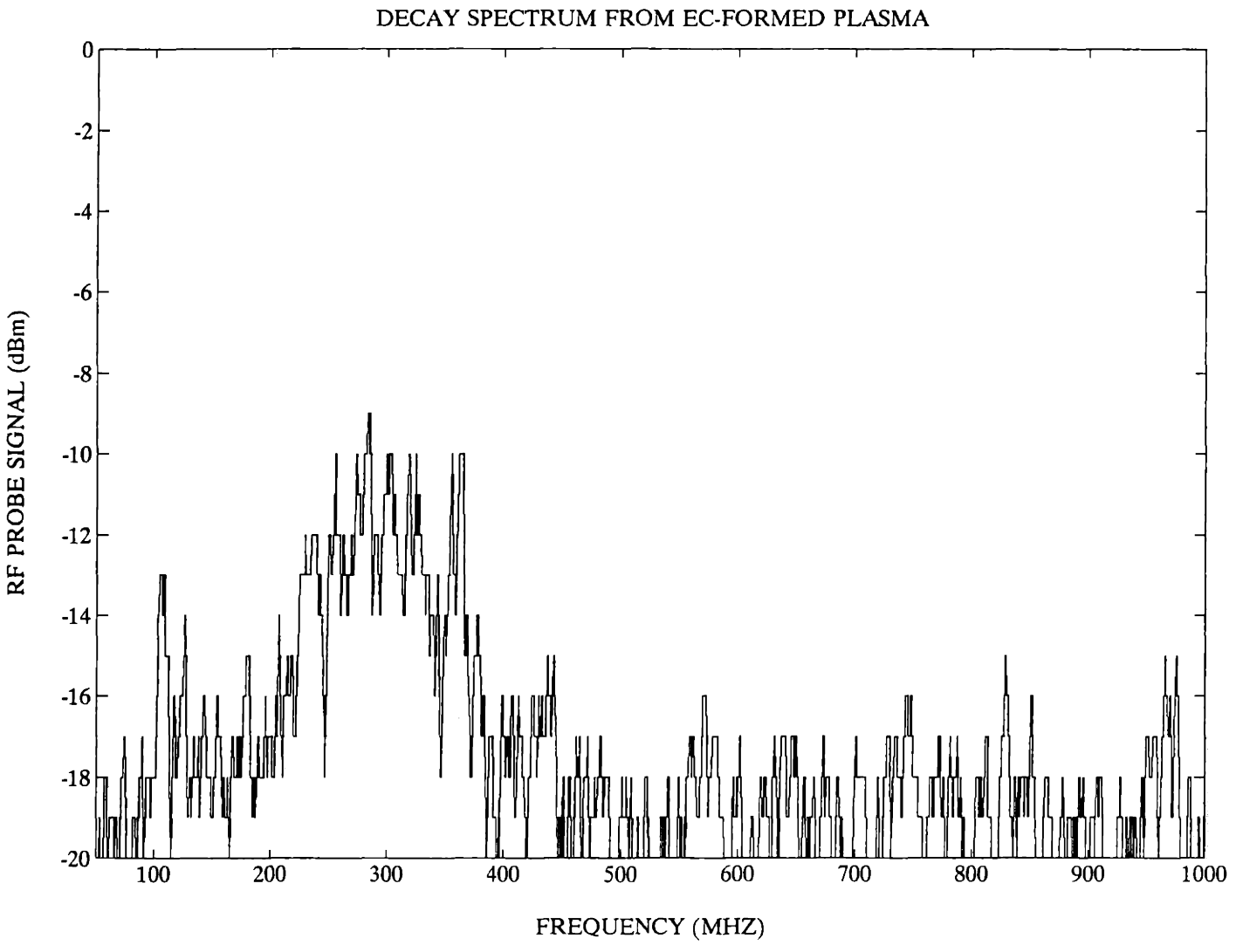
DECAY SPECTRUM FROM EC-FORMED PLASMA
RF PROBE SIGNAL (dBm)
0
-2
-4
-6
-8
-10
-12
-14
-16
-18
-20
100
200
300
400
500
600
700
800
900
1000
FREQUENCY (MHZ)

Figure 4-2

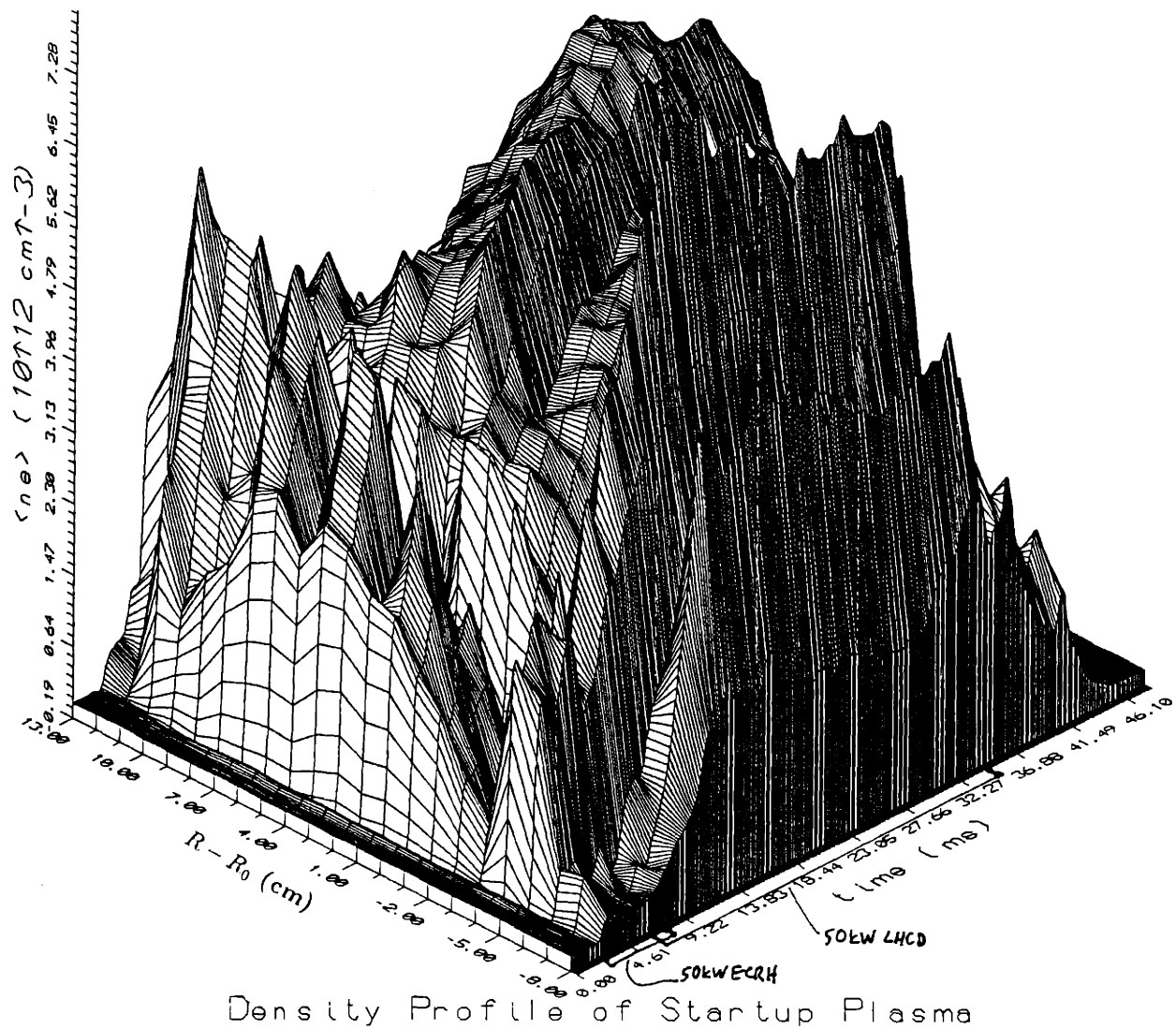

Density Profile of Startup Plasma

Figure 4-3

are drawn every 150 μs. Within 900 μs the density peak has moved outward and become somewhat double-peaked, with one peak at $R - R_0$ = 2-3 cm and another at 5-6 cm. The peak density at this time is about 2.5×10^{12} cm^{-3}, and the UH layer has moved out to $R - R_0 = +6.5$ cm. The peak at $R - R_0 = -5$ cm is not seen in all discharges, but it is seen to some degree in many discharges, both with inside and outside launch.

The dependence of the central line-averaged electron density on the hydrogen fill pressure is shown in Figure 4-4. These results confirm those of Anisimov, et. al., [19]in that a sharp boundary in fill pressure is observed below which breakdown is impossible for a given rf power. This boundary was near 3×10^{-5} torr for 40-50 kW of EC waves on Versator with 1 ms pulse length at 35 GHz. This boundary moved to lower pressures at lower EC power, also in agreement with simple theory and the results of reference [19]. Figure 4-5 shows the dependence on prefill pressure of the plasma density, the decay-wave amplitude, and the rms fluctuation level. These data were taken during 5 ms discharges formed by 25 kW of 28 GHz EC waves. The dependence of the density is qualitatively similar to that of Figure 4-4, with the breakdown boundary at lower pressure due to the lower wave power. The decay-wave amplitude and rms fluctuation level both decrease at a similar rate with increasing fill pressure. The fluctuations plotted here are in the loop voltage, but similar fluctuations are observed by the magnetic probes and by the Langmuir probe, and their dependences on prefill pressure are the same. This figure shows that a relationship may exist between the level of parametric decay activity (or the power level of EB waves in the plasma) and the level of turbulent plasma fluctuations, because both have a similar dependence on fill pressure. These EC-wave induced fluctuations are also observed during ohmically driven and LHCD discharges when EC waves are injected, as described later in this chapter and in Chapter 5. These fluctuations may significantly degrade the confinement of the fast current-carrying electrons under certain conditions.

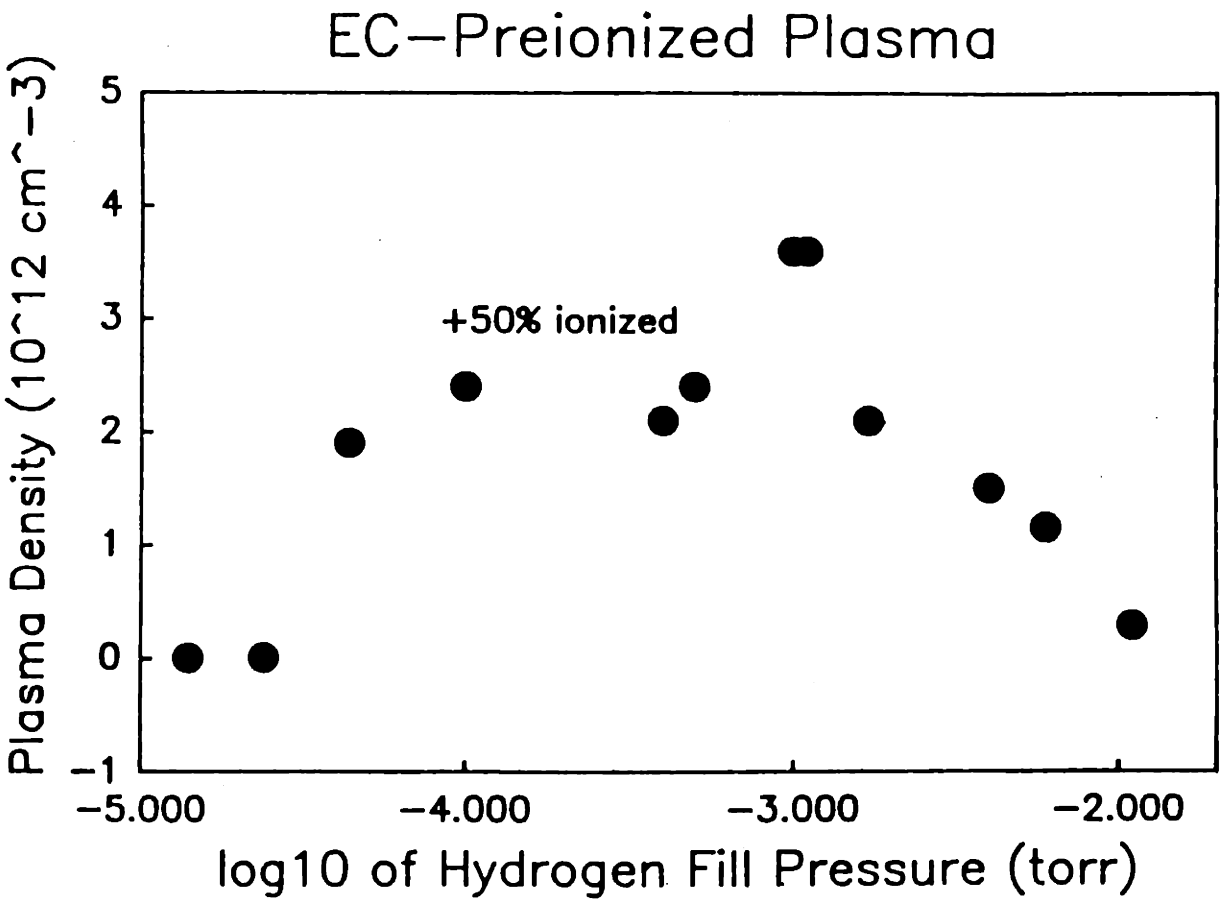

Figure 4-4 Dependence of plasma density on gas fill pressure. $P_{EC} \approx 50$ kW.

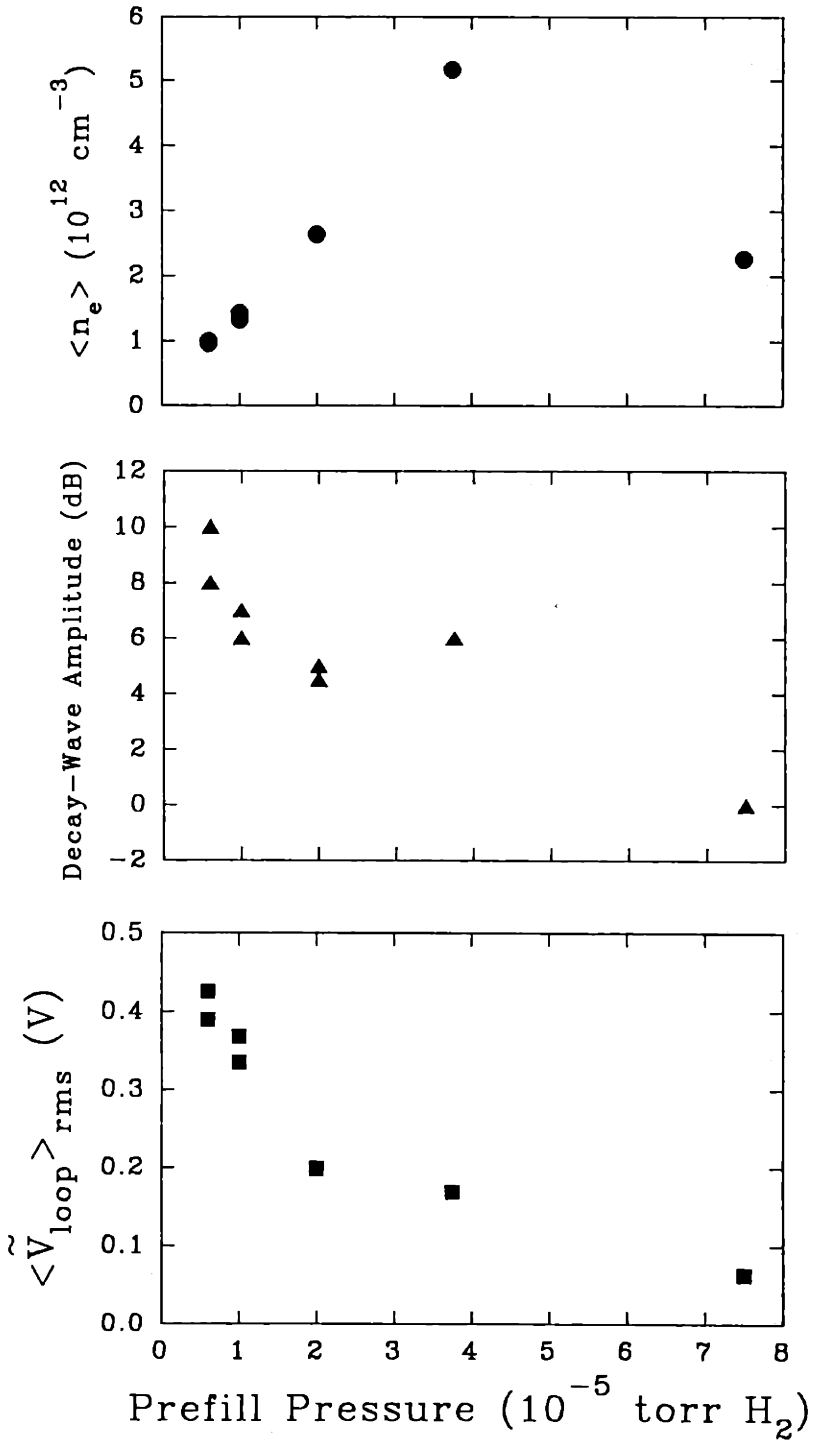
$<n_e>$ (10^{12} cm^{-3})
Decay-Wave Amplitude (dB)
$\tilde{<V_{loop}>}_{rms}$ (V)
Prefill Pressure (10^{-5} torr H_2)

Figure 4-5

A simple theory describing the confinement of EC-formed plasmas has been proposed by Nakao, et. al. [30]and Parail [83]. This theory is now described and compared to Versator experimental results. In a simple torus with only toroidal and vertical magnetic fields, the thermal electron dynamics are as shown in Figure 4-6. Thermal electrons are dragged along the magnetic field lines by the parallel electric field and drift perpendicularly, as shown. The parallel electric field is the small parallel component of the vertical electric field caused by the drift of the thermaal electrons, given by the sum of $\nabla \mathbf{B}$ and curvature drift:

$$\mathbf{v}_{eD} = -\frac{m_e}{e}\frac{\mathbf{R}_c \times \mathbf{B}}{R_c^2 B^2}\left(v_{\|}^2 + \frac{v_{\perp}^2}{2}\right) \tag{34}$$

where $\mathbf{R}_c$ is the radius of curvature vector, pointing toward the center of the curvature of the magnetic field lines, and $v_{\|}$ and $v_{\perp}$ are the parallel and perpendicular velocities, respectively, of the electron. The vector $\mathbf{R}_c = -R\hat{\mathbf{R}}$, where R is the major radius and $\hat{\mathbf{R}}$ is the major-radial unit vector, because only the toroidal field posesses curvature. To prevent rapid $\mathbf{E} \times \mathbf{B}$ drift in the $+R$ direction at the sound speed $\left(v_s = \sqrt{T_e/m_i}\right)$, the vertical electron circuit must be closed. This prevents the rapid buildup of a strong vertical electric field. Closure may be achieved by diffusion along the slanted field lines such that the vertical components of v_{eE} and v_{eD} are equal and opposite, where v_{eE} is the average electron parallel velocity under the influence of the parallel component of the electric field. For an isotropic Maxwellian plasma, this gives

$$\left|\frac{v_{eE}B_v}{B}\right| \approx \frac{m_e v_{te}^2}{eR\,|B|}. \tag{35}$$

For certain values of B_V/B, this approximation holds for a large fraction of the thermal electrons, not just for electrons with a precise initial pitch ($\equiv v_{\perp}/v$).

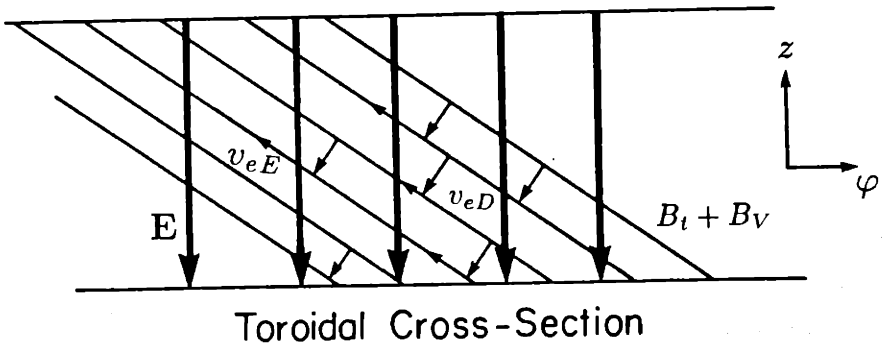

Figure 4-6 Confinement of thermal electrons in EC-formed plasma with B_V and B_t.

Dropping signs (so that all field quantities are positive) fluid theory gives the parallel electric field consistent with a known v_{eE}:

$$E_{\parallel} = \frac{m_e}{e} v_{eE} \nu_{ei}, \tag{36}$$

where ν_{ei} is the electron-ion collision frequency, and collisions with neutral hydrogen atoms have been neglected. Charge separation due to $\nabla \mathbf{B}$ plus curvature drift generates a vertical electric field, which is partially shorted by the flow of electrons back along the slanted field lines against the plasma resistance. The required vertical electric field is

$$E_v = E_{\parallel} \frac{B}{B_v} \approx \frac{\nu_{ei} v_{te}^2 B^3}{\omega_{ce}^2 R B_v^2}, \tag{37}$$

and the corresponding $\mathbf{E} \times \mathbf{B}$ drift velocity is

$$v_{\times} \approx \frac{\nu_{ei} v_{te}^2 m^2}{e^2 R B_v^2}. \tag{38}$$

This is generally much slower than the sound speed. For typical Versator parameters during EC-plasma formation, $v_{\times} \approx 200$ m/s for $B_v = 2.5$ mT, whereas $v_s \approx 4.4 \times 10^4$ m/s. For sufficiently small B_v, the approximations break down so that as $B_v \to 0$, $v_{\times} \to v_s$, rather than $v_{\times} \to \infty$. The above $\mathbf{E} \times \mathbf{B}$ drift is the major perpendicular loss channel, as has been demonstrated in experiments on the WT-2 tokamak [30]. In addition, electrons and ions are lost along field lines at the sound speed, given by ambipolar dynamics:

$$v_{amb} = \hat{\mathbf{v}}_{eE} \cdot \hat{\mathbf{z}} = \frac{B_v}{B} \sqrt{\frac{T_e}{m_i}}. \tag{39}$$

The electron confinement time is thus $\tau_e = a/(v_\times + v_{amb})$, where a is the minor radius. This gives

$$\tau_e = \left[A\frac{n_e}{T_e^{1/2}B_v^2} + C\frac{T_e^{1/2}B_v}{B} \right]^{-1}, \tag{40}$$

where A and C are constants. For Versator, $A \approx 5.5 \times 10^{-15}$ and $C \approx 1.3 \times 10^3$ for T_e in eV, B and B_v in Tesla, and n_e in cm^{-3}. This confinement time is plotted versus B_v for various electron temperatures and densities, in Figures 4-7 and 4-8. In Figure 4-7, the confinement time is plotted versus B_v for several electron densities from 1.0×10^{10} cm^{-3}to 5.0×10^{12} cm^{-3}for $T_e = 10$ eV. This plot clearly shows that the confinement time improves with decreasing density for $|B_v| \lesssim 3$ mT, and it is poor and roughly independent of density for $|B_v| \gtrsim 3$ mT. In Figure 4-8, the electron density is fixed at 1.0×10^{10} cm^{-3}and τ_e is plotted versus B_v for T_e ranging from 0.1 eV up to 100 eV. This plot shows that as T_e drops confinement is improved at all values of B_v, except $|B_v| \lesssim 0.5 - 1.0$ mT.

Figures 4-9 and 4-10 show profiles of electron density and H_α emission versus time for EC-formed plasmas on Versator. These data were taken prior to the tokamak rebuild in the Spring of 1991. This rebuild significantly reduced the radial error fields on Versator. About 40 kW at 35 GHz was injected in X-mode polarization from the high-field side for 1 ms. The toroidal field on axis was 1.25 T, and no vertical field was applied. In Figure 4-9, the density rises very rapidly after turn-on of the EC power, and the plasma quickly fills the chamber. It begins to sharply decay near the end of the EC pulse. The density decay rate then slows substantially in the 5 ms following the EC pulse. For example, identifying the e-folding time of the density at $R = R_0$ with τ_e yields confinement times of approximately 0.6 ms, 1.7 ms, and 7 ms at times $t = 2$ ms, $t = 5.5$ ms, and $t = 10$ ms from the data of Figure 4-9. At these times, $\langle n_e \rangle \approx 3.5 \times 10^{12}$ cm^{-3}, 1.4×10^{12} cm^{-3}, and 0.4×10^{12} cm^{-3}, respectively. For these parameters and $B_v = 2$ mT and $T_e = 10$ eV, the theory of

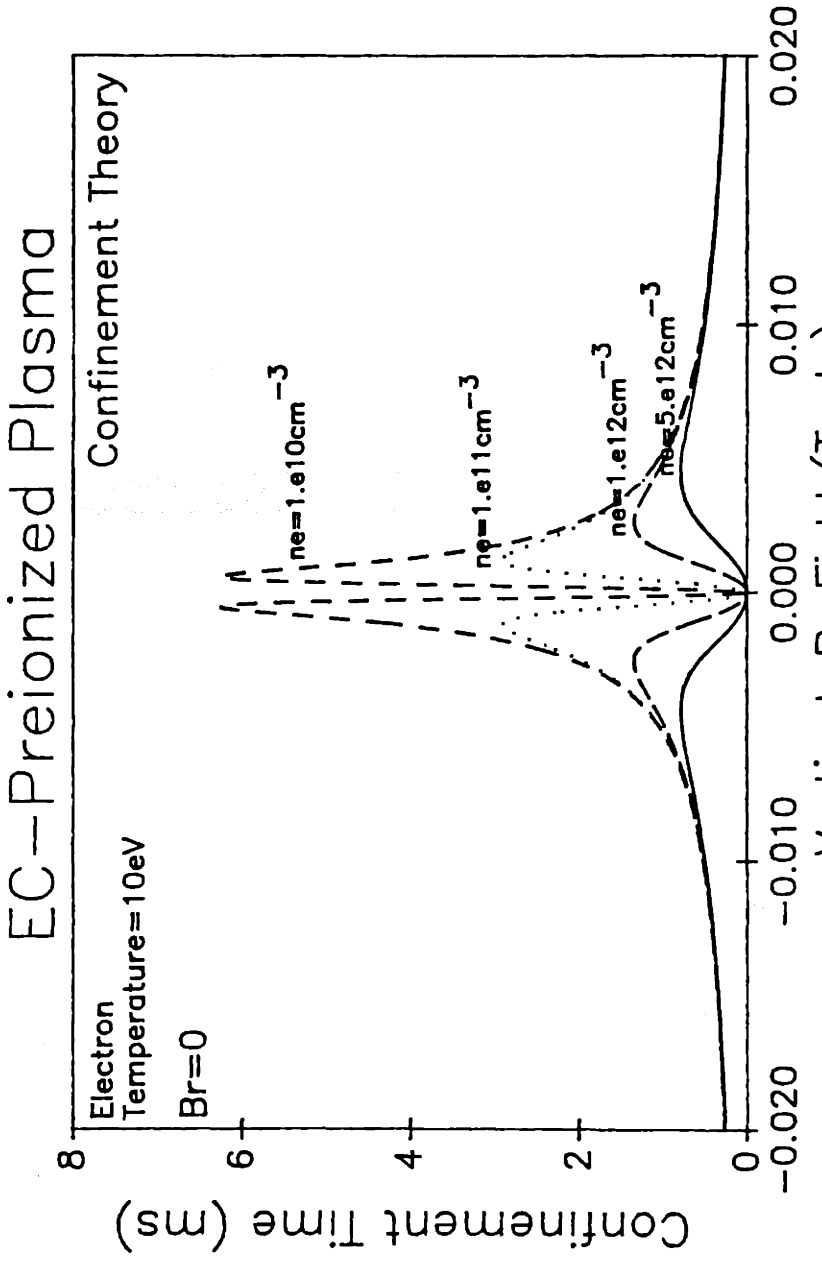
EC–Preionized Plasma
Confinement Theory
Electron
Temperature=10eV
Br=0
ne=1.e10cm^{-3}
ne=1.e11cm^{-3}
ne=1.e12cm^{-3}
ne=5.e12cm^{-3}
Confinement Time (ms)
0
2
4
6
8
−0.020
−0.010
0.000
0.010
0.020
Vertical B–Field (Tesla)

Figure 4-7

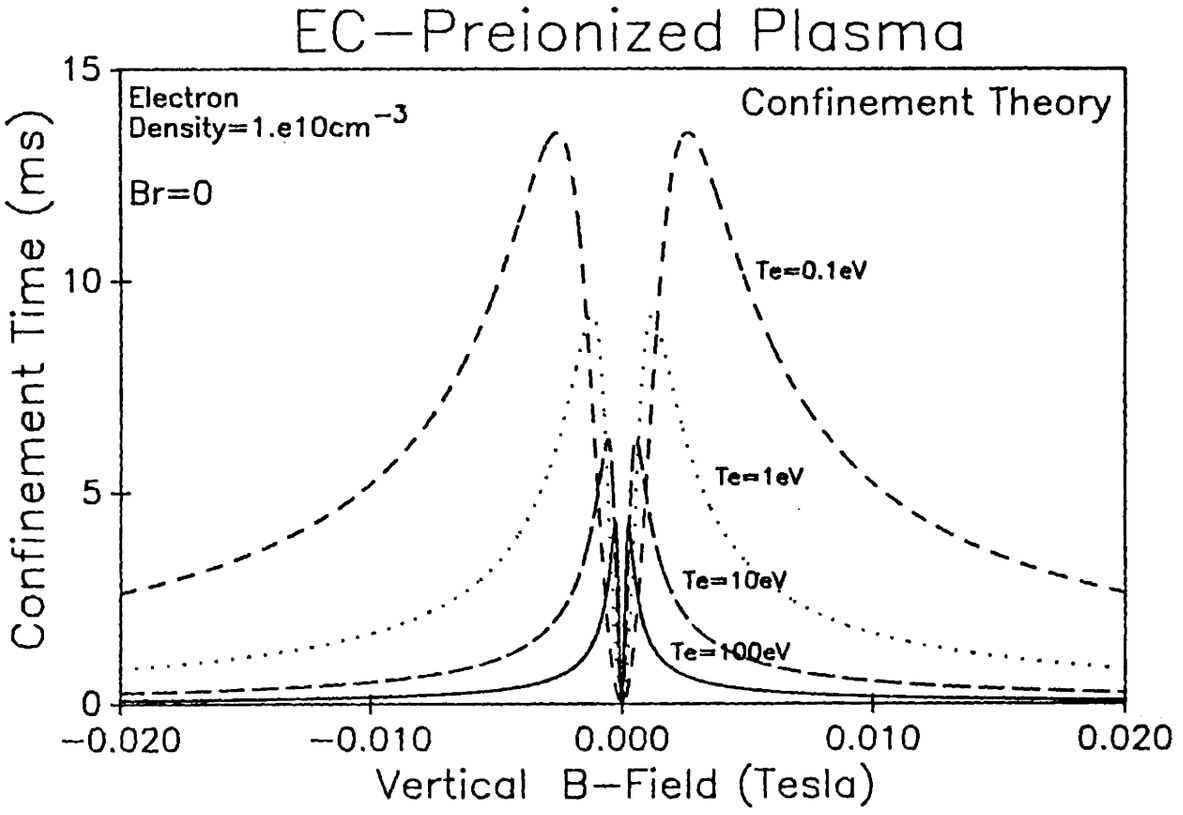
EC—Preionized Plasma
Electron
Density=1.e10cm^{-3}
Br=0
Confinement Theory
Te=0.1eV
Te=1eV
Te=10eV
Te=100eV
Confinement Time (ms)
15
10
5
0
−0.020
−0.010
0.000
0.010
0.020
Vertical B—Field (Tesla)

Figure 4-8

EC-PREIONIZED PLASMA
≈ 40 kW ECH
TIME (ms)
3.49
6.98
10.47
13.96
MAJOR RADIUS (cm)
52.50
50.20
47.90
45.60
43.30
41.00
(n_e)(in 3.6×10^{12} cm^{-3})
0.00
0.25
0.50
0.74
0.99
1.23
1.48

Figure 4-9

EC-PREIONIZED PLASMA
HALPHA EMISSION (ARB. UNITS)
0.00 0.55 1.10 1.65 2.21 2.76 3.31
≈40 kW ECH
0 1.2 1.91 5.82 8.73 11.63
TIME (ms)
MAJOR RADIUS (cm)
37.70 40.82 43.93 47.04 50.15 53.26

Figure 4-10

Figure 4-8 gives $\tau_e = 0.65$ ms, 1.7 ms, and 7 ms, respectively. Thus good agreement is found in the dependence of τ_e on $\langle n_e \rangle$ between the simple theory [30] [83]and the Versator experiments at $f = 35$ GHz. In Figure 4-10, the H_α emission, which is proportionial to the ionization rate, peaks at $R - R_0 \approx 2.25$ cm, between the EC and UH layers. The H_α emission dies off very rapidly after termination of the EC-wave pulse, as is expected because the EC waves are the dominant ionization mechanism.

The reduced $\mathbf{E} \times \mathbf{B}$-drift velocity is in the direction of increasing major radius R, so that the plasma density, which is produced in the region between the EC and UH layers, is expected to be appreciable only for $R > R_{EC}$, where R_{EC} is the major radius of the EC layer. This was not the case for the 1 ms, 35 GHz experiments, as shown in Figure 4-9. Perhaps this was due to the relatively large error fields present during the 35 GHz experiments, which were performed before the tokamak rebuild. In contrast, the 28 GHz experiments confirmed the above role of the EC-layer. This is shown in Figures 4-11 and 4-12, which show the plasma density as a function of time and major radius for the cases of $R_{EC} - R_0 = -5.5$ cm and $R_{EC} - R_0 = +2$ cm, respectively. For the $R_{EC} - R_0 = -5.5$ cm case, a peak density of about 1×10^{13} cm^{-3}is achieved and the plasma fills the chamber at major radii $R \gtrsim R_{EC}$. For the $R_{EC} - R_0 = +2$ cm case, the peak density is reduced to about 6×10^{12} cm^{-3}, and the density is significant only for $R - R_0 \gtrsim +3$ cm.

In order to estimate the relation between the electron temperature, density, and the injected EC power, the electron particle and energy confinement can be modeled as follows:

$$\frac{dn_e}{dt} = \langle \sigma v \rangle_i n_e n_a - \frac{n_e}{\tau_e} \tag{41}$$

$$\frac{3}{2}\frac{d(n_e T_e)}{dt} = (P_{EC} - P_{loss} - P_{rad})\, V_p^{-1} - \langle \sigma v \rangle_i\, n_e n_a E_{ion} - Q_{ei} - \frac{3}{2}\frac{n_e T_e}{\tau_E} \tag{42}$$

POSITION OF RESONANCE IN EC-FORMED PLASMA
R-R0 OF 28 GHZ EC RESONANCE
35 kW X-MODE
TIME (MS)
<ne> (10^12 cm^-3)
R-R0 (cm)
time (ms)

Figure 4-11

POSITION OF RESONANCE IN EC-FORMED PLASMA
R-R0 OF 28 GHZ EC RESONANCE
TIME (MS)
35 kW X-MODE
<ne> (10^12 cm^-3)
R−R0 (cm)
time (ms)

Figure 4-12

where P_{EC} is the launched rf power, P_{loss} is the rf losses (e.g., wall losses) and fast electron losses, $P_{rad} \approx 10^{-31} n_e N_{imp}$ (Wm^3) is the power radiated by impurities (assumed only oxygen and nitrogen), $Q_{ei} \approx 3 m_e n_e T_e / m_i \tau_{ei}$ is collisional energy transfer to ions, $E_{ion} \approx 30$ eV is the ionization energy for a hydrogen atom (including radiation and dissociation) [84], V_p is the plasma volume, n_a is the neutral hydrogen atom density, τ_E is the energy confinement time (which is set equal to τ_e), and τ_{ei} is the electron-ion collision time. Equations 41 and 42 are zero-dimensional in space. Solutions to the above equations are plotted in Figure 4-13, which shows the predicted electron temperature versus thermalized rf power for various densities, with $B_v = 5$ mT and $B_0 = 1.25$ T. This figure shows that the model predicts marginal breakdown and $T_e \lesssim 20$ eV, given the observed parameters of $n_e \approx 4$-5×10^{12} $\mathrm{cm}^{-3}$and $P_{EC} \approx 40$ kW. This is in crude agreement with experimental results. At low densities and low rf powers, this model predicts temperature higher than observed experimentally. This is because the parallel loss term dominates under these conditions, and parallel heat conduction reduces τ_E. This is not accounted for in the model.

Note from Figure 4-6 that the combined action of drift and the vertical electric field propel the thermal electrons to the left, for the chosen field directions. This generates a small toroidal plasma current, which depends on B_v. The superthermal electrons are selectively confined in a related way, generating a superthermal current in the same direction as the thermal current. The situation for superthermal electrons is shown in Figure 4-14. Electric fields and interactions with other particles are neglected, resulting in a simple competition between $\nabla \mathbf{B}$ plus curvature drift and parallel streaming along the slanted magnetic field lines. Ignoring relativity, selective confinement of superthermals with $B_v(\mathbf{v}_{e\|} \cdot \mathbf{B}) > 0$ is achieved when

$$\mathbf{v}_e \frac{B_v}{B} = \frac{m_e}{e} \frac{\mathbf{R} \times \mathbf{B}}{R^2 B^2} \left(v_{e\|}^2 + \frac{v_{e\perp}^2}{2} \right). \tag{43}$$

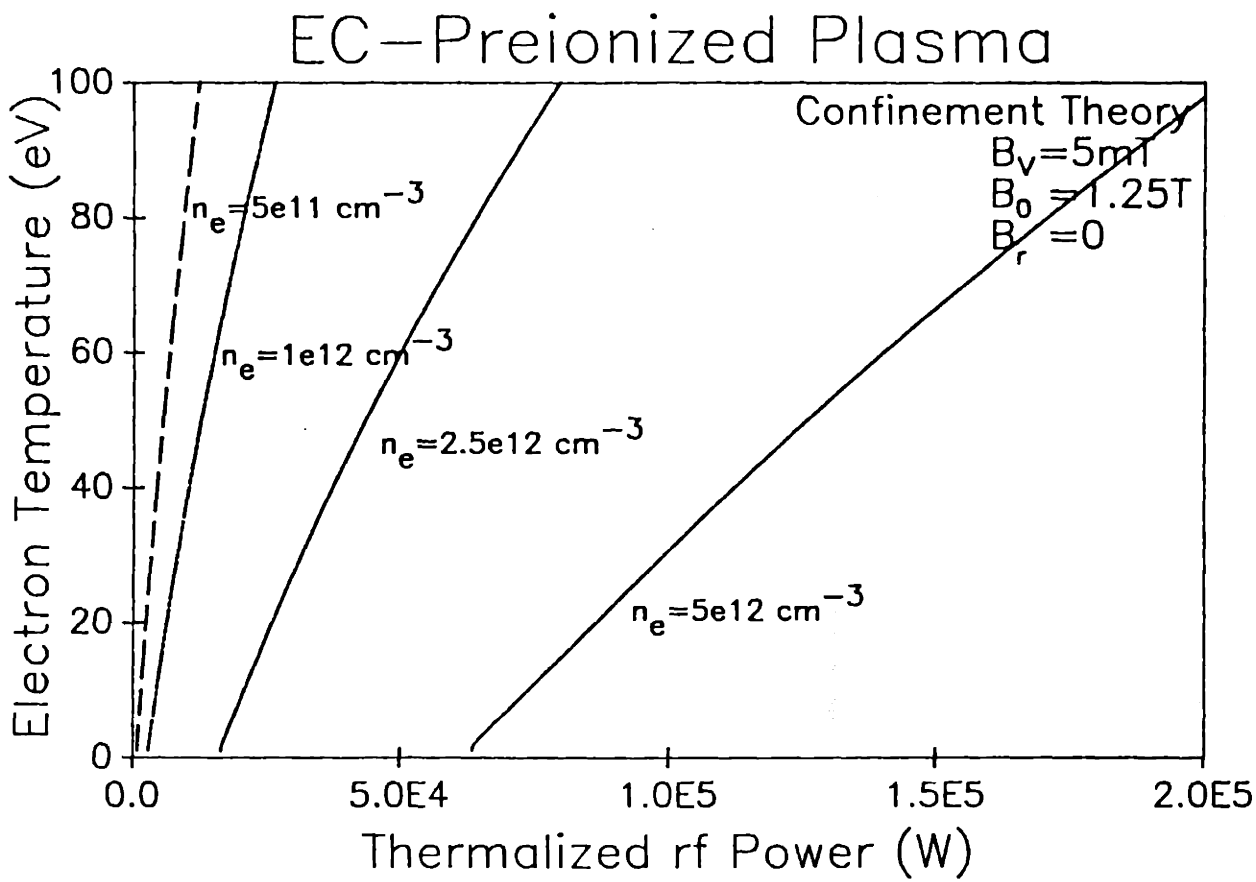
EC–Preionized Plasma
Confinement Theory
B_v=5mT
B_0 =1.25T
B_r =0
n_e=5e11 cm^{-3}
n_e=1e12 cm^{-3}
n_e=2.5e12 cm^{-3}
n_e=5e12 cm^{-3}
Electron Temperature (eV)
100
80
60
40
20
0
0.0
5.0E4
1.0E5
1.5E5
2.0E5
Thermalized rf Power (W)

Figure 4-13

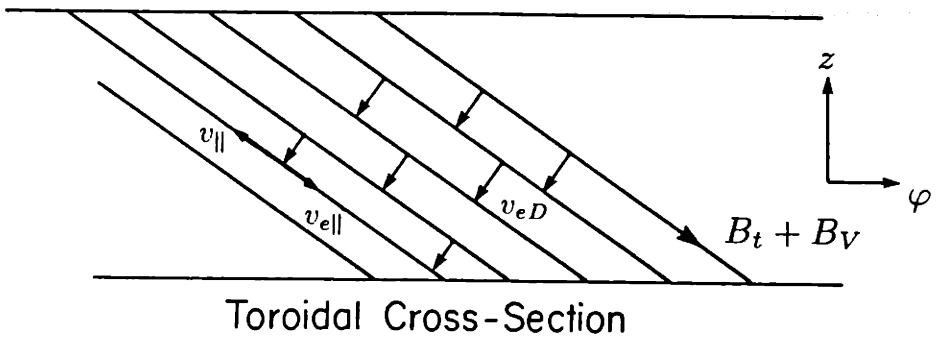

Figure 4-14 Confinement of superthermal electrons in EC-formed plasma with B_V and B_t.

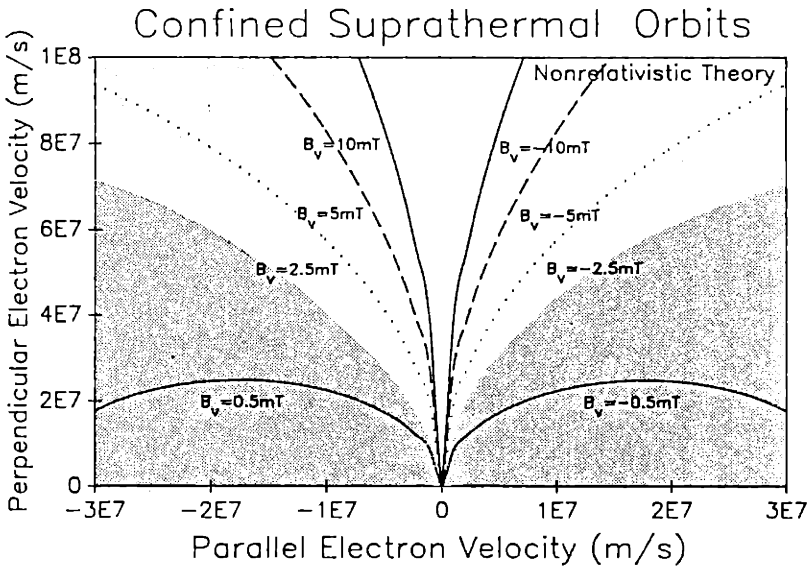

Figure 4-15

The solutions to this equation are ellipses in velocity space:

$$1 = \left(2\bar{v}_{\|}^2 - 1\right)^2 + 2\bar{v}_{\perp}^2 \tag{44}$$

where $\bar{v}_{\|} = v_{e\|} m_e / eB_v R$ and $\bar{v}_{\perp} = v_{e\perp} m / eB_v R$. These ellipses are plotted in Figure 4-15 for various vertical magnetic fields. This figure shows that smaller vertical fields are generally better for confining electrons with large parallel velocity. Such electrons may be generated by pitch-angle scattering of electrons with high $v_{\perp}$ that are created by the EC waves.

Strong evidence of confinement of superthermal electrons was found during experiments on Versator with 5 ms pulses of 32 kW of ECH at 28 GHz. These experiments were performed after the tokamak rebuild, which considerably reduced the nonaxisymmetric error fields. This is indicated in part by the fact that up to 850 A of plasma current was generated in these EC-formed discharges, as opposed to about 50 A prior to the rebuild. The bremstrahlung emitted by the superthermal electrons was detected with a silicon-lithium crystal and a pulse-height analyzer. These spectra are shown in Figures 4-16a and 4-16b for $B_0 = 1$ T and 0.9 T, respectively. A significant degradation in the total counts and in the X-ray temperature T_{SXR} is seen when the ω_{ce} layer is moved from $R = R_0$ to $R - R_0 = -4$ cm (corresponding to $B_0 = 1$ T and $B_0 = 0.9$ T). The count total for $B_0 = 1$ T was 147 and $T_{SXR} \approx 1.75$ keV, whereas the count total for $B_0 = 0.9$ T was 80 and $T_{SXR} \approx 0.75$ keV, excluding the three counts at 5 keV and 5.5 keV.

The dependence of the generated plasma current and the $2\omega_{ce}$ (70 GHz) emission on applied vertical field is shown in Figure 4-17. The $2\omega_{ce}$ emission is a good indicator of the presence of superthermal electrons on Versator. The dependence of I_p and $2\omega_{ce}$ emission on B_v are distinctly different. This indicates that the plasma current is primarily carried by thermal electrons. Thus the mechanism of Figure

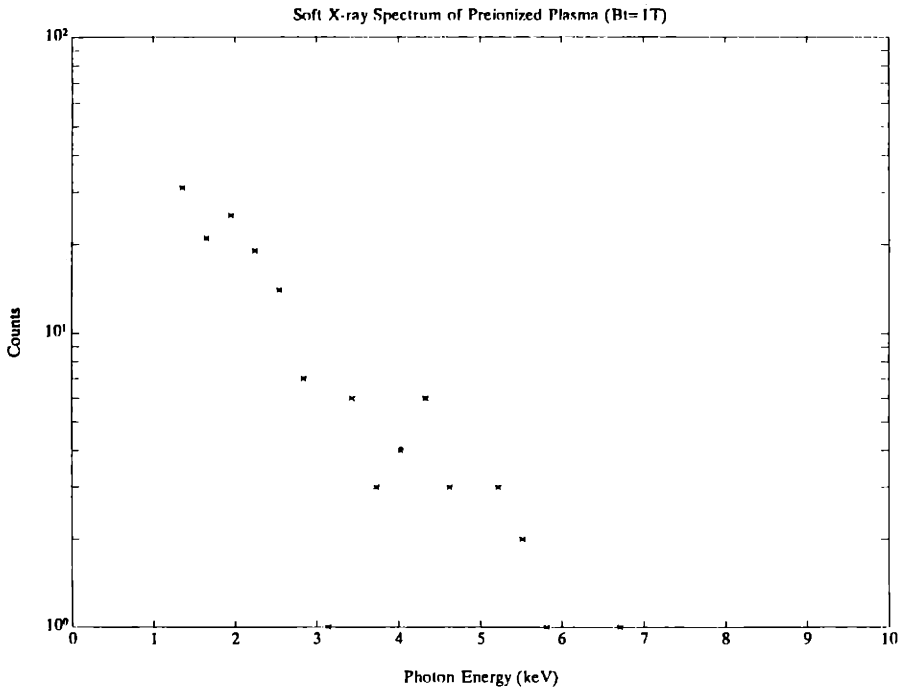

Figure 4-16a

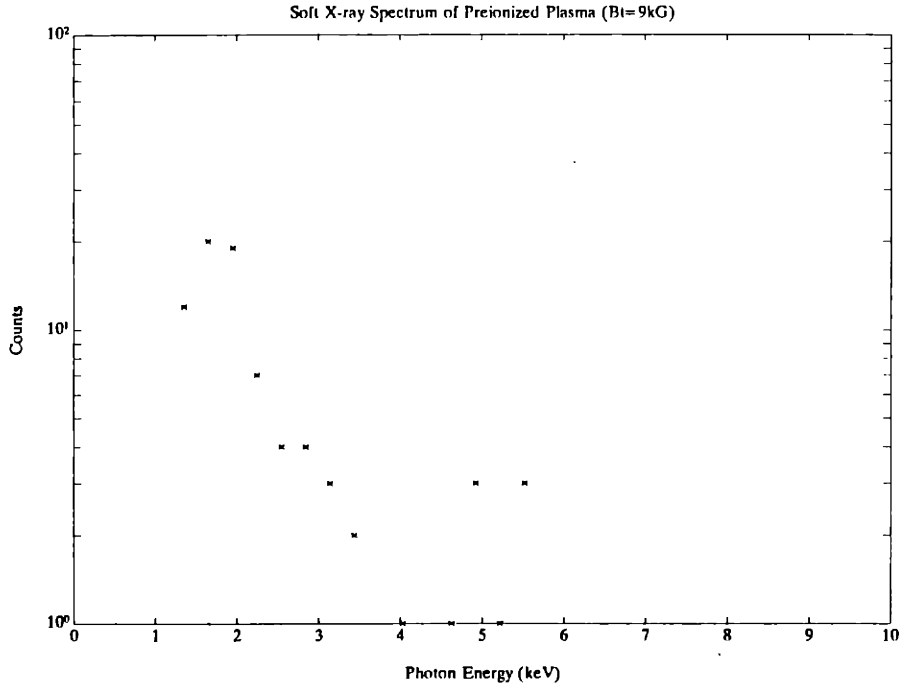

Figure 4-16b

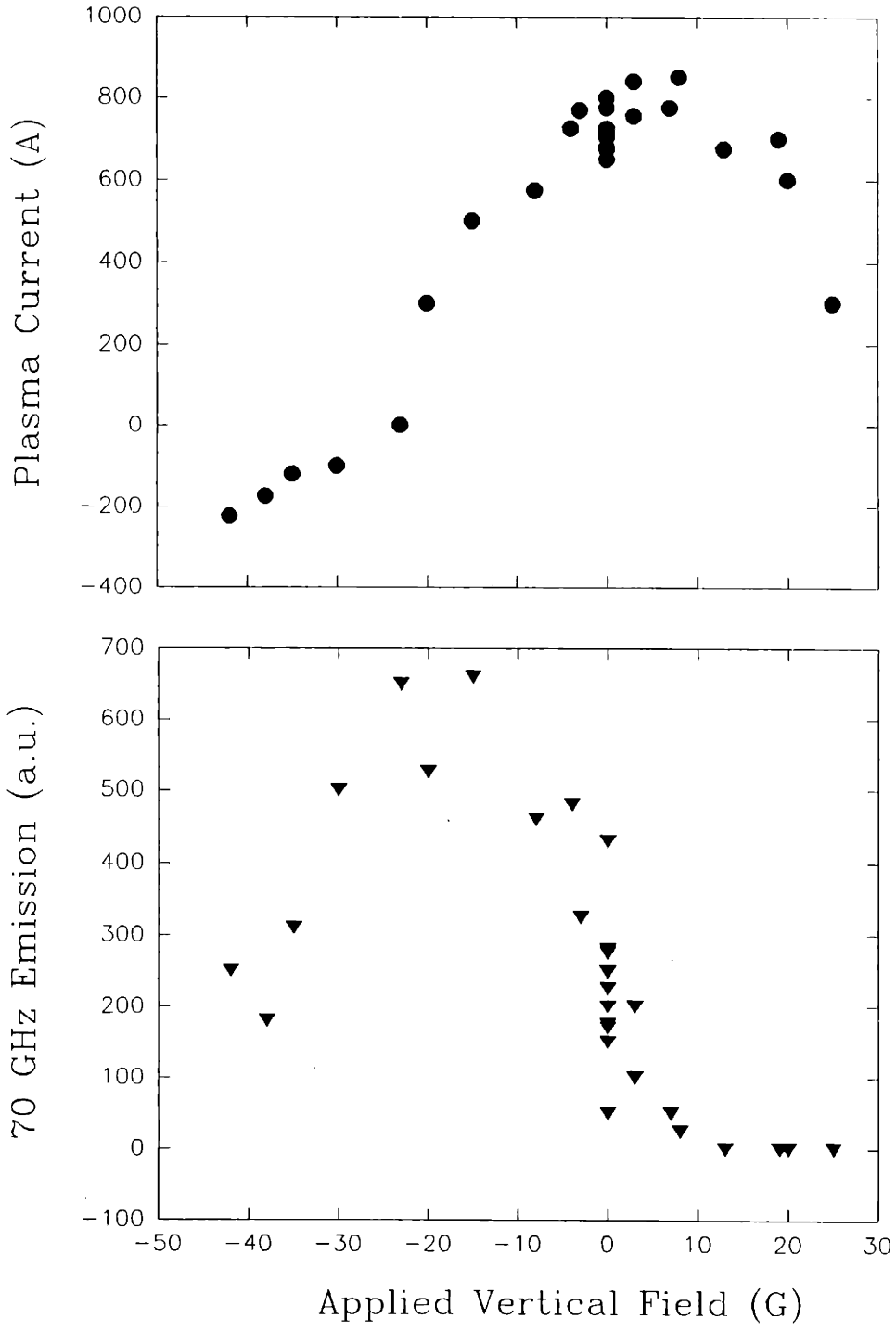

Figure 4-17 Dependence of I_p and $2\omega_{ce}$ on B_V for EC-formed plasma.

4-6 (thermal electron confinement) is more important in generating toroidal current than the mechanism of Figure 4-14 (superthermal electron confinement), when the populations of thermal and superthermal electrons are taken into account. A striking feature of these data is the asymmetry of the dependence of both I_p and the $2\omega_{ce}$-emission on B_v. The zero crossing of I_p is near $B_v = -2$ mT, suggesting that the toroidal field coils produce a vertical error field of +2 mT. However, $B_v = -2$ mT is not a perfect inflection point, because dI_p/dB_v is much greater to the right of the zero-crossing than to the left. This lack of symmetry could be caused by non-axisymmetric vertical error fields, or it may reflect a modification of the confinement mechanism brought about by the poloidal B-field created by I_p. Assuming I_p is contained within a 12 cm circle in the poloidal plane, centered on the plasma axis, $I_p = 850$ A gives $B_\theta = 14$ G at $R - R_0 = \pm 12$ cm. Thus closed flux surfaces may exist for $B_V \lesssim 10$ G. A broad maximum in the 70 GHz emission is seen near $B_v = -2$ mT, with a half-width of 2 mT. Assuming the vertical error field is +2 mT, this implies that the superthermal electrons generated by the EC waves lie in the shaded region of velocity space shown in Figure 4-15, according to the simple theory.

4.2 Electron Cyclotron Waves and Plasma Turbulence

During EC-wave injection on Versator, strong enhancement of edge magnetic and electrostatic tubulent fluctuations is observed. The magnetic fluctuations may cause anomalous losses of fast current-carrying electrons, and the electrostatic fluctuations may cause anomalous losses of thermal electrons. Hence both, particularly the magnetic fluctuations, are important to the understanding of current drive on Versator. In this section, a basic description of plasma magnetic turbulence is given,

measurements of fluctuations are described, and the fluctuation-induced enhancement of superthermal electron transport is calculated theoretically and compared to experimental results.

Plasma turbulent fluctuations, both magnetic and electrostatic, are suspected as the major cause of anomalously high electron particle and energy transport in tokamaks [85-88] . For current-drive, the primary concern is with the particle confinement of the fast, current-carrying electrons. For these electrons, it is expected that magnetic fluctuations cause greater transport than electrostatic fluctuations [85].

The basic theoretical description of magnetic fluctuations in a tokamak is now outlined, following the treatments of references [89] and [90]. The magnetohydrodynamic (MHD) equilibrium quantities q and β are defined as follows, assuming an axisymmetric toroidal plasma with circular poloidal cross-section. The safety factor $q = rB_0/RB_\theta$, where r is the minor radius, B_0 is the toroidal field on axis, R is the major radius, and B_θ is the poloidal magnetic field. The plasma volume-averaged beta, $\beta = \langle 2\mu_0 nT/B^2 \rangle$, is the ratio of the average plasma pressure to the average magnetic pressure. Generally, $\beta \ll 1$ and q monotonically increases from $r = 0$ to $r = a$ (the plasma edge). These conditions hold for the discharges on Versator considered in this thesis. Under these conditions, the magnetic-field variations outside the plasma (where magnetic probes can measure the fluctuations) can be computed as a linear noninteracting sum of fields generated by currents near each rational flux surface. A rational flux surface is a surface where $q = m/n$, where m and n are integers. In a tokamak with circular flux surfaces, the rational surfaces are nested tori.

The toroidal plasma is now approximated as a straight cylinder. Under these conditions, the axial component of the vector potential,

$$A_z(\mathbf{r}) = \mu_0 \int \frac{j_z(\mathbf{r}')}{|\mathbf{r} - \mathbf{r}'|}\, d\mathbf{r}', \tag{45}$$

is given outside the plasma by

$$A_z(r,\theta) = A_0 \ln(r) + \sum_{m=1}^{\infty} A_m \left[r^{-m} - \left(r/b^2\right)^m \right] e^{im\theta}. \tag{46}$$

A conducting wall has been assumed to exist at $r = b$. The conducting wall on Versator is square in cross-section, but Equation 46 still gives an adequate estimate of the screening effects of the wall on the modes. This effect is only significant very near the wall for moderate to high m. For the turbulent fluctuations considered here, the effect of the wall can be neglected, and the magnetic fields are

$$(-i)B_{mr} = B_{m\theta} = mA_m r^{-(m+1)} \tag{47}$$

Figure 4-18 shows the major plasma parameters for EC current-drive (ECCD) discharges for which fluctuation data are presented, and Figure 4-19 shows the parameters of the target discharge. The plasma current is ramped up rapidly by the ohmic-heating (OH) transformer at time $t \approx 5$ ms, and peaks at nearly 30 kA at $t = 8$ ms. The plasma current and the loop voltage fall rapidly during the following 10 ms. This is followed by a 20 ms period of slower decay of I_p and V_{loop}, during which 32 kW of EC power is injected in the X-mode polarization from the high-field side with $\alpha = 0°$, where α is the angle from the normal to $\mathbf{B}$, and $\alpha < 0$ is in the direction of the plasma current. The electron density slowly decays from about 3×10^{12} cm^{-3}to 2×10^{12} cm^{-3}prior to EC wave injection. This density is sufficiently low to allow the formation of a slideaway electron distribution function, in which a large fraction of the plasma current is carried by superthermal electrons. The electron density drops abruptly to 1×10^{12} cm^{-3}upon injection of the EC waves, and slowly rebuilds during the pulse. The 70 GHz ($2\omega_{ce}$ emission) cyclotron emission shown in Figure 4-18 is generated primarily by the superthermal electrons.

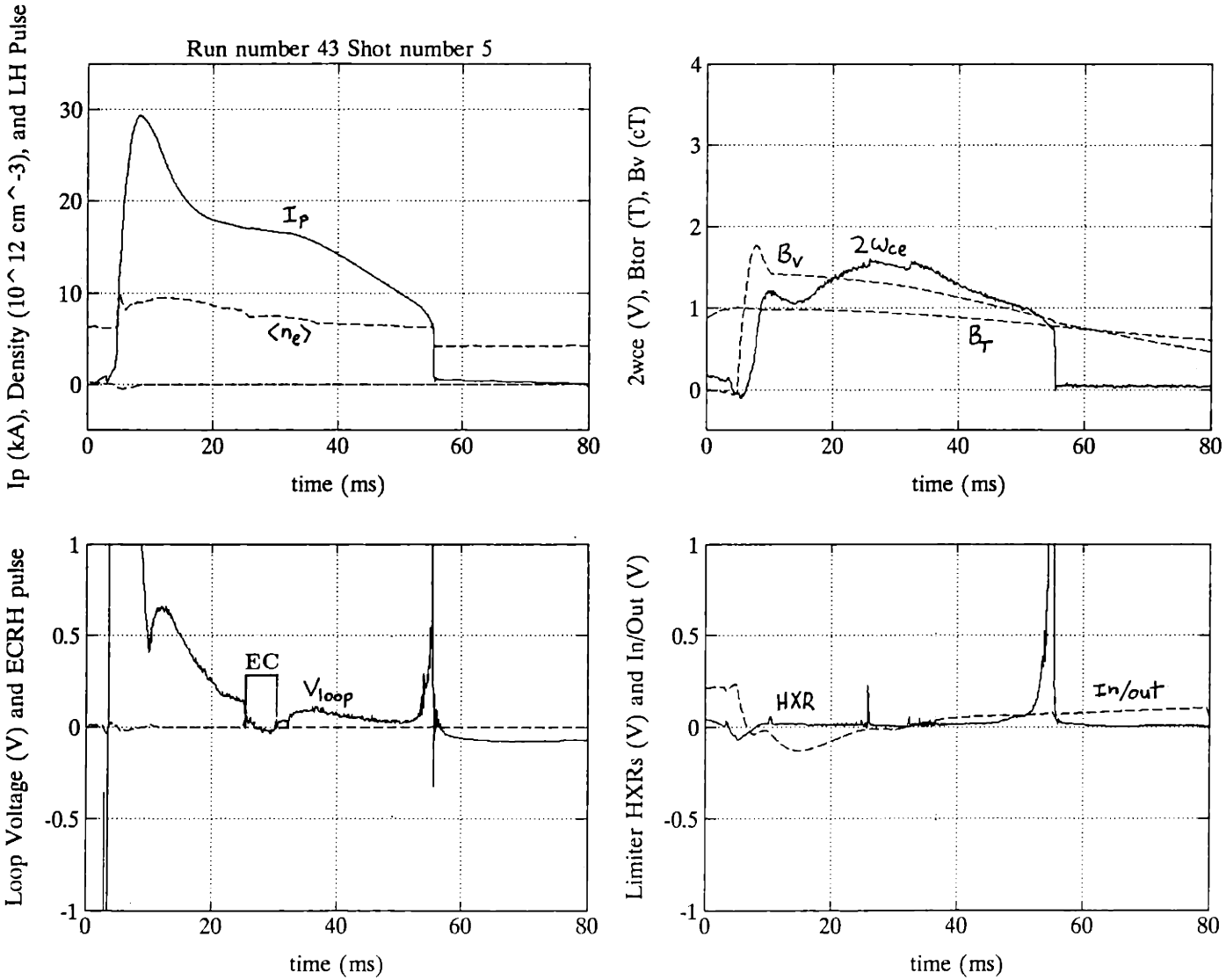

Figure 4-18 Plasma parameters for ECCD discharge with turbulence.

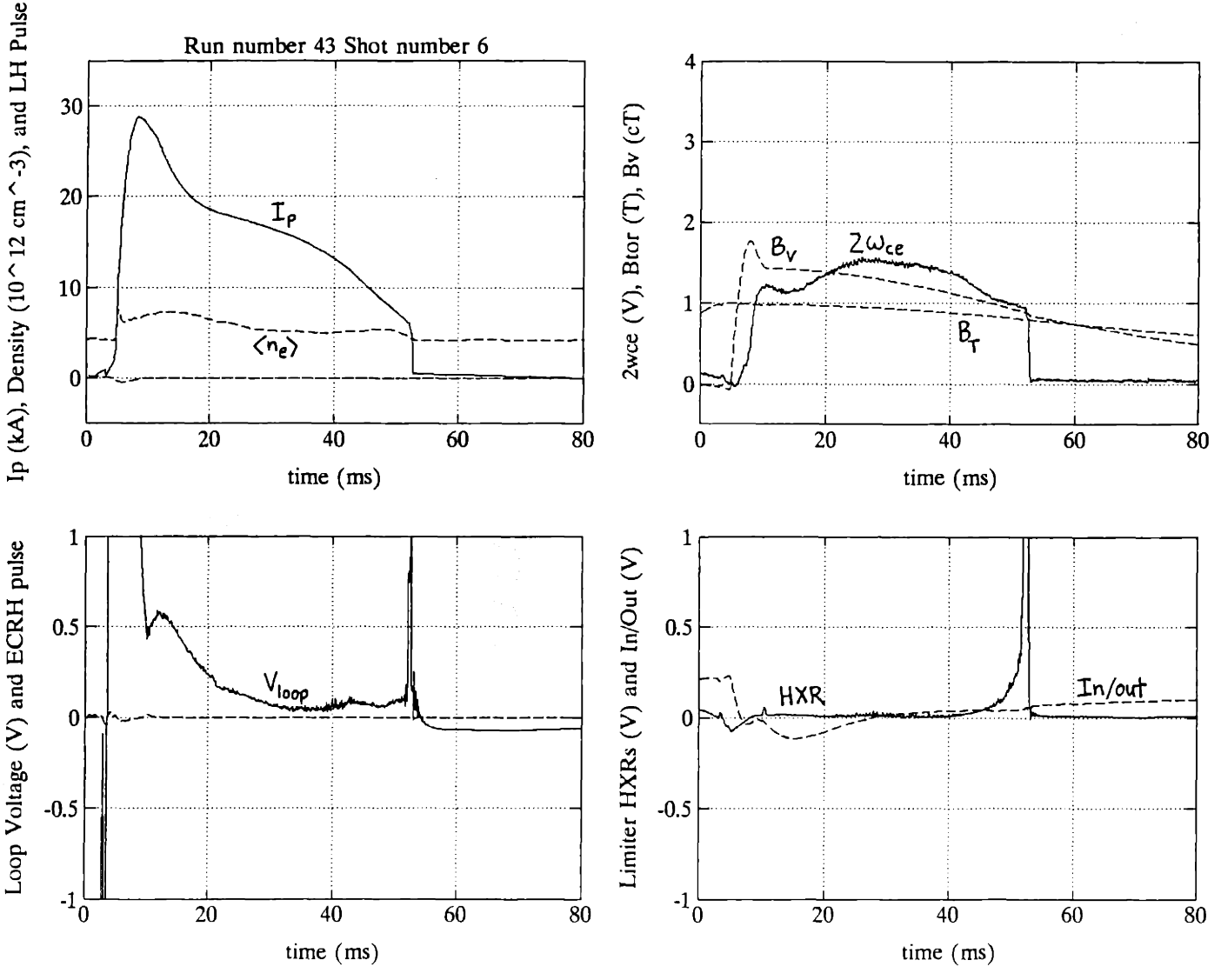

Figure 4-19 Plasma paramters for OH target discharge with turbulence.

When the EC waves are injected at $t = 25$ ms, the decay in I_p is partially arrested, and V_{loop} drops rapidly, reaching negative values near the end of the EC pulse. The plasma major radius expands during EC wave injection, indicating an increase in $\beta_p + \ell_i/2$, where $\beta_p \equiv \langle 2\mu_0 nT/B_p \rangle$, B_p is the poloidal magnetic field, and ℓ_i is the plasma internal inductance. This must be caused by either an increase in plasma pressure or in ℓ_i, because the plasma current (and hence the volume-averaged poloidal magnetic pressure) is raised by the EC pulse. The increase in plasma pressure must come from electron heating, because the electron density is constant or drops during EC wave injection, and EC-wave effects on ions are small. This could be heating of thermal electrons or superthermal electrons. The single-pass absorption is less than 1% for the X-mode at $\theta \approx 90°$ for the density and temperature of the bulk Maxwellian. Therefore direct heating of thermal electrons by the EC wave is unlikely. Mode conversion to the Electron Bernstein (EB) wave may occur near the upper-hybrid layer, however, and the EB waves may heat the thermal electrons. Another possibility is an increase in ℓ_i, which is caused by a narrowing of the plasma current radial profile. This might occur if the EC waves drive current mostly near the magnetic axis. However, the large increase in ℓ_i required to account for the outward motion is inconsistent with estimates of ℓ_i based on measured X-ray profiles. The increased signal on the magnetic probes is *not* due to the fact that the ECH pushes the plasma outward, closer to the probes. During discharges in which the ECH does not move the plasma outward, a strong increase in signal is still observed. Also, during discharges in which the ECH does move the plasma outward, the plasma is closest to the probe at the end of the ECH pulse, yet the enhanced turbulent signal is of uniform amplitude throughout the ECH pulse. The response of the signal to the ECH is much faster than the response of the in/out position.

The raw signal from magnetic probe #5 is shown in Figure 4-20 for the discharge of Figure 4-18 (with EC), and in Figure 4-21 for the discharge of Figure 4-19 (without EC). The voltage across the terminals of this coil has been digitized at a

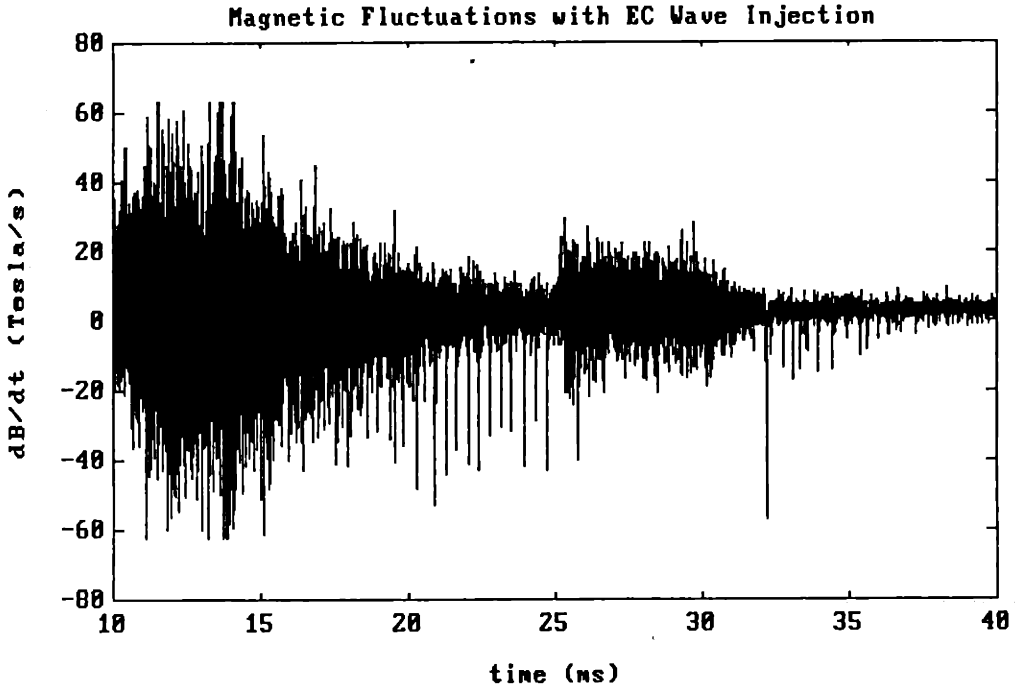

Figure 4-20

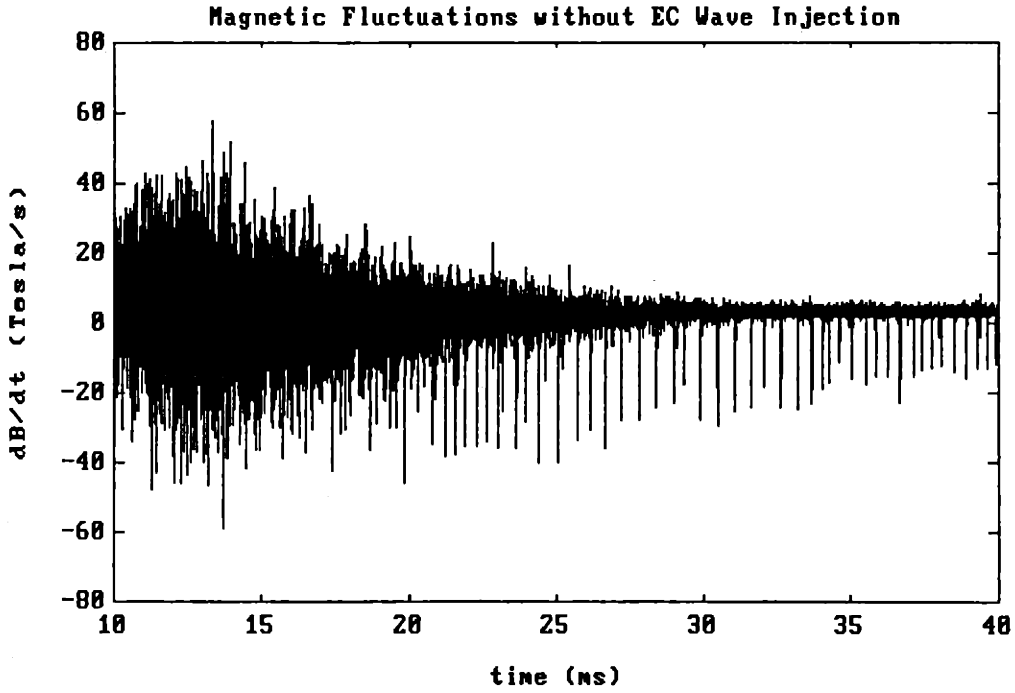

Figure 4-21

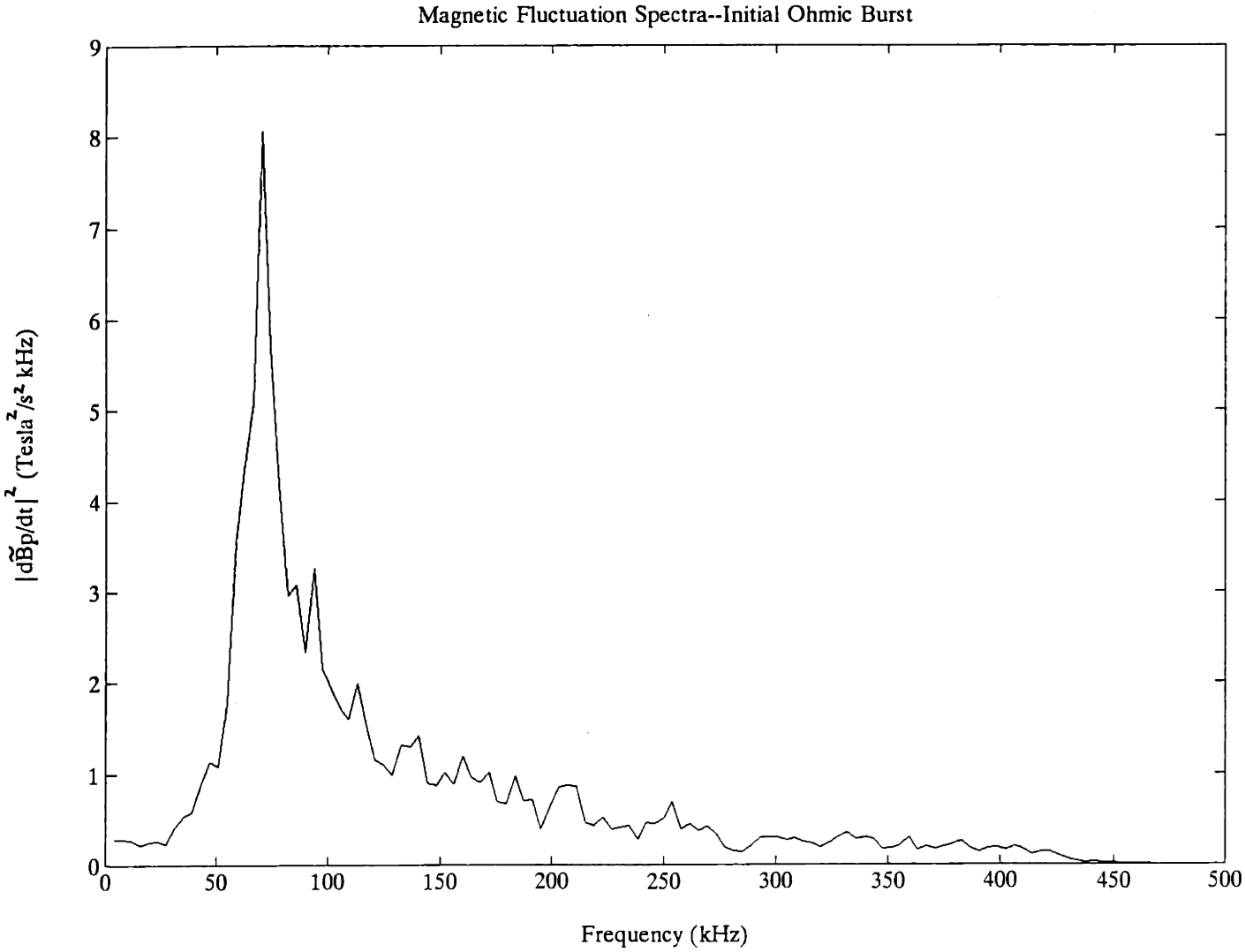
Magnetic Fluctuation Spectra--Initial Ohmic Burst
$|d\tilde{B}p/dt|^2$ (Tesla^2/s^2 kHz)
Frequency (kHz)
0
1
2
3
4
5
6
7
8
9
0
50
100
150
200
250
300
350
400
450
500

Figure 4-22

1 MHz sampling rate and divided by the effective area of the coil (0.0040 m^2). Note the large burst of activity during the high-current OH phase of the discharges. The power spectrum of $d\tilde{B}_p/dt$ during this time (averaged over both discharges) is shown in Figure 4-22. The majority of the spectral energy during this phase is in a mode of frequency $f = 70$ kHz, most likely with relatively low poloidal mode number m. The trailing spectrum from 100 kHz up to the filter rolloff at 400 kHz could be a consequence of the complicated time and spatial dependence of the 70 kHz mode, or it could be turbulence unrelated to this mode. At t=25 ms the EC waves are injected, and the magnetic fluctuations increase in amplitude, as can be seen from Figures 4-20 and 4-21. These signals do not contain a large single mode, but are almost evenly distributed across the frequency band 50-400 kHz. Figure 4-23 shows the power spectrum $|d\tilde{B}_p/dt|^2$ versus frequency for the period 25.5 ms$< t <$29.5 ms with and without EC-wave injection. Note that the vertical scale on this plot is 30 times smaller than on Figure 4-22. Also, the plot shows the square of the time derivative of $\tilde{B}_p$, which is weighted by the square of the frequency. The power spectrum of the actual fluctuating field, $|\tilde{B}_p|^2$, is plotted in Figure 4-24 for (a) the initial ohmic burst, (b) during EC-wave injection, and (c) without EC-wave injection but during the same phase of a similar discharge as (b). This power spectrum obeys Parseval's theorem: $B_p(\mathrm{rms}) = \sqrt{\int B_p^2(f)\,df}$. The integral over f is from zero to half the sampling frequency (the Nyquist frequency). The fluctuations are enhanced by an order of magnitude by the EC waves across a very broad frequency range 50 kHz$\lesssim f \lesssim$400 kHz, where the upper limit is determined by the filter roll-off.

Electrostatic fluctuations were observed using a floating Langmuir probe. The probe was inserted approximately 0.25 cm behind the edge of the limiter, and oscillations in its floating potential were filtered at 400 kHz and digitized at 1 MHz. These fluctuations are shown versus time in Figures 4-25 and 4-26. Note that the electrostatic activity is not as intense during the initial ohmic phase as the magnetic activity, at least as measured outside the plasma. The electrostatic fluctuations increase as a result of the EC waves, but not to as great a degree as the magnetic

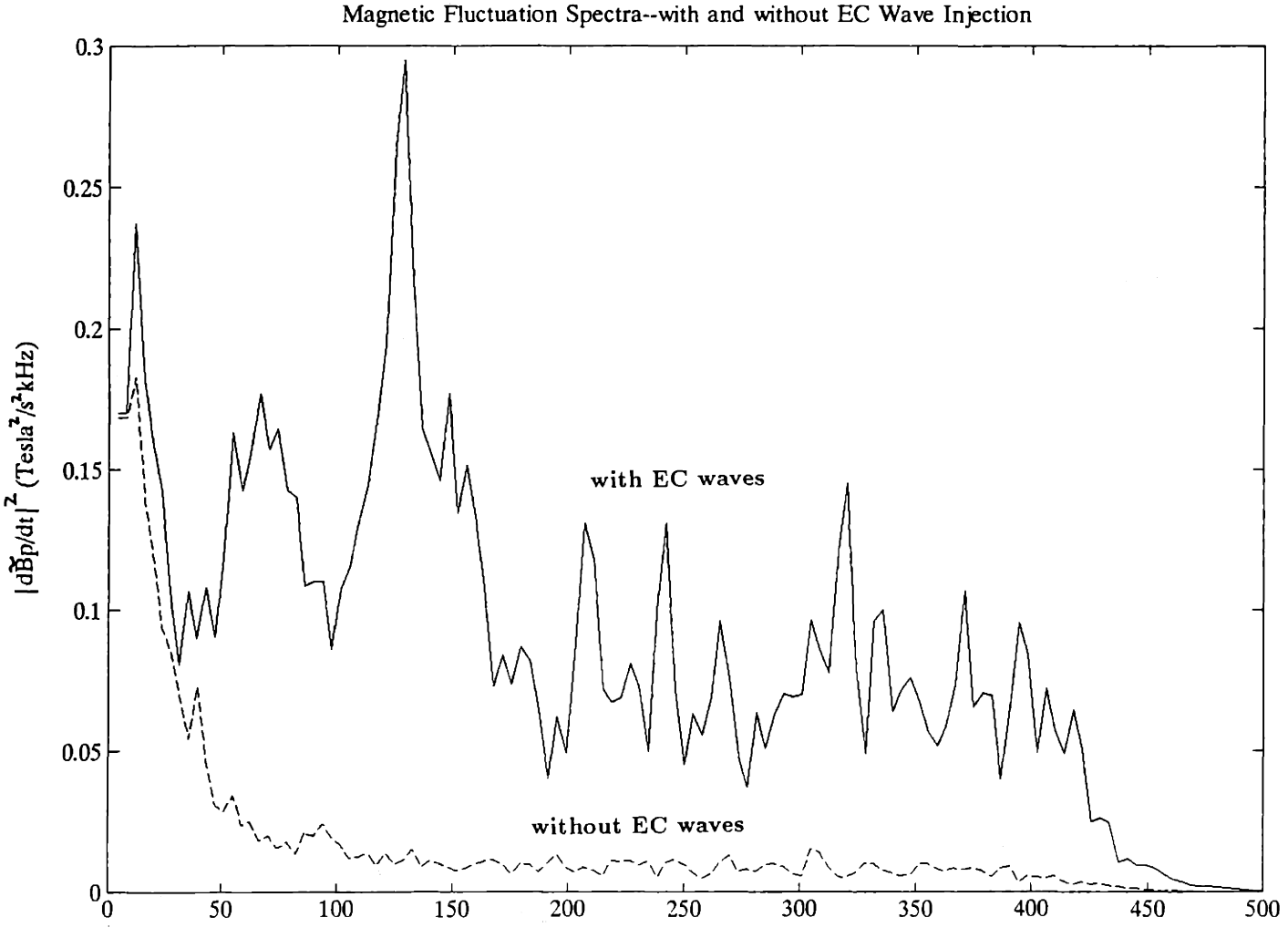
Magnetic Fluctuation Spectra--with and without EC Wave Injection
0.3
0.25
0.2
0.15
0.1
0.05
0
0
50
100
150
200
250
300
350
400
450
500
with EC waves
without EC waves
Frequency (kHz)

Figure 4-23

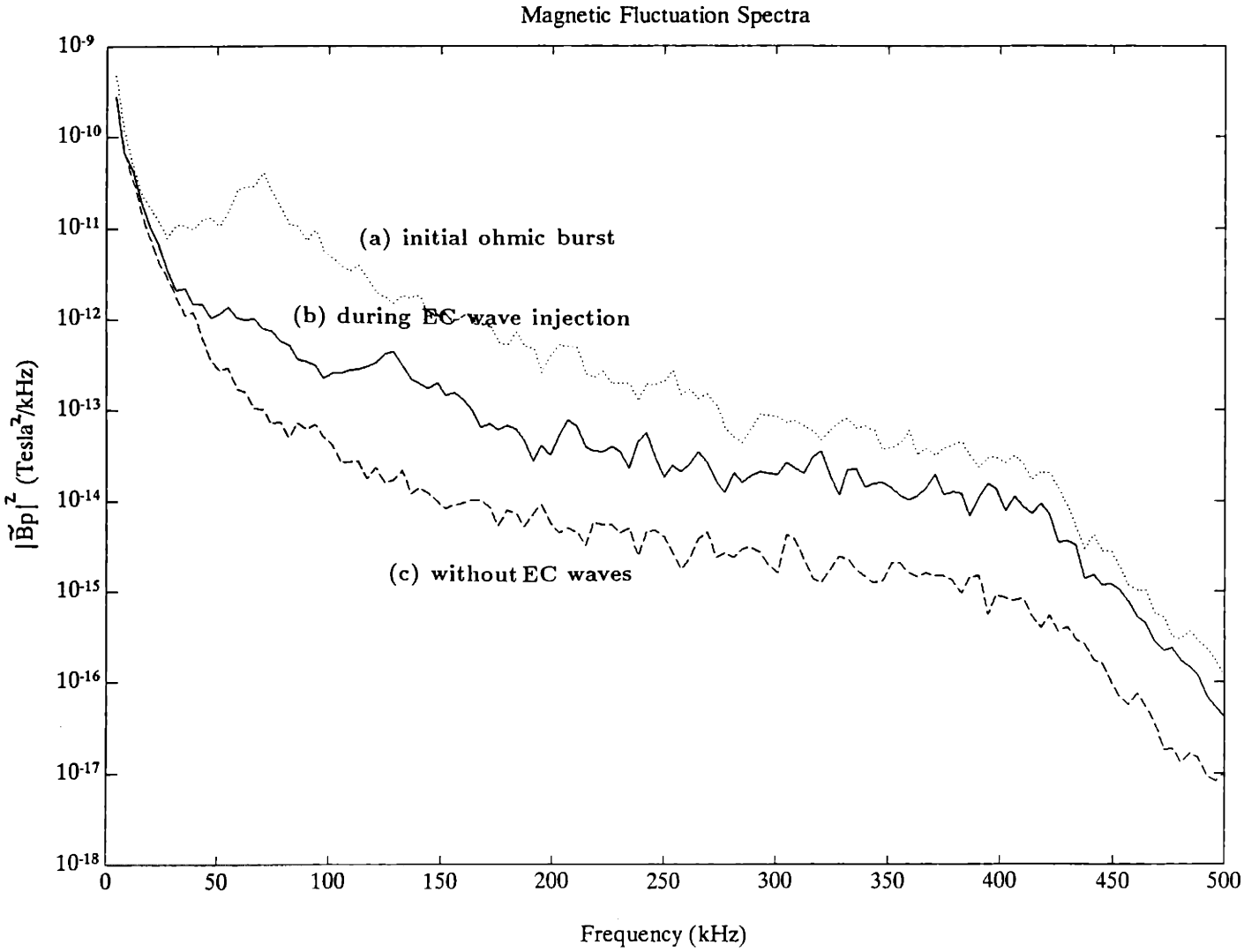
Magnetic Fluctuation Spectra
(a) initial ohmic burst
(b) during EC wave injection
(c) without EC waves
$|\tilde{B}p|^2$ (Tesla^2/kHz)
Frequency (kHz)
10^{-9}
10^{-10}
10^{-11}
10^{-12}
10^{-13}
10^{-14}
10^{-15}
10^{-16}
10^{-17}
10^{-18}
0
50
100
150
200
250
300
350
400
450
500

Figure 4-24

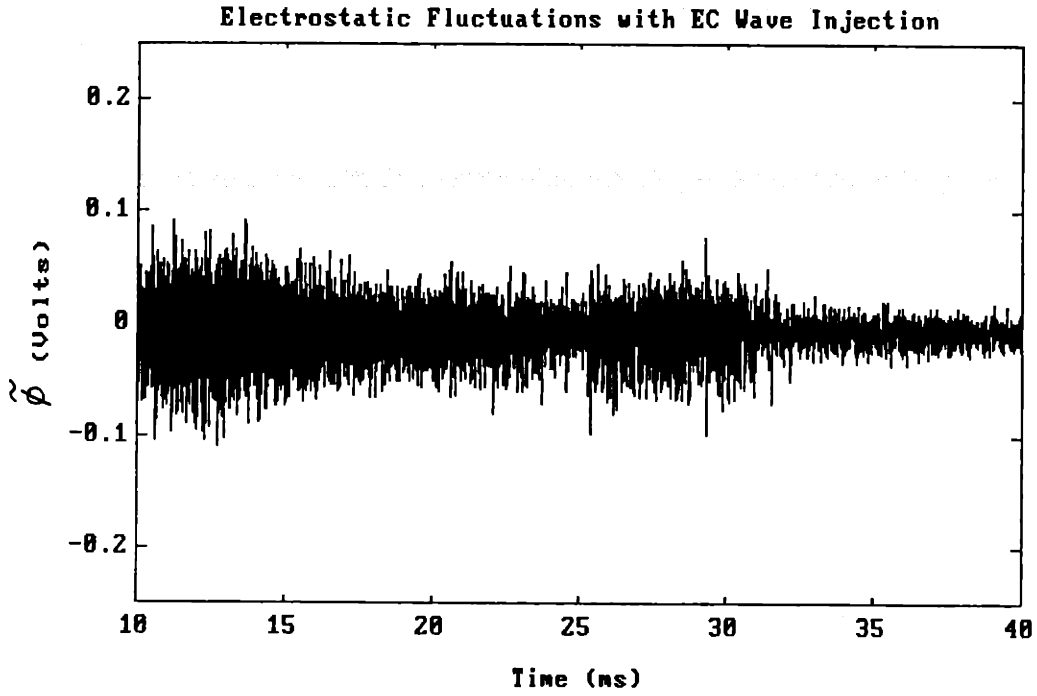

Figure 4-25

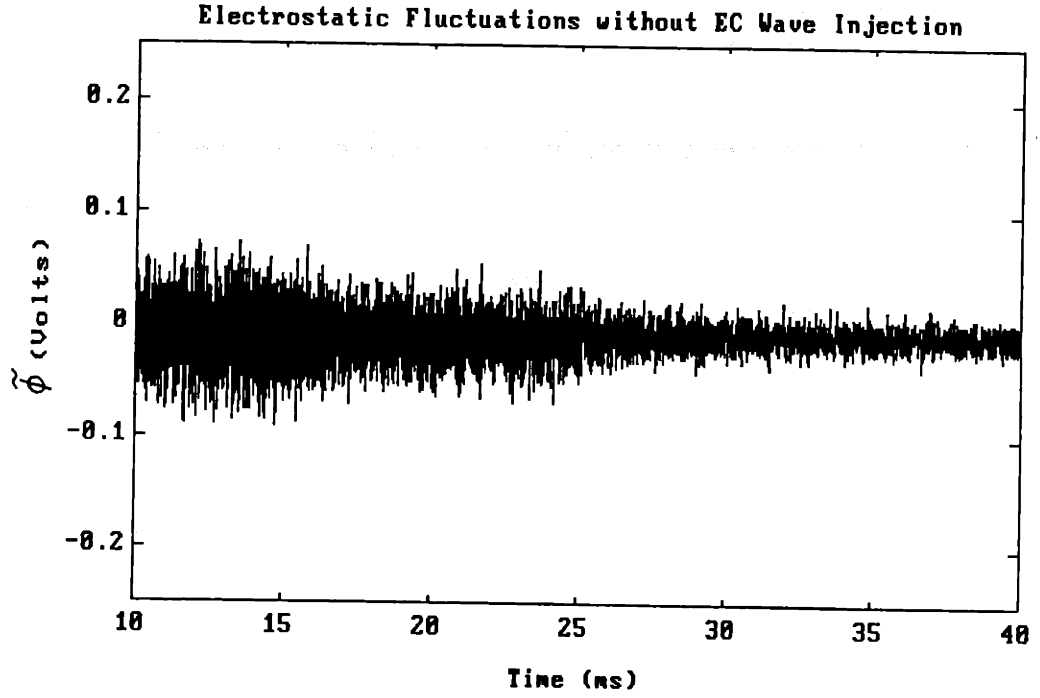

Figure 4-26

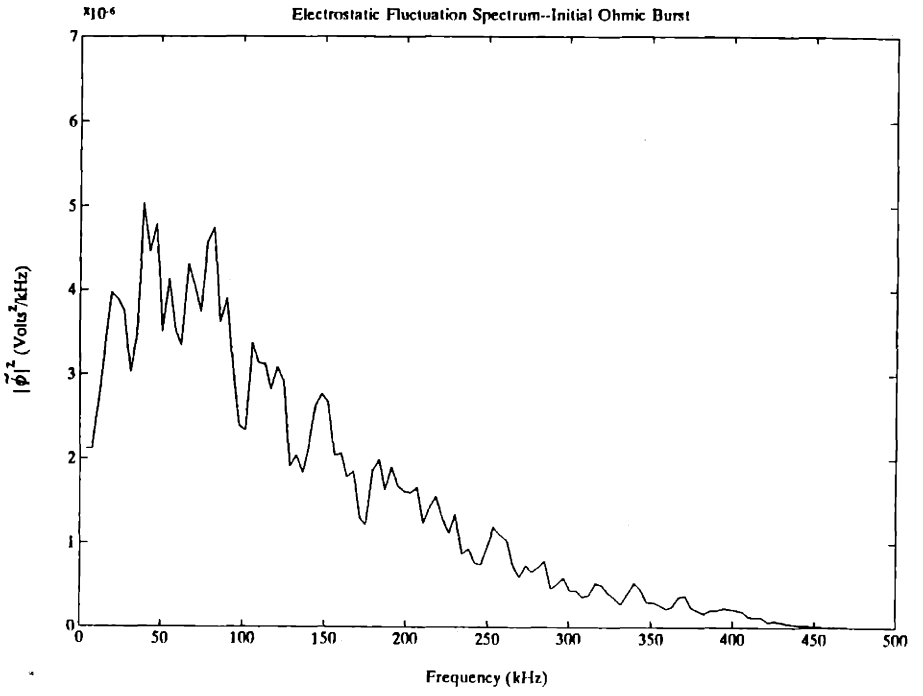

Figure 4-27

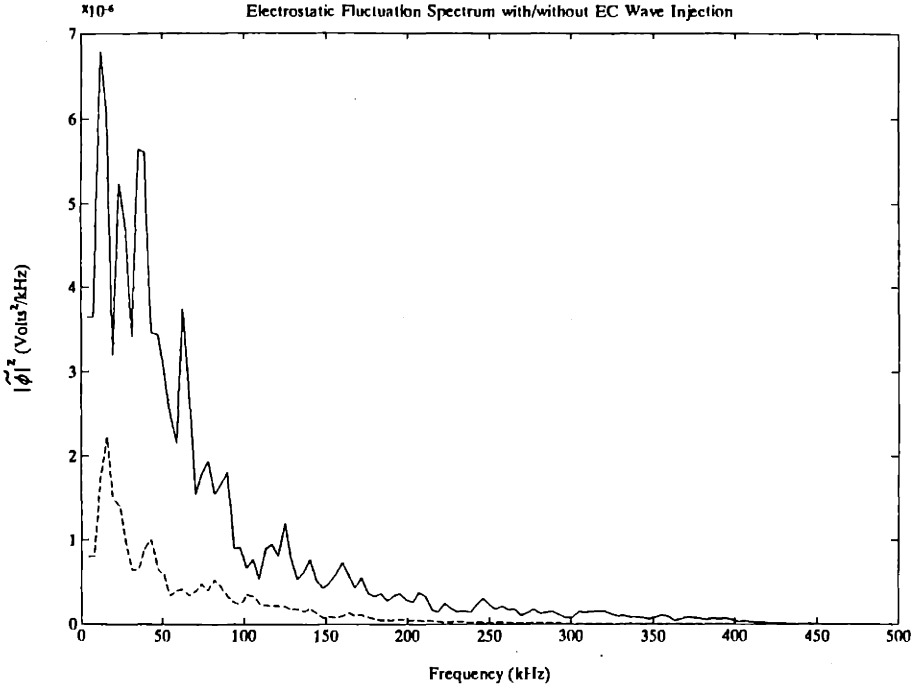

Figure 4-28

probe signal. The electrostatic fluctuation spectra are shown in Figures 4-27 and 4-28 for the initial ohmic phase and the EC-wave injection phase, respectively. In all cases the fluctuation level falls with increasing frequency, more so during the EC-wave phase than the initial ohmic phase. The electrostatic fluctuation levels are comparable for the initial ohmic and EC phases, in contrast to the magnetic fluctuation levels. Figure 4-28 shows that the EC waves enhance $|\tilde{V}_{float}|^2$ by about a factor of four at low frequencies ($\lesssim$ 50 kHz), and that this enhancement ratio increases with increasing frequency. There is no clear indication of large single-frequency modes in any of the electrostatic spectra.

Results on Versator suggest that the fluctuations are driven by some interaction of the EC waves and the plasma interior, rather than directly at the plasma edge. This is suggested by Figures 4-29 and 4-30, which show, on a fast time scale, the turn-on of the EC pulse and the magnetic probe signal for two different toroidal fields. The magnetic probe is located at R = 0.545 m, and the EC layer was located at R = 0.445 m and R = 0.393 m for Figures 4-29 and 4-30, respectively. Relative to the turn-on time of the EC wave power, the fluctuations reach their full enhancement about 80 μs later when R_{EC} = 0.393 m than when R_{EC} = 0.445 m. Approximating the distance between the locations of the turbulence source for the two cases as the distance between the EC layers (0.052 m) gives a propagation velocity of 650 m/s for the turbulent wavefront. The origin of the fluctuations appears to be much closer to the probe than the EC layer, but not all the way at the plasma edge, because for R_{EC} = 0.445 m the enhanced turbulence arrives at the probe within 20-50 μs of EC turn-on. This result is different from observations on the TEXT tokamak [89], in which the time-of-arrival of the enhanced turbulent signal was found not to depend on the position of the ω_{ce}-layer. The TEXT plasma is typically hotter, denser, and larger than on Versator.

We now estimate the radial diffusion coefficient for the superthermal electrons that would be expected from the observed level of magnetic fluctuations. Considered first are the low-m modes, such as the mode with frequency $f = 70\ kHz$ during the

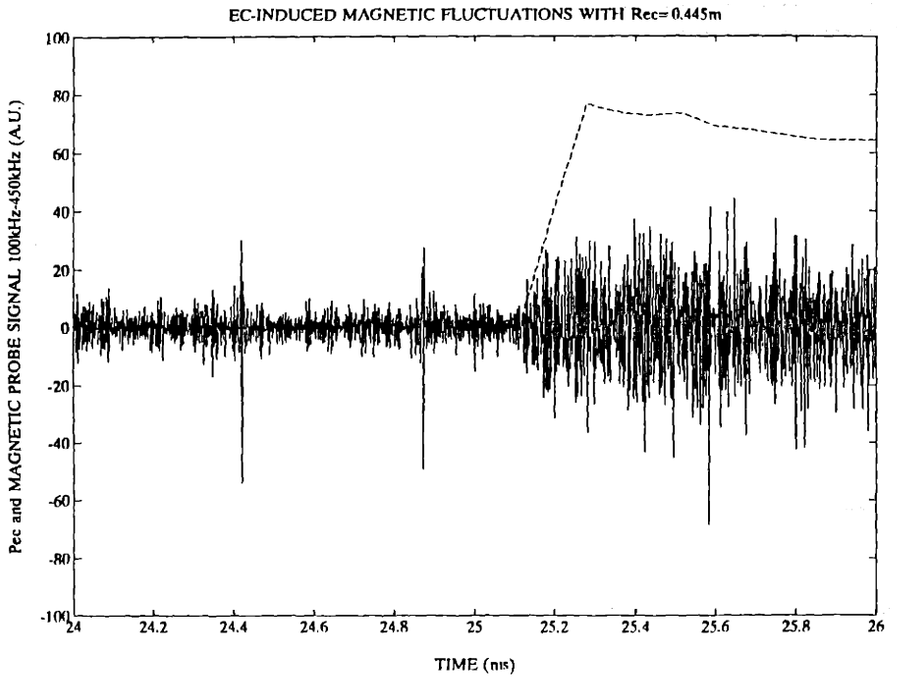

Figure 4-29

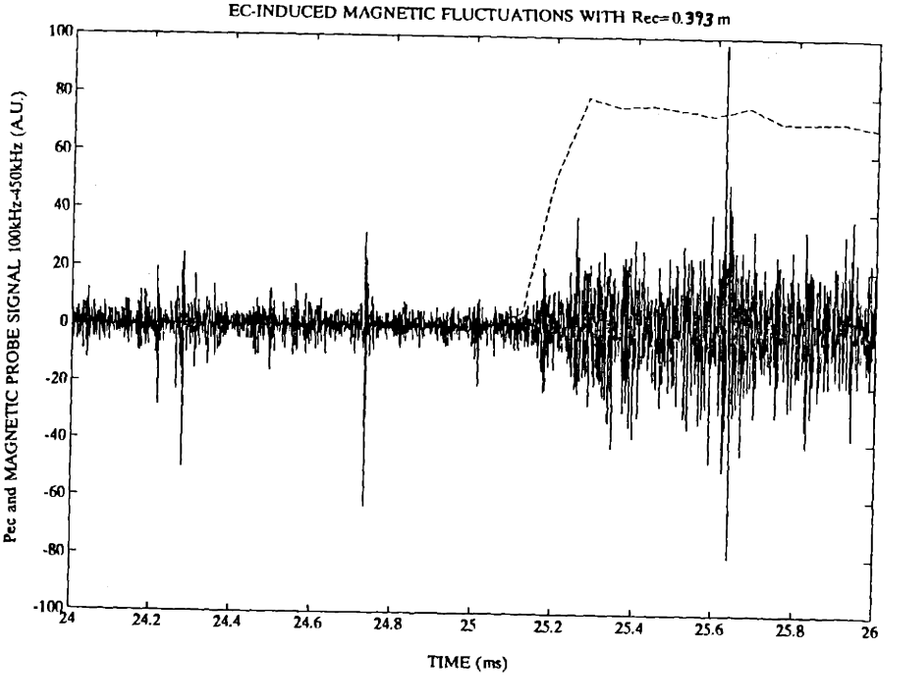

Figure 4-30

initial ohmic phase of the discharge shown in Figure 4-22. These modes are relatively long-lived (with lifetimes of at least several periods), so they are much more coherent than the higher-frequency turbulent modes, which usually have lifetimes of a fraction of a period [89]. The low-m modes are localized in radius near a rational flux surface. They perturb the equilibrium flux surfaces in such a way as to produce "magnetic islands" centered on the flux surface. These modes only affect transport in the neighborhood of the island. The commonly accepted expression for the island radial width is [91]

$$\Delta = 4\sqrt{\left[R\tilde{B}_r(m,n)/mB_0\right]\,|q^2(r_{m,n})/q'(r_{m,n})|}, \tag{48}$$

where m and n are the poloidal and toroidal mode numbers, respectively, of the mode, and $q' \equiv dq/dr$. An upper bound for the island width can be estimated for the discharges considered in this section. Because $q(r_{m,n}) = m/n$, the island width is clearly maximum for $n = 1$, giving $q = m$. The discharges of Figures 4-18 and 4-19 have $q(r = 13 \text{ cm}) \approx 7 - 10$ during the initial ohmic phase in which the low-frequency mode is observed. Also, $q(r = 0)$ is generally close to unity for ohmic discharges, and q is often assumed to increase as r^2 toward the edge. Thus we assume a q profile of the form $q = 1 + 9(r/13)^2$, and the maximum island width is attained near the edge, for the given constraints. Taking the limiting values of $q = m = 10$ at $R \approx 53$ cm and using $|B_r| = |B_p|$ from Equation 47 gives an island width of $\Delta \approx 0.17$ cm. Thus the coherent modes observed on Versator can affect transport in only a very narrow radial zone, and hence they are not important in determining the radial diffusion of electrons.

The diffusion of superthermal electrons by higher-m turbulent magnetic fluctuations is now considered. The diffusion of electrons by magnetic turbulence is caused by the wandering of each electron from one equilibrium flux surface to another as it follows the stochastic field line that is coincident with the electron's

guiding center. The diffusion coefficient is therefore proportional to the parallel velocity of the electron, and is given by [92,93]

$$D_m = v_{\|} \pi q R_0 \langle (\tilde{b_r}/B_0)^2 \rangle, \tag{49}$$

where $\tilde{b_r}$ is the radial fluctuating magnetic field and $\langle\rangle$ is an average over a flux surface. An estimate of D_m can be obtained using this formula and extrapolating the observed fluctuation levels at the plasma edge to smaller radii using Equation 47. This ignores the fact that the source for a given m, n turbulent "mode" is nonlocalized in radius. Also ignored is the possibility of averaging effects due to the displacement of the fast-electron orbits from the flux surfaces [94]. Ignoring these two effects tends to lead to an overestimate of the radial diffusion coefficient. Experiments on other tokamaks [95-97] indicate that the diffusion coefficient for superthermal electrons is smaller near the plasma center than closer to the edge, implying that the extrapolation assumption cannot be used all the way to the magnetic axis. Bearing this in mind, extrapolation of the measured turbulence level during ECCD (from Figure 4-24) inward from the probe location to the outer third of the plasma using Equation 47 and assuming $m \approx 15$ gives $\langle (\tilde{b_r}/B_0)^2 \rangle \approx 2 \times 10^{-9}$ at $r = 10$ cm. This gives a diffusion coefficient of 5 m^2/s for superthermal electrons with $v_{\|} = 1.5 \times 10^8$ m/s (corresponding to $E_{\|} \approx 80$ keV). This diffusion coefficient is large enough to cause fairly severe losses of the fast electrons. If, for example, it is assumed that one-third the plasma current is carried by fast electrons in the outer third of the plasma ($8 < r < 12$ cm) with $v_{\|} = 1.5 \times 10^8$ m/s ($E_{\|} \approx 80$ keV), and the density gradient scale length of these electrons is assumed to be $n_e^{fast}/\nabla n_e^{fast} = 4$ cm, then the outward flux of these electrons, given by $\Gamma = -D_m \nabla n_e^{fast}$, is approximately 1.25×10^{18} $m^{-2}s^{-1}$. This flux level implies that the fast electron population in this radial zone must be replaced every 0.25 ms to maintain the assumed plasma current and radial distribution of fast electrons.

This does not include other loss mechanisms, which will shorten the replacement time. This 0.25 ms replacement time is a lower bound on the confinement time of 80 keV electrons in the outer third of the Versator plasma due to losses caused by $m = 15$ magnetic turbulence. Higher-m turbulence will lead to higher calculated diffusion coeficients and shorter confinement times. If the magnetic turbulence is assumed to decrease considerably toward the magnetic axis, as has been suggested by experiments on other tokamaks [97], the outward flux of fast electrons close to the magnetic axis is less than the flux nearer the plasma edge. For example, consider a beam with the same number of 80 keV electrons (6.3×10^{14}) and gradient scale length (4 cm) as in the above example, located in the inner third of the plasma ($r < 4$ cm), and $\langle(\tilde{b}_r/B_0)^2\rangle \approx 2 \times 10^{-10}$ (ten times smaller than in the outer third of the plasma). The resulting diffusion coefficient is 0.5 m^2/s, the outward flux is $\Gamma = 6.25 \times 10^{17}$ m^{-2}/s, and the confinement time is 1.6 ms. Thus, given the above assumptions, the confinement time of 80 keV electrons on Versator in the presence of magnetic turbulence is 0.25 ms in the outer third of the plasma and 1.6 ms in the inner third. Good confinement of fast, current-carrying electrons during EC wave injection would thus only be expected for relatively peaked radial profiles of the fast electron density.

Also, the confinement of high-energy superthermal electrons is degraded much more by magnetic turbulence than is the confinement of low-energy superthermal electrons. For example, the confinement time of electrons with $E_\parallel = 1$ keV ($v/c = 0.0625$) is improved by a factor of 8.0 over that of 80 keV electrons due to the linear $v_\parallel$-dependence of D_m.

In addition to potential enhanced losses of superthermal electrons during EC-wave injection, the *thermal* electron confinement is observed to degrade during EC-wave injection on Versator. A similar phenomenon has been observed on other small tokamaks [98,99], but it is not observed on DIII-D, a large tokamak with hot plasma and nearly 100% single-pass absorption [100]. Figures 4-31 and 4-32 show the line-averaged electron density and H_α emission versus time for an electron-cyclotron

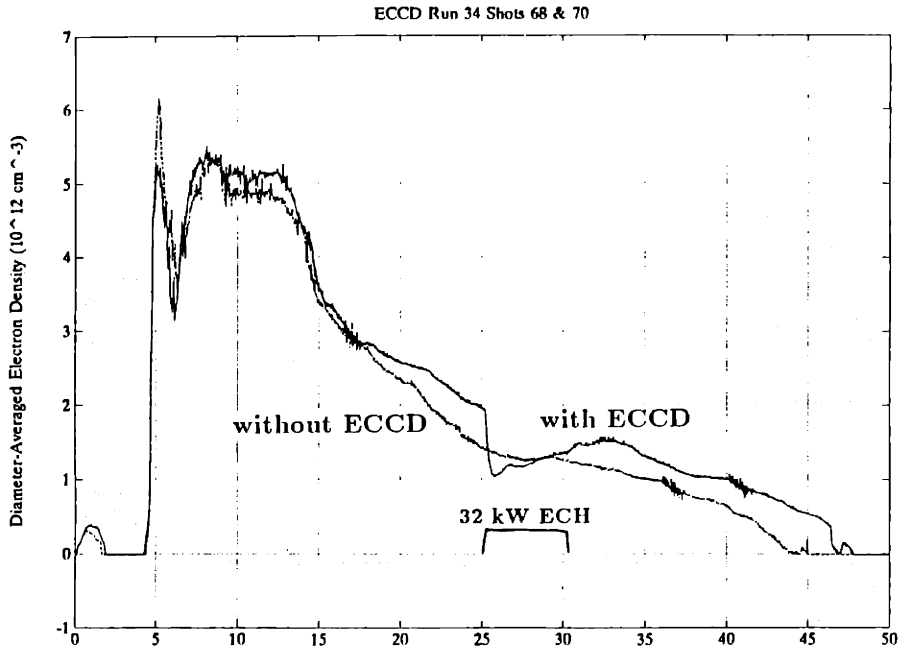

Figure 4-31 Density behavior during ECCD.

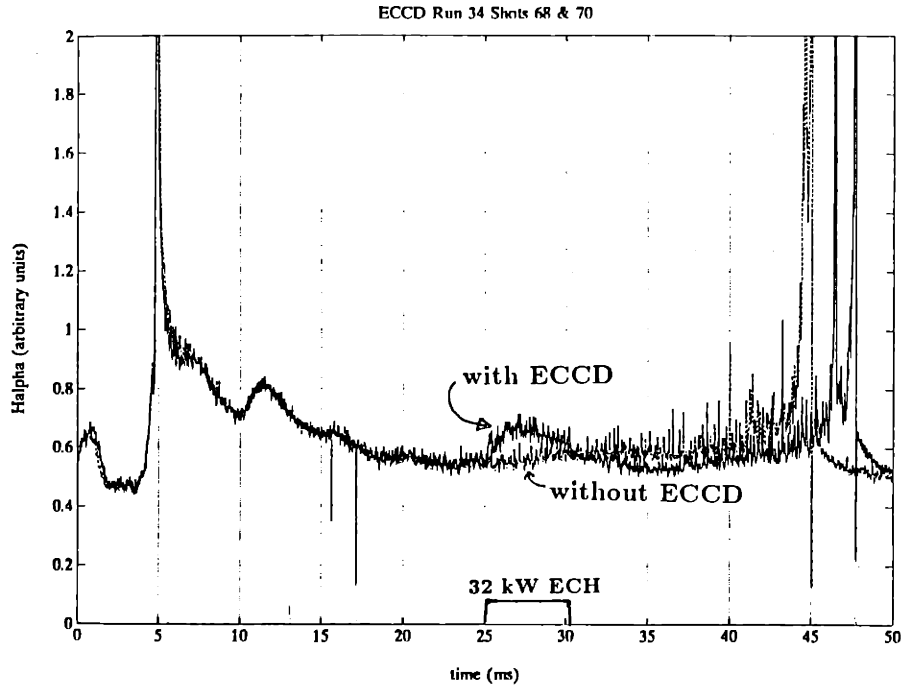

Figure 4-32 H_α dependence during ECCD.

current-driven (ECCD) discharge. The electron density drops and the H_α emission rises during EC-wave injection, clear indications that the thermal electron particle confinement time has decreased. Because the diffusion coefficient in Equation 48 is proportional to $v_\parallel$, the radial diffusion rates predicted for thermal electrons on Versator as a result of magnetic fluctuations are far below those observed experimentally. However, electrostatic turbulence becomes an important diffusion mechanism in this case. The electrostatic and magnetic fluctuations observed on Versator are not necessarily independent; they could both be manifestations of the same instability or instabilities. Electrostatic fluctuations in electron density and temperature result in pressure fluctuations, which can cause current fluctuations, which in turn cause magnetic fluctuations. In reference [99], the radial flux caused by electrostatic fluctuations was shown to be consistent with the observed enhancement of thermal electron transport during ECH on the DITE tokamak.

4.3 ELECTRON-CYCLOTRON CURRENT-DRIVE

4.3.1 Theory and Experimental Results

Recall from Chapter 1 that EC waves accelerate electrons primarily in the direction perpendicular to the confining magnetic field, diffusing them in the $v_\perp$ direction in velocity space. The EC waves heat electrons when the relativistic resonance condition is satisfied: $\omega - eB/\gamma m_0 = k_\parallel v_\parallel$, where $\gamma = (1 - v^2/c^2)^{-1/2}$ and m_0 is the electron rest mass. This equation is simply the condition that the time-averaged wave electric field is nonzero in the reference frame of the electron. This gives $\gamma - \omega_{ce}/\omega - N_\parallel \hat{p}_\parallel = 0$, where $\hat{p}_\parallel \equiv p_\parallel/m_0 c$, $\omega_{ce} \equiv eB/m_0$ and $N_\parallel \equiv ck_\parallel/\omega$. In the nonrelativistic limit ($\gamma = 1$) this gives $\hat{p}_\parallel = (1 - \omega_{ce}/\omega)/N_\parallel$, and the resonance

curves are straight lines in momentum space with $\hat{p}_{\|}$ =constant. For the general case $\gamma = 1 + \hat{p}_{\|}^2 + \hat{p}_{\perp}^2$, giving

$$\hat{p}_{\|} = \frac{N_{\|}(\omega_{ce}/\omega) \pm \sqrt{\left(N_{\|}^2 - 1\right)\left(1 + \hat{p}_{\perp}^2\right) + \omega_{ce}^2/\omega^2}}{1 - N_{\|}^2}, \tag{50}$$

where $\hat{p}_{\perp} \equiv p_{\perp}/m_0 c$. For a given $N_{\|}$ this equation describes an ellipse in momentum space, as shown in Figure 4-33. In this figure, resonance curves are plotted for $f = 28$ GHz, $B = 0.85$ T, and $0.55 < N_{\|} < 0.9$. No real solutions to Equation 50 exist for $N_{\|} < 0.527$ for the given ω_{ce}/ω.

In general, seven mechanisms can affect the plasma current during EC-wave injection: (1) parallel momentum transfer, (2) relativistic mass variation, (3) induced loop voltage, or parallel electric field, (4) selective reduction of the electron collision frequency, (5) selective trapping/detrapping of electrons, (6) selective electron losses, (7) the bootstrap current. First considering mechanism (3), the induced electric field resists variations in the plasma current:

$$E_{\|} = -\frac{1}{2\pi R}\frac{\partial LI}{\partial t}, \tag{51}$$

where $E_{\|}$ is the parallel electric field, L is the plasma self-inductance (internal plus external), and I is the total plasma current. This mechanism is important during ECCD on Versator only when LI is changing with time. To better understand the remaining mechanisms, the diffusion of electrons in velocity space by the EC waves is first described. Recall Equation 21, repeated here for convenience:

$$\frac{\partial f_0}{\partial t} = \frac{\partial}{\partial \mathbf{p}} \cdot \overline{\overline{\mathbf{D}}} \cdot \frac{\partial f_0}{\partial \mathbf{p}} + \left.\frac{\partial f_0}{\partial t}\right|_{coll} \tag{52}$$

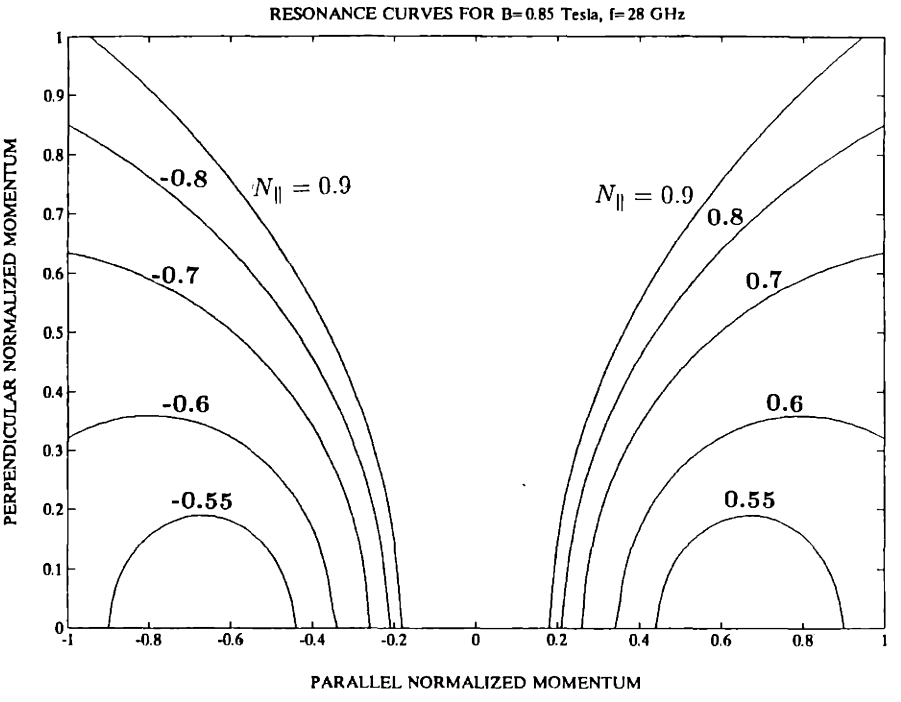

Figure 4-33

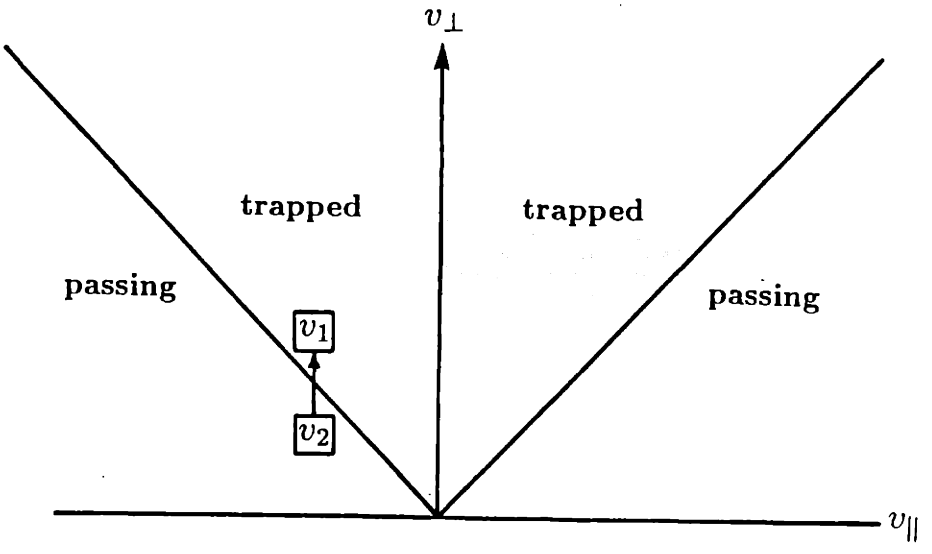

Figure 4-34 The Ohkawa current (selective trapping/detrapping of electrons).

This is the relativistic Fokker-Planck equation, a diffusion equation in velocity space. For EC waves with $\omega \approx \omega_{ce}$, the $n = 1$ term dominates the diffusion coefficient (Equation 22), giving:

$$D_{EC} = \frac{1}{V}\pi e^2 \int \frac{d^3k}{(2\pi)^3}\delta(\omega - k_{\|}v_{\|} - \omega_{ce})\alpha_{k1}^{*}\alpha_{k1} \tag{53}$$

where $\alpha_{k1} = \left(\varepsilon_{k1} + \frac{p_{\|}}{p_{\perp}}J_1 E_{kz}\right)\left(\frac{\omega_{ce}}{\omega}\hat{e}_{\perp} + \frac{N_{\|}v_{\perp}}{c}\hat{e}_{\|}\right)$, $\varepsilon_{k1} = (E_{kx} + iE_{ky})J_2 + E_{kx} - iE_{ky}$, and E_x, E_y, and E_z are the wave electric field components. For typical values for ECCD on Versator of $N_{\|} = 0.5$, $v_{\perp}/c = 0.05$-0.3, and $\omega \approx \omega_{ce}$, the $\hat{e}_{\perp}\hat{e}_{\perp}$ term (the perpendicular diffusion term) is ten to four hundred times larger than the $(\hat{e}_{\|}\hat{e}_{\|})$ parallel diffusion term. Thus perpedicular heating dominates over parallel momentum transfer for ECCD, and mechanism (1), is relatively unimportant. Mechanism (2), the variation of the current due to the relativistic variation of the electron mass, causes a reduction in the current as the electrons are heated by the EC waves. This is because the parallel momentum of each electron is conserved, and the electron's mass is increasing during heating so the electron's parallel velocity must decrease. Viewed another way, the electron velocity must always be less than the speed of light c. As the electron is heated toward $v_{\perp} \approx c$, the parallel velocity must become smaller to maintain $v_{\perp}^2 + v_{\|}^2 < c^2$. For ECCD on Versator this mechanism is not very important. For example, for a 20 keV tail electron with $v_{\|} = 8.2 \times 10^7$ m/s and $v_{\perp} = 0$, heated perpendicularly until its total energy is 100 keV (a rather extreme case), the final parallel velocity is 7.1×10^7 m/s, a 13% reduction.

Mechanism (4), the selective reduction of the electron collision frequency by perpendicular heating, is the principal mechanism of ECCD. This mechanism, which was described in section 1.3, is shown schematically in Figure 1-4b. The EC wave diffuses a group of electrons in velocity space from $\mathbf{v}_1$ to $\mathbf{v}_2$, where $\mathbf{v}_2 - \mathbf{v}_1$ is in the $v_{\perp}$ direction. In this case, no parallel momentum is transfered to the electron.

Due to the velocity dependence of the Coulomb cross section, the electron collision frequency decreases with increasing velocity, so that $\nu_e(v_2) < \nu_e(v_1)$, where ν_e is the electron collision frequency. Therefore the new group of electrons at $\mathbf{v}_2$ takes longer to mix back into the Maxwellian distribution than the "hole" that was left behind at $\mathbf{v}_2$. On average, this increases the number of electrons moving to the right, producing a net current.

Mechanism (5) involves the trapping and detrapping of electrons. Due to the $1/R$ variation of the toroidal magnetic field in a tokamak and the conservation of magnetic moment ($\mu \equiv v_\perp^2/2B$) along electron orbits, electrons with sufficiently high $v_\perp$ can be trapped in the region of low B centered on the outer midplane. For each flux surface in the plasma, a trapping boundary exists in velocity space given by $v_\perp/v_\parallel = \sqrt{R/r}$, where r is the minor radius of the flux surface and the velocities are defined on the outer midplane. For $v_\perp/v_\parallel > \sqrt{R/r}$, the electrons are trapped, and for $v_\perp/v_\parallel < \sqrt{R/r}$ they are passing. Figure 3-10 shows some trapped and passing electron orbits on Versator, as generated by the Matlab m-file ORBIT. [80]This code integrates the guiding-center trajectories of charged particles in a tokamak using a fourth-order Runge-Kutta integrator. Toroidal effects on the magnetic field are included to first order in the inverse aspect ratio $\epsilon = a/R$, where a is the minor radius. The applied vertical field and the Shafranov shift are second-order effects that are neglected. The plots in Figure 3-10 show the "banana" orbits of trapped electrons, and the orbits of passing electrons, which stay close to the flux surfaces, provided the electron energy is not very large. The trapped electrons' average toroidal velocity is given by a rate of precession as each electron bounces back and forth in its trapped orbit. This average toroidal velocity is typically two orders of magnitude slower than the toroidal velocity of passing electrons. Hence trapped electrons effectively carry no toroidal current. Mechanism (5) is illustrated in Figure 4-34, which shows how current can be generated by EC waves by selectively trapping electrons on either side of the $v_\parallel = 0$ axis in velocity space. This current is sometimes called the "Ohkawa current [101]." Very efficient current production is

possible via this mechanism, at least for a short time, because only an incremental amount of energy is required to boost electrons over the trapped/passing boundary if they are near the boundary initially. This current mechanism has never been observed experimentally, however.

Mechanism (6) is related to mechanism (5) in that high-energy trapped electrons are more prone to radial losses if before they were trapped they were traveling in the direction of the plasma current (so as to detract from it). This is shown in Figure 3-10, where it can be seen that a trapped electron forms a banana orbit to the outside of its passing orbit if it is traveling with the plasma current, and inside if it is traveling opposite to it. Because radial losses are enhanced at larger minor radii, the electrons with the banana orbits at larger r will tend to be lost sooner. This creates a sink in the trapped region of velocity-space that is asymmetric with respect to $v_{\|}$. As electrons drain into this sink via collisions, a toroidal current is generated.

Mechanism (7), the bootstrap current, is also dependent on electron trapping [102]. When the density is decreasing with increasing minor radius in the plasma, more trapped electrons are passing through point A in Figure 3-10 with inner banana orbits (traveling opposite the plasma current) than with outer banana orbits (traveling with the plasma current). The difference is $(dn_t/dr)\Delta_b$, where n_t is the density of trapped electrons, r is the minor radial coordinate, and Δ_b is the banana width. The banana width is proportional to $1/B_p$, where B_p is the poloidal magnetic field. Thus a current exists at point A, called the neoclassical diamagnetic current, given by

$$J_d = -\epsilon^{3/2} \frac{1}{B_p} \frac{\partial p}{\partial r}, \tag{54}$$

where $p = nT$ is the plasma pressure and $\epsilon \equiv r/R \ll 1$. The temperature gradient factors into the current in the same way as the density gradient, because a local

current is also generated if the trapped electrons traveling in one direction have higher parallel velocity, on average, than those traveling in the opposite direction. The neoclassical diamagnetic current given by Equation 54 is relatively small in a tokamak. However, these trapped electrons efficiently impart momentum to nearly-trapped passing electrons, thereby generating a much larger current:

$$J_b \approx -\epsilon^{1/2} \frac{1}{B_p} \frac{\partial p}{\partial r}. \tag{55}$$

This is the bootstrap current [102,103]. It is carried by the nearly-trapped passing electrons that obtain their net toroidal momentum from the trapped electrons. It is larger than the neoclassical diagmagnetic current by a factor $1/\epsilon$, and it can, in theory, contribute most of the current in a tokamak with high $\beta_p \equiv 2\mu_0 nT/B_p^2$. Significant bootstrap currents have been purported to exist in several recent tokamak experiments, including ECCD experiments on T-10 [104], but conclusive evidence is lacking. It has not been possible to measure the bootstrap current directly, and therefore it is measured by subtracting from the observed plasma current the calculated currents generated from all other known mechanisms. On Versator β_p is low during ECCD, so the bootstrap current is not expected to be significant for the thermal electrons. However, the boostrap current due to a small population of superthermal electrons may be significant during ECCD on Versator. In this case Equation 55 is invalid and the bootstrap current must be calculated numerically using a Fokker-Planck code such as CQL3D.

Figure 4-35 shows plasma parameters for a typical good ECCD discharge for the case of O-mode inside launch on Versator. Here, 40 kW is launched with $\alpha = +20°$, where α is the angle from the normal to $\mathbf{B}_0$, and negative α is in the direction of the plasma current. Upon injection of the EC waves at $t = 24$ ms the decay of the plasma current is arrested, and a steady $I_p = 15$ kA is maintained until turn-off of the EC power. The loop voltage falls from 0.15 V to zero within 1 ms after EC-wave

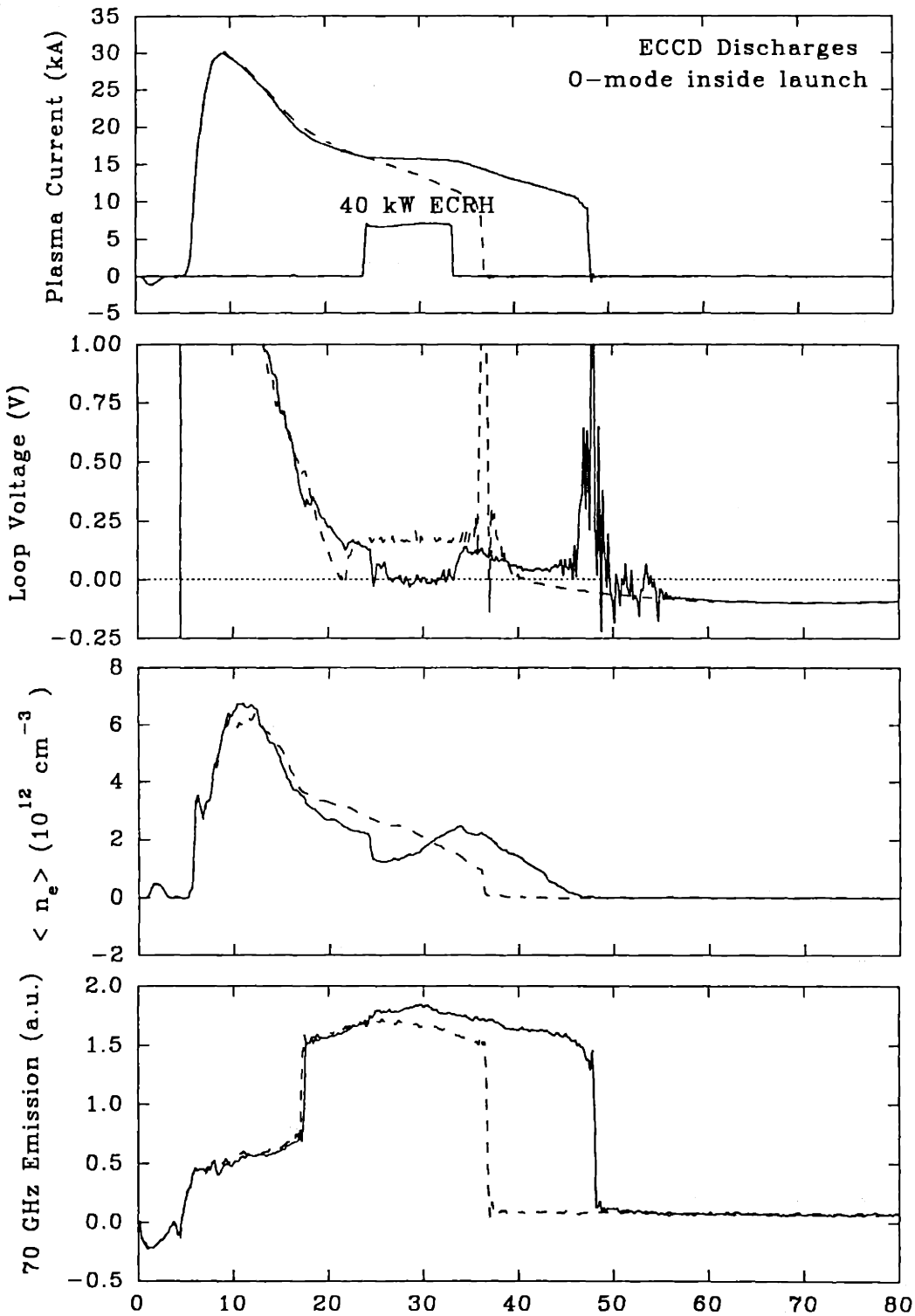
ECCD Discharges
O-mode inside launch
40 kW ECRH
Plasma Current (kA)
Loop Voltage (V)
< n_e > (10^12 cm^-3)
70 GHz Emission (a.u.)
Time (ms)

Figure 4-35

turn-on, and oscillates about zero until turn-off of the EC-wave power at $t = 33$ ms. The current-drive figure of merit $\eta = \langle n_e \rangle (10^{14}\ \mathrm{cm}^{-3}) I(\mathrm{kA}) R(\mathrm{m}) / P_{EC}(\mathrm{kW}) = 0.003$ for this discharge. This is 30% to 40% of the highest η achieved during LHCD on Versator. Upon turn-off of the wave power, V_{loop} jumps back up to about 0.15 V, and I_p begins to decay again. The negative loop voltage after plasma termination is caused by the decay of the applied vertical field. The glitch in V_{loop} and slightly different density behavior of the OH discharge for $t \approx 20$ ms is due to different timing of the firing of a secondary vertical-field capacitor bank during the OH discharge. The density during the OH target discharge builds to $6 \times 10^{12}\ \mathrm{cm}^{-3}$during the peak in I_p near $t = 10$ ms, then decays at an average rate of $1.3 \times 10^{11}\ \mathrm{cm}^{-3}$/ms until plasma termination at $t = 36$ ms. For the ECCD discharge, the density rapidly decreases upon EC-wave injection, from $2.2 \times 10^{12}\ \mathrm{cm}^{-3}$to $1.2 \times 10^{12}\ \mathrm{cm}^{-3}$in the first 0.5 ms of the microwave pulse. This is followed by a gradual buildup of the density until its prior value of $2.2 \times 10^{12}\ \mathrm{cm}^{-3}$is attained at the end of the EC pulse. Upon EC turn-off, the density decays again at about the same rate as during the OH discharges. This density behavior was commonly observed during ECCD on Versator. The ECCD efficiency decreased rapidly as the target density was raised above $\langle n_e \rangle = 3 \times 10^{12}\ \mathrm{cm}^{-3}$. The 70 GHz emission is enhanced during ECCD over the OH value. Note that significant emission is present for the OH target discharge, indicating the presence of a "slideaway" electron tail. No dependence of plasma or current-drive parameters on launched EC-wave polarization was observed. Due to transmission-line limitations, only about 32 kW of X-mode could be injected. At the density shown, this was not sufficient to fully arrest the decay of the plasma current. However, for a given power level, O-mode and X-mode ECCD discharges were indistinguishable.

The general independence of current-drive and plasma parameters on EC-wave launch angle is shown in Figure 4-36 for 40 kW of O-mode launched from the high-field side. Target discharges with inside, centered, and outside equilibria are shown. These are defined by the location $R - R_0$ of the current channel, as measured by

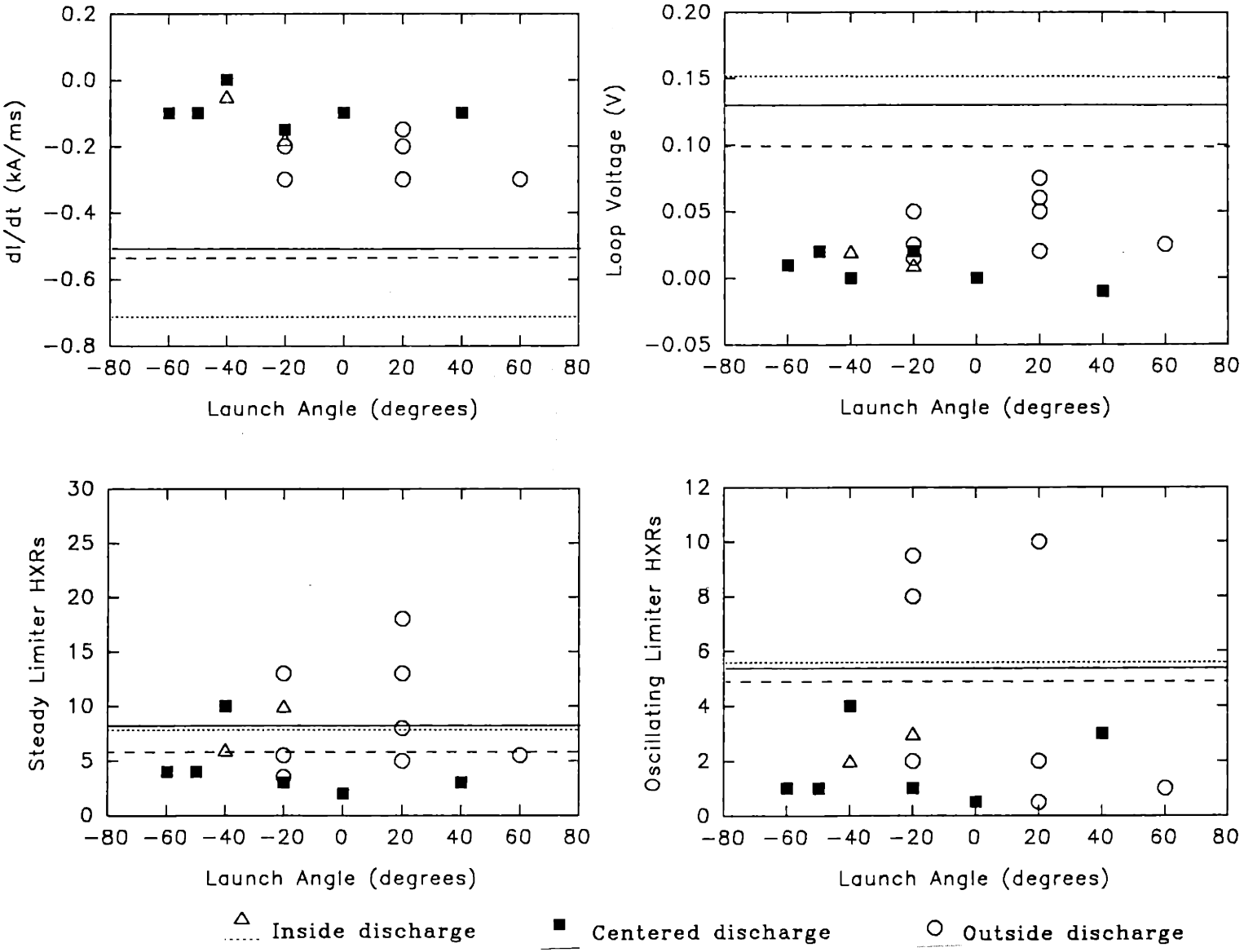
dI/dt (kA/ms)
Launch Angle (degrees)
Loop Voltage (V)
Launch Angle (degrees)
Steady Limiter HXRs
Launch Angle (degrees)
Oscillating Limiter HXRs
Launch Angle (degrees)
Inside discharge
Centered discharge
Outside discharge

Figure 4-36

magnetic pickup coils. The inside discharges have $R - R_0 \lesssim -0.5$ cm, the centered discharges have -0.5 cm $\lesssim R - R_0 \lesssim +1$ cm, and the outside discharges have $R - R_0 \gtrsim +1$ cm. The horizontal solid, dashed, and dotted lines in each plot indicate the values for the target OH discharges with centered, inside, and outside equilibria, respectively. The effectiveness of the ECCD is given by dI_p/dt and V_{loop} during the EC pulse, as compared to the ohmic case, and high dI_p/dt and low V_{loop} are desireable. As can be seen in the upper two plots in Figure 4-36, these two parameters are generally independent of launch angle for ECCD on Versator. Inside target equilibria yielded the greatest increase in dI_p/dt and decrease in V_{loop} relative to the ohmic case, but centered target OH discharges, which had a higher dI_p/dt and lower V_{loop} than the inside target discharges, yielded ECCD parameters at least as good as for the targets with inside equilibria. The outside target equilibria yielded poorer results, with dI_p/dt below and V_{loop} above those of the centered and inside discharges for all angles measured.

Also plotted in Figure 4-36 are the steady and oscillating components of the limiter hard X-ray emission. These X-rays are detected by a sodium-iodide crystal detector placed outside the vacuum chamber, viewing the limiter (as shown in Figure 2-1). Because the X-rays must penetrate the 0.25-inch-thick stainless-steel vacuum chamber before entering the detector, only photons with energy greater than about 100 keV are detected. The steady limiter X-ray emission is an indication of the level of fast-electron losses induced by the EC-waves (perhaps via magnetic fluctuations, as described in the previous section). The oscillating X-ray emission is indicative of the anomalous Doppler instability, which the EC-waves tend to stabilize. As can be seen from Figure 4-36, inside and centered equilibria again produce more desireable results than outside equilibria, with no clear dependence on launch angle. The steady X-ray emission is reduced for the centered discharges, while it is on average increased for the outside discharges. The oscillating X-ray emission is reduced by the EC-waves for the inside and centered target equilibria, and there is no clear effect for the outside equilibria. The lack of dependence on launch angle of all

parameters may imply that the single-pass absorption is weak, even for the non-Maxwellian target electron distribution. In this case the waves presumably reflect off the vacuum chamber walls and sufficiently isotropize before being completely absorbed. Another possibility is that absorption occurs in a regime in which the resonance curves for all launch angles converge to one region of velocity space. This possibility will examined below in more detail.

Additional plasma parameters are shown in Figure 4-37 for the same ECCD discharges as shown in Figure 4-36. The density, the position of the current channel, and $\beta_p + \ell_i/2$ (averaged over the EC pulse) are plotted. All parameters are found to be independent of launch angle, with the possible exception of the density for centered target equilibria, which drops more at large negative launch angles. The plasma density is always found to drop during ECCD on Versator. Depending on the toroidal field (i.e., the location of the EC layer) relative to the current channel, this drop can vary in magnitude and steepness. For the discharges shown in Figure 4-37, the drop is clearly greatest for outside target equilibria. For some of the centered and inside discharges, the drop is very small, about 10% or less. The radial position of the current channel, $R - R_0$, is plotted for the various equilibria, again versus launch angle. This plots clearly shows that the larger the major radius of the target discharge, the greater the outward perturbation of the major radius by the EC-waves.

The best ECCD efficiencies were achieved on Versator when the EC-layer was located toward the high-field side of the plasma. Figure 4-38 shows the dependence of the loop voltage and dI_p/dt on the location of the EC-layer. For these discharges, all parameters were kept constant except the toroidal field, which was scanned from 0.75 T to 1.2 T at $R = R_0$ on a shot-to-shot basis. About 32 kW was injected from the high-field side with $\alpha = 0°$ in the X-mode polarization. The highest efficiency was achieved when $B(R = R_0) \approx 0.85$ T, placing the EC-layer at $R - R_0 \approx -6$ cm. This is in spite of the fact that the current channel and the fast-electron channel are located at larger major radii, in the range $0 \lesssim R - R_0 \lesssim +6$ cm.

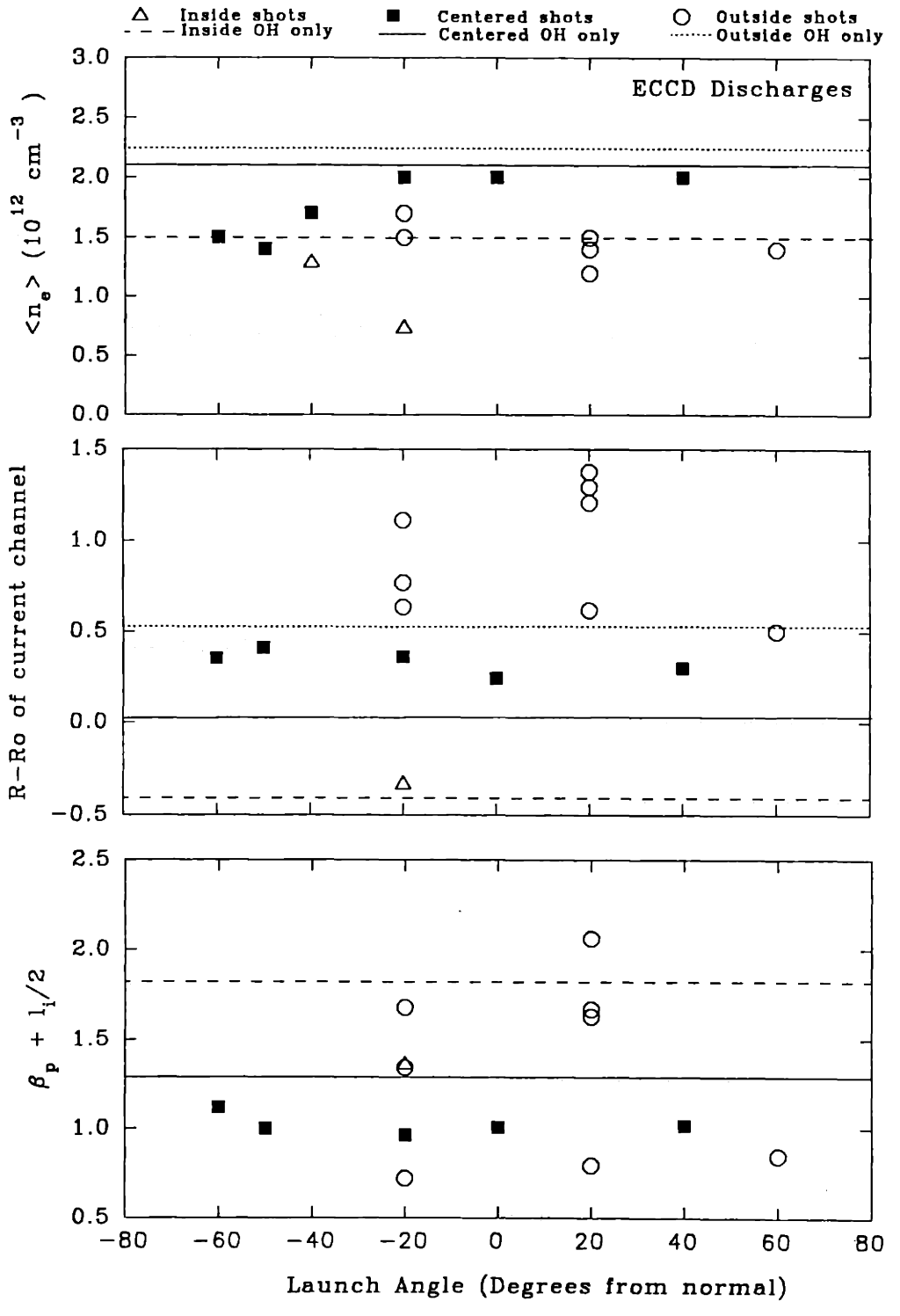
Inside shots
Inside OH only
Centered shots
Centered OH only
Outside shots
Outside OH only
ECCD Discharges
<n_e> (10^12 cm^-3)
R-Ro of current channel
β_p + l_i/2
Launch Angle (Degrees from normal)

Figure 4-37

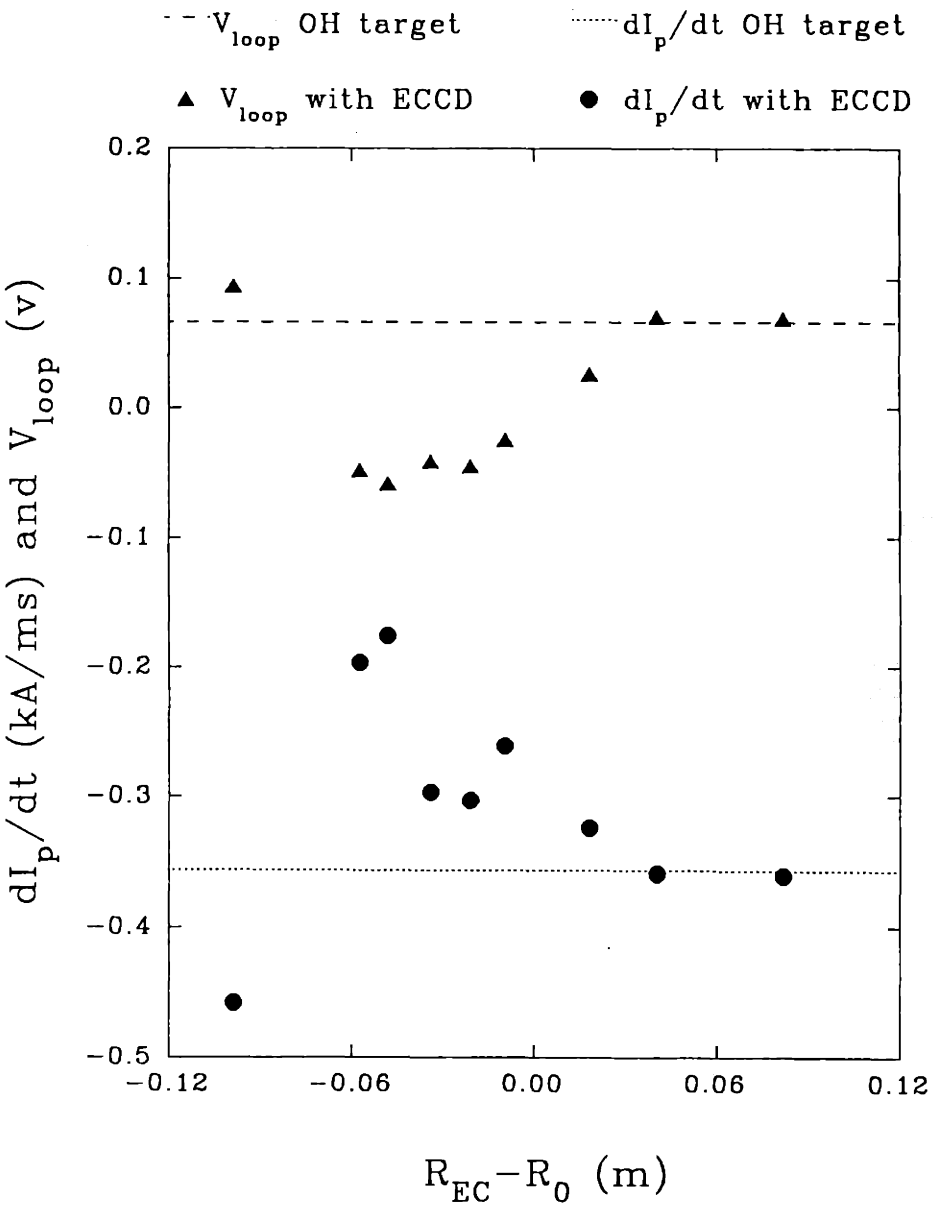
V_{loop} OH target
dI_p/dt OH target
V_{loop} with ECCD
dI_p/dt with ECCD
0.2
0.1
0.0
−0.1
−0.2
−0.3
−0.4
−0.5
−0.12
−0.06
0.00
0.06
0.12
dI_p/dt (kA/ms) and V_{loop} (v)
$R_{EC}-R_0$ (m)

Figure 4-38

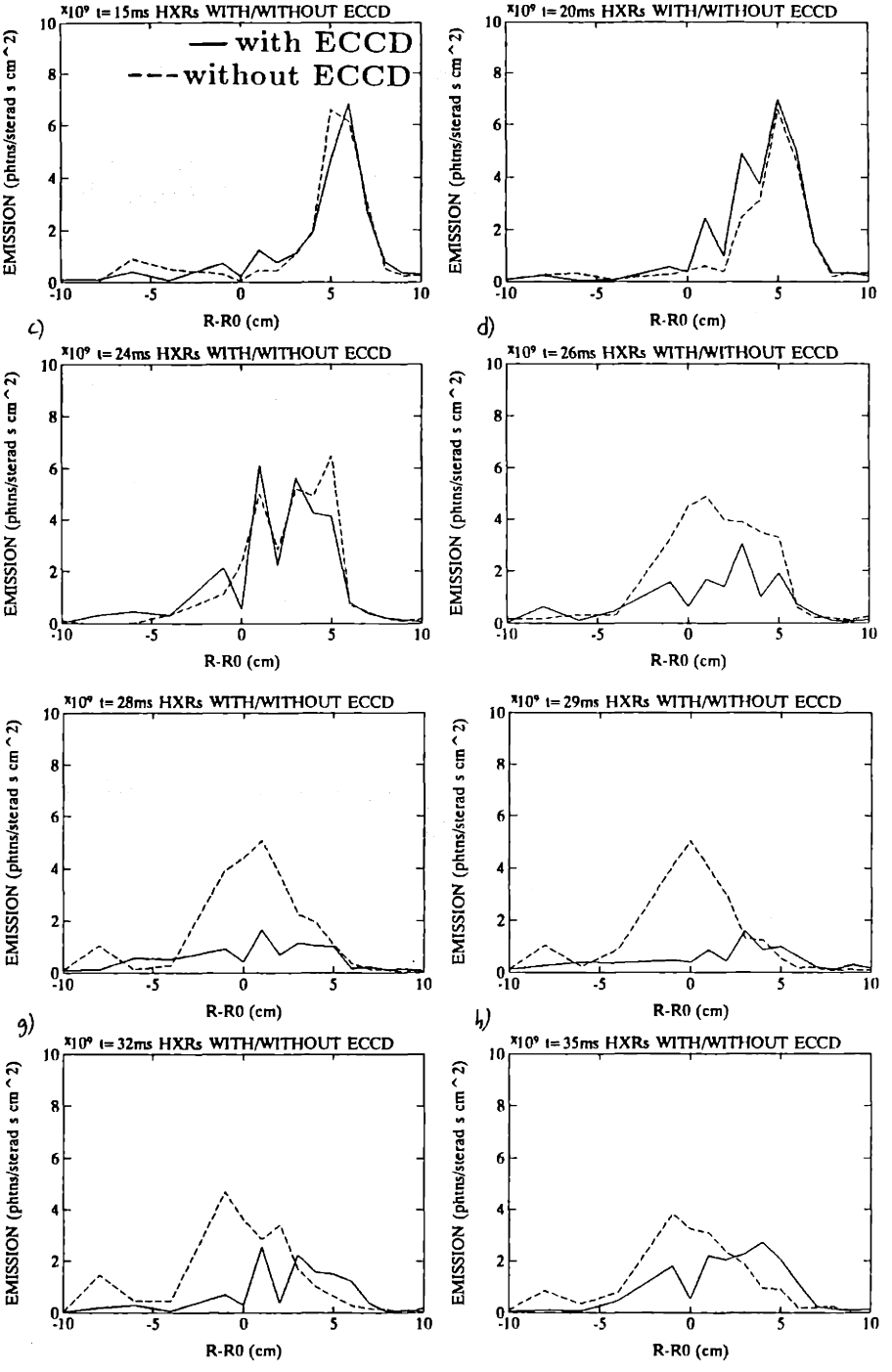
x10⁹ t=15ms HXRs WITH/WITHOUT ECCD
— with ECCD
---without ECCD
x10⁹ t=20ms HXRs WITH/WITHOUT ECCD
c)
d)
x10⁹ t=24ms HXRs WITH/WITHOUT ECCD
x10⁹ t=26ms HXRs WITH/WITHOUT ECCD
x10⁹ t=28ms HXRs WITH/WITHOUT ECCD
x10⁹ t=29ms HXRs WITH/WITHOUT ECCD
g)
h)
x10⁹ t=32ms HXRs WITH/WITHOUT ECCD
x10⁹ t=35ms HXRs WITH/WITHOUT ECCD
EMISSION (phtns/sterad s cm^2)
R-R0 (cm)

Figure 4-39

Profiles of perpendicular hard X-ray emission as a function of major radius are shown in Figure 4-39. The emission shown is integrated over the energy range of the detector, approximately 20-500 keV. The profiles were obtained by moving a single detector between reproducible discharges. For the ECCD plasma (represented by the solid curves) about 32 kW of X-mode was launched with $\alpha = 0°$ from the high-field side during the time 25 ms $< t <$ 30 ms and $B_t(R = R_0) \approx 0.85$ T. As can be seen from Figure 4-39a through 4-39c, the profiles for the two cases are about the same prior to EC-wave injection, indicating good discharge reproducibility. From $t = 15$ ms to $t = 24$ ms, the emission profile evolves from very peaked and centered near $R - R_0 = +6$ cm to broader with a plateau-like maximum extending from $R \approx R_0$ to $R - R_0 \approx +5$ cm. The apparent dip in emission at $R - R_0 = 2$ cm at $t = 24$ ms may be caused by moderate irreproducibility of the in/out position of the plasma at this time. Within 1 ms of the beginning of the EC-wave pulse, the perpendicular hard X-ray emission collapses to about half the emission of the OH discharges. As the ECCD progresses, the hard X-ray emission further decreases until, at $t = 29$ ms, the emission integrated over major radius is less than 15% of the OH case. Within 2 ms after termination of the EC pulse, the emission builds again, centered near $R - R_0 = 3.5$ cm, while the OH discharges remain well-centered. This dramatic drop in perpendicular hard X-ray emission during ECCD may be caused by the drop in V_{loop} to zero.

Data were also taken with the soft X-ray detector described in Chapter 2. This is a silicon-lithium crystal detector sensitive to photons in the energy range $E \lesssim 30$ keV. The detector has a beryllium window that filters out photons with $E \lesssim 1$ keV. For the data presented here, photons with $E \lesssim 2$ keV were filtered out to exclude noise and improve the recorded count rate at higher energies. The detector views horizontally across the midplane. The soft X-rays were consistently and strongly enhanced by EC-wave injection. The time dependence of this emission, averaged over twenty-two discharges, is shown in Figure 4-40 for the cases with and without ECCD. About 30 kW of X-mode was injected from the high-field side with

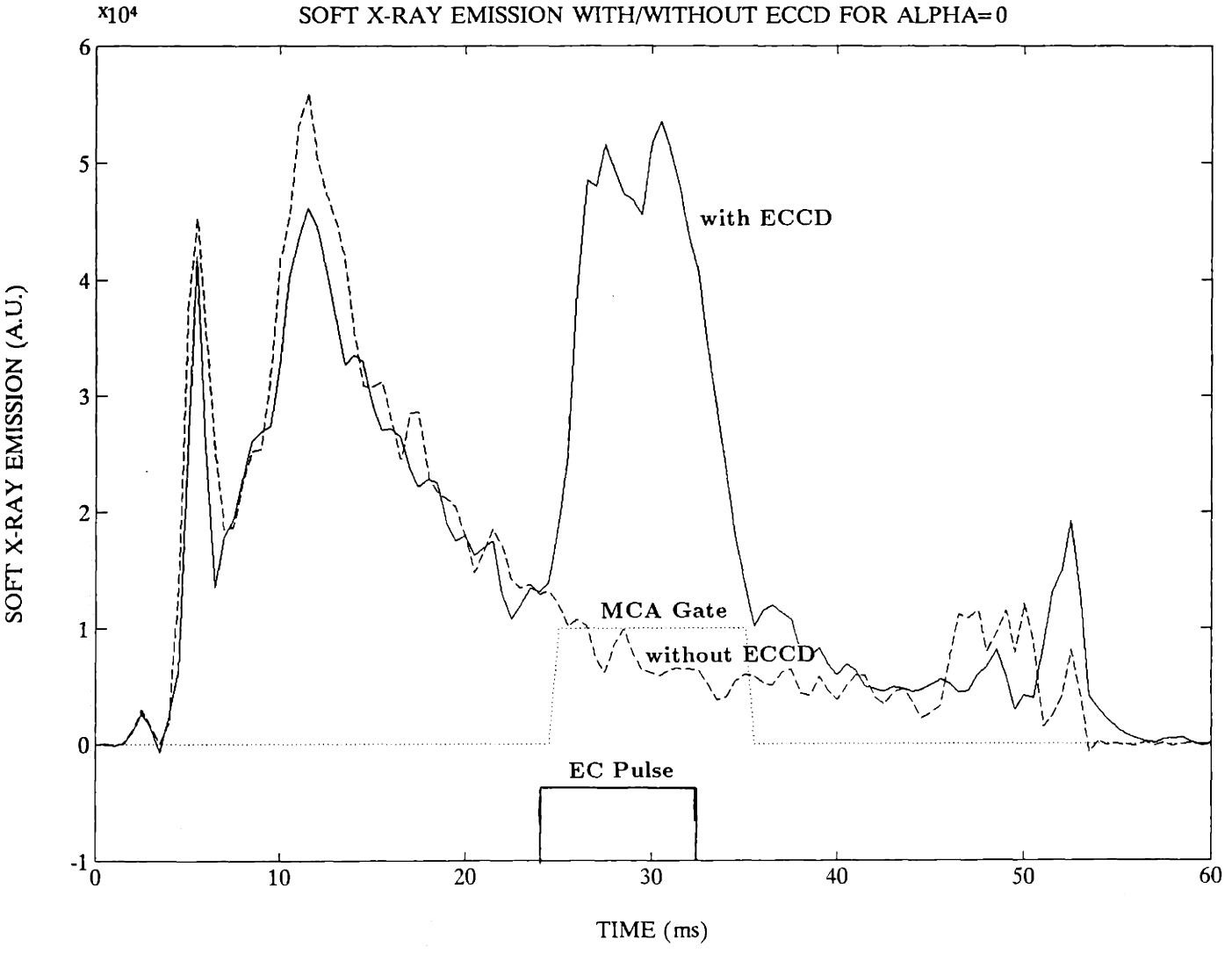
x10⁴
SOFT X-RAY EMISSION WITH/WITHOUT ECCD FOR ALPHA=0
SOFT X-RAY EMISSION (A.U.)
TIME (ms)
with ECCD
MCA Gate
without ECCD
EC Pulse
6
5
4
3
2
1
0
-1
0
10
20
30
40
50
60

Figure 4-40

$\alpha = 0°$ during the period 24 ms$< t <$ 32.5 ms. A fivefold enhancement of the emission is observed due to the EC waves. The spectra for these OH and ECCD discharges are shown in Figure 4-41. The emission is enhanced more at low energy (3-10 keV) than at higher energy ($\gtrsim$ 15 keV) by the EC waves, effectively cooling the emission. The iron emission peak near $E = 6.5$ keV is relatively reduced by the EC waves, but a nickel emission peak is produced near $E = 8.2$ keV.

Figure 4-42 shows the time dependence of the energy-integrated soft X-ray emission for O-mode injection from the high-field side at $\alpha = \pm 70°$ during the period 25 ms$< t <$ 33 ms. The emission is strongly enhanced over the ohmic value for both launch angles, although not as strongly as for the $\alpha = 0°$ X-mode case. This is primarily due to a dependence on α and the conditions of the target discharges rather than on launched polarization, because O-mode ECCD discharges with $\alpha = 0°$ showed enhancement similar to the X-mode case of Figure 4-41. The emission for $\alpha = -70°$ during ECCD is somewhat stronger initially than for $\alpha = +70°$, but near the end of the EC-wave pulse, the $\alpha = +70°$ case has stronger emission. The energy spectra for these two cases are shown in Figure 4-43. In both cases the spectra are elevated above the OH target spectrum by about a factor of two-and-a-half. The spectrum for $\alpha = +70°$ is slightly hotter than for $\alpha = -70°$. The spectra and time traces were averaged over eleven discharges for each case.

4.3.2 Summary of Experimental Observations and Analysis

The experimentally observed features of ECCD on Versator can be summarized as follows. Current drive is observed with an efficiency $\eta \lesssim 0.003$, which is 30%-40% of the maximum achievable LHCD efficiency of Versator. Current drive is possible only when $\langle n_e \rangle \lesssim 5 \times 10^{12}$ cm^{-3}, with the efficiency falling very rapidly above $\langle n_e \rangle = 3 \times 10^{12}$ cm^{-3}. Maximum efficiency is achieved when the EC layer is located near $R_{EC} - R_0 = -6$ cm (on the high-field side near $r/a = 0.5$), even though hard X-ray and magnetic measurements indicate the fast-electron and current channels are

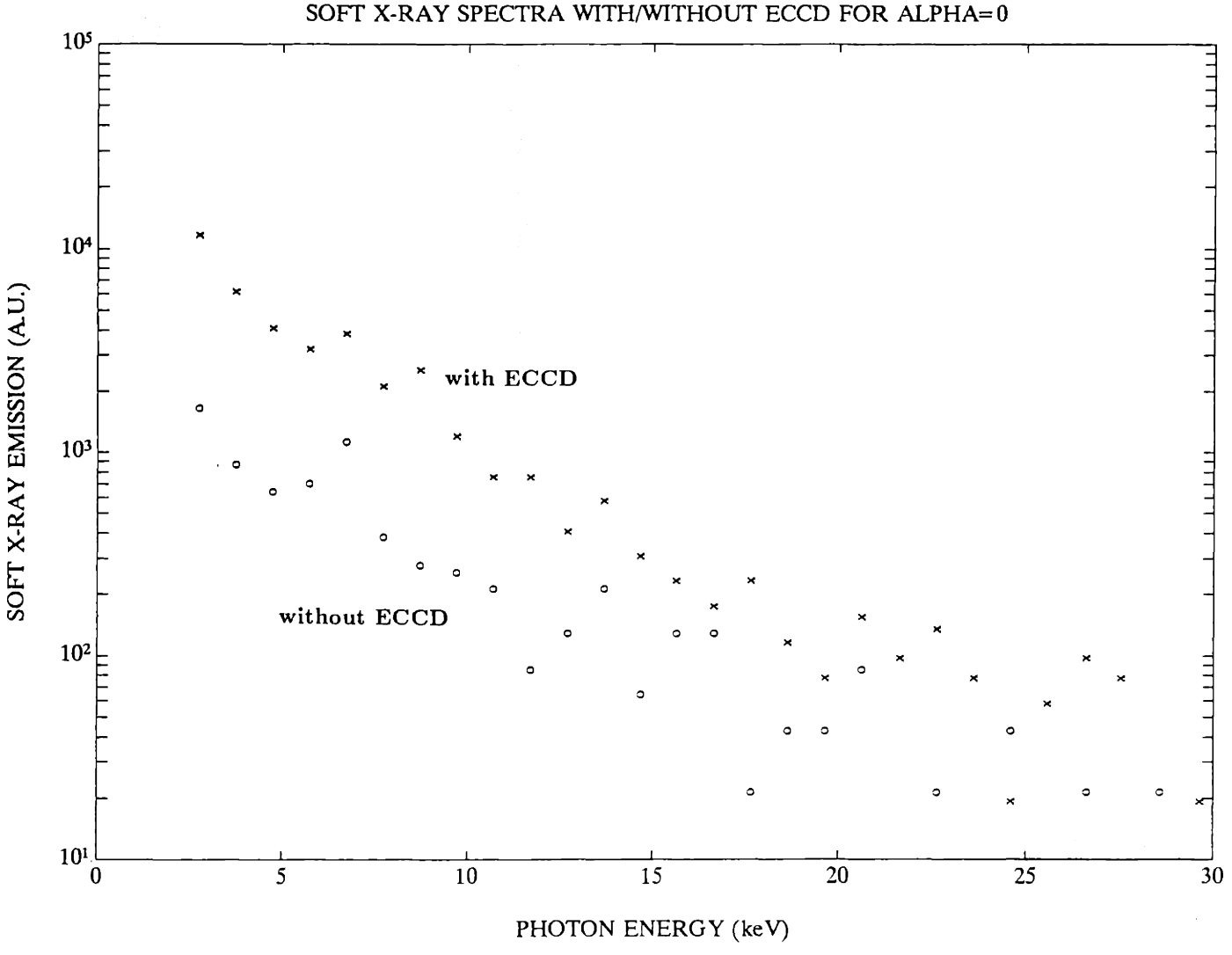
SOFT X-RAY SPECTRA WITH/WITHOUT ECCD FOR ALPHA=0
SOFT X-RAY EMISSION (A.U.)
PHOTON ENERGY (keV)
with ECCD
without ECCD
10^5
10^4
10^3
10^2
10^1
0
5
10
15
20
25
30

Figure 4-41

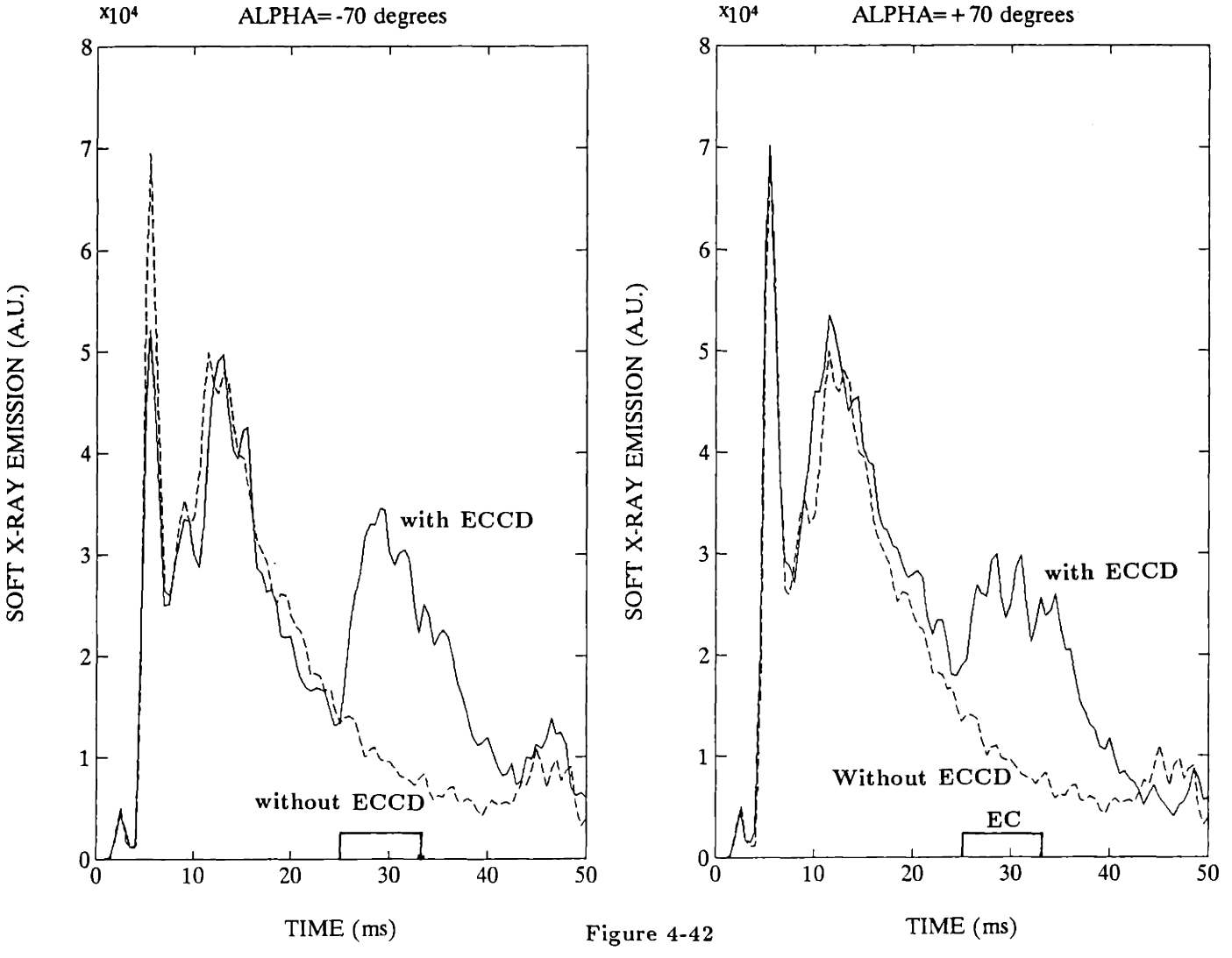
x10⁴
ALPHA=-70 degrees
SOFT X-RAY EMISSION (A.U.)
with ECCD
without ECCD
TIME (ms)
x10⁴
ALPHA=+70 degrees
SOFT X-RAY EMISSION (A.U.)
with ECCD
Without ECCD
EC
TIME (ms)

Figure 4-42

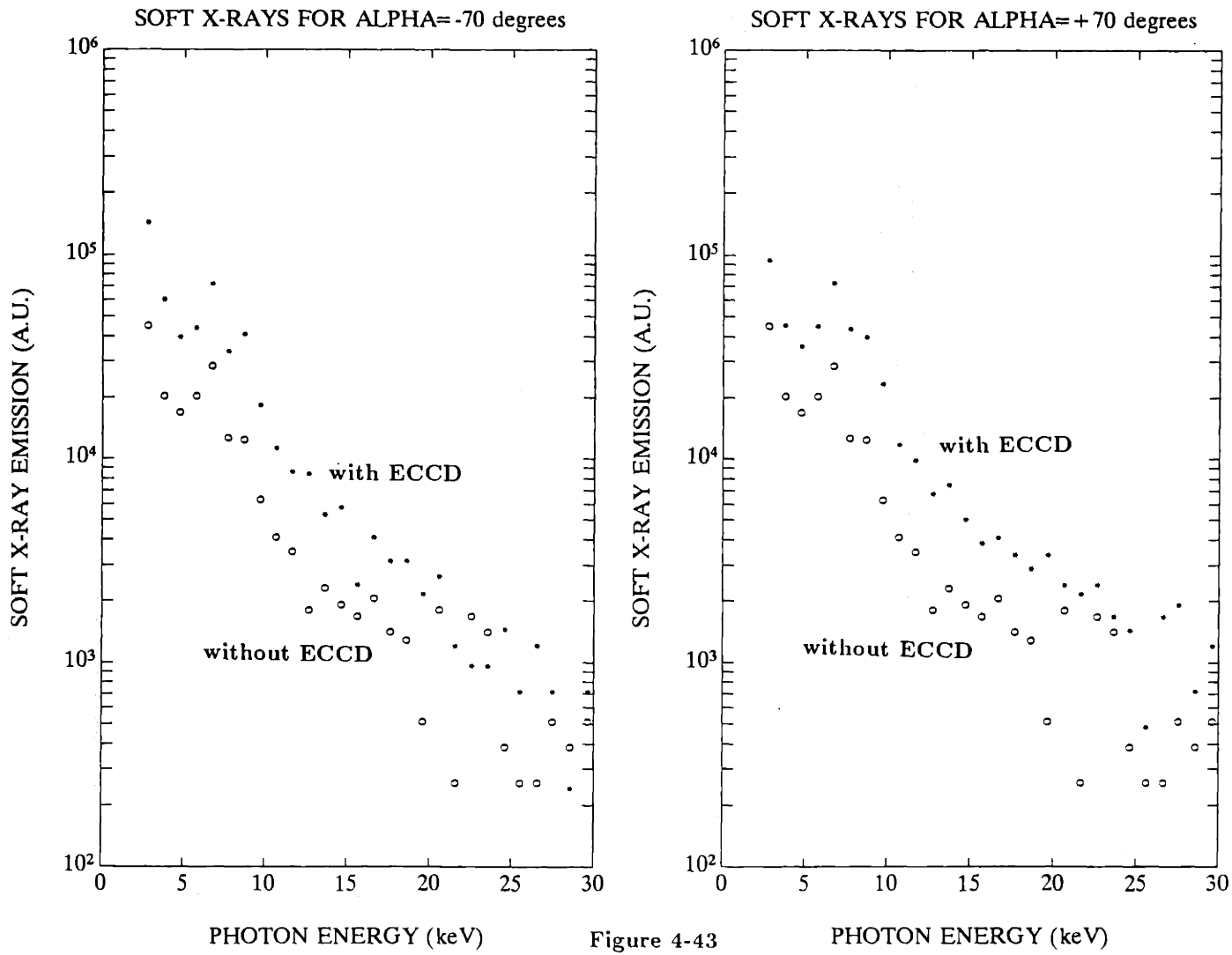
SOFT X-RAYS FOR ALPHA=-70 degrees
SOFT X-RAYS FOR ALPHA=+70 degrees
SOFT X-RAY EMISSION (A.U.)
PHOTON ENERGY (keV)
with ECCD
without ECCD
10^6
10^5
10^4
10^3
10^2
0
5
10
15
20
25
30

Figure 4-43

located at $R \geq R_0$. No current drive is observed when the EC layer is located on the low-field side ($R \geq R_0$). No dependence on launch angle or launched polarization is observed of any bulk plasma or current-drive parameters. Target discharges with well-centered or inside equilibria yield better ECCD parameters than do target discharges with outside equilibria. Soft X-ray emission in the range 2-20 keV is strongly enhanced during ECCD, especially for $\alpha = 0°$. The emission in this energy range is slightly hotter and occurs sooner in the EC pulse for $\alpha = +70°$ than for $\alpha = -70°$, but otherwise no dependence on α is seen. For some discharges, the perpendicular hard X-ray emission with $E \gtrsim 20$ keV is dramatically reduced during ECCD, but this effect may depend on toroidal field.

We now analyze the above experimental observations with the aim of discovering the most likely mechanism(s) for ECCD on Versator. First, it may be concluded that either single-pass absorption of the EC waves is weak, or absorption occurs in a region of momentum-space where resonance curves for many different $N_{\|}$'s converge. This is because no dependence was found of current-drive parameters on the launch angle or on the launched polarization. Weak single-pass absorption could cause this by requiring many bounces off of the vacuum chamber walls for full absorption, giving the waves the opportunity to isotropize. An exception is the stronger enhancement of the soft X-rays for $\alpha = 0°$ than for $\alpha = \pm 70°$. This could be due to better coupling and lower wall and port losses for $\alpha = 0°$.

Second, the rapid decrease in ECCD efficiency for $\langle n_e \rangle \gtrsim 3 \times 10^{12}$ cm^{-3}to $\eta = 0$ at $\langle n_e \rangle = 5 \times 10^{12}$ cm^{-3}suggests that low collisionality is necessary for ECCD on Versator. Low collisionality prior to EC wave injection on Versator leads to the formation of a "slideaway" electron population. This is a parallel tail in the electron distribution function caused by the parallel electric field. Lower collisionality during EC wave injection may improve ECCD by enhancing the bootstrap current.

Third, the EC waves heat many electrons into the energy range 2-20 keV from lower energies. This is indicated by the strong increase in perpendicular X-ray

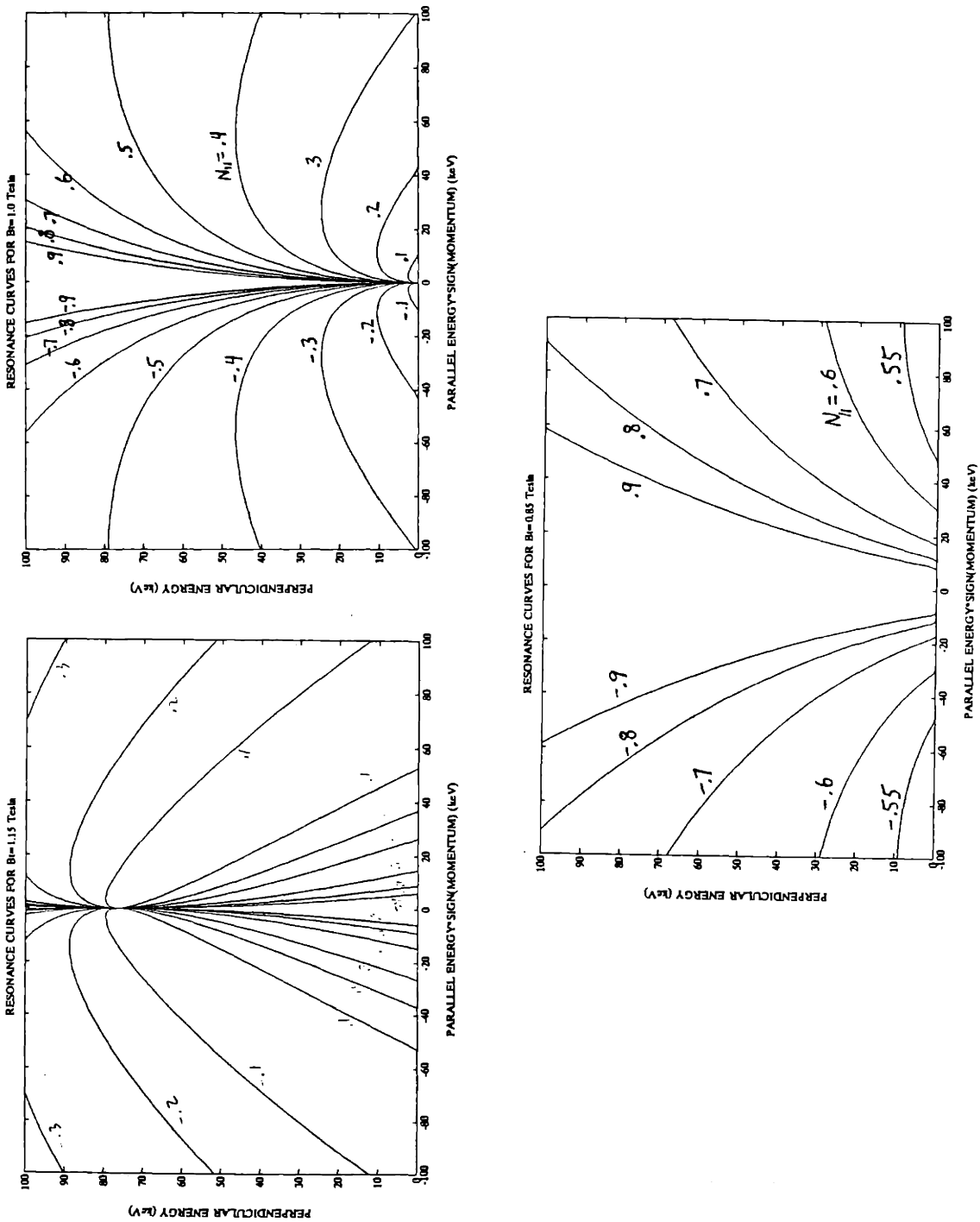
RESONANCE CURVES FOR Bt= 1.15 Tesla
PERPENDICULAR ENERGY (keV)
PARALLEL ENERGY*SIGN(MOMENTUM) (keV)
RESONANCE CURVES FOR Bt= 1.0 Tesla
PERPENDICULAR ENERGY (keV)
PARALLEL ENERGY*SIGN(MOMENTUM) (keV)
RESONANCE CURVES FOR Bt= 0.85 Tesla
PERPENDICULAR ENERGY (keV)
PARALLEL ENERGY*SIGN(MOMENTUM) (keV)

Figure 4-44

emission in this energy range, as observed by the silicon-lithium detector. This implies that strong heating is occuring along resonance contours that pass within 2 keV or so of the origin in "energy" space. The resonance curves for $\omega_{ce}/\omega = 0.85$, 1.0, and 1.15 with $\omega = 2\pi \times 28$ GHz are shown in Figures 4-44 for various $N_{\|}$'s. These curves take on their irregular shape in the transformation from relativistic momentum space to relativistic "energy" space. It can be seen from these figures that resonance curves pass into the region $E \lesssim 2$ keV only for $\omega_{ce}/\omega \approx 1$, or with $\omega = 2\pi \times 28$ GHz, only for $0.98 < B < 1.02$ T. In this case *all* the resonance curves converge in this region, regardless of launch angle. Thus the electrons heated in this way must be very near the EC layer. This conclusion is given quantitative support by the output of the TORCH code [77]. This code computes the ray trajectories and damping rates of EC waves in a Maxwellian plasma. Forthe case of $B(R = R_0) = 0.85$ T, $T_e = 2$ keV throughout the plasma, $\alpha = 45°$, and a density at the EC-layer of 1×10^{11} cm^{-3}, TORCH predicts 100% single-pass absorption, localized near the EC layer. Note that the predicted absorption by the low-density tail is much greater than the estimated 23% single-pass absorption by the thermal electrons. This may explain the observed importance of low density for successful ECCD. Low density reduces the electron collisionality, allowing the formation of a "slideaway" tail on the electron distribution function by the parallel electric field prior to EC-wave injection.

The conclusions of the previous paragraph, together with the result that the best ECCD is achieved when the EC layer is located near $R_{EC} - R_0 \approx -6$ cm, indicates that the best ECCD is achieved under conditions in which electrons are heated into the energy range 2-20 keV near $R - R_0 = -6$ cm, on the high-field side of the plasma. This may be related to trapped-electron effects. In the high-field region of its orbit, an electron can be heated to arbitrarily high perpendicular energy without becoming trapped. If this heating occurs in the low-field region of its trajectory (the region $R > R_0$) however, the electron will become trapped and will no longer carry current. Because the best ECCD efficiency is observed

under conditions in which the heated electrons are not trapped, the Ohkawa current (mechanism 5) is probably not responsible for much of the driven current, because it depends on electron trapping. Thus mechanisms 4 and 7, or a combination thereof, remain as the most likely ECCD mechanisms on Versator. These mechanisms are the selective reduction in the collision frequency and the bootstrap current.

CHAPTER 5
COMBINED ELECTRON CYCLOTRON HEATING AND LOWER HYBRID CURRENT DRIVE EXPERIMENTS

In this chapter the current-drive effects of simultaneously launching lower-hybrid (LH) waves and electron cyclotron (EC) waves into the Versator plasma are described. Several issues are highlighted by the experimental results and are examined, including the following: 1) the physical mechanisms of EC/LH transformerless startup, and the differences, if any, between combined EC/LH current drive in these plasmas versus those started by ohmic power. 2) the combined efficiency of current drive by LH and EC waves and the extent of its agreement with simple theoretical predictions based on velocity-space diffusion; 3) the extent to which the efficiency is modified by fast-electron trapping and losses, by the anomalous Doppler instability, and by other effects.

In the following sections, first the theory for combined LH/EC current drive is reviewed for a plasma slab, analyzing the velocity-space quasilinear diffusion of electrons by the waves. Data are then presented and analyzed from transformerless-startup discharges, and the results of EC-heating of these discharges are described. Experiments are then described in which EC-waves are injected into high-density LHCD discharges very similar to those of Chapter 3. Then the results of EC-wave injection into medium and low density discharges are described, including measurements of magnetic and electrostatic turbulence. The effects of electron trapping and losses due to ECH-induced turbulence are discussed. The anomalous Doppler instability (ADI) is then described, and the stabilizing effect of electron cyclotron heating (ECH) on the ADI is demonstrated experimentally.

5.1 THEORETICAL PRINCIPLE OF COMBINED EC/LH CURRENT DRIVE

The theoretical basis for the effects of combined EC-wave heating and LHCD can be described by returning to the Fokker-Planck equation, which describes the velocity space diffusion of electrons by waves and collisions. This is given by Equation 21 and is rewritten here for convenience

$$\frac{\partial f_0}{\partial t} = \frac{\partial f_0}{\partial \mathbf{p}} \cdot \overline{\overline{\mathbf{D}}} \cdot \frac{\partial f_0}{\partial \mathbf{p}} + \left.\frac{\partial f_0}{\partial t}\right|_{coll}. \tag{56}$$

The rf diffusion coefficient $\overline{\overline{\mathbf{D}}} \approx D_{LH}\hat{e}_{\|}\hat{e}_{\|} + D_{EC}\hat{e}_{\perp}\hat{e}_{\perp}$, where D_{LH} is the lower-hybrid diffusion coefficient, and D_{EC} is the electron-cyclotron diffusion coefficient. D_{LH} is the $n = 0$ term of Equation 22 and is given by Equation 25; D_{EC} is the $n = 1$ term of Equation 22 and is given by Equation 53. The lower-hybrid waves diffuse electrons in the $v_{\|}$-direction in velocity space via Landau resonance at $v_{\|} = \omega/k_{\|}$, and the electron-cyclotron waves diffuse electrons in the $v_{\perp}$-direction in velocity space via cyclotron resonance at $v_{\|} = (\omega - \omega_{ce})/k_{\|}$. The last term on the right-hand-side of Equation 56 is the relativistic collision operator for $u \gg 1$ and $T_e = T_i$. It is given by [105]

$$\left.\frac{\partial f_0}{\partial \tau}\right|_{coll} = \frac{\gamma\,(Z_{eff}+1)}{u^3 \sin\theta}\frac{\partial}{\partial\theta}\sin\theta\frac{\partial f_0}{\partial\theta} + \frac{2}{u^2}\frac{\partial}{\partial u}\left(\frac{\gamma^3}{u}\frac{\partial f_0}{\partial u} + \gamma^2 f_0\right) \tag{57}$$

where θ is the angle in velocity space from the positive $v_{\|}$ axis. The current generated by the effect of the EC waves on this collision term is generally 10 to 100 times

greater than by direct diffusion by the EC waves via the second term, as explained in sections 1.3 and 4.3.

Based on Equation 56, it has been predicted [105,106] that the current-drive efficiency of combined ECH and LHCD can be greater than LHCD or ECCD efficiency. The velocity-space diffusion associated with this "synergistic" current-drive effect betweeen EC waves and LH waves is shown schematically in Figure 5-1. Depending on $N_{||}$ and ω_{ce}/ω, the EC waves may heat the low-$v_{||}$ end or the high-$v_{||}$ end of the LHCD tail, as shown. The magnitude of the increased current-drive efficiency predicted for combined ECH/LHCD is dependent on the parallel resonant velocity of the EC-heated electrons. For EC resonance toward the high-$v_{||}$ end of the LHCD tail, the effect of the EC waves is mainly to increase the population and decrease the average collisionality of electrons at high $v_{||}$ by increasing $T_{\perp}$. Decreasing the average collisionality increases the theoretical current-drive efficiency, because the electrons then retain their parallel momentum longer.

For EC resonance toward the low-$v_{||}$ end of the LHCD tail, the population of electrons that are accelerated by the LH waves is increased and the average collisionality of this population is decreased, increasing the theoretical current-drive efficiency.

Because higher-velocity tail electrons retain their parallel momentum longer, the steady-state tail population and current-drive efficiency are greater for EC heating of the high-$v_{||}$ end of the LHCD tail than for EC heating of the low-$v_{||}$ end. This is shown in Figure 5-2, which shows distribution functions computed in reference [105]. The distribution functions are plotted on a logarithmic scale and flipped about the horizontal axis. Figure 5-2a shows EC heating of the low-$v_{||}$ end of the LH tail and Figure 5-2b shows EC heating of the Maxwellian plasma without LHCD. The incremental current-drive efficiency of the EC waves is more than three times greater for the LHCD target plasma versus the Maxwellian, even though the EC resonant velocity and EC power dissipated is nearly the same for both cases. This

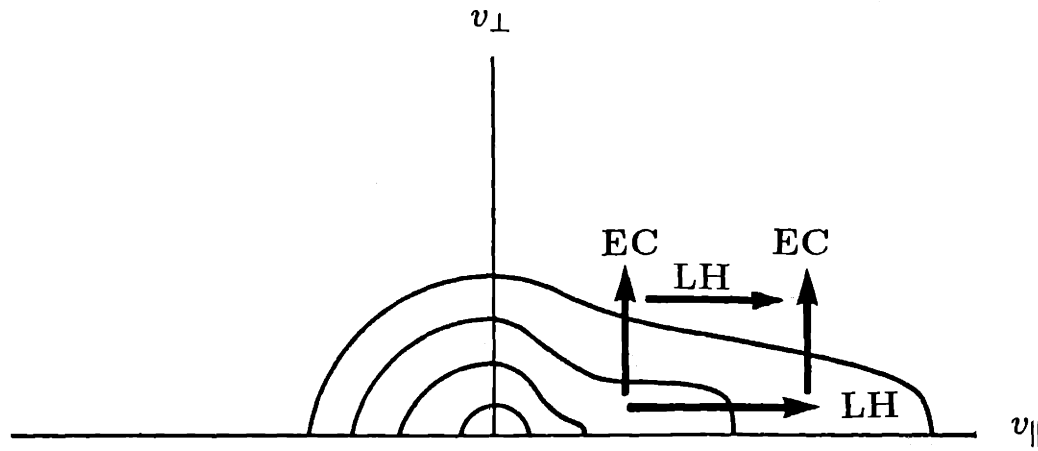

Figure 5-1 Schematic showing the diffusion of electrons by EC and LH waves.

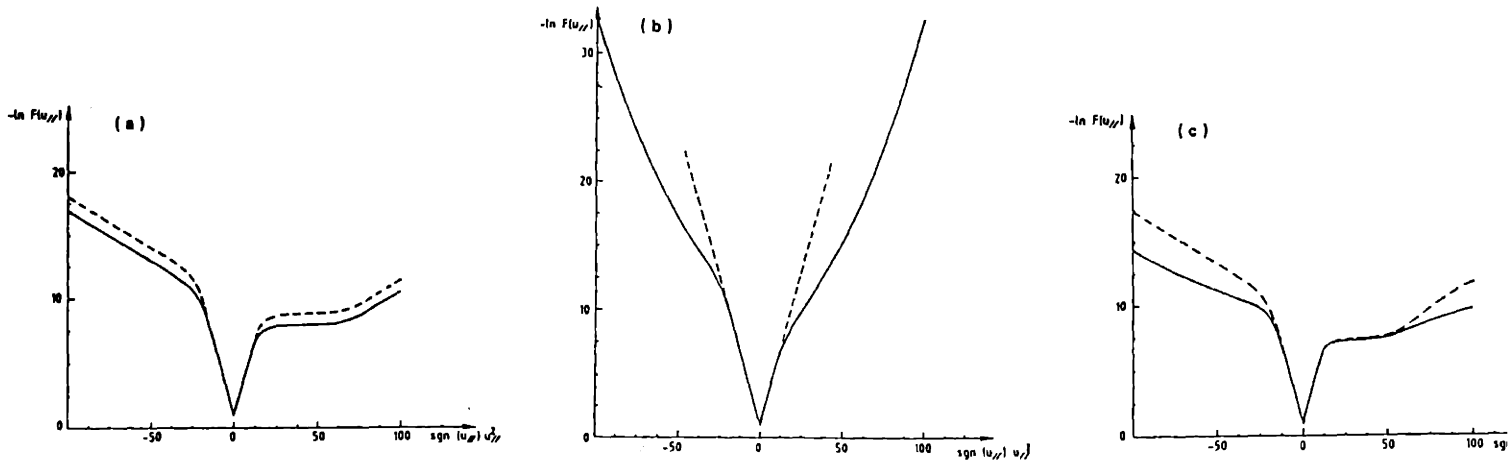

$F(u_\parallel)$ versus $u_\parallel^2$ at steady state for LH waves (dashed curve) and for the ECLH system (full curves). (a) LH and EC waves for $\psi = -45°$ at r = 30 cm, (b) EC waves at $T_e(0) = 3$ keV, and (c) LH and EC waves for $\psi = -15°$ at r = 15 cm. The dashed curve in (b) is the initial Maxwellian.

Figure 5-2 (from reference [105]).

is because the average parallel velocity of the current-carrying electrons is greater (leading to greater current), and the average total velocity of the current-carrying electrons is greater (leading to lower dissipated LH power per electron). For the computations shown, the dissipated LH power was held fixed, so the LH waves were able to drive more current at the same power level due to the reduced collisionality of the tail electrons heated by the EC waves.

Figure 5-2c shows EC heating of the high-$v_{||}$ end of the LH tail. The efficiency for this case is 1.7 times greater than for EC heating of the low-$v_{||}$ end of the LHCD tail, 1.4 times the efficiency of the LH waves alone, and more than five times greater than for ECCD of the Maxwellian. The high efficiency is due to the high velocity of the new current-carrying electrons. The combination of EC heating and pitch-angle scattering off of ions increases the distribution function at parallel velocities greater than the maximum resonant velocity of the LH waves.

Thus, based on the theory of quasilinear diffusion of electrons in velocity space, a current-drive synergism is expected betweeen LH and EC waves. The remainder of this chapter is devoted to describing and interpreting experiments on the Versator-II tokamak designed to test this synergism.

5.2 ELECTRON CYCLOTRON HEATING OF TRANSFORMERLESS STARTUP DISCHARGES

Experiments are now described in which the tokamak plasma is formed without the use of the ohmic-heating transformer. These plasmas are similar to those of the combined LHCD/ECH experiments reported most extensively in the literature, perfomed by the WT-2 and JIPPT-IIU groups in Japan [37, 107]. These experiments were described briefly in Chapter 1.

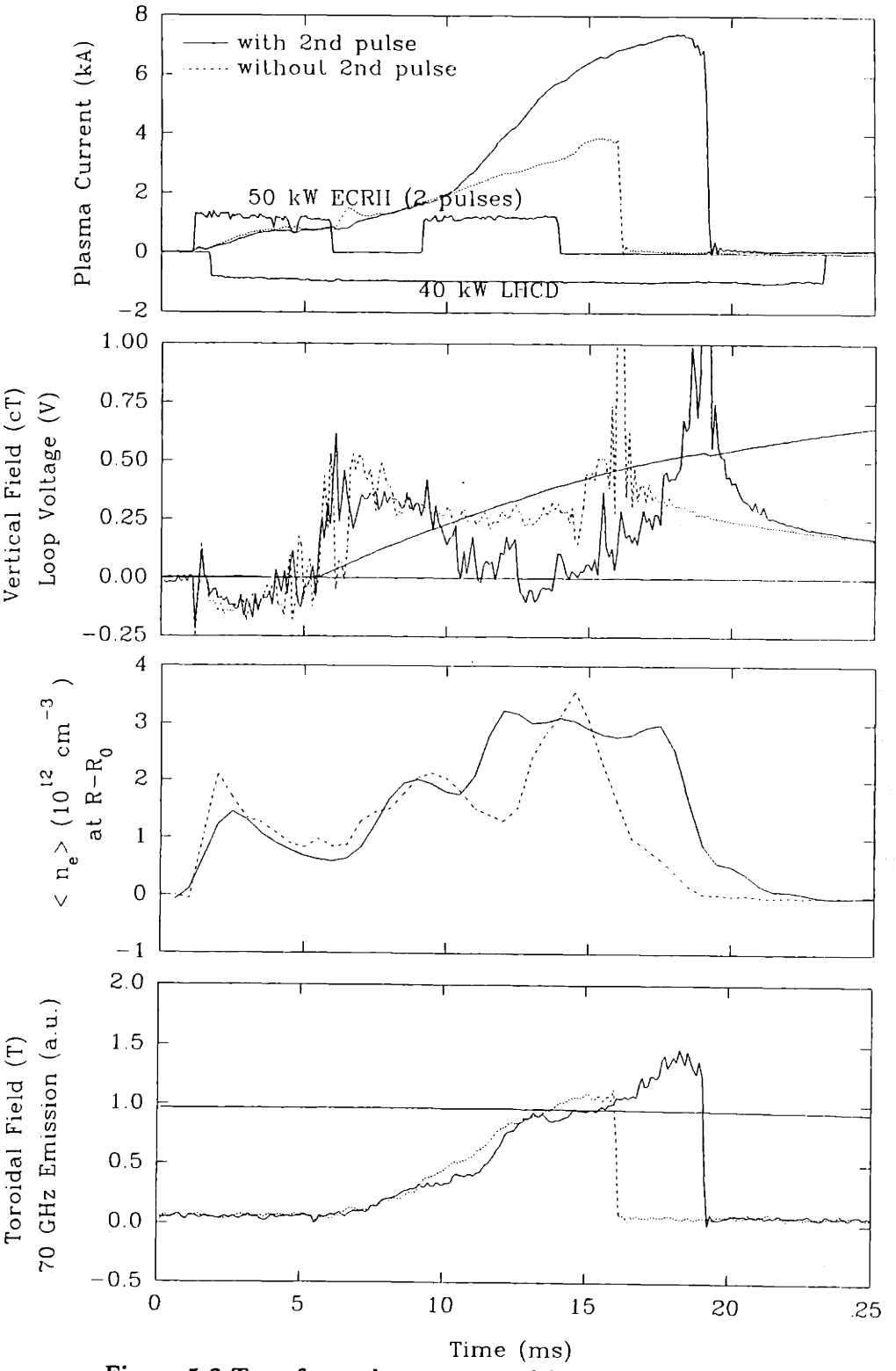

Figure 5-3 Transformerless startup with and without second EC pulse.

The time evolution of a transformerless startup discharge on Versator is shown in Figure 5-3. The ohmic heating coil was open circuited for the entire run. The plasma was preionized by a 50 kW 5 ms pulse of EC waves launched from the high-field side in the O-mode polarization with $\alpha = 0°$. An initial plasma current of $I_p \lesssim 1$kA was formed as described in section 4.1. A 40 kW, 21 ms LH pulse was injected 1 ms after the beginning of the ECH pulse, and the vertical field was ramped up at $t = 5.5$ ms very near the end of the preionizing ECH pulse. The combination of the LHCD and the small loop voltage generated by the ramping vertical field accelerated the electron tail of the preionized plasma, and the plasma current ramped up steadily. A minimum of about 20 kW of LH waves and a ramp-rate $0.25 < dB_V/dt < 0.75$ T/s were both found to be necessary for successful transformerless startup on Versator.

Without the application of a second ECRH pulse, I_p ramped up steadily at 0.4 kA/ms before abruptly terminating at $t \approx 16$ ms. This termination occured before the end of the LHCD pulse, and it was unpreventable, even though a wide range of vertical field timings and ramp rates, gas puff settings, and LH-wave phasings and power levels were tried. It is similar in some respects (e.g., the behavior of the plasma current and the in/out position of the current channel) to the termination of a normal ohmic or LHCD discharge on Versator after power input to the plasma has been shut off, resulting in radiative collapse. This suggests that the fast electron tail for these LHCD startup discharges is poorly confined and poorly coupled to the thermal electron population. The confinement time of the LHCD tail as previously measured on 15-20 kA Versator discharges is 0.5-1.5 ms [58], and the confinement time with $I_p = 3 - 4$ kA is expected to be shorter. By comparison, the collision time for a fast electron with the bulk is $\tau_{coll} = (1/\nu_0) v_{fast}^3 / v_{te}^3 \approx 7.5$ ms for a 10 keV electron and 84 ms for a 50 keV electron for these discharges with $\langle n_e \rangle = 2 \times 10^{12}$ cm^{-3}. Thus the vast majority of superthermal electrons in this energy range are lost before transfering their energy to the thermal electrons. This problem of early discharge termination was much worse prior to the Spring 1991

rebuild of the tokamak, in which the alignment of the toroidal field coils was improved. Presumably the reduction of error fields is responsible for the improved performance. This problem has not been reported by others who have performed similar experiments (with or without a second ECH pulse) on larger tokamaks with better electron confinement [37, 48, 107].

The loop voltage drops to -0.12 V during the middle of the preionization phase, in which $dI_p/dt > 0$ and $dB_V/dt = 0$, then jumps up to $+0.35$ V when the vertical field is ramped up. This jump is caused by the changing vertical flux from dB_v/dt linked by the plasma: $V_{loop}^{B_V} = -\pi \left(R^2 - R_{at}^2\right) dB_V/dt$, where $R_{at} \approx 0.25$ m is the major radius of the anti-transformer coils, which are connected in series with the vertical field coils. The toroidal magnetic field at $R = R_0$ is nearly constant at 0.95 T during the discharge, so that the cyclotron resonance layer for 28 GHz is at $R - R_0 = 0.385$ m. The 70 GHz plasma emission polarized perpendicular to B_0, as viewed horizontally from the outer midplane, rises steadily from $t \approx 6.5$ ms (1 ms after V_{loop} jumps positive) until plasma termination.

When a second ECH pulse of equal power and pulse length to the first is launched at $t = 9$ ms, the plasma current rampup rate doubles to 0.8 kA/ms, the loop voltage drops, and the discharge is extended in time. After the second ECH pulse, V_{loop} climbs again to about 0.25 V then rises rapidly near the end of the discharge. The electron density at $R = R_0$ climbs abruptly from 2×10^{12} cm^{-3} to 3×10^{12} cm^{-3} simultaneously with the rise in dI_p/dt. Both the loop voltage and the EC waves appear to affect the 70 GHz emission. The 70 GHz emission apparently is emitted by electrons that are accelerated by the parallel electric field and then pitch-angle scattered, and by electrons heated by the EC waves. Note that no significant 70 GHz emission is observed during the EC-wave and LH-wave injection prior to the creation of a positive loop voltage by the ramping vertical field. The perpendicular 70 GHz emission begins to ramp up 1-2 ms after the turn-on of the positive V_{loop}, which is comparable to the pitch-angle scattering time in these discharges of an electron with $E_{\|} \approx 3.5$ keV.

Although the current-drive efficiency is strongly enhanced by the second ECH pulse, the current would have to flattop at $I_p = 74$ kA at $n_e = 3\times10^{12}$ cm^{-3} with the given total rf power of 90 kW to attain the same overall current-drive efficiency as achievable during conventional LHCD discharges on Versator. Because the plasma current reaches only 10% of this value these discharges do not demonstrate an EC/LH current-drive synergism.

The equilibrium quantities q_a, $\beta_p + \ell_i/2$, and the in/out position of the current channel are shown in Figures 5-4 and 5-5 for the cases of without and with the second ECRH pulse, respectively. For the case of no second ECRH pulse, the plasma current channel forms and moves to a position near $R - R_0 = 4$ cm by the time I_p has risen to 1.5 kA. It moves outward slowly until $t = 12.5$ ms, then moves sharply inward to $R = R_0$ as the density rises abruptly. During this period, $q_a(r = 13$ cm) falls steadily from 175 to 50, and $q(r = 8$ cm) correspondingly falls from 108 to 31, where $q(r = 8$ cm) is calculated assuming all the plasma current is located within $r = 8$ cm. This radius appears from hard X-ray data to be the effective edge of the superthermal current channel. During the slowly-outward-moving period from $t = 8$ ms to 14 ms, $\beta_p + \ell_i/2$ steadily increases from 4 to 4.8, then drops suddenly at $t = 14$ cm during the abrupt inward motion of the current-channel just prior to termination of the discharge.

When a second ECRH pulse is injected from $t = 9$ ms to $t = 14$ ms, the plasma is forced inward and $\beta_p + \ell_i/2$ is reduced from 3 to 1.6. After turn-off of the ECRH, $\beta_p + \ell_i/2$ holds nearly steady at 1.6-1.8 until termination of the discharge.

Vertically-line-averaged density profiles are shown for a sequence of times in Figure 5-6 for the cases with and without the second ECRH pulse. A series of highly similar discharges was taken for each case, and the profiles were obtained by moving the remote-controlled movable interferometer horns between shots. The profile at $t = 3$ ms (during preionization) is peaked way to the outside at $R - R_0 \approx 9$ cm at the relatively high value of 6×10^{12} cm^{-3}. The density is essentially zero for

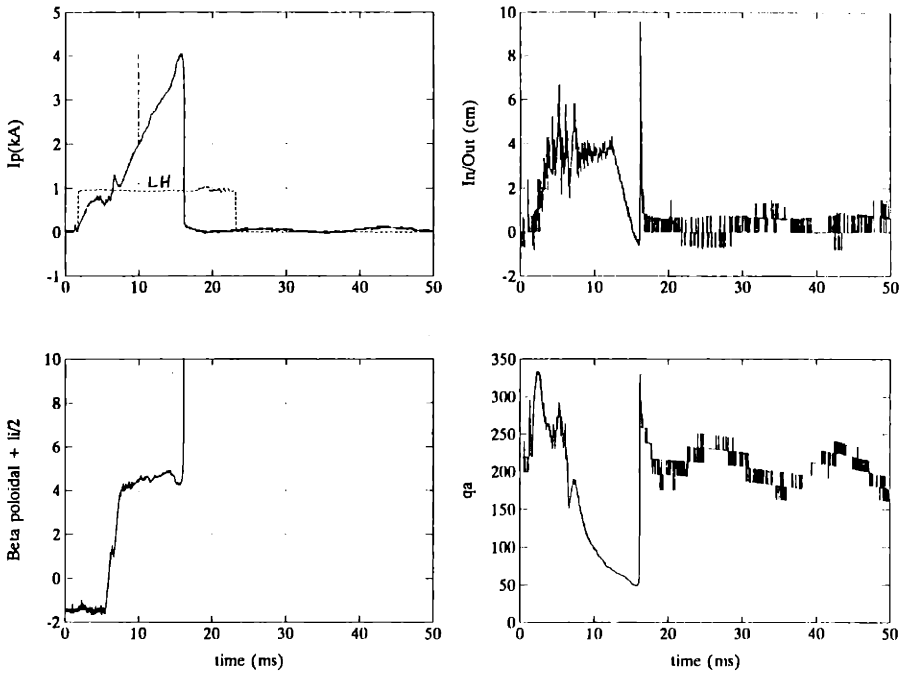

Figure 5-4 Equilibrium quantitles for startup without second EC pulse.

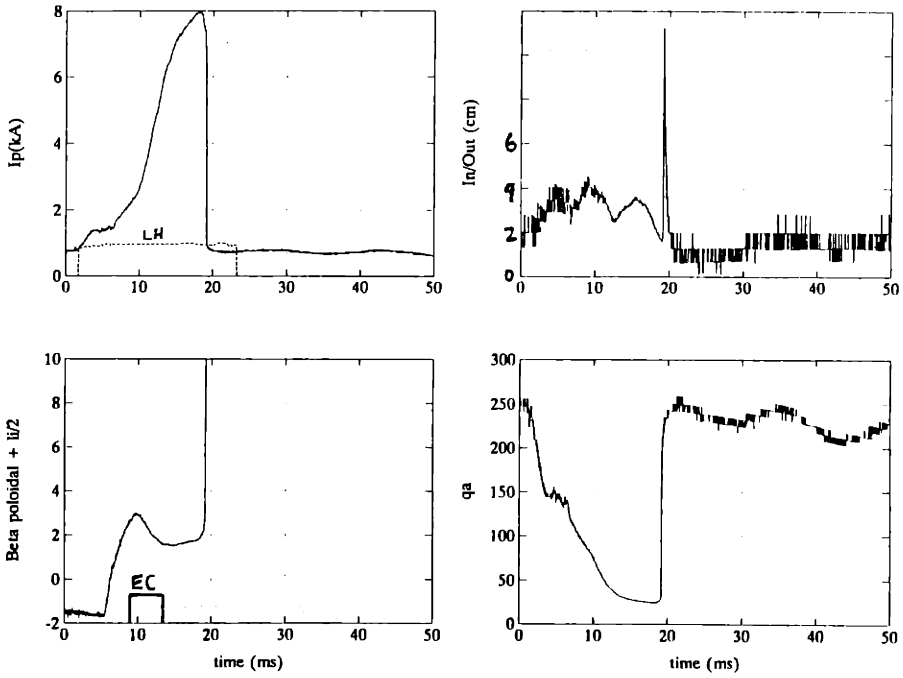

Figure 5-5 Equilibrium quantitles for startup with second EC pulse.

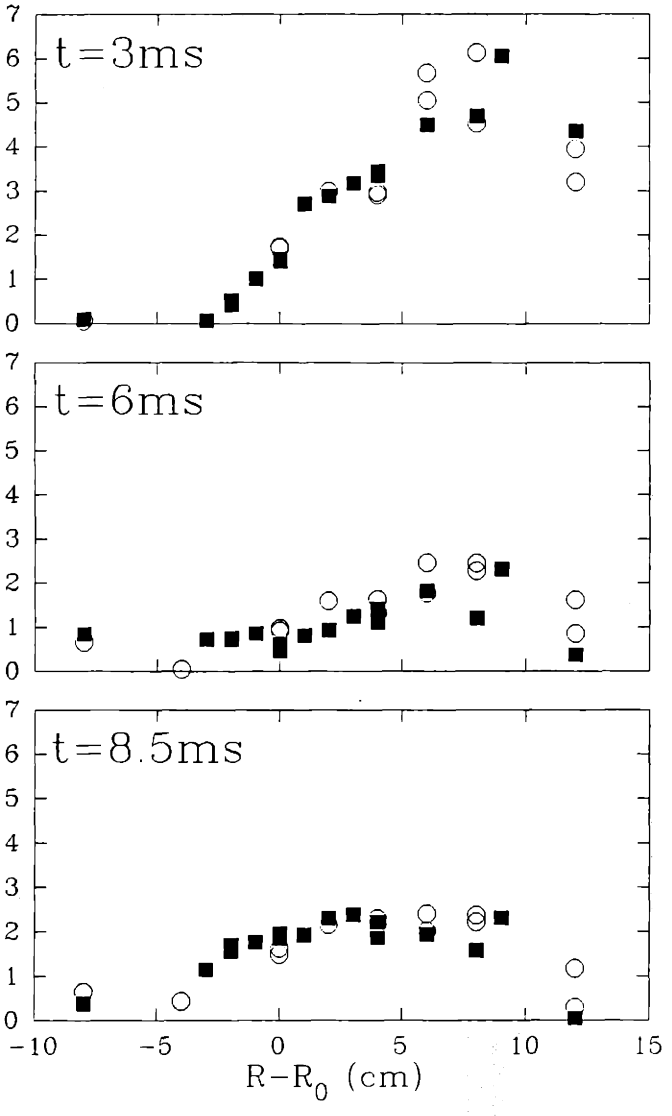

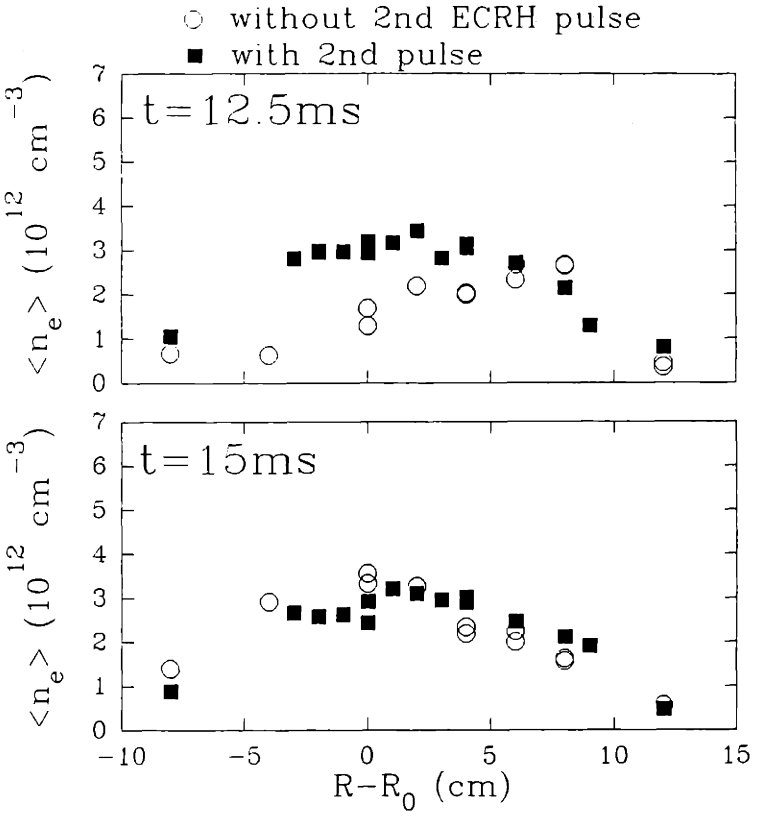

Figure 5-6 Density profiles for transformerless startup plasmas with and without 2nd ECRH pulse from t=9ms to 14ms. The preionizing ECRH pulse is from t=1ms to 6ms, and 40kW of LH waves are on from t=1.75ms to 23ms. EC wave is launched with O-mode polarization at P_{EC}=50kW.

$R - R_0 \leq -3$ cm and increases almost linearly from $R - R_0 = -3$ cm to +9 cm before falling to about 4×10^{12} cm^{-3} at $R - R_0 = +12$ cm. Recall that the EC-layer is at $R - R_0 = -2$ cm. This profile is typical for preionization plasmas on Versator in which the plasma current is insufficient to close the flux surfaces over most of the plasma cross-section. The plasma forms in the region between the cyclotron layer and the upper-hybrid layer and drifts outward in R at the reduced $\mathbf{E} \times \mathbf{B}$ drift velocity, as discussed in section 4.1. The density profile severely collapses soon after the LH waves are injected, as is shown in frame 2 of Figure 5-6, which shows the density profile at $t = 6$ ms. Under the influence of the LH waves and the small loop voltage, the density profile rebuilds, and it is considerably broader and more centered in the vacuum chamber at $t = 8.5$ ms, peaked at $R - R_0 = +4$ cm (agreeing with the in/out measurement of the position of the current channel shown in Figure 5-4). The second ECH pulse is injected during the time 9 ms $< t <$ 14 ms. During the period 9 ms $\leq t \leq$ 12.5 ms, the profile for the case without the second pulse changes little, moving slightly toward the outside. However, the profile for the case with the second ECH pulse builds and becomes more centered, with $\langle n_e \rangle_{peak} = 3.4 \times 10^{12}$ cm^{-3} at $R - R_0 = 2$ cm. After $t = 12.5$ ms, the discharge without the second pulse shifts rapidly toward smaller R and climbs in density prior to discharge termination, whereas the profile for the shot with the second pulse remains steady. Thus at $t = 15$ ms the density profiles for the two cases are similar.

Profiles of the hard X-rays emitted in the range 30 keV $\lesssim E_{\|} \lesssim$ 500 keV for the two cases at times throughout the discharges are shown in Figure 5-7. Emission is first observed at $R - R_0 = +8$ cm at a low level during the early period after shut-off of the preionizing ECH pulse at $t = 6$ ms. For the case without the second ECH pulse, the emission at this radius grows until $t \approx 12$ ms, when the plasma begins its sudden inward motion. The emission at $R - R_0 = +4$ cm grows first, then the emission at $R - R_0 = 0$ cm and $R - R_0 = -4$ cm grows rapidly to a much higher value during the 4 ms prior to discharge termination. Note that the scales change considerably from frames 2 to 3, 3 to 4, and 4 to 5 in Figure 5-7.

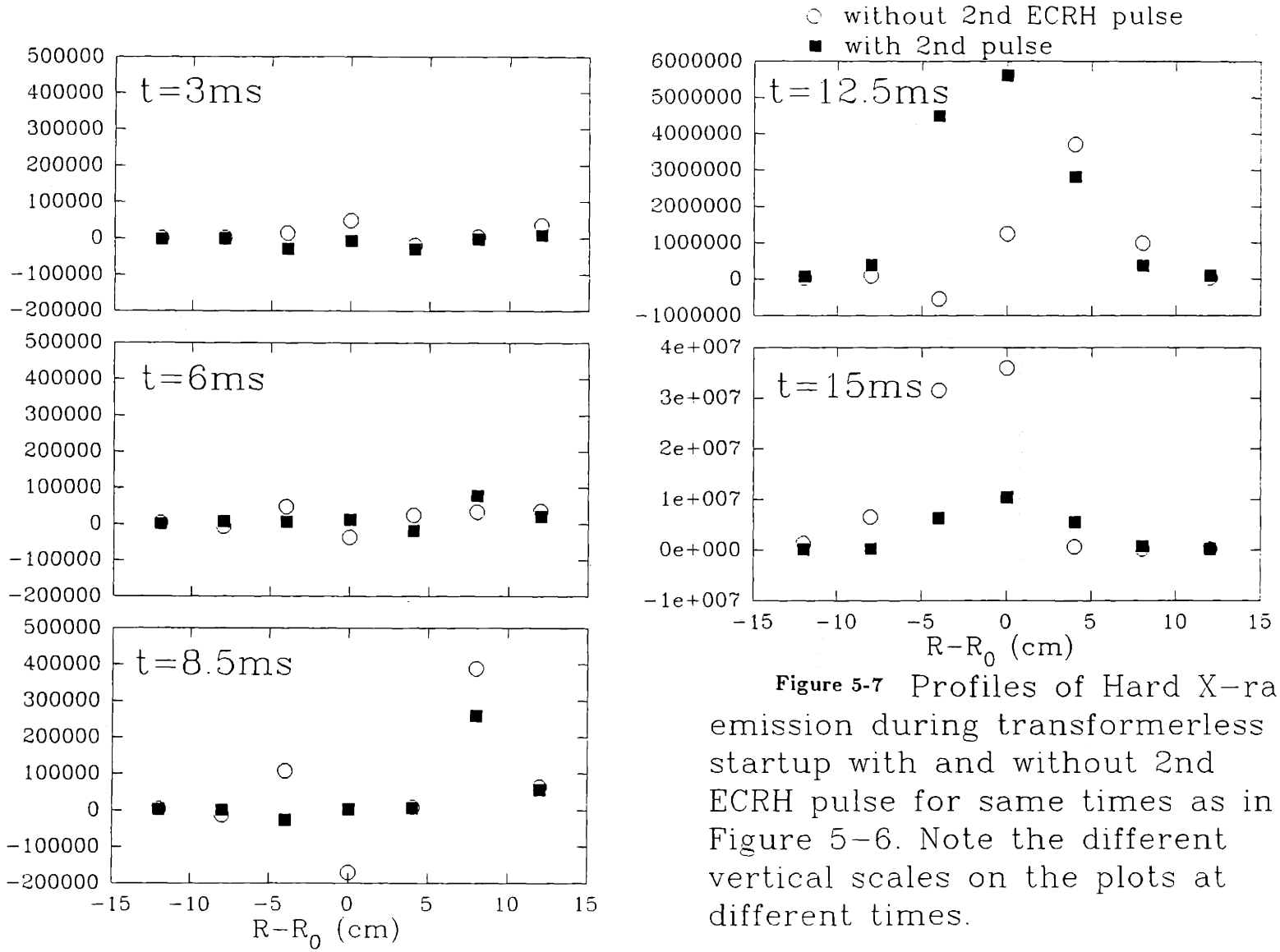

Figure 5-7 Profiles of Hard X-ray emission during transformerless startup with and without 2nd ECRH pulse for same times as in Figure 5-6. Note the different vertical scales on the plots at different times.

These hard X-ray profiles suggest that the fast electrons are first confined far to the outside near $R = R_0 = +8$ cm, where they form the current channel. This is also where the density profile is peaked at $t = 6$ ms, indicating that closed flux surfaces first form in this region. As the plasma current rises, $\beta_p + \ell_i/2$ gradually increases and the plasma remains to the far outside, suggesting that the plasma pressure is building as well. This correlates with the idea that the fast electron population is growing about $R - R_0 = +8$ cm. At $t = 12.5$ ms, the fast-electron population begins a rapid shift toward the inside, together with a rapid growth in the magnitude of the emission. By $t = 15$ ms, the emission is very strong, and is localized to $R - R_0 \leq 0$, just prior to termination of the plasma current. Interestingly, the emission at $R - R_0 = -8$ cm grows again at $t = 18$ ms, implying that a small population of superthermal electrons is confined even when I_p is very small.

The fast electron channel is well-centered and symmetric about $R = R_0$ as a result of the second ECH pulse, as can be seen from frames 4 and 5 of Figure 5-7.

5.3 ECH OF HIGH-DENSITY LHCD DISCHARGES

Figure 5-8 shows the time history of a typical high-density LHCD discharge on Versator, with and without EC-heating of the fast electron tail. The LHCD target discharges are very similar to those described in Chapter 3. They are started by full ohmic drive, in contrast to those of the previous section, and 40 kW of LH waves is subsequently injected with $f = 2.45$ GHz and $\Delta\phi = \pi/2$ at t =12.5 ms. This drives the loop voltage from about 1 V down to 0.2 V, and the plasma current is maintained approximately constant until turn-off of the LH power at $t = 35$ ms. The electron density at $R = R_0$ rises to $\langle n_e \rangle \approx 1.2 \times 10^{13}$ cm^{-3} during the initial ohmic phase, then drops sharply to $\langle n_e \rangle = 8 \times 10^{12}$ cm^{-3} upon injection

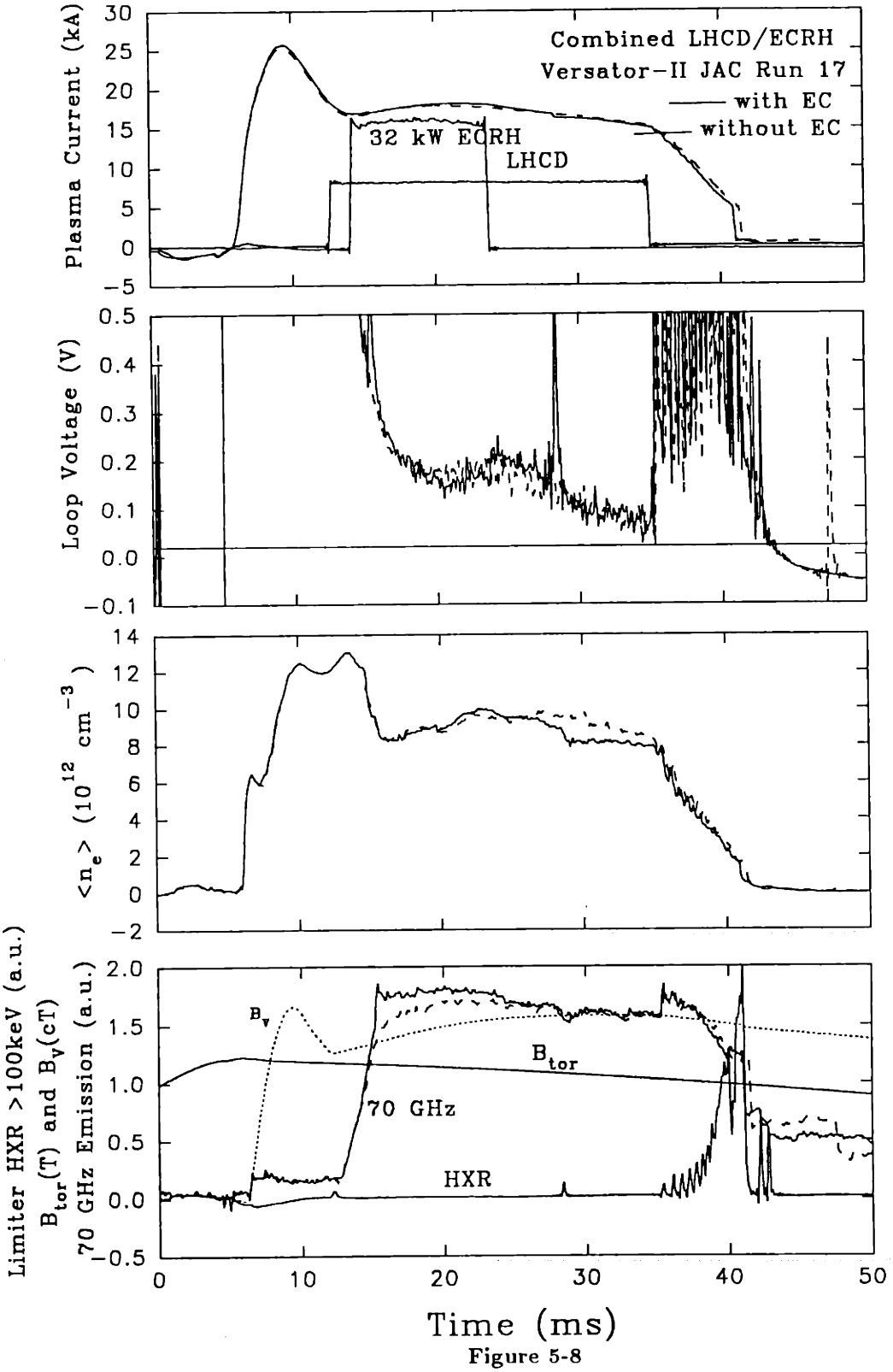
Combined LHCD/ECRH
Versator-II JAC Run 17
with EC
without EC
32 kW ECRH
LHCD
Plasma Current (kA)
Loop Voltage (V)
<n_e> (10^{12} cm^{-3})
Limiter HXR >100keV (a.u.)
B_{tor}(T) and B_v(cT)
70 GHz Emission (a.u.)
B_v
B_{tor}
70 GHz
HXR
Time (ms)

Figure 5-8

of the LH waves. The density subsequently remains flat or slightly increases with time during the LH pulse. Without the injection of EC waves, the loop voltage decreases steadily from 0.2 V to 0.075 V during the LH pulse as the ohmic input power decreases. When EC waves are injected during the period 14-24 ms, the plasma current is slightly enhanced, and V_{loop} drops from 1.75 V to 1.50 V. This 14% drop is followed by an abrupt rise to 0.2 V upon termination of the EC pulse. The 70 GHz cyclotron emission turns on during the ohmic startup phase, and rises rapidly by an order of magnitude upon injection of the LH waves. When EC waves are injected from t =14 ms to 24 ms, the 70 GHz emission is further enhanced by 15% over the emission for LH alone. When the EC pulse is delayed 5 ms to 19-29 ms, no enhancement in I_p, drop in V_{loop}, or enhancement of the 70 GHz emission are observed. This figure shows that injection of EC waves from 14 ms to 24 ms into high-density LHCD discharges has a small beneficial effect.

The equilibrium quantities for discharges with and without EC-wave injection are shown in Figures 5-9 and 5-10, respectively. These figures show that the plasmas are well-centered, with $q_a \approx 13$ and $0.5 < \beta_p + \ell_i/2 < 1.0$ during the LH pulse, and that the EC waves have very little, if any, effect on the plasma equilibrium quantities. Similarly, the EC waves appear to have little effect on the bulk electron density profile, as shown in Figure 5-11. This figure shows the line-averaged electron density as a function of $R - R_0$ for t =18 ms, 23 ms, 28 ms, and 33 ms for the cases of LH alone, LH+EC from 14-24 ms, and LH+EC from 19-29 ms. The EC waves are launched from the high-field side in the X-mode polarization with various launch angles relative to the static magnetic field, primarily with $\alpha = 0°$ or $\alpha = -20°$. The variation in plasma parameters due to changes in the launch angle was found to be no greater than the random variation from shot to shot. The data indicate that the injection of the EC waves does not significantly alter the density profile at any of the times shown, except perhaps the apparent broadening toward the outside of the discharges with EC waves launched between 19 and 29 ms. All the profiles show a slight broadening with time from t = 18 ms to 28 ms.

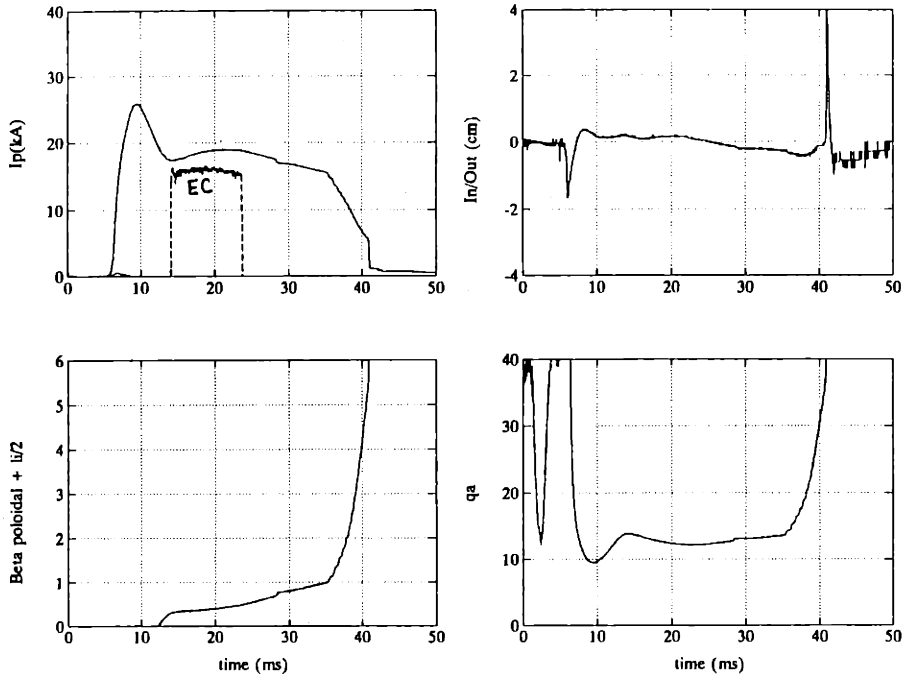

Figure 5-9 Equilibrium quantities for EC-heated high-density LHCD discharge.

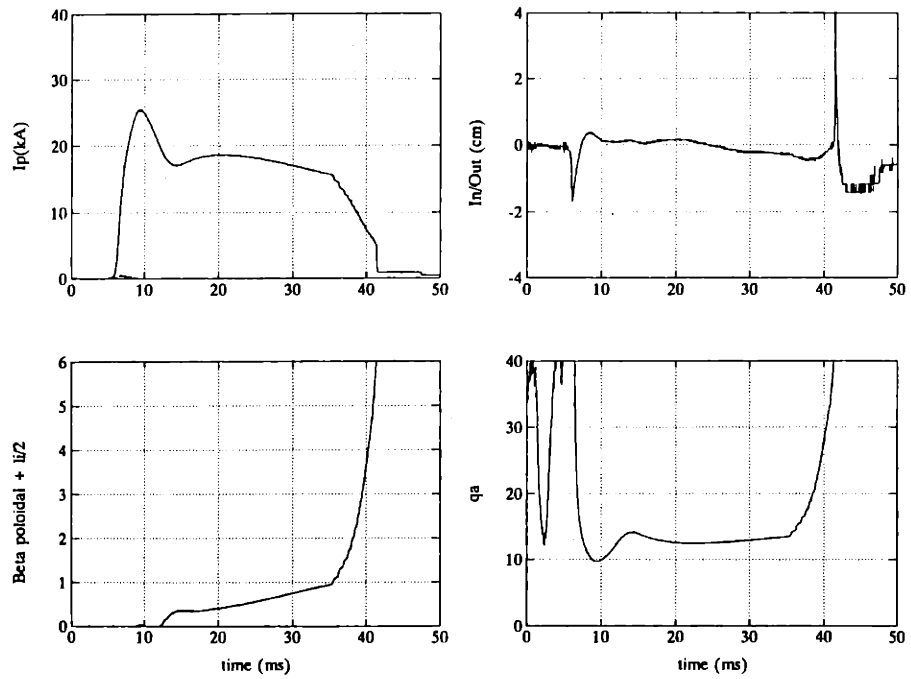

Figure 5-10 Equilibrium quantities for high-density LHCD discharge.

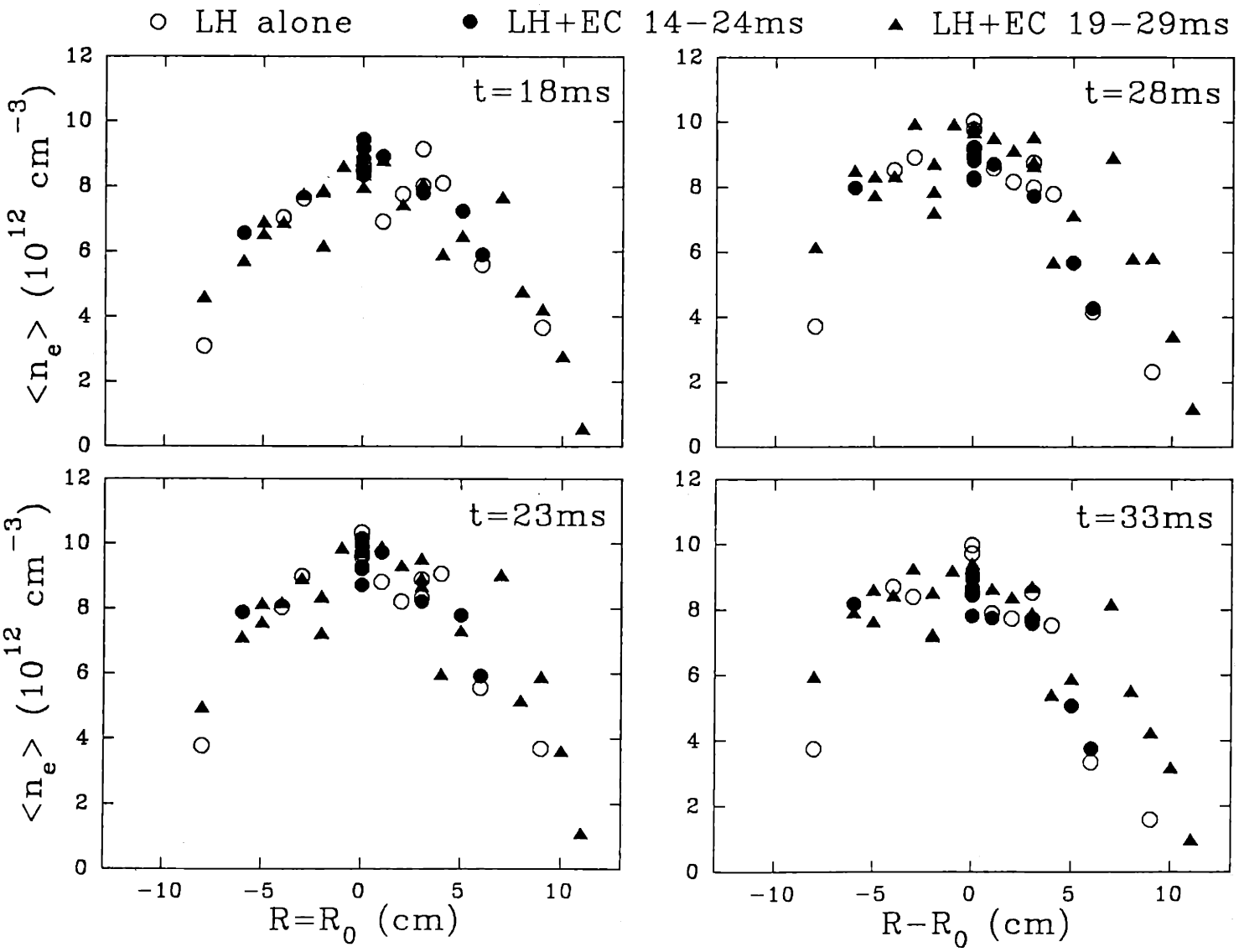

Figure 5-11 Density profiles for high-density EC/LH discharges.

The plasma hard X-ray emission is strongly enhanced by the EC waves launched from $t = 14$ ms to 24 ms, as shown in Figure 5-12 and 5-13. Figure 5-12 shows the time evolution of the hard X-ray emission at seven major radii for the shots with LH alone. Note that these discharges are similar in most respects to those of Chapter 3. The emission rises rapidly from small values when the LH turns on, peaking midway through the LH pulse. The emission is centered about $R = R_0$, except for the anomalous emission peak near $R - R_0 = -8$ cm as described in Chapter 3. Note that emission at all radii other than $R - R_0 = -8$ cm rise when the LH shuts off and a large loop voltage returns.

When EC waves are injected, the emission at $R = R_0$ is double the value at $t = 19$ ms without ECH, and gradually decreases during the EC pulse. This suggests that the superthermal electrons are heated less effectively later in the EC pulse when the toroidal magnetic field is lower. The emission drops dramatically upon shutoff of the EC power. Figure 5-14 shows the time evolution of the hard X-rays for the case of EC-waves launched 19-29 ms. In contrast to the earlier launch, for this case the hard X-rays are only enhanced near the beginning of the pulse 19 ms$\leq t \leq$22 ms, and they are supressed somewhat during the remainder of the EC pulse, especially at $R = R_0$ and $R - R_0 = -8$ cm. A plot of the location of the EC-resonance layer as a function of time for these discharges is shown in Figure 5-15. Note that the EC-heating zone for electrons with high $v_{||}$ is closer to the plasma center during the early part of the discharge for most possible launch angles.

Radial profiles of the hard X-ray emission and temperature are shown in Figures 5-16 and 5-17. These data were averaged over the EC pulse. Virtually no effect on the averaged profiles is observed for the 19-29 ms EC pulse, but strong central enhancement of the emission is caused by the 14-24 ms EC pulse. This implies strong central heating of electrons in the energy range of ~20-30 keV by the EC waves.

The magnetic fluctuations for these discharges are reduced by the LHCD and enhanced by the ECH, as shown in Figure 5-18. The edge electrostatic fluctuations

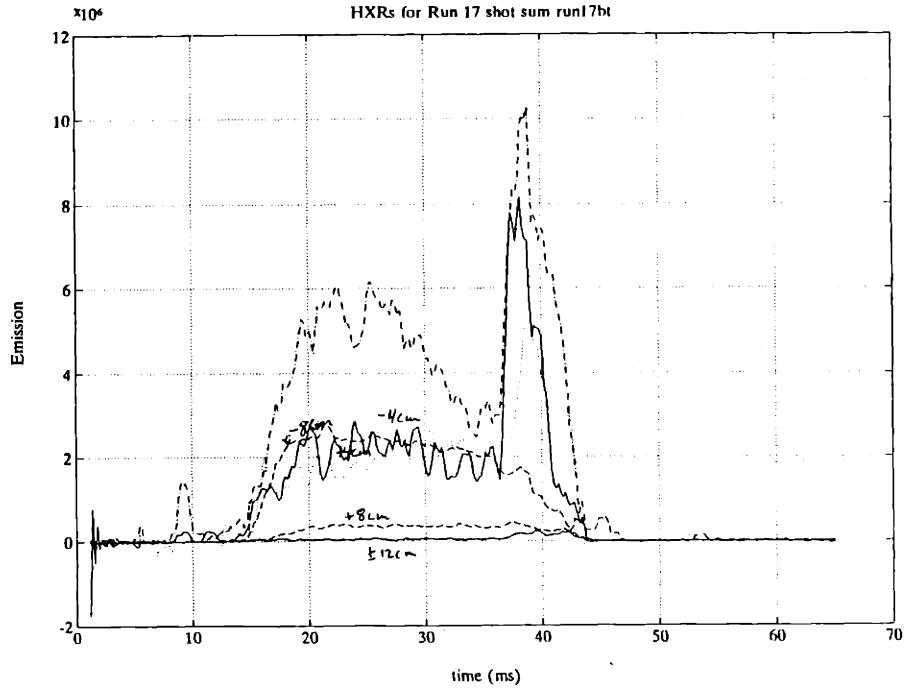

Figure 5-12 Hard X-ray time-dependence for high-density LHCD discharges.

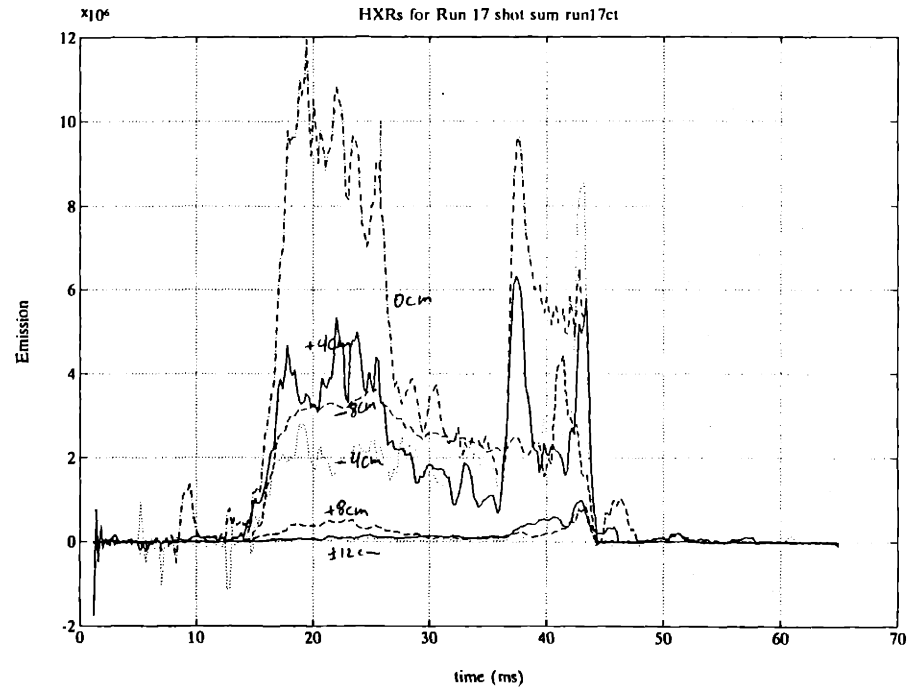

Figure 5-13 Hard X-rays for high-density LHCD discharges EC-heated 14-24 ms.

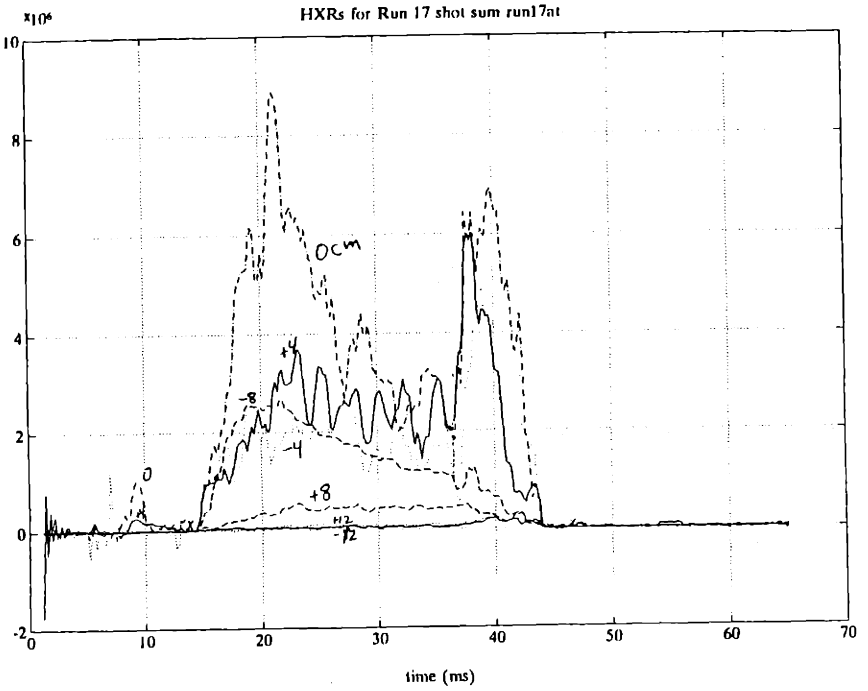

Figure 5-14 Hard X-rays for high-density LHCD discharges EC-heated 19-29 ms.

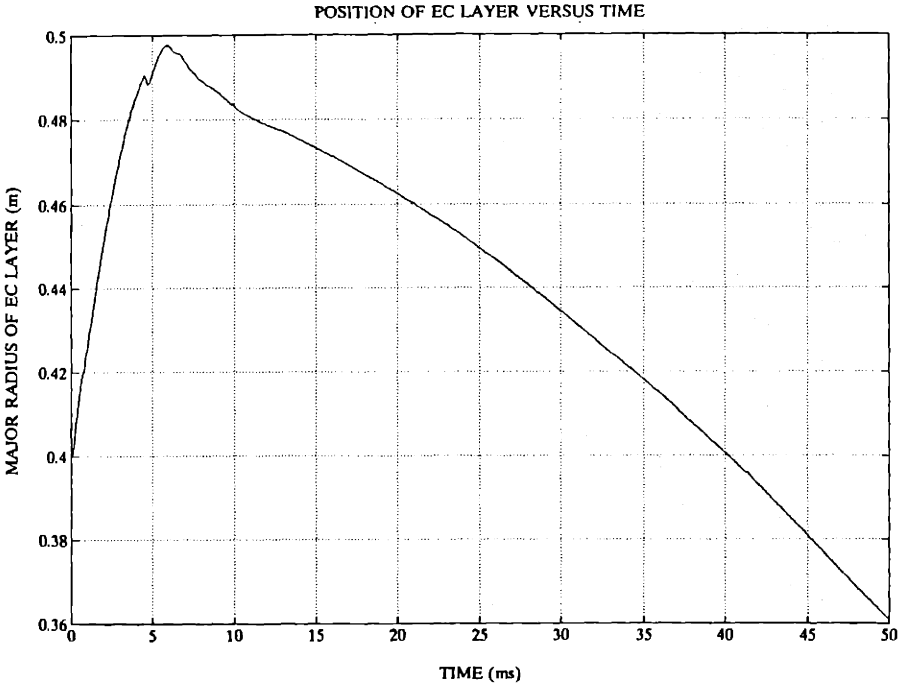

Figure 5-15 Location of EC layer vs. time for EC-heated LHCD discharges.

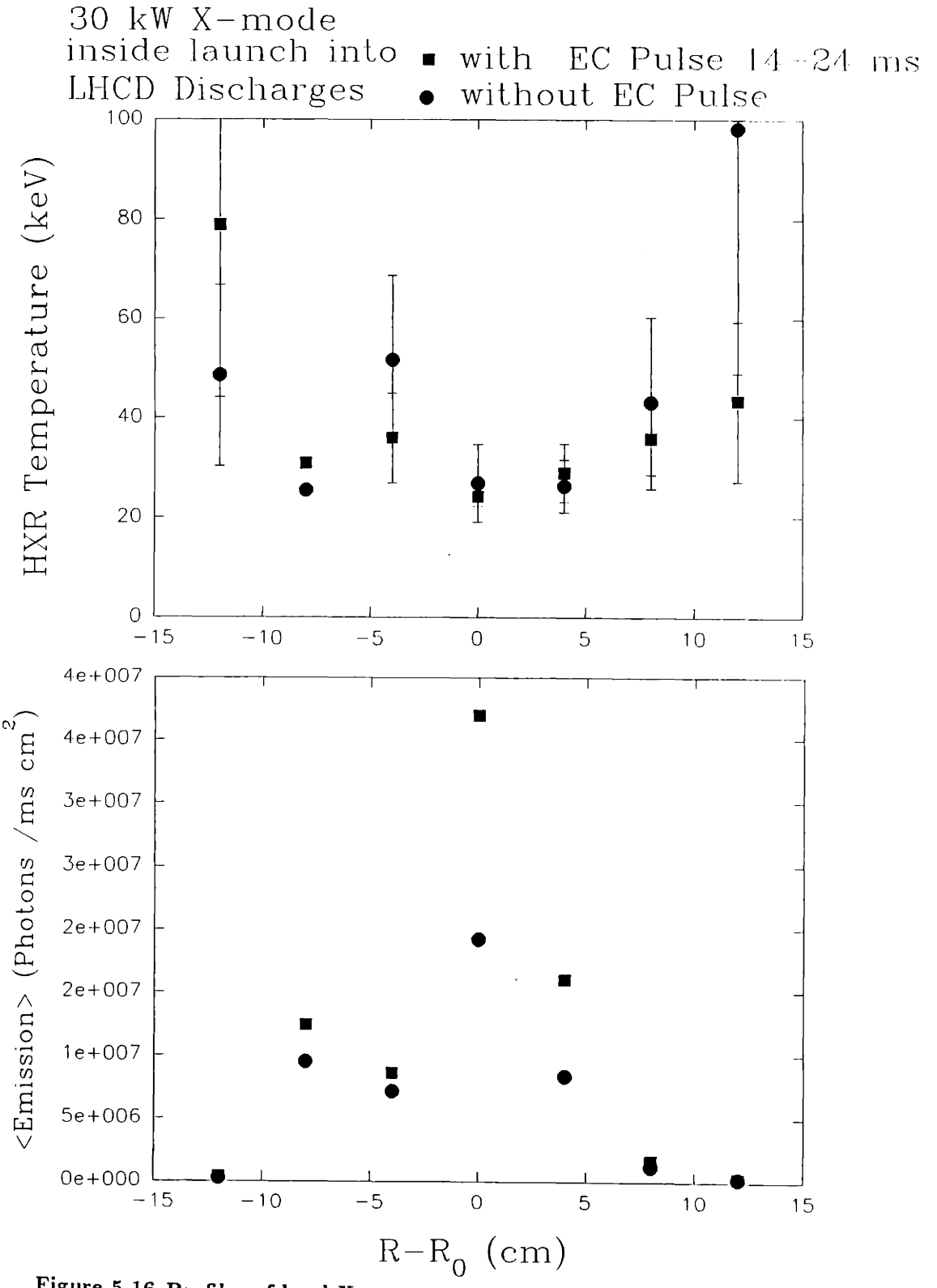

Figure 5-16 Profiles of hard X-ray temperature and emission for EC 14-24 ms.

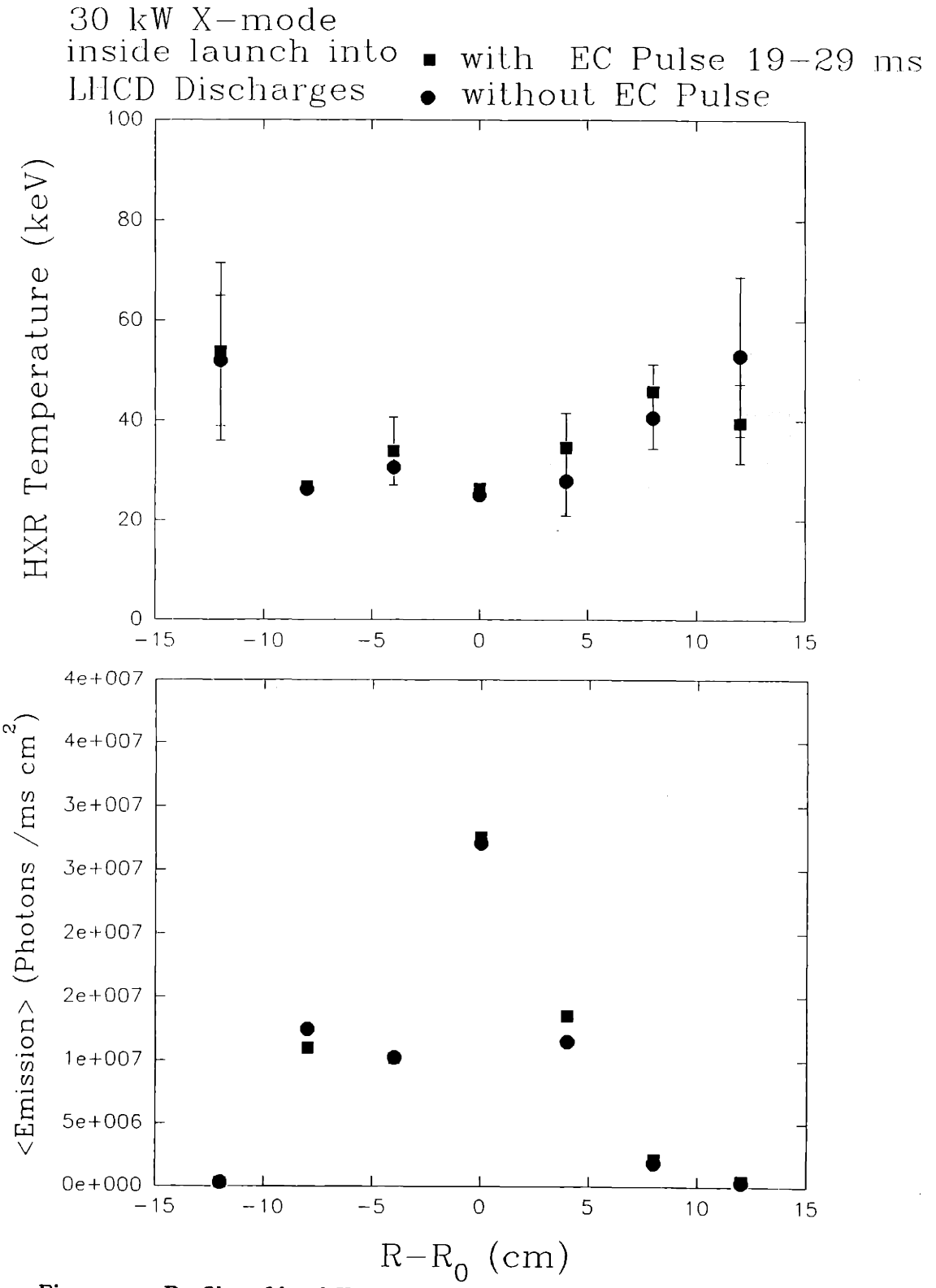

Figure 5-17 Profiles of hard X-ray temperature and emission for EC 19-29 ms.

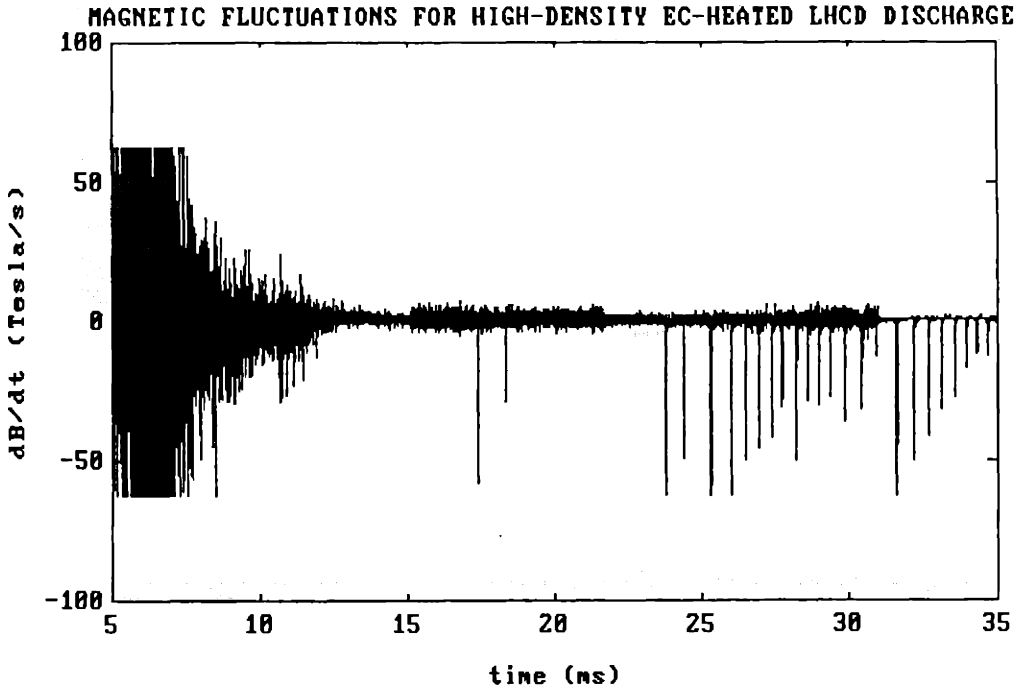

Figure 5-18

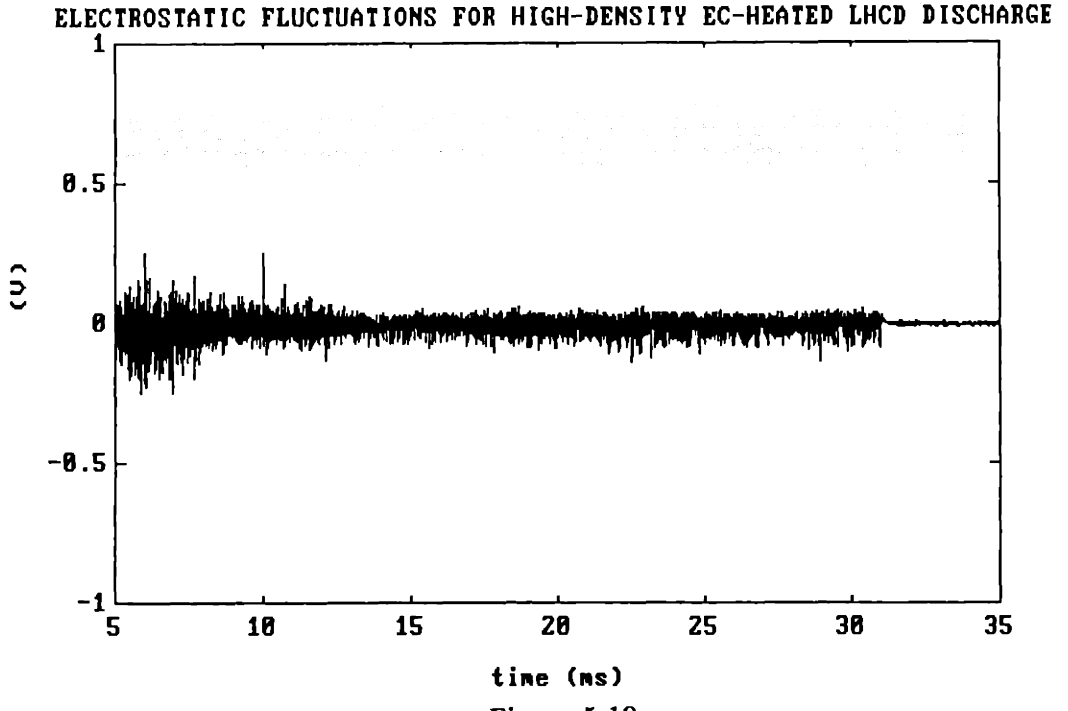

Figure 5-19

are at most slightly affected by the LH and EC waves, as shown in Figure 5-19. The magnitude of the enhancement of the magnetic fluctuations by the EC waves is greater during lower-density discharges, such as were shown in Section 4.2. These magnetic fluctuations may decrease the current drive efficiency by inducing fast electron losses, as will be described in more detail in the following section.

5.4 ECRH OF MEDIUM- AND LOW-DENSITY LHCD DISCHARGES

5.4.1 Experimental Results

The data of the previous section showed that a small increase in the plasma current and decrease in the loop voltage is achieved when EC waves are injected into LHCD plasmas with $\langle n_e \rangle = 8 \times 10^{12}$ cm^{-3}at $R = R_0$, and strong heating of the superthermal electrons is observed. In this section, observations on ECRH of LHCD discharges in the range $\langle n_e \rangle = 2 - 6 \times 10^{12}$ cm^{-3} are reported. The most important effect of lowering the density in this situation is to lower the Dreicer electric field. The Dreicer field is given by $E_D = 4\pi n_e e^3 \ln \Lambda / 2T_e$, where $\ln \Lambda \approx 15$ is the Coulomb logarithm. This is the electric field strength along the static magnetic field for which an electron traveling at the thermal speed will run away, i.e., the acceleration of the electron due to the electric field is greater than the drag on it due to collisions. As the density is lowered on Versator from the high- to the mid- and low-10^{12} cm^{-3} range, the population of electrons accelerated by the loop voltage to parallel velocities much greater than the thermal velocity increases exponentially. At the lower densities these electrons carry a significant portion of the plasma current. When LH waves are injected into the lower-density plasmas, the resulting parallel electron tail is hotter and extends to higher energy than in the higher-density case.

This causes the anomalous Doppler instability to become intense, degrading the plasma current and causing large spikes on the loop voltage and limiter hard X-ray signal. Also, at low density the superthermal tail absorbs the EC waves more effectively and the tail is more subject to radial losses caused by magnetic turbulence (because the tail extends to higher $v_{\|}$ and the magnetic turbulence is stronger).

Figure 5-20 shows the time history of the major plasma parameters for discharges with and without ECH with $\langle n_e \rangle = 5.5 \times 10^{12}$ cm^{-3} at $R = R_0$. Approximately 32 kW of EC waves is injected in mostly O-mode polarization from the high-magnetic-field side with $\alpha = +20°$. As with the majority of experimental runs, the behavior was generally independent of launch angle and polarization, within shot-to-shot variation, except possibly for large angles $|\alpha| \geq 60°$. The O-mode polarization was used because more power can be transmitted to the antenna this way. 32 kW of LH waves is injected starting at $t = 14$ ms, and the plasma current begins to flattop at 15 kA. At $t = 17.5$ ms the anomalous Doppler instability (ADI) turns on, as evidenced by the large spikes in V_{loop}. This was accompanied by an abrupt drop in dI_p/dt from zero to -5 kA/ms. Without injection of EC waves, dI_p/dt remained at this value until the LH waves are shut off at $t = 31.5$ ms. The average loop voltage during this phase is zero or slightly negative due to the LHCD and the decaying vertical magnetic field.

When EC-waves are injected from $t = 20$ to 25 ms, the plasma current begins to decay slightly faster at about $dI_p/dt = -5.75$ kA/ms, the average value of V_{loop} increases, and the oscillations on V_{loop} decrease in amplitude. The 70 GHz emission, which becomes intense early in the LH pulse, is unaffected by the EC waves, except that oscillations on it associated with the ADI are supressed during the EC pulse, and then return 1-2 ms afterwards. The toroidal field decays gradually during the shot and is 0.9 T during the EC pulse, putting the cyclotron layer at $R - R_0 = -4$ cm. This field is lower than for the discharges of Section 5.3. Similar results were obtained at this density with $B_t(R = R_0) = 1.2$ T, except that the increase in limiter hard X-ray signal was smaller. The limiter hard X-ray emission (>100 keV),

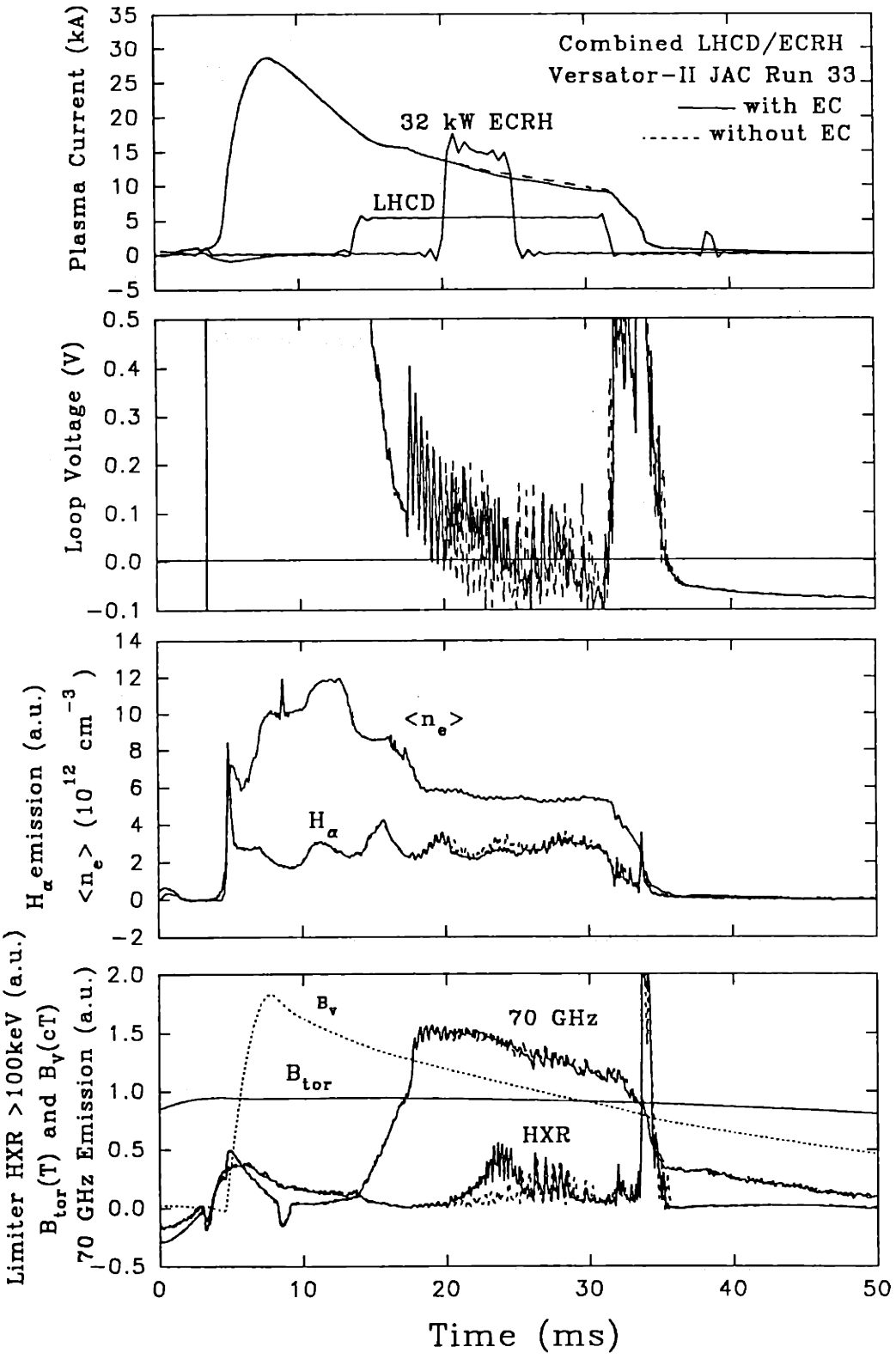
Combined LHCD/ECRH
Versator-II JAC Run 33
with EC
without EC
32 kW ECRH
LHCD
Plasma Current (kA)
Loop Voltage (V)
<n_e>
H_α
H_α emission (a.u.)
<n_e> (10^12 cm^-3)
B_v
B_tor
70 GHz
HXR
Limiter HXR >100keV (a.u.)
B_tor(T) and B_v(cT)
70 GHz Emission (a.u.)
Time (ms)

Figure 5-20

which was very quiet during the high-density discharges of section 5.3, contains oscillations from the ADI in the case of LH alone. In the case with EC injection, the amplitude of the oscillations is reduced somewhat in the first half of the EC pulse, but the DC level of the emission rises substantially. This indicates a substantial increase in the steady loss rate of fast electrons during EC wave injection. The waveforms on the 70 GHz and limiter HXR emissions during times prior to $t = 15$ ms are due to pickup from the ohmic system and can be disregarded. The plasma equilibrium quantities for these discharges are shown in Figures 5-21 and 5-22. These equilibrium quantities were affected little by the EC pulse.

Three of the parameters relating to electron confinement are plotted in Figure 5-23 as a function of dI_p/dt for a series of shots during this run. The average limiter hard X-ray emission for 20 ms$< t <$ 25 ms is plotted versus dI_p/dt. This flux is proportional to the energy-integrated flux of high-energy electrons ($E \gtrsim 100$ keV) bombarding the limiter. Because the electrons follow the magnetic flux surfaces to a good approximation, most of the fast electrons that are lost strike the limiter, and emit bremstrahlung. Thus the limiter hard X-ray flux is a good diagnostic of the fast electron loss rate. In Figure 5-23, it can be seen that as dI_p/dt decreases with EC wave injection, the limiter hard X-ray flux increases. This suggests that the decrease in current is caused by ECH-enhanced losses of the high-energy current-carrying electrons. The percent change in the bulk electron density and the H_α emission is also shown as a function of dI_p/dt. These parameters are roughly independent of dI_p/dt and the presence of EC waves, indicating that for these discharges, the EC waves do not significantly enhance or degrade the confinement of the thermal electron population. Also, this confinement is not correlated with dI_p/dt, implying that the thermal electrons are not the primary current carriers in this case.

Time traces of the soft X-ray emission for LHCD discharges with $\langle n_e \rangle = 4 \times 10^{12}$ cm^{-3}and $\Delta\phi = 180°$ are shown in Figure 5-24 with and without ECH. The LH waves were injected with $\Delta\phi = 180°$ to avoid strong excitation of the ADI. The emission increases about 15% during ECH. This is a much weaker enhancement

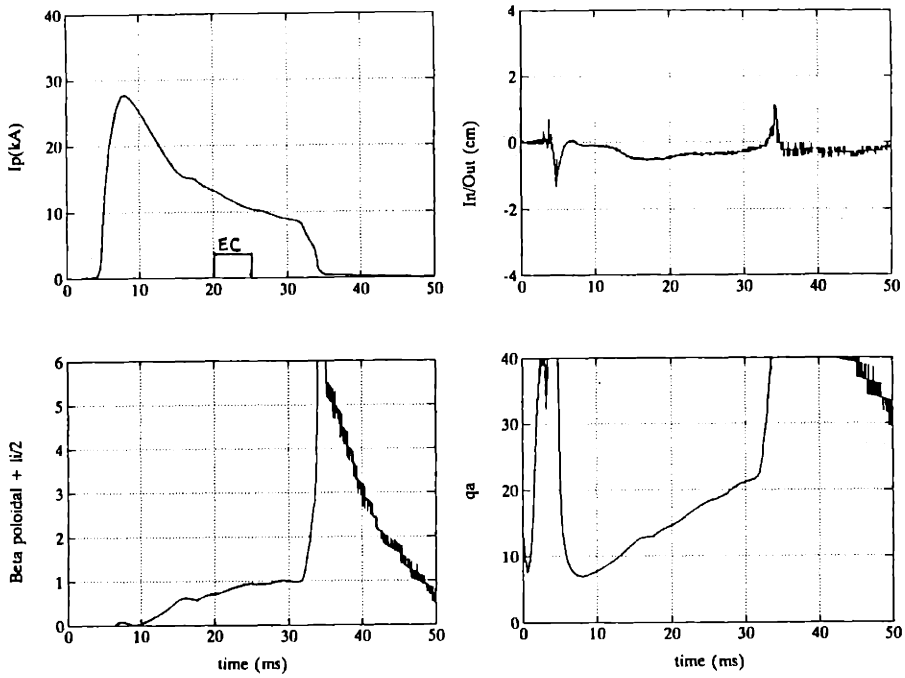

Figure 5-21 Equilibrium quantities for medium density EC-heated LHCD discharge.

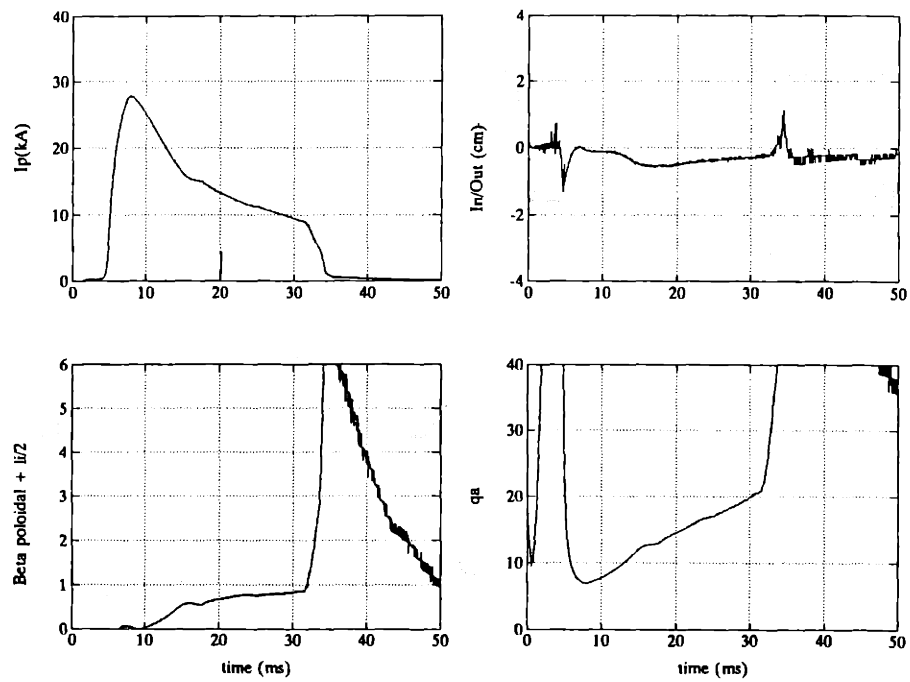

Figure 5-22 Equilibrium quantities for medium density LHCD discharge.

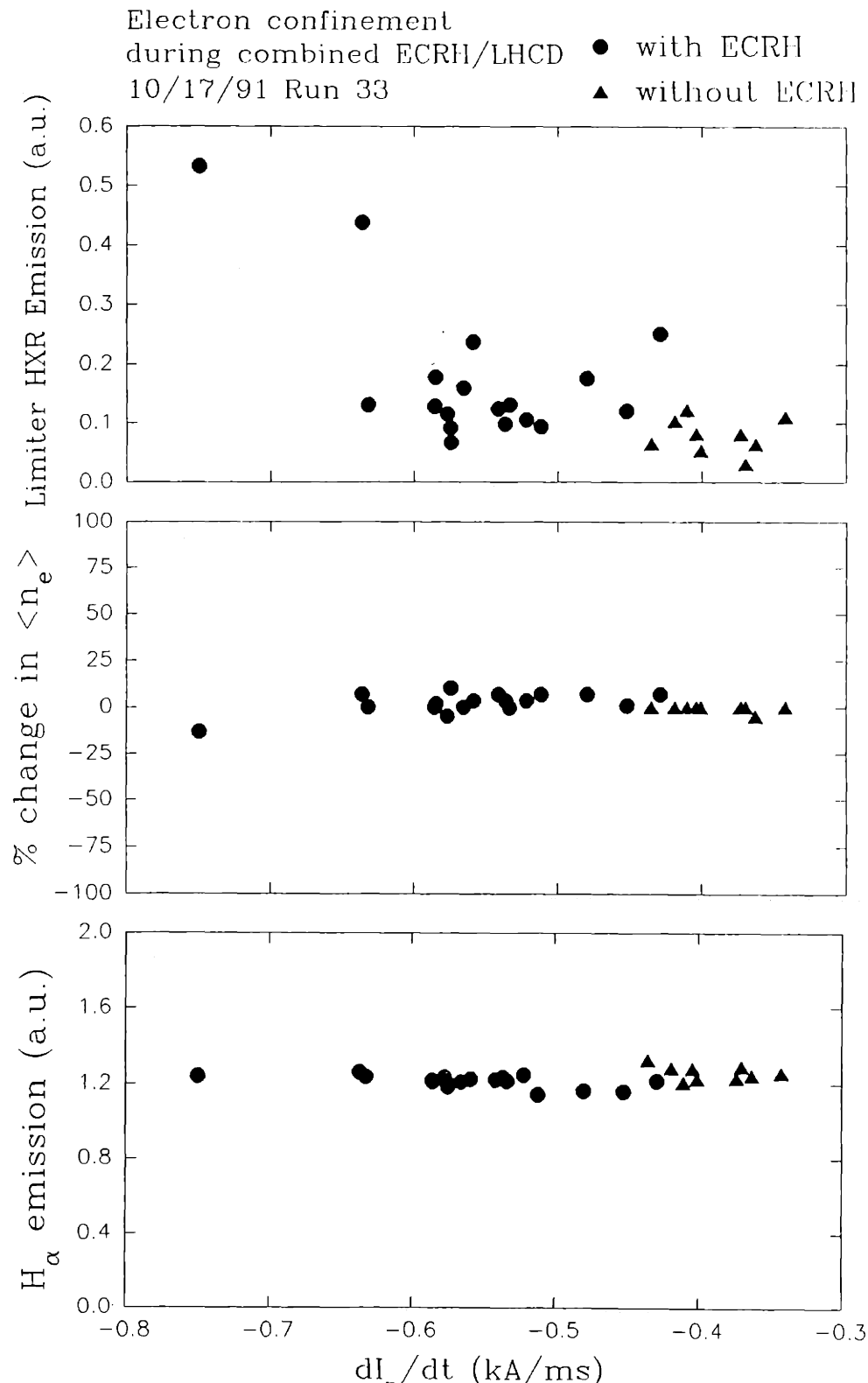

Figure 5-23 Electron confinement parameters versus dI_p/dt.

than was observed for the ECCD discharges of Chapter 4, indicating that the LH waves produce a significant fraction of the X-rays.

Magnetic fluctuations for medium density 20 kA LHCD discharges with and without EC wave injection are shown in Figures 5-25 and 5-26, respectively. Magnetic fluctuations for a 30 kA OH-sustained discharge are shown in Figure 5-27. The signal in Figure 5-27 has been scaled by two-thirds to account for the difference in I_p. It is clear from Figure 5-25 that LHCD reduces the fluctuations and ECH enhances them. The ECH enhancement is stronger than in the high-density discharges of the previous section. These magnetic fluctuations may cause the observed increased fast electron losses during ECH on Versator.

The fast electron losses and current suppression by ECH are even more severe at low density. In this case, a very hot, high-energy parallel electron tail is created by the loop voltage and LH waves. It is difficult to control the ADI with $\Delta\phi = 90°$ at this density. A series of low-density LHCD discharges with $\langle n_e \rangle \approx 2 \times 10^{12}$ cm^{-3}and $\Delta\phi = 90°$ are shown in Figure 5-28. This figure shows the plasma current, loop voltage, 70 GHz emission, and line-averaged density at $R = R_0$ versus time for the following four cases: 1) short LH alone, 2) long LH plus ECH, 3) short LH plus ECH, and 4) long LH alone. The long and short LH pulses and the ECH pulse are shown together with the plasma current. Comparing cases 2 (long LH alone) and 4 (long LH pluse ECH), a strong degradation in the driven current can be seen when the EC waves are combined with the LHCD. This is accompanied by a drop in the 70 GHz emission upon EC wave injection, an indication of a reduction in the superthermal electron population. The large features on the 70 GHz emission before $t = 12$ ms are pickup from the OH system and should be ignored. For case #4 the density behaves similarly to ECCD discharges of section 4.3: the density rapidly decreases in the first 1-3 ms of the ECH pulse, then steadily increases. Case #3, in which EC waves are injected after a short LHCD pulse, shows considerably more driven current (I_p is higher and V_{loop} is lower) than either case #1 (short LH alone) or case #2 (long LH plus ECH).

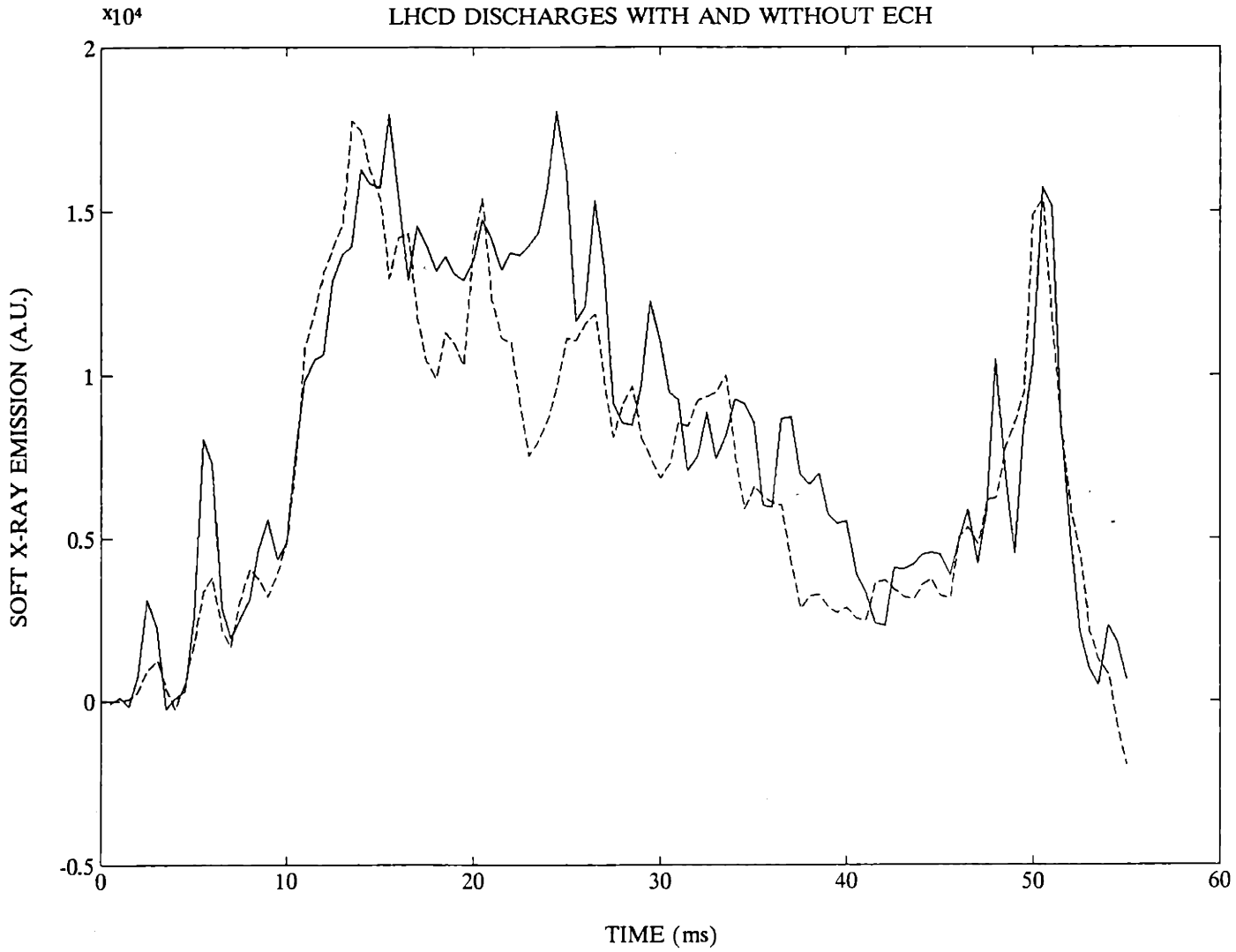

Figure 5-24 Soft X-ray emission for LHCD discharges with and without ECH.

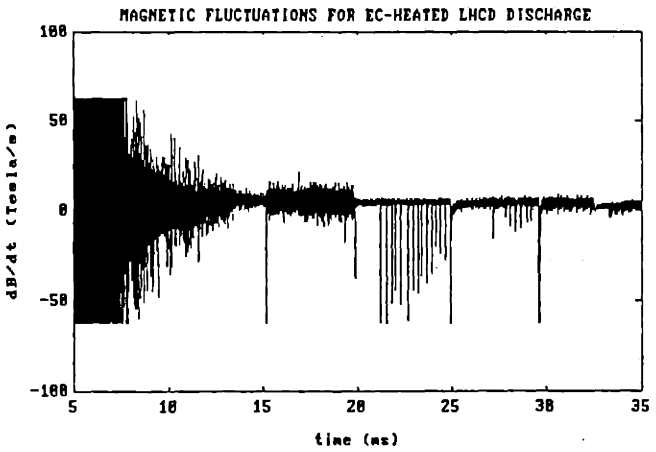

Figure 5-25

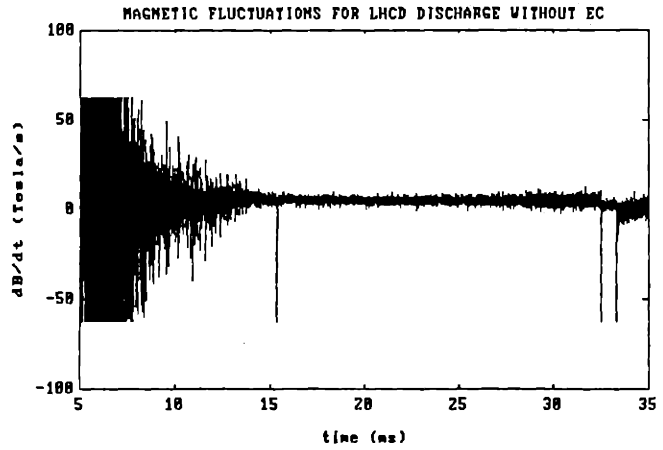

Figure 5-26

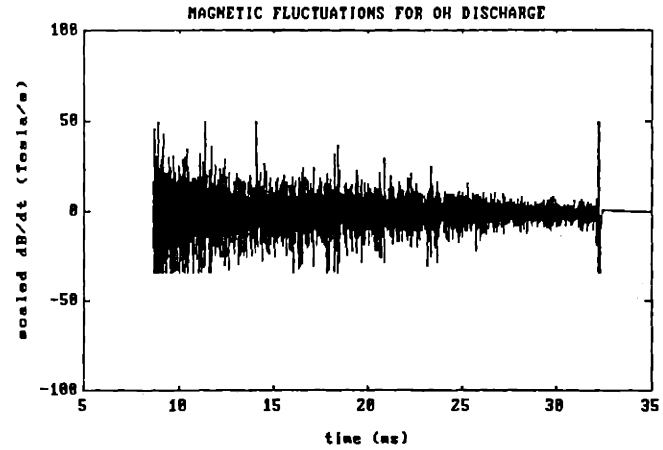

Figure 5-27

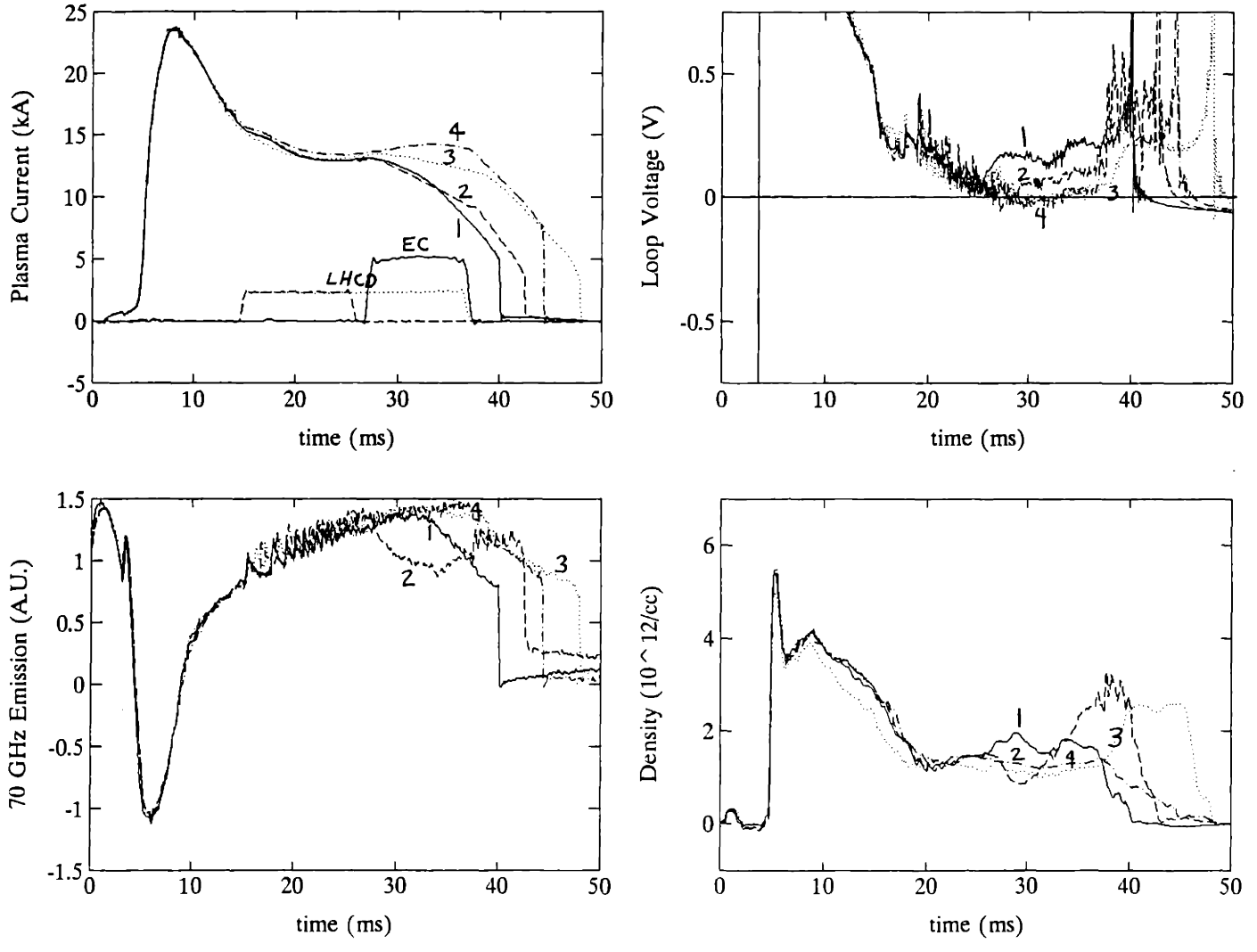

Figure 5-28 Plasma paramters for low-density LHCD discharges with/without ECH.

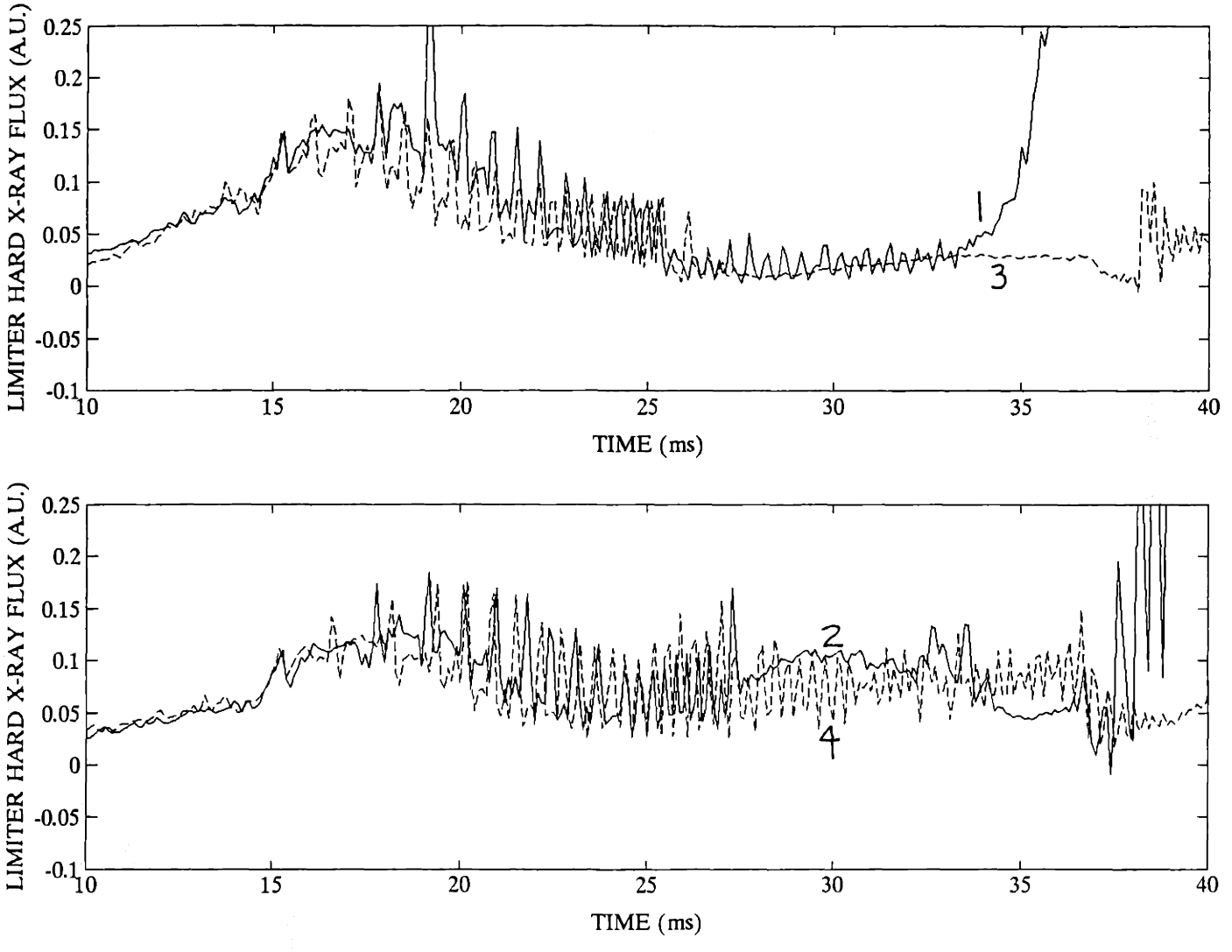

Figure 5-29 Limiter hard X-rays for the discharges of Figure 5-28.

Figure 5-29 shows the limiter hard X-ray flux for the four cases. Note that the steady flux during the ECH pulse of case #2 is considerably higher than the others, indicating that the loss rate of electrons with $E > 100$ keV is strongly enhanced during combined ECH and LHCD at low density.

5.4.2 Analysis of Efficiency Degradation

Trapping and losses of the current-carrying electrons decrease the current-drive efficiency. Trapping has usually been neglected in past theoretical treatments of combined LHCD/ECH because it is assumed that the absorbing electrons have $v_{\|} \gg v_{\perp}$. To test this assumption, the ORBIT code was used to follow the orbits of EC-heated fast electrons on Versator [80]. A typical high-energy current-carrying electron in a Versator LHCD discharge has $E_{\|} \approx 50$ keV and $E_{\perp} \ll E_{\|}$. Figure 5-30 shows the evolution of the orbit of an electron with initial energy of 50 keV and pitch=0.1 (from the LHCD) that is subsequently heated by the EC waves. It is assumed that EC waves with all possible $N_{\|}$'s are present in the region toroidally near the antenna, so that the electron is given a 50 keV "kick" in perpendicular energy at each toroidal pass, regardless of its velocity. The initial parallel velocity of the electron is opposite to the plasma current, so that it adds to the current. The initial location of the electron is at $R - R_0 = +9.5$ cm and $Z = 0$, far from the magnetic axis so as to maximize trapping effects. The drift orbit of the circulating electron is shifted toward larger major radius upon each heating event, until it is heated from 200 keV to 250 keV on the outer (high-R) part of its orbit and becomes trapped. For current-contributing electrons, the trapped "banana" orbits form on the inside of the circulating orbits, so trapping does not cause the immediate loss of the electron.

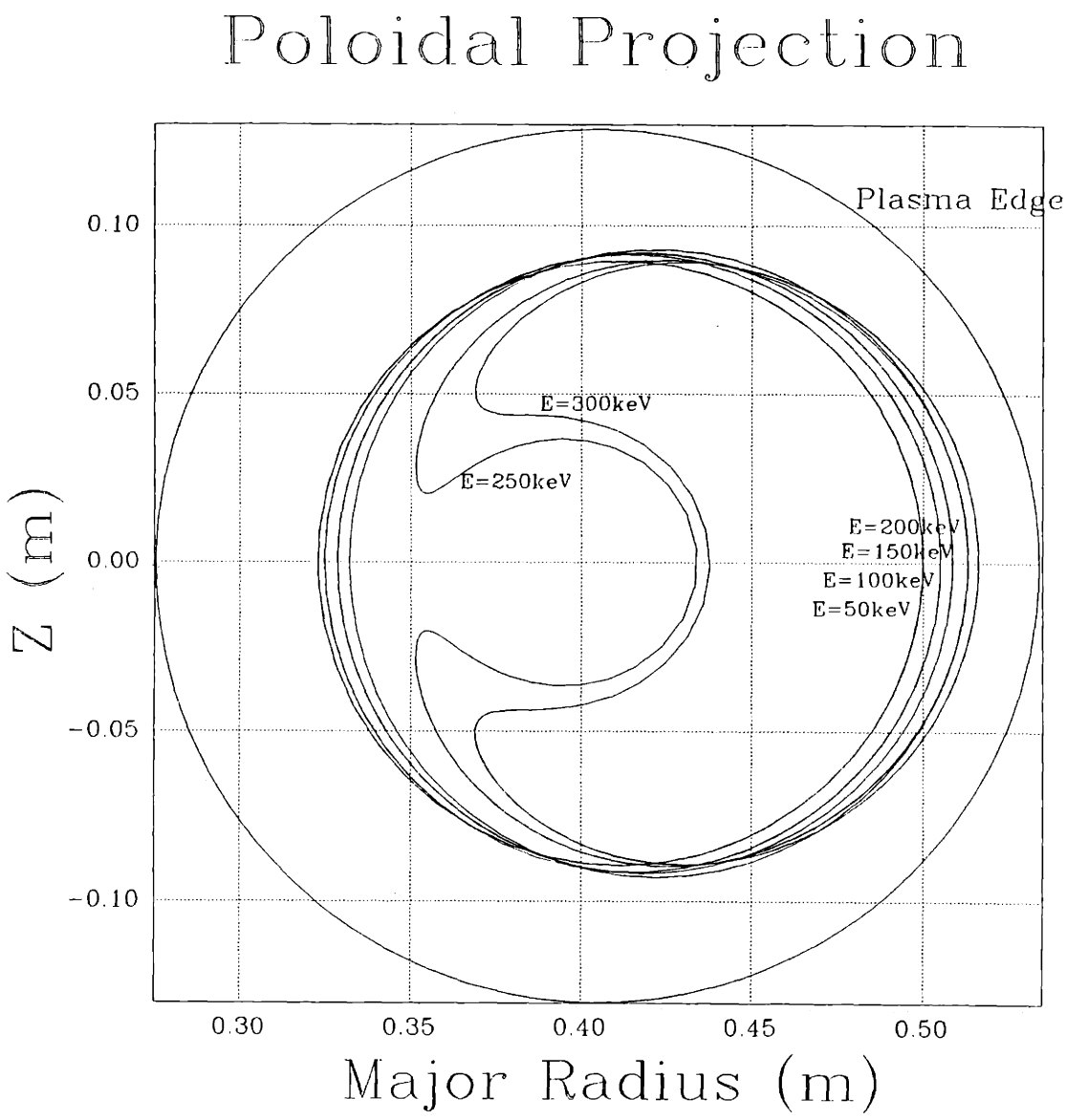

Figure 5-30

Orbits for 50keV electron born at R=0.50m, Z=0m with pitch=0.1 and $v_{||0}>0$ and then heated perpendicularly by 50keV at each toroidal pass. Electron is current-contributing, then becomes trapped. $q_a=10$, $q_0=2$, $B_{tor}=1.15T$.

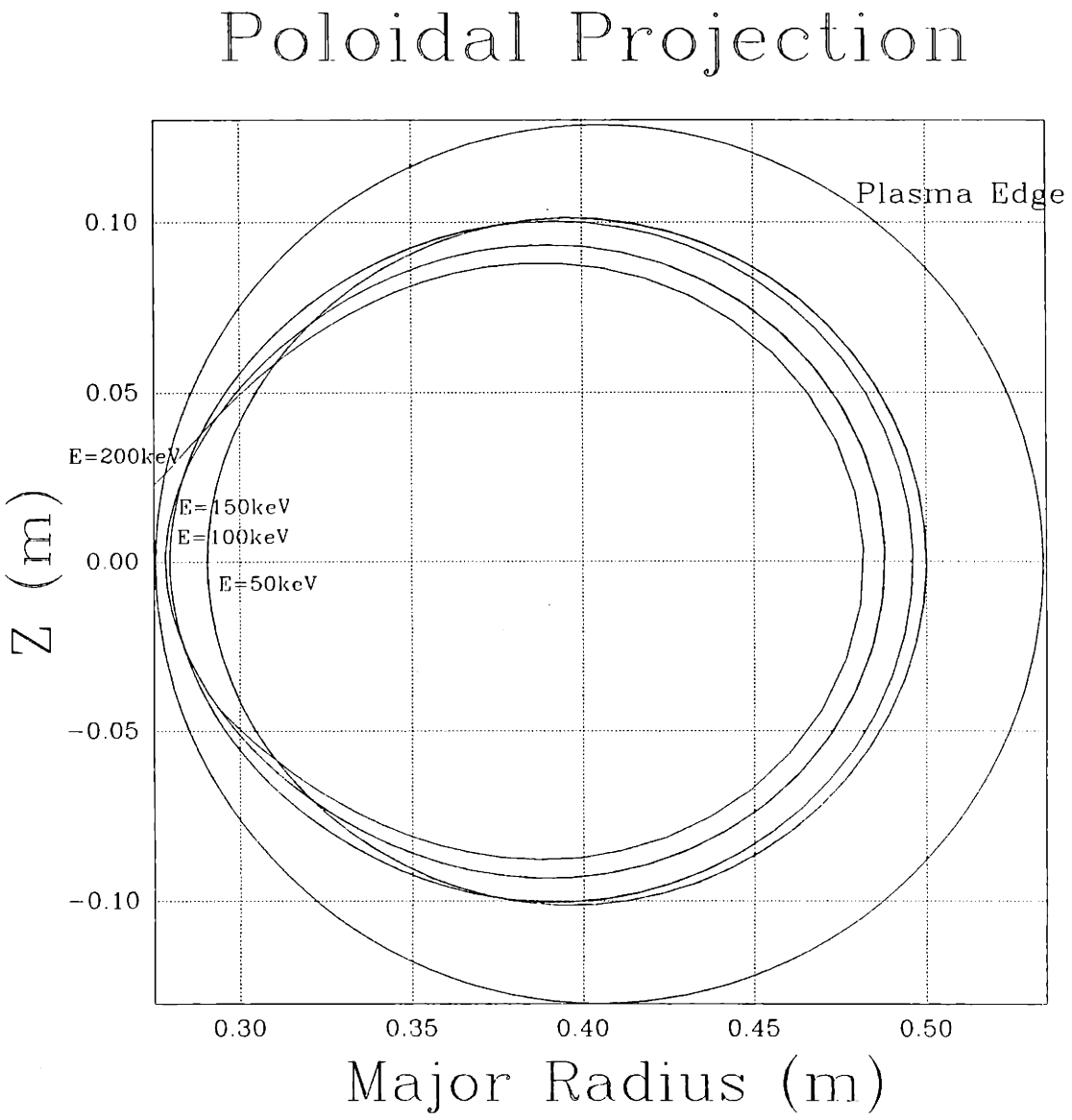

Figure 5-31

Orbits for 50keV electron born at R=0.50m, Z=0m with pitch=0.1 and $v_{||0}<0$ and then heated perpendicularly by 50keV at each toroidal pass. Electron is counter-current, then becomes trapped and lost. $q_a=10$, $q_0=2$, $B_{tor}=1.15T$.

If $v_{||}$ is reversed, the situation is as shown in Figure 5-31. The circulating orbits migrate toward smaller major radii as the electron is heated. When the electron is heated from 150 keV to 200 keV, it becomes trapped and is immediately lost. For such electrons with $v_{||}$ in the same direction as I_p (so as to subtract from the plasma current) the banana orbits form on the outside of the circulating orbits. Hence electron trapping can cause immediate loss of reverse-current electrons. The examples shown are extreme, because the electron starts near the edge and is heated very rapidly. Also, the migration of the circulating orbits is dependent on at least partial symmetry of the poloidal locations of the heating events, and these locations depend on q and the initial electron position. Hence such rapid, unidirectional migration of the circulating orbits does not occur in most cases. Also, even at the large minor radius chosen, the electron must be heated to 4-5 times its initial parallel energy to be trapped. Finally, only the reverse-current electrons can be promptly lost by trapping. Thus it appears unlikely that trapping or trapping-induced losses can significantly reduce the current-drive efficiency of EC heated LHCD discharges on Versator.

On the other hand, enhanced magnetic turbulence caused by EC heating could significantly degrade the current-drive efficiency of EC-heated LHCD discharges on Versator. The coefficient for diffusion of electrons by magnetic turbulence, given by Equation 49, is $D = v_{||}\pi q R_0 \langle (\tilde{b}_r/B_0)^2 \rangle$. It was shown in section 4.2 that at densities of $\langle n_e \rangle \approx 2 \times 10^{12}$ cm^{-3}, the EC-induced magnetic turbulence was typically $\langle (\tilde{b}_r/B_0)^2 \rangle \approx 2 \times 10^{-9}$ in the outer-third of the plasma column. For fluctuations with poloidal mode number $m = 15$, this was shown to give a confinement time of roughly 0.25 ms for electrons with $E_{||} = 80$ keV, whereas the confinement time for superthermal electrons during LHCD on Versator is 0.5-1.5 ms [58]. Thus confinement of superthermal current-carrying electrons in the outer-third of the plasma column is theoretically predicted to be degraded by $m = 15$ EC-induced magnetic turbulence at the levels observed on Versator, and confinement in the intermediate-third could be degraded as well. Also, because the spatial diffusion coefficient is

proportional to $v_{\|}$, the confinement time is inversely proportional to $v_{\|}$. Thus at low densities, when the Dreicer field is low and the population of superthermal electrons during LHCD is large and extends to high energy ($\sim$ 300 keV), these fast current-carrying electrons are expected to be rapidly lost due to EC-induced magnetic turbulence. This is compounded by the fact that the observed fluctuation levels are higher at lower density. At the higher densities of section 5.3, the current carried by electrons with $E_{\|} > 100$ keV is much smaller. Hence the degradation in I_p due to magnetic turbulence is predicted to be much smaller, and the observed limiter X-ray flux with $E \gtrsim 100$ keV is greatly reduced.

5.5 THE ANOMALOUS DOPPLER INSTABILITY

The anomalous Doppler instability (ADI) has been observed in tokamaks since early experiments were performed [108]. It is sometimes refered to as the Parail-Pogutse instability after those who first described it theoretically [109, 110]. The ADI is driven by the free energy present in an anisotropic electron distribution function. In a tokamak, the instability is caused by the formation of a high-energy tail in the electron distribution function in the parallel direction, caused typically by a DC electric field or by LHCD [111], or a combination thereof. A qualitative picture of f_e before and after the onset of the instability is shown in Figure 5-32. The ADI near-elastically diffuses electrons along near-constant energy contours toward higher $v_{\perp}$ and lower $v_{\|}$. After this diffusion, f_e is subject to the "bump-on-tail" instability (driven by $vdf/dv > 0$), which modifies f_e toward the state shown in Figure 5-31. Thus the interplay between these two instabilities tends to restrict the parallel tail and restore isotropy to f_e. The theory of the ADI is described in Appendix F, where it is shown that the threshold for instability is given by:

$$v_b > 3\left(\frac{\omega_{ce}}{\omega_{pe}}\right)^{3/2} v_{cr} \tag{58}$$

where $v_b = eE_0t/m$ is the beam velocity. Note $v_b \propto B^{3/2}n_e^{1/4}$, so that Equation 58 implies that it is harder to excite the ADI in regions of high magnetic field and, to a much weaker degree, high density. Thus the ADI is more stable when the plasma is located towards the inside of the vacuum chamber ($R < R_0$), where ω_{ce} is largest.

Under certain conditions, strong stabilization of the ADI by ECH was observed on Versator, as shown in Figure 5-33. These discharges are started by moderate ohmic heating power, which brings the plasma current rapidly up to 8 kA. The vertical equilibrium field coil is fired at about $t = 6.5$ ms, which induces an additional loop voltage, causing the plasma current to rise to 9 kA. At $t = 9$ ms, 45 kW of lower-hybrid waves are injected for 21 ms, causing the plasma current to rise to 14 kA and V_{loop} to drop rapidly. At $t = 12.5$ ms, the onset of the ADI is evident for both discharges in Figure 5-33. For the discharge without ECH, the instability quickly reaches a large, steady-state amplitude with the spikes in V_{loop} occuring every 0.6 ms or so with an amplitude of 0.3 V. This is accompanied by a rapid step-like decline in the plasma current from 14 kA to 7 kA in a period of 12 ms, followed by collapse of the discharge at $t = 25$ ms. The line-averaged electron density peaks at 9×10^{12} cm^{-3} during the peak in OH power input at $t \approx 6$ ms, then falls rapidly to about 4×10^{12} cm^{-3}. This fall is arrested by the lower-hybrid waves at $t = 9$ ms and the density rises to 5×10^{12} cm^{-3}. The density then begins to fall again, and at $t = 12.5$ ms, it has fallen to 4×10^{12} cm^{-3}, at which point the ADI turns on. As the ADI quickly reaches a large steady state amplitude, the density maintains a steady rate of fall, accompanied by bursts that are in phase with bursts in V_{loop}.

For the EC-heated discharge, 40 kW at 28 GHz is radiated into the plasma during the time 13.5 ms$< t <$21.5 ms from the high-field side with primarily O-mode polarization and a launch angle of +60°. As is clear from Figure 5-33, the

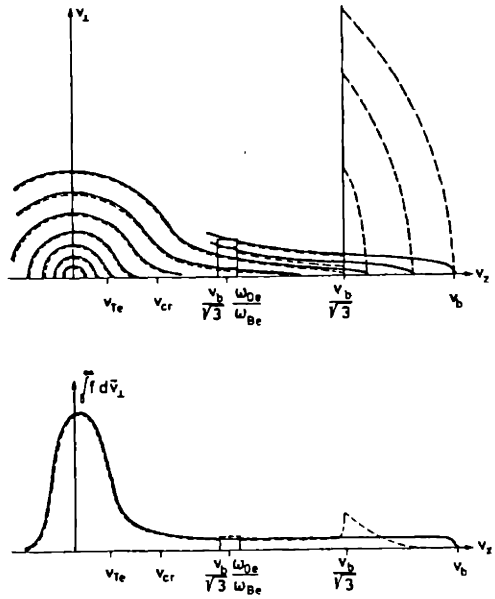

Change in the electron distribution function as a result of instability due to the anomalous Doppler effect:
—— – *value of f_e before instability;*
- - - - - – *value of f_e after instability.*

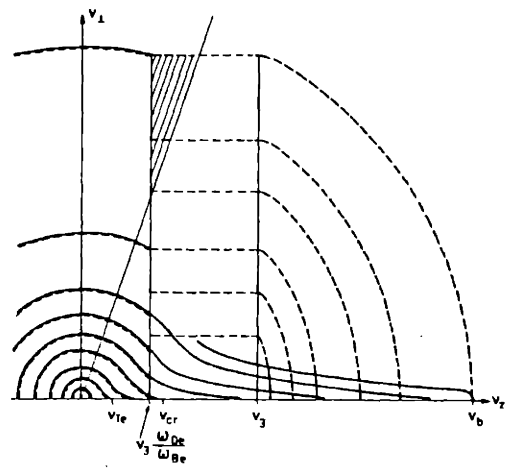

Electron distribution function after both stages of instability (dotted lines). The region of locally trapped fast electrons is hatched.

Figure 5-32 from reference [110].

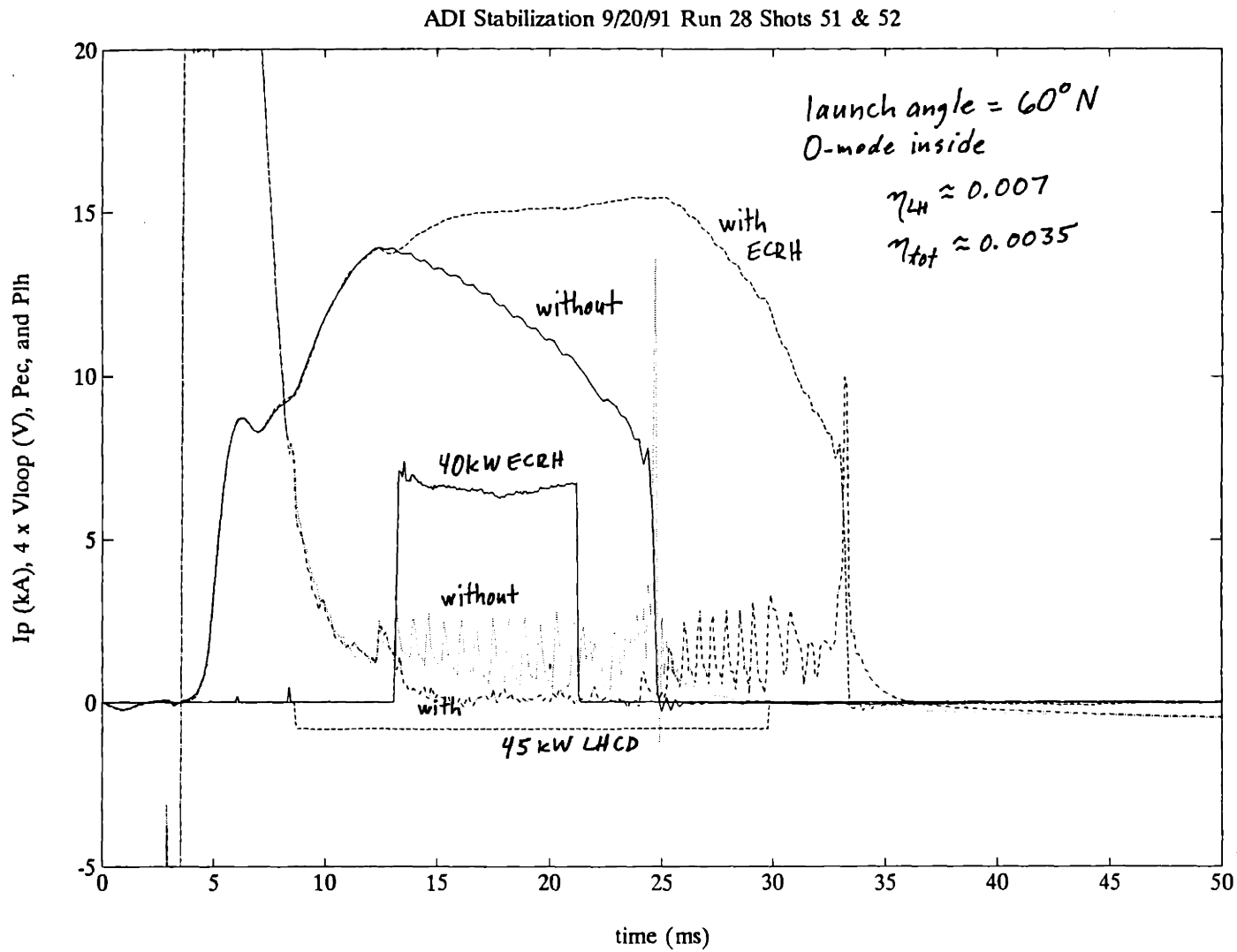

Figure 5-33 Stabilization of the ADI by EC waves.

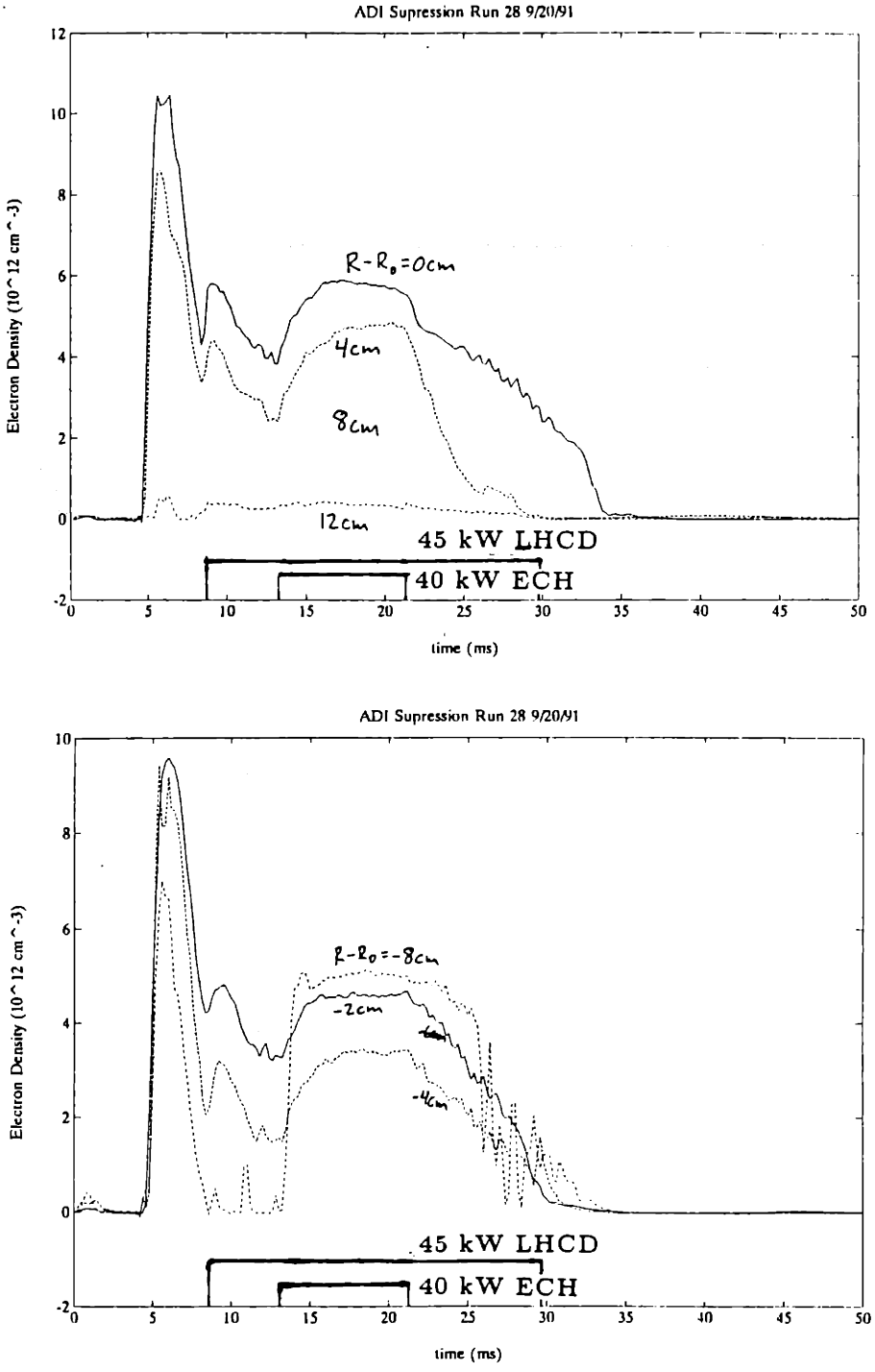

Figure 5-34 Density profile broadening during ADI stabilization.

injected EC waves strongly stabilize the anomalous Doppler instability. Upon EC wave injection, the decay in I_p is arrested and I_p ramps up to 15 kA. The spikes in V_{loop}, limiter hard X-rays, and $\langle n_e \rangle$ are immediately supressed, and no evidence remains of the ADI. The loop voltage drops rapidly to zero (within 2 ms) and remains zero throughout the ECH pulse. The central electron density rises from 3.5×10^{12} cm^{-3} to 5.5×10^{12} cm^{-3} during the first 2 ms of the ECH pulse and remains at that value for the duration of the ECH pulse. As is shown in Figure 5-34, the density profile significantly broadens during this time, with the largest density increases (as a percentage of initial density) at $R - R_0 = \pm 8$ cm. The density signal at $R - R_0 = -8$ cm may not be accurate, due to possible "fringe skipping" by the interferometer. As can be seen from Figure 5-34. the ADI remains stable for about 3-4 ms after ECH turnoff. During this time, the density is steadily falling, and equals 4×10^{12} when the ADI turns on again and I_p starts rapidly falling. The current drive figure of merit for the stabilized discharges is $\eta = \langle n_e \rangle I_p R_0 / P_{rf} = 0.008$ when only the lower-hybrid wave power is included in the calculation and 0.004 when both LH and EC wave power is included. Thus for these discharges, the ECH stabilizes the ADI but does not enhance the overall current-drive efficiency beyond $\eta = 0.01$, which is the typical best value achievable on Versator-II. This is shown in Figure 5-35, where the shaded region indicates the best η's typically achieved on Versator. It is shown that the the efficiency of ADI-stabilized discharges is weakly dependent on launch angle, with better efficiencies achieved at launch angles far from normal to $\mathbf{B}$, especially in the direction of I_p (negative launch angles in Figure 5-35). Similar dependence on launch angle is observed for the density rise during ECH, with the highest rises in central $\langle n_e \rangle$ ($\approx 5 \times 10^{12}$ cm^{-3}) occuring at $\alpha = -70°$.

Data from the radial HXR detector array is shown in Figures 5-36, 5-37, and 5-38. For discharges with ECH, the hard X-ray intensity is seen to peak sharply at $R = R_0$, and a bit less sharply after the bulk electron density profile is divided out. The profile is asymmetric, with emission at $R - R_0 = +4$ cm double that at -4 cm but emission at $+8$ cm about ten times smaller than at -8 cm. The hard X-ray

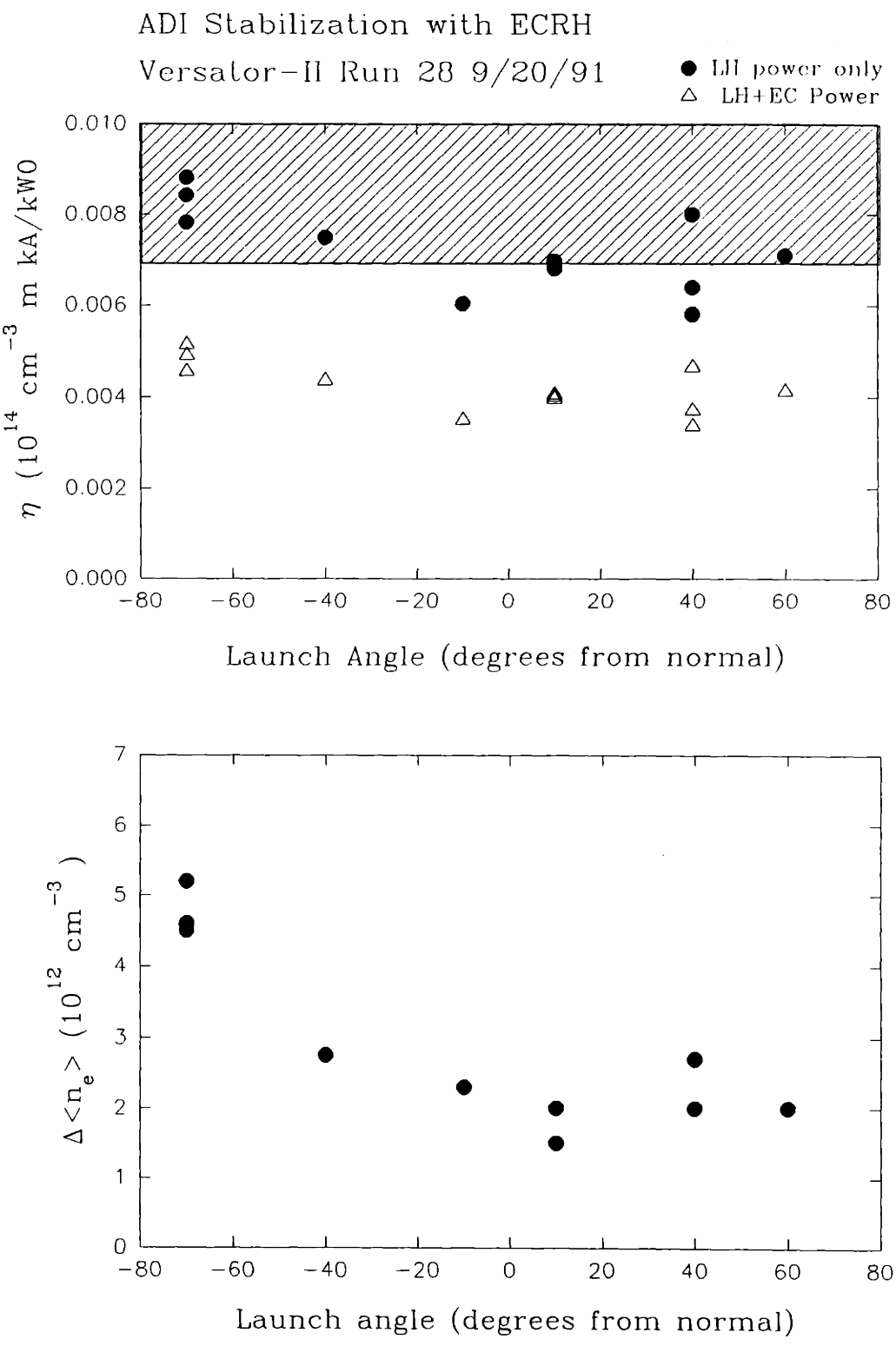
ADI Stabilization with ECRH
Versator-II Run 28 9/20/91
● LH power only
△ LH+EC Power
η (10^14 cm^-3 m kA/kW0
0.010
0.008
0.006
0.004
0.002
0.000
-80 -60 -40 -20 0 20 40 60 80
Launch Angle (degrees from normal)
Δ<n_e> (10^12 cm^-3)
7
6
5
4
3
2
1
0
-80 -60 -40 -20 0 20 40 60 80
Launch angle (degrees from normal)

Figure 5-35

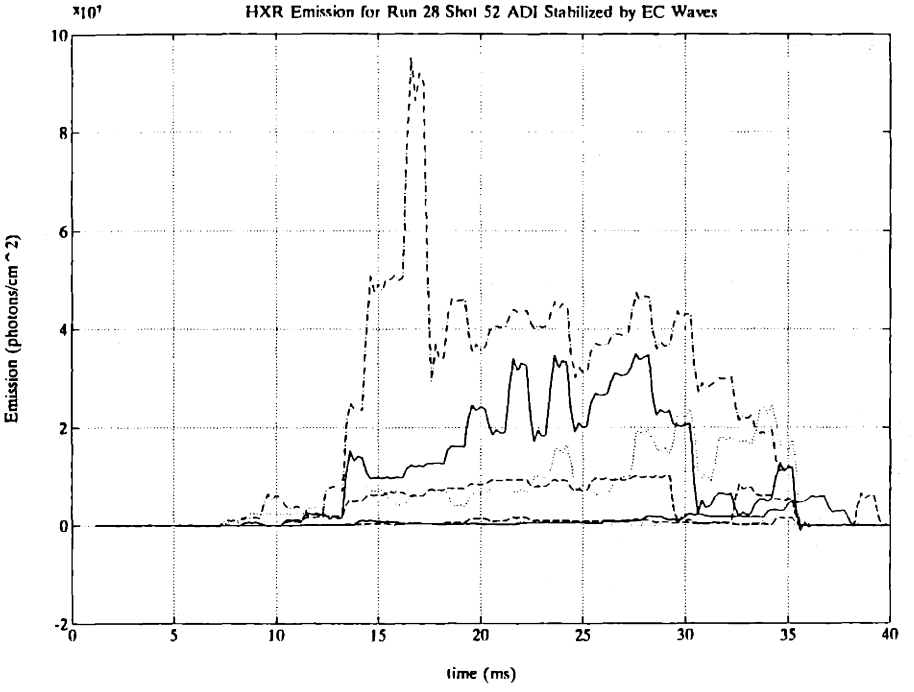

Figure 5-36 Hard X-rays for ADI-stable EC/LHCD discharge.

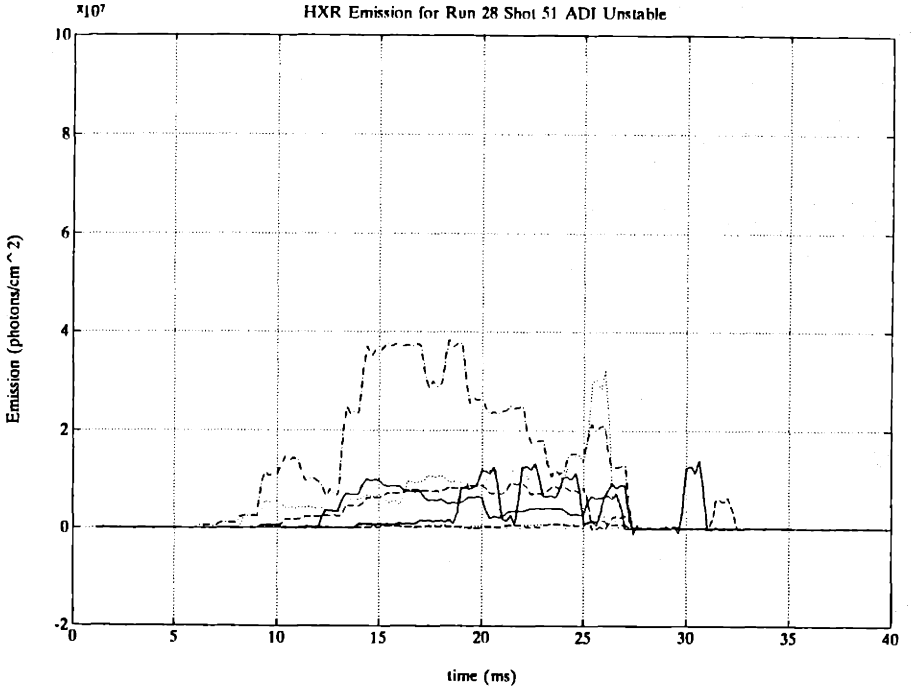

Figure 5-37 Hard X-rays for ADI-ustable LHCD discharge.

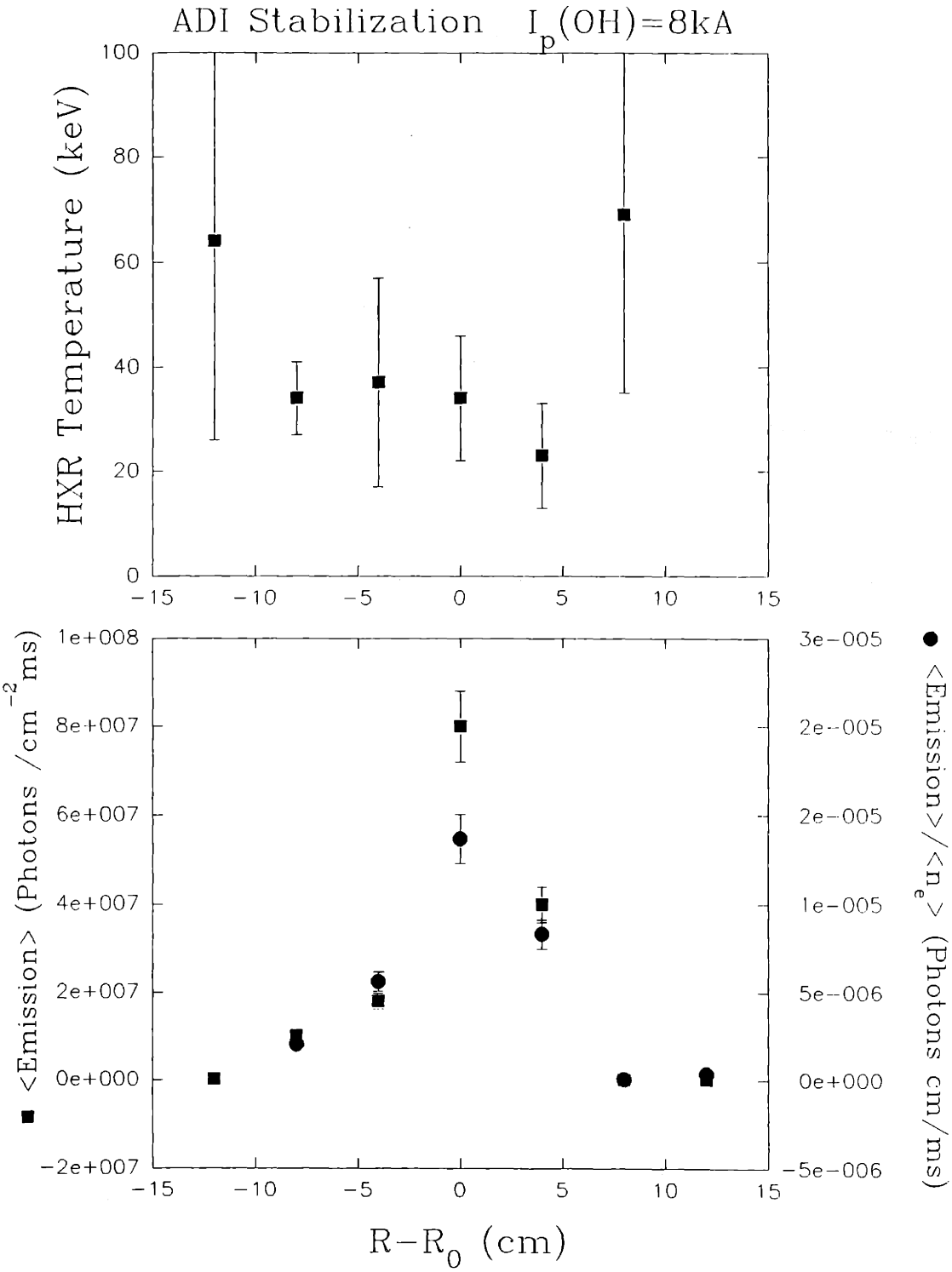

Figure 5-38 Hard X-ray temperature and emission profiles for ADI stabilization.

temperature profile is asymmetric, being hotter toward the inside ($R \leq R_0$). The temperature is hottest near the plasma edge at $R - R_0 = \pm 12$ cm, but the error bars are large at these radii due to the small number of counts available.

The equilibrium quantities for the stable and unstable discharges are shown in Figures 5-39 and 5-40. The in/out position of the plasma is greater for the stable discharge, but $\beta + \ell_i/2$ is lower. This is because the increase in I_p due to ADI stabilization is greater than the increase in plasma pressure (if such an increase in plasma pressure occurs at all).

The effects of changing the vertical equilibrium field on the ADI are shown in Figure 5-41. For discharges with 21 kW LHCD and 32 kW of ECH, the ADI is stabilized only at the higher B_v, which pulls the plasma inward to smaller major radius. This is consistent with Equation 58, which shows that the ADI is more stable at higher magnetic field (smaller major radius).

Three mechanisms exist that could explain the stabilization of the ADI by the EC waves: 1) perpendicular heating of the superthermal electron tail; 2) raising of the plasma density by interaction with the thermal electrons, thereby increasing the Dreicer field and decreasing the superthermal tail population; 3) enhancement of the radial loss rate of the superthermal electrons. All three of these mechanisms stabilize the ADI by reducing the anisotropy of the superthermal electron distribution function. There is no evidence of perpendicular heating of the tail electrons by ECH on Versator for the toroidal field considered, although this possibility cannot be ruled out. There is, however, evidence of enhanced losses of the superthermal electrons, and the bulk density rises. The increase in the Dreicer field and/or the enhanced losses may therefore be the most likely stabilization mechanisms.

5.6 CONCLUSIONS

Quasilinear theory predicts a current-drive synergism between LH and EC

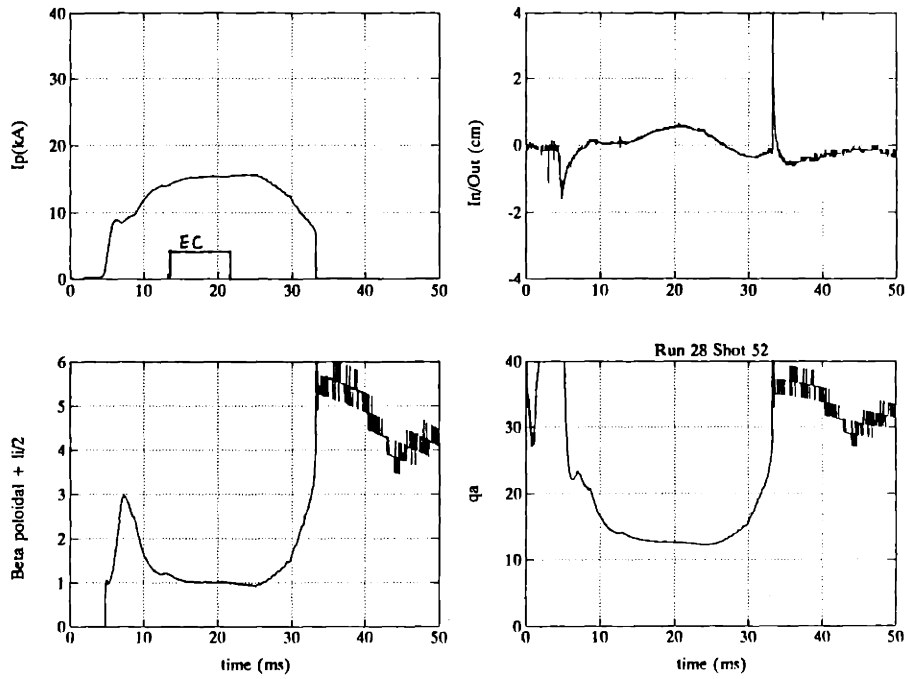

Figure 5-39 Equilibrium quantities for ADI-stable EC/LHCD discharge.

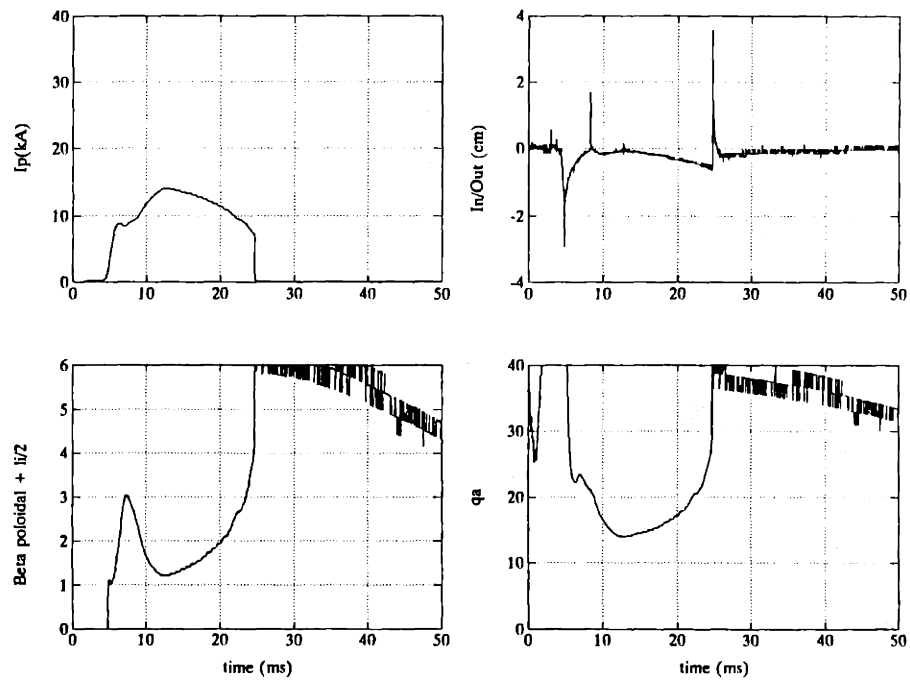

Figure 5-40 Equilibrium quantities for ADI-unstable LHCD discharge.

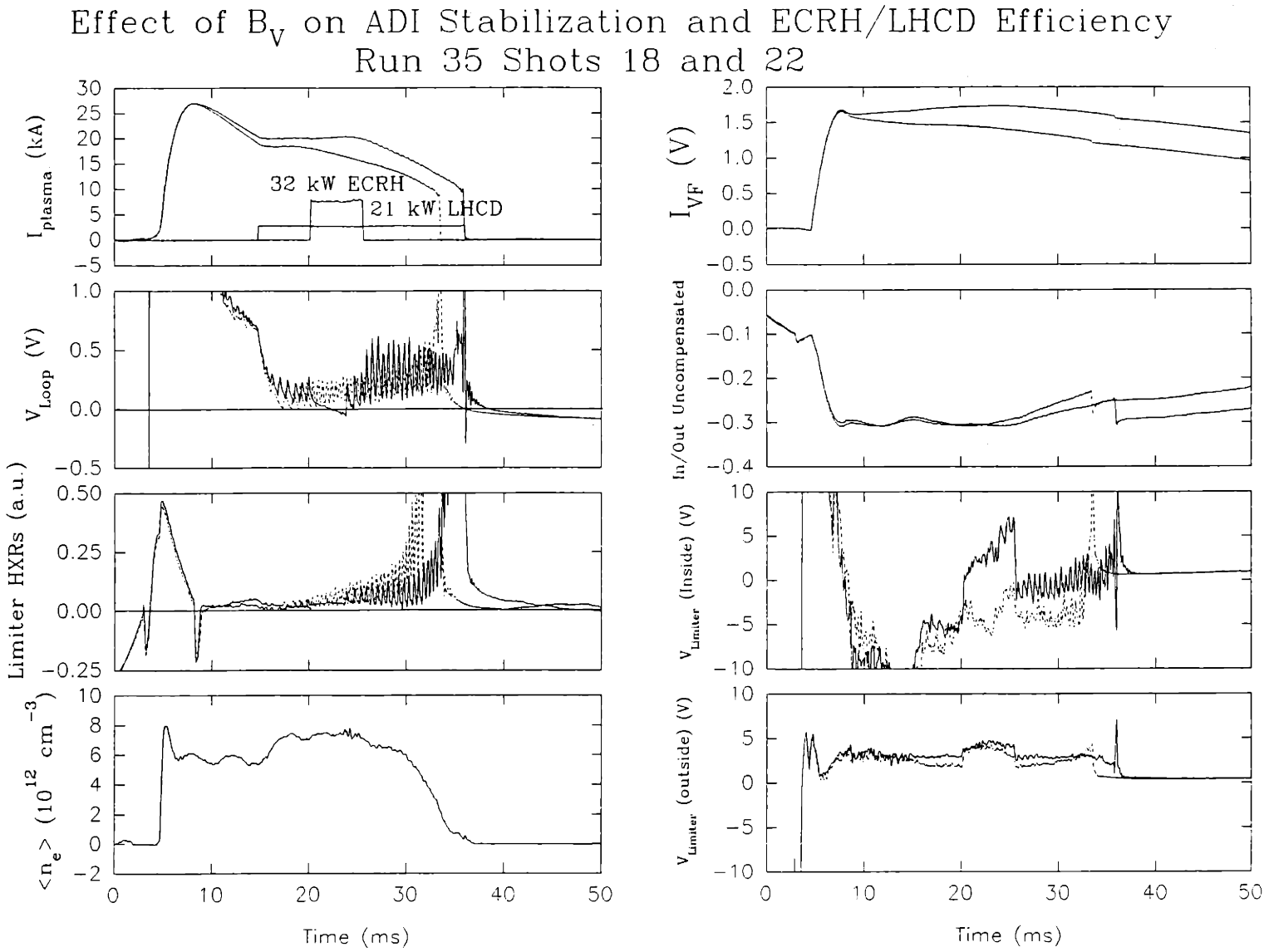

Figure 5-41 Effect of vertical field on ADI stabilization.

waves. This is caused by the lower collisionality of the EC-heated tail electrons. Computational modeling suggests that the combined current-drive efficiency of EC and LH waves can exceed the efficiency of either type of waves alone.

On Versator this synergism is not seen. For EC-heating of LHCD transformer-less startup plasmas, an enhancement of the plasma current ramp-up rate is observed, confirming the results of [49], but the overall current-drive efficiency is still far below the best achievable LHCD efficiency on Versator. This improved ramp-up rate could be a result of changes in the plasma caused by the EC waves that make it a more suitable target for the LH waves. For example, the plasma density is raised, the population of mildly superthermal electrons is enhanced, and the plasma column is more centered in the vacuum chamber as a result of the ECH. These changes may improve the coupling between the LH waves and the target electrons and decrease radial loss of the current-carriers.

At high plasma density ($\langle n_e \rangle = 8 \times 10^{12}$) a small increase in driven current is observed with the injection of EC waves into LHCD discharges. A large increase in the X-ray emission is observed from the plasma center for $\omega_{ce}/\omega = 1.15$, but not at lower fields. The increased X-ray flux is mostly low energy, with $E \lesssim 35$ keV. ECH-induced magnetic turbulence levels are small at this density, and the enhanced radial losses of the superthermal electrons due to this turbulence are predicted to be comparable to or less than the losses caused by other mechanisms on Versator.

As the density is lowered, the EC-induced magnetic turbulence increases in magnitude, the superthermal tail during LHCD increases in average $v_{\|}$, the losses of superthermal electrons become more severe, and the incremental current driven by the EC waves goes from slightly positive to negative. Reducing the toroidal magnetic field also tends to increase the losses of the superthermals. The losses of high-energy superthermals decreases and the EC/LH current-drive efficiency increases when the LH antenna waveguide phasing is switched from $\Delta\phi = 90°$ to $\Delta\phi = 180°$. It is known that, on Versator, the average $v_{\|}$ of the superthermal current-carrying

population is significantly reduced for LHCD discharges with $\Delta\phi = 180°$. The observed losses and reduction in the current-drive efficiency cannot be explained by trapping or trapping-induced losses. The observations are consistent with estimates of the loss rates of the superthermal electrons caused by EC-induced magnetic turbulence.

The anomalous Doppler instability (ADI) during LHCD is stabilized by injection of EC waves under some conditions. The ADI is stabilized by reducing the anisotropy of the superthermal electron distribution function. The EC waves may accomplish this by perpendicularly heating the LHCD tail, by increasing the bulk density (possibly via the electron Bernstein wave) and thereby increasing the Dreicer field, or by enhancing the loss of the high-energy part of the LHCD tail by ECH-induced turbulence. There is no evidence of perpendicular heating of the tail electrons by ECH on Versator for the toroidal field considered, although this possibility cannot be ruled out. There is, however, evidence of enhanced losses of the superthermal electrons, and the bulk density rises. The increase in the Dreicer field and/or the enhanced losses may therefore be the most likely stabilization mechanisms.

CHAPTER 6
CONCLUSIONS

A two-parallel-temperature tail has been observed during LHCD discharges on the Versator-II tokamak. This measurement was made using an electron cyclotron transmission (ECT) diagnostic [58], which was improved significantly for these measurements [60]. The cold tail extends to parallel energy $E_{||} \approx 4.5$ keV with parallel temperature $T_{tail}^{cold} \approx 1.5$ keV, and the hot tail extends to $E_{||} > 150$ keV with $T_{tail}^{hot} > 40$ keV. Code modeling with CQL3D suggests that the cold tail is initiated by high-$N_{||}$, low-power waves from the forward sidelobe of the antenna spectrum with $10 < N_{||} < 15$. The main power lobe, which is launched with $1 < N_{||} < 5$, creates and sustains the hot tail and helps to sustain the cold tail, via $N_{||}$-upshift to $7 \lesssim N_{||} \lesssim 10$. The reverse power lobe with $-10 < N_{||} < -5$ creates most of the reverse tail, part of which is scattered by ions, adding to the cold forward tail and enhancing the net plasma current. In agreement with earlier code modeling [72], the CQL3D code predicts that the $N_{||}$-upshift of the main power lobe is insufficient to bridge the spectral gap during LHCD on Versator. Inclusion of the sidelobes in the model is essential for correctly predicting the experimentally observed plasma current. A similar explanation may apply to LHCD results on other small tokamaks [33, 65, 66]. In addition, this may help to explain the increase in current-drive efficiency with increase in volume-averaged electron temperature observed on the JT-60 tokamak [75].

Radial profiles of X-ray emission in the energy range 20 keV $\lesssim E \lesssim$ 500 keV during LHCD are consistent with the ECT measurements. They show the emission to be peaked on axis, but with a large off-axis peak 8 cm toward the high-field side. This peak may caused by a hot electron ring created near the mouth of the LH antenna.

During plasma formation experiments using EC waves, radial density profiles have been obtained on a shot-to-shot basis and show that the plasma is initiated at the EC layer and then moves toward the upper-hybrid (UH) layer. This is consistent with theory, which predicts that after initiation the plasma is heated by damping of electron Berstein (EB) waves. These waves result from both linear mode conversion and nonlinear parametric decay near the UH layer. The 300 MHz ion decay-wave is observed during plasma formation, indicating that parametric decay is occuring. The confinement of EC-formed plasmas is found to agree with simple theory [30] [83], which predicts that the plasma flows outward in major radius at a reduced $\mathbf{E} \times \mathbf{B}$ velocity. This is supported by the density profile measurements, which show negligible density at major radii inside the EC layer. Up to ~1 kA of toroidal current is observed in these plasmas. This current is a consequence of the thermal electron confinement, which is asymmetric [30, 82]. Soft X-rays with energies up to 6 keV are observed with $T_{sxr} \lesssim 1.75$ keV, indicating the presence of a superthermal electron population.

Electron-cyclotron current drive (ECCD) is observed at densities below $\langle n_e \rangle = 3 \times 10^{12}$ cm^{-3}. The efficiency $\eta \equiv \langle n_e \rangle I_p R_0 / P_{rf} = 0.003$ is 30%-40% of the maximum achievable LHCD efficiency on Versator. The plasma X-ray emission is strongly enhanced only at energies $E \lesssim 30$ keV, with the strongest enhancement in the range 1 keV $\lesssim E \lesssim$ 10 keV. This indicates that the EC-driven current is carried primarily by electrons with $E \lesssim 10$ keV. According to wave damping theory these electrons are heated by the EC waves within ~2-4 cm of the EC layer. The highest ECCD efficiency is achieved when the EC layer is located 5–6 cm to the high-field side of the plasma axis. This implies that during efficient ECCD discharges, electrons are EC-heated on the high-field side into the energy range of a few keV. No current drive is observed when the EC layer is located on the low-field side ($R_{EC} \geq R_0$). The efficiency is independent of launch angle and launched polarization. Well-centered or inside target equilibria yield better ECCD than do target discharges with outside equilibria.

The EC waves enhance plasma magnetic turbulence in the frequency range 50 kHz $\lesssim f \lesssim$ 400 kHz by up to an order of magnitude. Assuming $m = 15$, it is estimated that this reduces the confinement time of electrons with $E_{\|} = 80$ keV from $\tau_e = 0.5$-1.5 ms to $\tau_e < 0.25$ ms in the outer third of the plasma and $\tau_e < 1.6$ ms in the inner third, while the effect on electrons with 1 keV$\approx E_{\|} \lesssim$10 keV is small. Thus the EC-enhanced magnetic turbulence does not affect the low-energy superthermal electrons suspected of carrying the EC-driven current. The time-of-arrival of the turbulence to probes at the plasma boundary is dependent on the location of the EC layer, with the signal arriving sooner when the EC and UH layers are closer to the probes. This suggests that the turbulence is not driven at the plasma edge. Plasma electrostatic turbulence is increased by the EC waves to a lesser degree (up to a factor of four). The magnetic turbulence is reduced by LHCD. This is consistent with past measurements showing that LHCD improves the thermal electron particle confinement on Versator. The thermal electron particle confinement is observed to degrade during ECCD.

Transformerless startup of the tokamak plasma has been achieved by launching LH waves into EC-formed plasmas. These plasmas have $\beta_p + \ell_i/2 \gtrsim 4$, and the peaks in their density and X-ray profiles are near $R - R_0 = +8$ cm. When a second EC pulse is launched into these plasmas, dI_p/dt doubles and the loop voltage is reduced to near zero. However, the overall efficiency of the combined EC/LH current drive is still far below the best LHCD efficiency achievable on Versator. The second EC pulse causes the plasma density and fast-electron channel to move to the center of the vacuum chamber at $R = R_0$ by building the density at $R \lesssim R_0$. This may cause the increase in dI_p/dt by providing a better target plasma for the LH waves.

Quasilinear theory predicts a current-drive synergism between EC and LH waves, but this is not observed experimentally on Versator. This is at least in part because the EC waves enhance the losses of the fast, current-carrying electrons generated by the LH waves in the range $E_{\|} \lesssim 150$ keV. This is indicated by increased X-ray flux from the limiter during EC wave injection. These losses may be caused

by the observed EC-enhanced magnetic turbulence. The enhanced turbulence and losses decrease with increasing plasma density, and thus may not degrade EC/LH current-drive efficiency in a high-density, reactor-grade plasma.

APPENDIX A
DISPERSION OF LH AND EC WAVES

A.1 Lower-Hybrid Waves

First, we analyze the case of lower-hybrid waves. Applying the lower-hybrid approximating condition, $\omega_{ci}^2 \ll \omega^2 \ll \omega_{ce}^2$, yields the following for the dielectric tensor elements:

$$K_{xx} \approx 1 + \frac{\omega_{pe}^2}{\omega_{ce}^2} - \frac{\omega_{pi}^2}{\omega^2} \tag{59}$$

$$K_{xy} \approx \frac{-i\omega_{pe}^2}{\omega\omega_{ce}} \tag{60}$$

$$K_{zz} \approx 1 - \frac{\omega_{pe}^2}{\omega^2} \tag{61}$$

The further approximation that $|K_{zz}| \gg K_{xx}$ is made. This is valid for waves in the lower-hybrid range of frequencies (LHRF) everywhere in the plasma except at the very edge. This yields the following dispersion relation [112]:

$$\frac{2K_{xx}}{-K_{zz}} N_\perp^2 = N_\parallel^2 - \left(K_{xx} + \frac{K_{xy}^2}{K_{zz}} \right)$$

$$\pm \sqrt{\left[N_\parallel^2 - (\sqrt{K}_{xx} + \sqrt{K_{xy}^2/K_{zz}})^2 \right] \left[N_\parallel^2 - (\sqrt{K}_{xx} - \sqrt{K_{xy}^2/K_{zz}})^2 \right]} \tag{62}$$

The two roots of this dispersion relation are called the slow wave and the fast wave, named after their perpendicular phase velocities. Requiring $N_\perp^2$ to be positive yields the following condition on $N_\parallel$: [112]

$$N_\parallel^2 > \left[\frac{\omega_{pi}}{\sqrt{\omega_{ci}\omega_{ce}}} + \sqrt{1 + \frac{\omega_{pi}^2}{\omega_{ci}\omega_{ce}}\left(1 - \frac{\omega_{ci}\omega_{ce}}{\omega^2}\right)} \right]^2 . \quad (63)$$

Lower-hybrid waves are evanescent in regions of the plasma for which the above inequality is violated. Making an equality out of it and solving for ω_{pi} gives the density at which the fast and slow wave roots coalesce, i. e. , the mode-conversion layer. At this layer an inward-propagating fast wave is converted to an outward-propagating slow wave, and vice-versa [113, 114]:

$$\frac{\omega_{pi}}{\omega} = N_\parallel Y \pm \sqrt{1 + N_\parallel^2 (Y^2 - 1)} \quad (64)$$

where $Y^2 = \omega^2/\omega_0^2$ and $\omega_0^2 = \omega_{ce}\omega_{ci}$. Curves showing the accessibility condition for the fast and slow waves with $Y^2 < 1$ are shown in Figure A-1 [54]. For $Y^2 > 1$ the accessibility curve looks like the left half of Figure A-1a. For $Y^2 < 1$ a local maximum in the right-hand-side of Equation 63 exists at $\omega_{pi}^2/\omega^2 = Y^2/(1 - Y^2)$ where

$$N_{\parallel min} = \frac{1}{\sqrt{1 - Y^2}} \quad (65)$$

Propagation to higher densities requires no further increase in $N_\parallel$.

Lower-hybrid waves also exhibit a "cutoff" region, which is a low-density region near the plasma edge where the waves cannot propagate (as can be seen in Figure A-1, where $N_\perp^2 < 0$ near $\omega_{pi}^2 = 0$). To determine the cutoffs properly, all three components of the wave-vector, N_x, N_y, and N_z, must be explicitly included. This

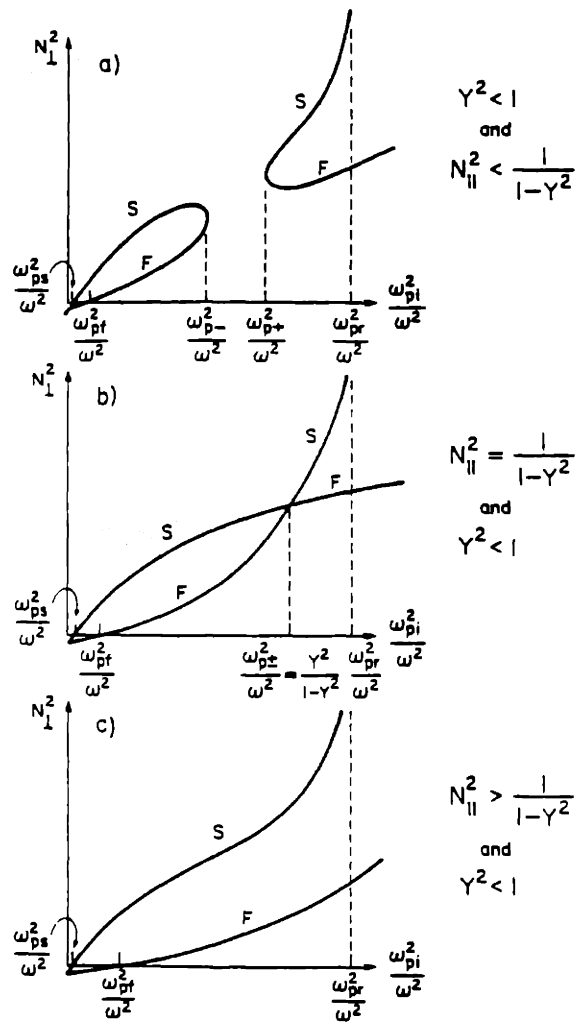

Figure A-1 Plot of $N_\perp^2$ versus density (ω_{pi}^2/ω^2), showing the slow and fast roots of the lower-hybrid dispersion relation. The slow- and fast-wave cutoffs are ω_{ps}^2/ω^2 and ω_{pf}^2/ω^2. The lower-hybrid resonance is at ω_{pr}^2/ω^2 and the points where the slow and fast waves meet are ω_{p-}^2/ω^2 and ω_{p+}^2/ω^2 (from ref. [54])

is necessary for the coupling problem because the plasma boundary is an inherent inhomogeneity. The direction of $\mathbf{B_0}$ and the normal to the plasma surface are innate to the problem. The wave-vector can have components in each of these directions and perpendicular to both. Hence, three components are required.

The wave equation becomes

$$\begin{pmatrix} K_{xx} - N_z^2 - N_y^2 & K_{xy} + N_y N_x & N_z N_x \\ K_{yx} + N_x N_y & K_{yy} - N_x^2 - N_z^2 & N_z N_y \\ N_x N_z & N_y N_z & K_{zz} - N_x^2 - N_y^2 \end{pmatrix} \begin{pmatrix} E_x \\ E_y \\ E_z \end{pmatrix} = 0. \quad (66)$$

The dispersion relation is obtained as before by setting the determinant of this system of equations to zero. The cold plasma approximation yields $K_{zx} = K_{zy} = K_{xz} = K_{yz} = 0$, $K_{yy} = K_{xx}$, and $K_{xy} = -K_{yx}$. The lower-hybrid approximating condition gives simplified dielectric-tensor elements as before, and the fast- and slow-wave cutoff conditions can quickly be obtained from the resulting equation. For cutoff, $N_x \to 0$, yielding the following:

$$K_{zz}(K_{xx} - N_z^2 - N_y^2)(K_{xx} - N_z^2) + K_{zz}K_{xy}^2 = 0. \quad (67)$$

This equation has two solutions. The slow-wave cutoff density is given by $K_{zz} = 0$, so that the slow-wave is evanescent at electron densities below $n^s_{cutoff} = \omega^2 m_e \epsilon_0 / e^2$. The fast-wave cutoff is given by

$$(K_{xx} - N_z^2 - N_y^2)(K_{xx} - N_z^2) + K_{xy}^2 = 0, \quad (68)$$

giving an approximate cutoff density of

$$n^f_{cutoff} = (m_e \epsilon_0 / e^2)\omega\omega_{ce}\sqrt{(1 - N_z^2 - N_y^2)(1 - N_z^2)}. \quad (69)$$

For typical Versator-II parameters of $\omega_{ce}/2\pi = 28$ GHz, $\omega/2\pi = 2.45$ GHz, $N_z^2 = 4$, $N_y^2 = 0$, this gives $n^f_{cutoff} \approx 34 n^s_{cutoff}$, making the fast-wave more difficult to launch with an external antenna. A slow-wave antenna was used for the LHCD experiments described in this thesis because it was readily available and because the slow wave has a well-established record of success in driving current in tokamaks.

A.2 Electron-Cyclotron Waves

The polarization and dispersion of electron cyclotron waves in a cold plasma is now reviewed. For these waves, $\omega \approx \omega_{ce} \approx \omega_{pe}$, and ion motion is usually neglected. First we examine only "near perpendicular" propagation for simplicity. In this case, $N_{||} \approx 0$ and Equation 9 becomes

$$(K_{zz} - N_\perp^2) \begin{vmatrix} K_{xx} & K_{xy} \\ -K_{xy} & K_{yy} - N_\perp^2 \end{vmatrix} \approx 0. \tag{70}$$

The two roots of this equation are called the ordinary mode (O-mode) and the extraordinary mode (X-mode). The dispersion relation of the O-mode is simply

$$N_\perp^2 = K_{zz}. \tag{71}$$

In the cold plasma limit (valid away from cyclotron resonance) this reduces to

$$N_\perp^2 = 1 - \frac{\omega_{pe}^2}{\omega^2}. \tag{72}$$

This equation shows that propagation of the O-mode can only occur for $\omega > \omega_{pe}$. The dispersion relation of the X-mode is

$$N_\perp^2 = \frac{(K_{xx}K_{yy} + K_{xy}^2)}{K_{xx}}. \tag{73}$$

In the cold plasma limit, this gives the following, known as the Appleton-Hartree dispersion relation for the X-mode [115]:

$$N_\perp^2 = \frac{\left[\omega\left(\omega + \omega_{ce}\right) - \omega_{pe}^2\right]\left[\omega\left(\omega - \omega_{ce}\right) - \omega_{pe}^2\right]}{\omega^2\left(\omega^2 - \omega_{pe}^2 - \omega_{ce}^2\right)}. \tag{74}$$

This equation shows that for the X-mode to propagate, one of the following conditions must be satisfied:

$$\omega_{pe}^2 < \omega(\omega - \omega_{ce}) \tag{75}$$

or

$$\omega^2 - \omega_{ce}^2 < \omega_{pe}^2 < \omega(\omega + \omega_{ce}). \tag{76}$$

Equation 74 holds away from cyclotron resonance and away from the "upper-hybrid" resonance, where $\omega^2 = \omega_{pe}^2 + \omega_{ce}^2$. The above regions of propagation, and the complementary regions of evanescence, are shown in Figure A-2a and A-2b for the O-mode and X-mode, respectively.

In a cold plasma with near-perpendicular propagation, the polarization of the O-mode is along the magnetic field, so that it only has a z-component of the electric field. The polarization of the X-mode can be obtained by combining Equation 73 and line 2 of Equation 8:

$$\frac{E_x}{E_y} = -\frac{K_{xy}}{K_{xx}}. \tag{77}$$

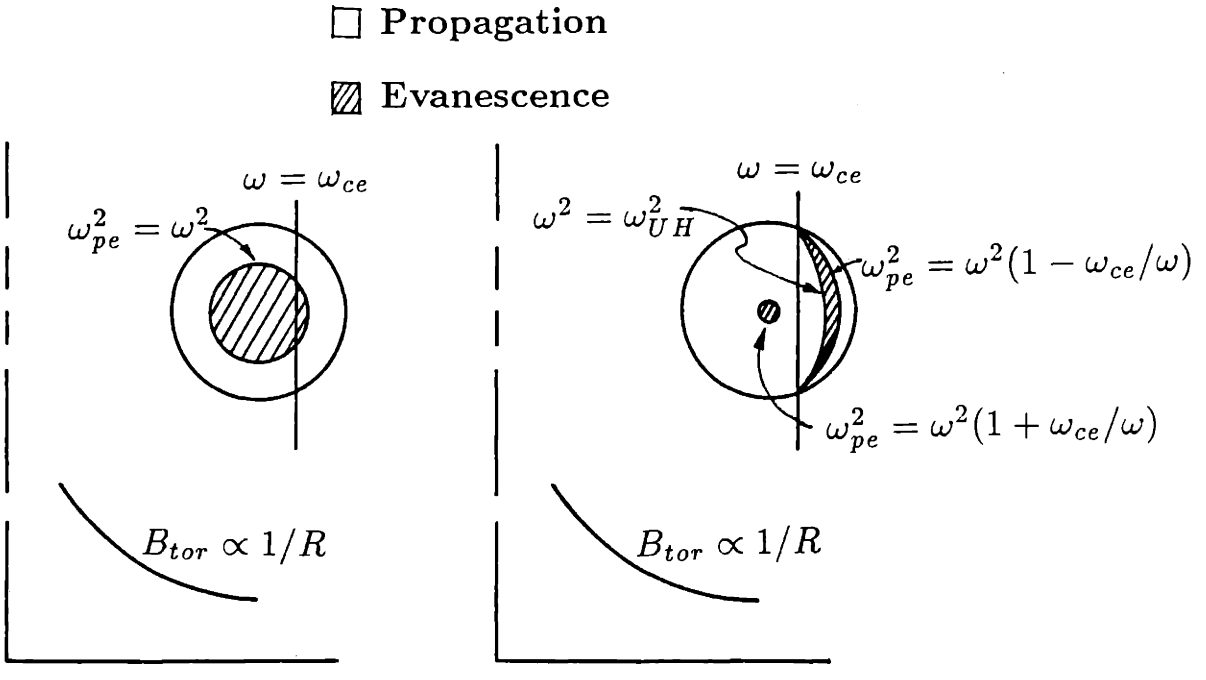

Figure A-2a O-mode cutoff for near-perpendicular propagation near $\omega = \omega_{ce}$.

Figure A-2b X-mode cutoffs and upper-hybrid resonance for near-perpendicular propagation near $\omega = \omega_{ce}$.

So the X-mode is elliptically polarized (in general) in the plane perpendicular to the magnetic field. In the cold-plasma limit, this reduces to

$$\frac{E_x}{E_y} = -i\frac{\omega_{ce}\omega_{pe}^2}{\omega\left(\omega^2 - \omega_{ce}^2 - \omega_{pe}^2\right)}. \tag{78}$$

This shows that at the plasma edge, where $\omega_{pe}^2 \ll \omega^2 \sim \omega_{ce}^2$, the polarization is linear in the y-direction. Also, at cyclotron resonance ($\omega = \omega_{ce}$) the polarization becomes circular, in the direction *opposite* to that of the electron gyromotion. In this case no energy is transfered between wave and particle, when averaged over a gyro-orbit. Thus in the cold plasma limit for perpendicular propagation, the X-mode is not absorbed at the fundamental cyclotron resonance.

For arbitrary launch angle $\mathbf{k}\angle\mathbf{B}$ the dispersion relation becomes more complicated. For a cold plasma, the Appleton-Hartree dispersion relation becomes [115]

$$N^2 = 1 - \left(\frac{\omega_{pe}^2}{\omega^2}\right)\frac{2\left(\omega^2 - \omega_{pe}^2\right)}{2\left(\omega^2 - \omega_{pe}^2\right) - \omega_{ce}^2\left(\sin^2\theta \pm \rho\right)} \tag{79}$$

with

$$\rho^2 \equiv \sin^4\theta + 4\left(\frac{\omega^2 - \omega_{pe}^2}{\omega\omega_{ce}}\right)^2\cos^2\theta. \tag{80}$$

The plus sign in the denominator of Equation 79 describes the X-mode, the minus sign describes the O-mode, and $\theta \equiv \mathbf{k}\angle\mathbf{B}_0$ is the angle between the wave vector and the confining magnetic field. Equation 79 reduces to Equations 72 and 74 when $\theta = \pi/2$.

For angles satisfying $N|\cos\theta| > v_{te}/c$ and $\sin^4\theta \gg 4(1 - \omega_{pe}^2/\omega_{ce}^2)^2\cos^2\theta)$ (which is the case for all off-perpendicular propagation angles considered in this thesis), the polarization of the O-mode is given by [115]

$$\frac{E_y}{E_z} = i\left(1 - \omega_{pe}^2/\omega_{ce}^2\right)\cos\theta \tag{81}$$

and

$$\frac{E_x - iE_y}{E_z} + \frac{\omega - \omega_{ce}}{\omega_{ce}}\tan\theta = -\sqrt{2\left(1 - \omega_{pe}/\omega_{ce}\right)}\frac{v_{te}}{c}\frac{1}{Z(\zeta)}. \tag{82}$$

where $Z(\zeta)$ is the plasma dispersion function, defined by

$$Z(\zeta) = \frac{1}{\sqrt{\pi}}\int_{-\infty}^{+\infty}\frac{e^{-t^2}}{t - \zeta}\,dt, \tag{83}$$

and $\zeta \equiv (\omega - \omega_{ce})/\sqrt{2}k_{\|}v_{te}$. For the X-mode, the polarization is

$$E_y/E_z = -i\left(2 - \omega_{pe}^2/\omega_{ce}^2\right)^{-1}\frac{1}{\cos\theta} \tag{84}$$

and

$$\frac{E_x - iE_y}{E_z} + \frac{\omega - \omega_{ce}}{\omega_{ce}}\tan\theta = -2\sqrt{\left(1 - \omega_{pe}/2\omega_{ce}\right)}\left(1 + \omega_{pe}^2/\omega_{ce}^2\right)\left(\omega_{ce}^2/\omega_{pe}^2\right)\frac{v_{te}}{c}\frac{1}{Z(\zeta)}, \tag{85}$$

provided that $\omega_{pe} < \omega_{ce}$.

APPENDIX B
ABSORPTION OF EC WAVES

First, the dielectric tensor elements are derived in the following way. The relativistic, linearized Vlasov equation is integrated along the zeroth-order particle orbits [115]. Assuming plane-wave solutions, this integration gives an expression for the first-order (oscillating) distribution function $\tilde{f}_j$ for each particle species, which in turn gives the first-order current $\mathbf{J}= \sum_j Z_j e \int \mathbf{v} \tilde{f}_j \, d^3p$, where the integral is over momentum. This $\mathbf{J}$ is then substituted into Equation 3 to obtain the dielectric tensor (identical to Equation 4 but with all elements nonzero in general), from which all the wave characteristics may be obtained. The resulting integral expressions for the dielectric tensor elements $\overline{\overline{\mathbf{K}}}_{ij}$ are extremely complicated, and have not yet been reduced to usable form for the general case. However, useful expressions can be obtained if a number of simplifying assumptions are made. The dielectric-tensor elements are still complicated in this case, and they will not be listed here. Instead, they shall be used to find the damping rates in the regimes of interest. Only waves near the first electron-cyclotron harmonic ($\omega \approx \omega_{ce}$) in a weakly relativistic ($v_{te}^2 \ll c^2$) Maxwellian plasma are considered. In most cases, it is valid to apply the WKB approximation ($\partial/\partial \mathbf{r} \ll \mathbf{k}$) and to assume the damping is weak ($\mathrm{Im}\, k \ll \mathrm{Re}\, k$), where $\frac{\partial}{\partial \mathbf{r}}$ is applied to plasma equilibrium quantities. In this case, the plasma can be considered to be locally homogeneous, and the power damping coefficient α can be obtained by applying energy balance, giving [115]

$$\alpha = \frac{\omega \epsilon_0 \mathbf{E}^* \cdot \overline{\overline{\mathbf{K}}}_a \cdot \mathbf{E}}{2\,|\mathbf{S}|} \tag{86}$$

where

$$\mathbf{S}(\mathbf{k}_r,\omega) \equiv \frac{1}{2\mu_0}\mathrm{Re}\,(\mathbf{E}\times\mathbf{B}^*) - \frac{\omega\epsilon_0}{4}\frac{\partial K_{h,ij}}{\partial \mathbf{k}_r}\mathbf{E}_\mathbf{i}^*\mathbf{E}_\mathbf{j}. \tag{87}$$

The first term of $\mathbf{S}$ is the Poynting flux, and the second term is the flux of wave-coherent kinetic energy, which is zero for a cold plasma. So the absorbed power is determined by the wave polarization and amplitude and the anti-Hermitian part of the dispersion tensor, $\overline{\overline{\mathbf{K}}}_a$. The energy flux $\mathbf{S}(\mathbf{k},\omega)$ is determined by the polarization and the Hermitian part of the dispersion tensor, $\overline{\overline{\mathbf{K}}}_h$.

Applying Equation 86 to the case of near-perpendicular propagation of the O-mode near the fundamental $\omega = \omega_{ce}$ in a Maxwellian plasma, the absorbed power and absorption coefficient are given by [115]

$$\frac{\omega\epsilon_0}{2}\mathbf{E}^*\cdot\overline{\overline{\mathbf{K}}}\cdot\mathbf{E} = \frac{\omega\epsilon_0}{2}\epsilon''_{7/2}(z_1)\,|E_z|^2 \tag{88}$$

and

$$\alpha_O = \frac{1}{2c}N'_\perp\left(\frac{\omega_{pe}}{\omega_{ce}}\right)^2\frac{-\omega_{ce}F''_{7/2}(z_1)}{\left|1+\frac{\omega_{pe}^2}{2\omega_{ce}^2}F'_{7/2}(z_1)\right|} \tag{89}$$

where $\epsilon_q = \epsilon'_q + i\epsilon''_q$, $F_q = F'_q + iF''_q$,

$$\epsilon_q(z_1) \equiv \frac{2q-3}{2^{q-1/2}\,(q-5/2)!}\frac{\omega_{pe}^2}{\omega_{ce}^2}\left(\frac{\omega v_{te}}{\omega_{ce}c}\right)^{2q-7}N_\perp^{2q-5}F_q(z_1), \tag{90}$$

$$F_q(z_1) \equiv -i\int_0^\infty \frac{d\tau'}{(1-i\tau')^q}e^{iz\tau'}, \tag{91}$$

and $z_1 = c^2(\omega - \omega_{ce})/v_{te}\omega$. The above expression for the absorption coefficient, Equation 89, can be calculated numerically. The result can then be used in a ray-tracing calculation to determine the EC-wave damping along each ray path. This is done in Chapter 4, using the EC ray-tracing and damping code TORCH. [77]Here the damping is estimated by noting that $N'_\perp$ and F'' are both of order unity, so that the O-mode absorption coefficient reduces to [115]

$$\alpha_O \approx \frac{\omega_{pe}^2}{c\omega_{ce}}. \tag{92}$$

For Versator parameters, this gives $\alpha_O \approx 6\ \mathrm{cm}^{-1} n_e\ (10^{13}\ \mathrm{cm}^{-3})$. Defining the line width for absorption using $\Delta\omega \equiv \int_0^\infty \alpha\, d\omega/\alpha_{max}$ yields the following for the line width across the fundamental resonance [115]:

$$\Delta R = \frac{R_0 \Delta\omega}{\omega_{ce}} = 166 v_{te}^2/c^2(\mathrm{cm}). \tag{93}$$

For typical ohmic target discharges on Versator, $150 \lesssim T_e \lesssim 250$ eV, so $v_{te}^2/c^2 \approx 8 \times 10^{-4}$ and the line width is about 1 mm. Combining this result with Equation 92 gives an approximate O-mode single-pass absorption of $1 - \exp(\alpha_O \Delta) \approx 13\%$ for a plasma density at the resonance layer of $5 \times 10^{12}\ \mathrm{cm}^{-3}$. For EC-formed discharges with $15\ \mathrm{eV} \lesssim T_e \lesssim 30$ eV, the single-pass absorption is an order-of-magnitude lower.

For the X-mode, the absorbed power is given by [115]

$$\begin{aligned}\frac{\omega}{4\pi}\mathbf{E}^* \cdot \overline{\overline{\mathbf{K}}}_a \cdot \mathbf{E} = &\frac{\omega}{4\pi}\epsilon''_{5/2}(z_1)\Bigg[\left|E_x - iE_y\right|^2 \\ &- \lambda\frac{F''_{7/2}(z_1)}{F''_{5/2}(z_1)}\left(\left|E_y\right|^2 - \left|E_x\right|^2\right), \\ &+ \frac{3\lambda^2}{2}\frac{F''_{9/2}(z_1)}{F''_{5/2}(z_1)}\left|E_y\right|^2\Bigg]\end{aligned} \tag{94}$$

where $\lambda \equiv k_\perp^2 r_{ce}^2$ and r_{ce} is the electron gyroradius. For waves with left-handed circular polarization in the plane perpendicular to **B**, the first two terms on the right-hand-side are zero, and for $\lambda = 0$ the thrid term is zero. This expression shows that the absorption is caused by the noncircularity of the polarization and the finiteness of the electron gyroradius. To a good approximation, the energy flux is purely electromagnetic for the X-mode, and the absorption coefficient is given approximately by [115]

$$\alpha_X \approx \alpha_O v_{te}^2/c^2. \tag{95}$$

This shows that, for quasiperpendicular propagation, the damping of the X-mode is much weaker than that of the O-mode. For Versator ohmic discharge parameters, this gives $\alpha_X \approx 0.0023$ cm^{-1}. The line width for the X-mode is $3.2R_0 v_{te}^2/c^2 \approx 1$ mm, giving a single-pass absorption of 0.02%. This clearly demonstrates that on Versator, the absorption of the X-mode by the thermal electron population is negligible for quasiperpendicular propagation, whereas the absorption of the O-mode is weak but not negligible.

For oblique propagation, the absorption coefficients for the O-mode and the X-mode are given by [115]

$$\alpha_O = \frac{1}{\sqrt{2}} \frac{\omega_{pe}^2}{\omega_{ce}^2} \frac{v_{te}}{c^2} \frac{\omega_{ce}}{|\cos\theta|} \mathrm{Im}\left(Z^{-1}(\zeta_1)\right) \tag{96}$$

and

$$\alpha_X = 2\sqrt{2}\left(1 - \frac{\omega_{pe}^2}{2\omega_{ce}^2}\right)^2 \left(1 + \frac{\omega_{pe}^2}{\omega_{ce}^2}\right)^2 \frac{\omega_{ce}^3 v_{te}}{\omega_{pe}^2 c^2} |\cos\theta| \, \mathrm{Im}\left(Z^{-1}(\zeta_1)\right). \tag{97}$$

These can be approximated as

$$\alpha_O \approx \frac{\omega_{pe}^2 v_{te}}{\omega_{ce} c^2 |\cos\theta|} \tag{98}$$

and

$$\alpha_X \approx \frac{\omega_{ce}^3 v_{te} |\cos\theta|}{\omega_{pe}^2 c^2} \tag{99}.$$

For Versator parameters as above with $\omega_{pe} = \omega_{ce}$ and $\theta = 45°$, this gives $\alpha_O = 0.12$ cm^{-1} and $\alpha_X = 0.46$ cm^{-1}. The line width for both modes is given by [116]

$$\Delta R \approx \frac{R_0 v_{te}}{\sqrt{2}c} |\cos\theta|. \tag{100}$$

The line width is therefore about 0.56 cm, and the single-pass absorption by the thermal electrons for the O-mode is approximately 6% and for the X-mode it is approximately 23%. Thus for $\theta = 45°$, the absorption of the X-mode is stronger than the O-mode absorption for $\omega_{pe}^2/\omega_{ce}^2 = 0.5$. These absorption values are in reasonable agreement with values given by TORCH [77]. In this density range, the O-mode absorption increases with increasing density, and the X-mode absorption decreases with increasing density.

APPENDIX C
MODE CONVERSION AND PARAMETRIC DECAY

The process of linear mode conversion between the cold plasma X-mode and the hot plasma EB wave is briefly described here, following the analysis of reference [3]. Here the designations cold plasma, warm plasma, and hot plasma refer to the condition that $k_\perp r_{ce}$ is small, comparable to, or large compared to unity. The linear dispersion relations for the two modes are solved, and $N_\perp^2$ is plotted versus density or ω/ω_{pi}, as shown in Figure C-1. This reveals that the solutions for the two modes pass near one another at the upper-hybrid layer, and that they are in fact joined by the solution for the electron plasma wave, which is the solution in this region under the "warm plasma" approximation. The dispersion relation near the upper-hybrid layer under the warm-plasma approximation is then inverse-Fourier-transformed, and four linearly independent solutions are found that are open integrals in the complex plane. The integrals may be performed using the method of steepest descents, and the required integration contours connect propagating solutions for the X-mode and the EB mode with phase velocities in the same direction on the high-density side of the upper-hybrid layer to an evanescent wave on the low-density side. Because the EB wave has opposed phase and group velocities, this shows that an X-mode approaching the upper-hybrid layer from higher density will be reflected and converted to an EB wave propagating away from the upper-hybrid layer toward higher density, and vice versa. A similar mode conversion may take place in the presence of an inhomogeneous magnetic field.

The process of parametric decay of the electromagnetic X-mode into an electrostatic electron Bernstein wave and a low frequency ion mode is now examined [4]. We describe the dispersion relations for the modes, and show the selection rules

and power threshold for the decay process. The relevant decay process takes place near the upper-hybrid (UH) frequency and the fundamental EC frequency. The selection rules that must be obeyed for this process to occur are the following:

$$\omega_0(\mathbf{k}_0) = \omega_1(\mathbf{k}_1) + \omega_2(\mathbf{k}_2) \tag{101}$$

$$\mathbf{k}_0 = \mathbf{k}_1 + \mathbf{k}_2, \tag{102}$$

where ω_0 and $\mathbf{k}_0$ are the pump (X-mode) wave frequency and wavenumber, ω_1 and $\mathbf{k}_1$ are the frequency and wavenumber of the low-frequency ion mode, and ω_2 and $\mathbf{k}_2$ are the frequency and wavenumber of the EB wave. The EB wave (a sideband to the pump wave) is a normal mode of the system, obeying a dispersion relation of the form $K_r(\omega_2, \mathbf{k}_2) = 0$. This is not necessarily true for the low-frequency mode, which is called a quasi-mode when the normal-mode condition is not satisfied. In our case the quasi-mode is a heavily damped lower-hybrid wave. The dispersion relations for the modes are given by:

$$\omega_1^2 = \omega_{lh}^2 \left[1 + \frac{k_\parallel^2}{k^2} \frac{m_i}{m_e} + 3\lambda_e \frac{T_i}{T_e} \frac{\omega_{ce}\omega_{ci}}{\omega_1^2} \right] \tag{103}$$

$$\omega_2^2 = \omega_{uh}^2 - \omega_{pe}^2 \left[\lambda_e + \frac{k_\parallel^2}{k^2} \frac{\omega_{ce}^2}{\omega_{uh}^2} \right] \tag{104}$$

where $\lambda_e = k_\perp^2 r_{ce}^2$, $\omega_{uh} = \omega_{pe}^2 + \omega_{ce}^2$, and $\omega_{lh} = \omega_{pi}/(1 + \omega_{pe}^2/\omega_{ce}^2)$. It is assumed that $\omega_{pe}^2 \lesssim \omega_{ce}^2$, $\lambda_e \ll 1$, and $k_\parallel^2/k^2 \ll 1$.

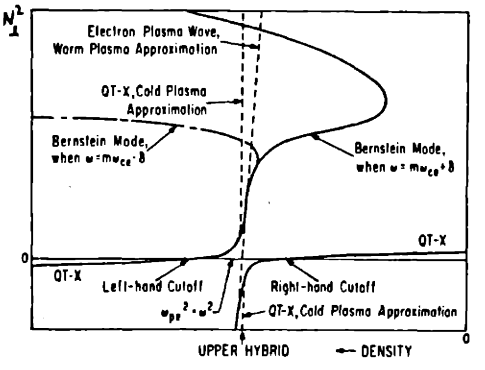

Figure C-1 Dispersion of the X-mode, the electron plasma wave, and the electron Berstein wave, showing mode conversion (from ref. [3]).

APPENDIX D
ONE-DIMENSIONAL LHCD THEORY

In quasi-linear theory, the effect of LH waves on plasma electrons is encapsulated into a quasilinear diffusion coefficient, D_{QL}, which enters the one-dimensional Fokker-Planck equation as follows:

$$\frac{\partial f}{\partial t} = \frac{\partial}{\partial v_{\|}} D_{QL}(v_{\|}) \frac{\partial f}{\partial v_{\|}} + \left.\frac{\partial f}{\partial t}\right|_c \tag{105}$$

where $\left.\frac{\partial f}{\partial t}\right|_c$ is the Fokker-Planck collision operator, which includes Coulomb scattering in both the parallel and perpendicular directions. Equation 105 is obtained from the quasi-linear Vlasov equation and the Fokker-Planck description of collisions. Integrating Equation 105 over the perpendicular direction, assuming f is Maxwellian in $v_{\perp}$, yields the following equation for high velocity electrons:

$$\frac{\partial f}{\partial \tau} = \frac{\partial D(w)}{\partial w} \frac{\partial f}{\partial w} + \frac{\partial}{\partial w}(2 + Z_i)\left(\frac{1}{w^3}\frac{\partial f}{\partial w} + \frac{f}{w^2}\right) \tag{106}$$

where $w = v_{\|}/v_{th}$, $\tau = \nu_0 t$, $\nu_0 = \nu' w^3$, $\nu' = \omega_{pe}^4 \ln\Lambda / 2\pi n_e v_{\|}^3$, $D(w) = D_{QL}/\nu_0 v_{th}^2$, and Z_i is the charge state of the ions.

With strong LH waves, it is assumed that $D(w) \gg 1$ for $w_1 < w < w_2$ and zero otherwise, so that the steady-state solution to Equation 106 is approximately flat for $w_1 < w < w_2$ and roughly Maxwellian outside this region (see Figure D-1). The level of the plateau is found by evaluating the bulk Maxwellian at $w = w_1$:

$$f(w)\Big|_{w_1 < w < w_2} \approx f(w_1) = \frac{e^{-w_1^2}}{\sqrt{\pi}}. \tag{107}$$

The current carried by the resonant electrons with $w_1 < w < w_2$ is given by

$$\begin{aligned} J &= \int_{w_1}^{w_2} n_e e w v_{th} f(w_1)\, dw \\ &= n_e e v_{th} \frac{e^{-w_1^2}}{\sqrt{\pi}} \left(\frac{w_2^2 - w_1^2}{2} \right). \end{aligned} \tag{108}$$

In the steady-state, the power absorbed by the resonant electrons from the waves is equal to the power absorbed by the bulk from the resonant electrons via Coulomb collisions, assuming the resonant electrons are perfectly confined. This dissipated power is given by the following:

$$P_d = \int_{w_1}^{w_2} n_e m_e v_{th}^2 \nu_s w^2 f(w_1)\, dw \tag{109}$$

where $\nu_s = \nu'(v_{th}^3/v_{\|}^2)(2 + Z_i)$ in the limit $v_{\|}/v_{th} \gg 1$, which is a good approximation for the high velocity resonant electrons [8], and Z_i is the charge state of the background ions. Evaluating the above integral yields

$$P_d = n_e m_e v_{th}^2 \nu' \, \frac{e^{-w_1^2}}{\sqrt{\pi}} \, (2 + Z_i) \, \ln(w_2/w_1). \tag{110}$$

The total driven current over the total input power is given by

$$\frac{I}{P} = \frac{\langle J \rangle}{2\pi R \langle P_d \rangle} \tag{111}$$

where $\langle\ \rangle$ indicates an average over the plasma cross-section, and toroidal symmetry is assumed. The current-drive figure of merit η is obtained by combining Equations

108,110, and 111, giving

$$\begin{aligned}\eta &= \frac{\overline{n}_e(10^{20}\mathrm{m}^{-3})I(\mathrm{kA})R(\mathrm{m})}{P(\mathrm{kW})} \\ &\approx 0.0054T(\mathrm{keV})\left(\frac{w_2^2 - w_1^2}{2}\right)\frac{1}{(2+Z_i)\ln(w_2/w_1)}.\end{aligned} \tag{112}$$

Note that η is proportional to velocity squared. Expressed in terms of the $N_\parallel$ of the LH wave spectrum, the figure of merit is

$$\eta \cong \frac{1.4}{2+Z_i}\,\frac{1/N_{\parallel 2}^2 - 1/N_{\parallel 1}^2}{2\ln(N_{\parallel 1}/N_{\parallel 2})} \tag{113}$$

where $N_{\parallel 2} < N_\parallel < N_{\parallel 1}$. This shows that waves with high parallel phase velocity (low $N_\parallel$) drive current more efficiently. This is because they resonate with faster electrons, which carry more current and collide less frequently with background electrons and ions.

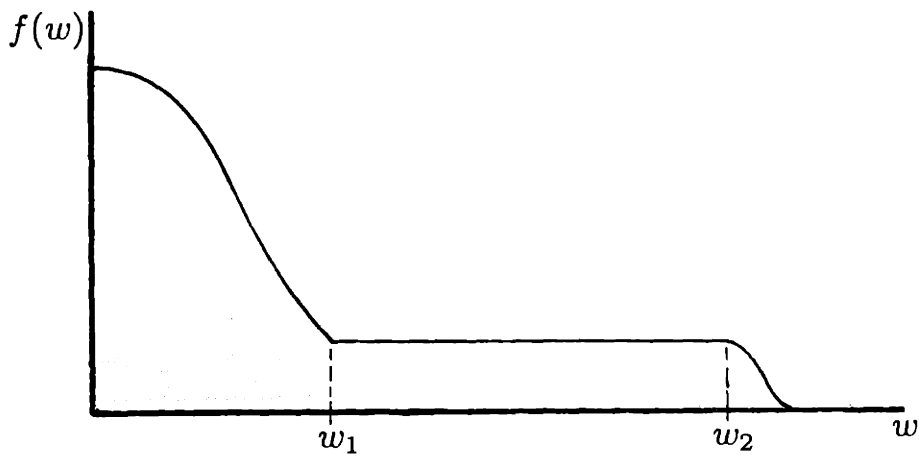

Figure D-1 Assumed distribution of electrons in the presence of strong LH waves.

APPENDIX E
ANOMALOUS DOPPLER INSTABILITY THEORY

Following the analysis of references [109]and [110], the linear growth of the instability and the action of the waves on f_e are described by the following two quasilinear equations:

$$\frac{\partial f}{\partial t} + \frac{\epsilon E_0}{m}\frac{\partial f}{\partial v_\parallel} = \left(\frac{\partial}{\partial v_\parallel} - \frac{v_\parallel}{v_\perp}\frac{\partial}{\partial v_\perp}\right) D_1 \left(\frac{\partial}{\partial v_\parallel} - \frac{v_\parallel}{v_\perp}\frac{\partial}{\partial v_\perp}\right) f + \frac{\partial}{\partial v_\parallel} D_0 \frac{\partial f}{\partial v_\parallel} + \left.\frac{\partial f}{\partial t}\right|_{collisions} \tag{114}$$

$$\frac{dW_k}{dt} = 2\gamma_k W_k \tag{115}$$

where

$$D_0 = 4\left(\frac{\pi e}{m}\right)\int d\mathbf{k} k_\parallel^2/k^2 W_k \delta\left(\omega_k - k_\parallel v_\parallel\right) \tag{116}$$

$$D_1 = \left(\frac{\pi e}{m}\right)\int d\mathbf{k}\frac{k_\parallel^2}{k^2} W_k \frac{k_\perp^2 v_\perp^2}{\omega_{ce}^2}\delta\left(\omega_{ce} - k_\parallel v_\parallel\right) \tag{117}$$

$$\gamma_k = -\frac{\nu_{ei}}{2} + \frac{2\pi^2 e^2 \omega_k}{mk^2}\int d\mathbf{v}\delta(\omega_k - k_\parallel v_\parallel) k_\parallel \frac{\partial f}{\partial v_\parallel} + \frac{\pi^2 e^2}{2mk^2}\int d\mathbf{v}\frac{k_\perp^2 v_\perp^2}{\omega_{ce}^2} k_\parallel \left(\frac{\partial}{\partial v_\parallel} - \frac{v_\perp}{v_\parallel}\frac{\partial}{\partial v_\perp}\right) f \tag{118}$$

$$W_k = \frac{k^2 |\varphi|_k^2}{4\pi} \tag{119}$$

$\omega_k = \omega_{pe} k_\parallel / k$ and φ is the wave potential. The first term on the right hand side of Equation 114 describes the diffusion of electrons along constant energy contours due to the anomalous Doppler effect. For $\epsilon = \frac{1}{2} m_e \left(v_\perp^2 + v_\parallel^2 \right)$ =constant, the operator $\partial/\partial v_\parallel - \left(v_\parallel / v_\perp \right) \partial/\partial v_\perp$ vanishes for any function of ϵ. The second term on the right-hand-side of Equation 114, which acts in a different part of velocity space, is the ordinary one-dimensional diffusion term, corresponding to parallel diffusion by parallel gradients and directly affecting the electron energy. Coulomb collisions (the third term on the right-hand-side) are neglected because $v \gg v_{te}$ for the region of interest. Because the two remaining terms of Equation 114 act in different regions of velocity space, the equation can be solved separately for each part.

For $v > v_{cr} = eE_0 / m\nu_{ei}(v)$ (the critical runaway velocity) the electron distribution function can be approximated by:

$$f_0 = n_0 \left(\frac{m}{2\pi T} \right)^{3/2} e^{-E_D/E_0} \left(1 + v_{cr}^2 / v_\parallel^2 \right) e^{-v_\perp^2 / v_{Te}^2} \Theta \left(v_b(t)/v_\parallel - 1 \right)$$

where E_D is the Dreicer field, Θ is a step function that equals zero for negative argument and one for positive argument, and $T_\perp^{tail} = T^{bulk}$ has been assumed (this can be a relatively poor assumption; see reference [117] for a discussion of the corrections for $T_\perp^{tail} > T^{bulk}$). This gives the following for the wave growth rate:

$$\begin{aligned} \gamma_k = & -\frac{\nu_{ei}}{2} + \frac{\omega_{pe}^2 \omega_k}{k^2 v_{te}} e^{-E_D/E_0} \Big[-\frac{2v_{cr}^2 |k_\parallel|^3}{\omega_k^3} + \frac{k_\perp^2}{2k_\parallel \omega_{ce}} \left(1 + \frac{v_{cr}^2 v_\parallel^2}{\omega_{ce}^2} \right) \\ & \Theta \left(k_\parallel v_b(t)/\omega_{ce} - 1 \right) \Big] - \nu_{ei}/2. \end{aligned} \tag{120}$$

The following three conditions apply at the stability threshold: $\gamma_k = 0$; $\partial\gamma_k/\partial k_{||} = 0$; $\partial\gamma_k/\partial k_{\perp} = 0$. These conditions, applied to Equation 120, give the following threshold for instability:

$$v_b > 3\left(\frac{\omega_{ce}}{\omega_{pe}}\right)^{3/2} v_{cr} \tag{121}$$

where $v_b = eE_0t/m$ is the beam velocity. Note $v_b \propto B^{3/2}n_e^{1/4}$, so that Equation 121 implies that it is harder to excite the ADI in regions of high magnetic field and, to a much weaker degree, high density. Thus the ADI is more stable when the plasma is located towards the inside of the vacuum chamber ($R < R_0$), where ω_{ce} is largest.

The threshold velocity v_b is determined by the competition between wave growth in the velocity-space-region $v_{||} = \omega_{ce}/k_{||} = v_b$ due to the anomalous Doppler effect and cyclotron damping in the region $\omega_k/k_{||} \approx \omega_{pe}/k = v_b\omega_{pe}/\sqrt{3}\omega_{ce}$. As mentioned in the beginning of this section, the wave growth is caused by the near-elastic diversion of electrons along near-constant-energy contours near $v_{||} = \omega_{ce}/k_{||}$ (the first term on the right hand side of Equation 114), and the waves are simultaneously damped in the region $\omega_k/k_{||} \approx v_b\omega_{pe}/\sqrt{3}\omega_{ce}$, forming a raised plateau there. The resulting distribution function is unstable to the "bump-on-tail" instability, and further evolves as shown in Figure 5-34.

References

[1] Lawson, J.D., *Proc. Phys. Soc.*, Sect. B **70,** 6 (1957).

[2] Tamm, I.E., and Sakharov, A.D., in *Plasma Physics and the Problem of Controlled Theromonuclear Reactions, Vol. 1* edited by M.A. Leontovich (Pergamon Press, New York, 1961).

[3] Stix, T. H., *Phys. Rev. Lett.* **15** 878 (1965).

[4] Porkolab, M., "Parametric Decay Instabilities in ECR Heated Plasmas," in *Proc. of 2nd Workshop on Hot Electron Ring Phys.* San Diego, December 1981, Ed. N. A. Uckan NTIS Rep. No. CONF-811203, p.237-246 (1982).

[5] Bernstein, I. B., *Phys. Rev.* **109** 10 (1958).

[6] Fisch, N.J., and Boozer, A.H., *Phys. Rev. Lett.* **45** 720 (1980).

[7] Antonsen, T.M. Jr., in *Wave Heating and Current Drive in Plasmas*, V.L. Granatstein and P.L. Colestock, Eds. New York: Gordon and Breach, 1985, p. 287.

[8] Fisch, N.J., *Phys. Rev. Lett.* **41** 873 (1978).

[9] Fuchs, R. A., et. al., *Phys. Fluids* **28** 3619 (1985).

[10] Karney, C.F.F., and Fisch, N.J., *Phys. Fluids* **28** 116 (1985).

[11] Yamamoto, T., et. al., *Phys. Rev. Lett.* **45** 716 (1980).

[12] Luckhardt, S.C., Porkolab, M., Knowlton, S.F., et. al., *Phys. Rev. Lett* **48** 152 (1982).

[13] Bernabei, S., et. al., *Phys. Rev. Lett.* **49** 1255 (1982).

[14] Porkolab, M., Schuss, J. J., Lloyd, B., et. al., *Phys. Rev. Lett.* **53** 40 (1984).

[15] Moreau, D., and Gormezano, C., *Plasma Phys. & Controlled Fusion* **33** 1621 (1991).

[16] Tsuji, S., Ushigusa, K., Ikeda, Y., et. al., *Phys. Rev. Lett.* **64** 1023 (1990).

[17] Leuterer, F., Söldner, F. X., McCorkick, K., et. al., *Nucl. Fusion* **31** 2315 (1991).

[18] Moriyama, S., Nakamura, Y., Nagao, A., *Nucl. Fusion* **30** 47 (1990).

[19] Anisimov, A. I., et. al., *Sov. Phys. Tech. Phys.* **16,** 546 (1971).

[20] Anisimov, A. I., et. al.,*Sov. Phys. Tech. Phys.* **18,** 459 (1973).

[21] Anisimov, A. I., et. al., *Sov. Phys. Tech. Phys.* **20,** 626 (1975).

[22] Anisimov, A. I., et. al., *Sov. Phys. Tech. Phys.* **20,** 629 (1975).

[23] Bulyginskii, D. G., et. al., *Sov. J. Plasma Phys.* **6** 11 (1980).

[24] Robinson, D. C., et. al., *Proc. 3rd Int. Symp. on Heating in Toroidal Plasmas*, Grenoble (1982), Vol. II, p. 647.

[25] Gilgenbach, R. M., et. al., *Nucl. Fus.* **12** 319 (1981).

[26] Kulchar, A. G., et. al., *Phys. Fluids* **27** 1869 (1984).

[27] Lloyd, B. and Edlington, T., *Plasma Phys. and Contr. Fusion* **28** 909 (1986).

[28] Suzuki, N., *Proc. European Phys. Soc.* Moscow (1981) Vol. 5H, p. 307.

[29] Cho, T., et. al., *J. Phys. Soc. Japan* **53** 187 (1984).

[30] Nakao, S., Ogura, K., Terumichi, Y., et. al., *Phys. Lett.* **96A** 405 (1983).

[31] Cho, T., et. al., *Nucl. Fus.* **26** 349 (1986).

[32] Holly, D. J., et. al., *Nucl. Fus.* **21** 1483 (1981).

[33] Ohkubo, K., et. al., *Nucl. Fus.* **21** 1320 (1981).

[34] Alcock, M. W., Lloyd, B., Morris, A. W., et. al., in *Plasma Phys. and Controlled Nucl. Fusion Research* 1982 (Proc. 9th Int. Conf., Baltimore, 1982) Vol. 2, IAEA, Vienna 51 (1983).

[35] Lloyd, B., Edlington, T., O'Brien, M. R., et. al., *Nucl. Fusion* **28** 1013 (1988).

[36] Luce, T. C., James, R. A., Fyaretdinov, A., et. al., in *Plasma Phys. and Controlled Nucl. Fusion Research* 1990 (Proc. 13th Int. Conf. Washington, 1990) Vol. 1, IAEA, Vienna 631 (1991).

[37] Ando, A., Ogura, K., Tanaka, H., *Phys. Rev. Lett.* **56** 2180 (1986).

[38] Tanaka, H., Ando, A., Ogura, K., et. al., *Phys. Rev. Lett.* **60** 1033 (1988).

[39] Tanaka, H., Ogura, K., Ando, A., et. al., *Nucl. Fusion* **31** 1673 (1991).

[40] Lloyd, B., Ainsworth, N. R., Alcock, M. W., et. al., in *Applications of RF Waves to Tokamak Plasmas* (Proc. Course and Workshop Varenns, 1985), Vol. 2 CEC Brussels 804 (1985).

[41] Cirant, S., Argenti, L., Mantica, P., et. al., *Plasma Phys. Controlled Fusion* **30** 1879 (1988).

[42] Nakamura, M., Minami, T., Hanada, K., et. al., *Nucl. Fusion* **31** 1485 (1991).

[43] Mantica, P., Vayakis, G., Hugill, J., et. al., *Nucl. Fusion* **31** 1649 (1991).

[44] Kim, Y. J., Gentle, K. W., Ritz, Ch. P., et. al., *Phys. Fluids B* **3** 674 (1991).

[45] Kubo, S., et. al., *Phys. Rev. Lett.* **50** 1994 (1983).

[46] Shimozuma, T., et. al., *J. Phys. Soc. Japan* **54** 1360 (1985).

[47] Ogura, K., et. al., *J. Phys. Soc. Japan* **55** 13 (1986).

[48] Toi, K., Ohkubo, K., Kawahata, K., et. al., *Phys. Rev. Lett.* **52** 2144 (1984).

[49] Ohkubo, K., et. al., *Nucl. Fus.* **25** 732 (1985).

[50] Ando, A., et. al., *Nucl. Fus.* **26** 107 (1986).

[51] Hoshino, K., et. al., *Contr. Fus. and Plasma Phys.* Proc. 12th Europ. Conf. Budapest, 1985, Vol. 9F, Pt. II, p. 184.

[52] Kawashima, H., Yamamoto, T., Hoshino, K., et. al., *Nucl. Fusion* **31** 495 (1991).

[53] Alikaev, V. V., Gorelov, Yu. A., Ivanov, D. P., et. al., *JETP Lett.* **49** 6 (1989).

[54] Mayberry, M., Ph.D. Thesis, MIT (March 1985).

[55] Read, M. E., et. al., *IEEE Trans. Microwave Theory and Tech.* **MTT-28** 875 (1980).

[56] Lloyd, B., private communication, Culham Lab., UK (1988).

[57] Squire, J.P. Ph.D. Thesis, Massachusetts Institute of Technology, to be submitted December 1992.

[58] Kirkwood, R. K., Hutchinson, I. H., Luckhardt, S. C., and Squire, J. P., *Nucl. Fusion* **31** 1938 (1991).

[59] Kirkwood, R.K., Hutchinson, I.H., Luckhardt, S.C., and Squire, J.P., *Nucl. Fusion* **30** 431 (1990).

[60] F. Skiff, D.A. Boyd, and J.A. Colborn, 18th European Phys. Soc. Conf. Controlled Fusion and Plasma Phys., Berlin, June 1991, and to be submitted to *Nuclear Fusion.*

[61] Colborn, J. A., Porkolab, M., Squire, J. P., et. al., submitted to *Phys. Rev. Lett.* June 4, 1992.

[62] Kennel, C.F., and Engelmann, F., *Phys. Fluids* **9** 2377 (1966).

[63] Bers, A., Ram, A. K., *Proc. IAEA Technical Mtg.* Arles, France (1991), in press.

[64] Bonoli, P., Englade, R., *Phys. Fluids* **29** 2937 (1986).

[65] Nakamura, M., et. al., *Phys. Rev. Lett.* **47** 1902 (1981).

[66] Ohkubo, K., et. al., *Nucl. Fusion* **22** 203 (1982).

[67] Mayberry, M.J., et. al., *Phys. Rev. Lett.* **55** 829 (1985).

[68] Liu, C.S., Chan, V.S., Bhadra, D.K., and Harvey, R.W., *Phys. Rev. Lett.* **48** 1479 (1982).

[69] Andrews, P.L., *Phys. Rev. Lett.* **54** 2022.

[70] Wégrowe, J.-G., *AIP Conf. Proc. #190* Amer. Inst. Phys.:New York (1989) p. 182.

[71] Ohkubo, K., et. al., IPPJ-697, Inst. of Plasma Phys., Nagoya Univ. (1984).

[72] Bonoli, P., Mayberry, M. J., and Porkolab, M., Paper #1-C9, Sherwood Plasma Phys. Theory Mtg., New York (1986).

[73] Mayberry, M. J., Ph.D. Thesis, MIT (March 1985) pp. 91-93.

[74] Kupfer, K., and Bers., A., *Phys. Fluids B* **3** 2783 (1991); Bers., A., and Ram, A.K., Proc. IAEA Technical Mtg. Arles, France (1991), in press.

[75] Imai, T. and the JT-60 Team, paper CN-53/E-1-3, IAEA, 13th Int'l. Conf. Plasma Phys. & Contr. Nucl. Fusion Res. Wasington DC (1990).

[76] Mazzucato, E., and Efthimion, P., *Nucl. Fusion* **25** 1681 (1985).

[77] Meyer, R.C., Porkolab, M., Smith, G.R., Kritz, A.H. *Nucl. Fusion* **29** 2155 (1989).

[78] R.W. Harvey, M.G. McCoy, G.D. Kerbel, *AIP Conf. Proc.* **159** (1987) 49.

[79] Squire, J. private communication, April, 1992.

[80] Colborn, J. A., ORBIT, a MATLAB m-file (unpublished).

[81] Rohatgi, R., Ph.D. Thesis, Massachusetts Institute of Technology (1986) p. 89.

[82] Goodman, T., Whaley, D., Pochelon, A., Paper 3S25, Bull. Am. Phys. Soc. Vol. 36, #9 (Oct. 1991) p. 3242.

[83] Parail, et. al., IAEA Conf. Proc. IAEA-CN-44/F-IV-4 (1984).

[84] Hinnov, E., Bishop, A.S., Fallon, H., Jr., *Plasma Phys.* **10** 291 (1968).

[85] Wooten, A.J., Carreras, B.A., Matsumoto, H., et. al., *Phys. Fluids B* **2** 2879 (1990).

[86] Liewer, P. C., *Nucl. Fusion* **25** 543 (1985).

[87] Robinson, D. C., *Turbulence and Anomalous Transport in Magnetized Plasmas* (Ecole Polytechnique, Palaiseau, France, 1986), p. 21

[88] Surko, C. M., in *Turbulence and Anomalous Transport in Magnetized Plasmas* (Ecole Polytechnique, Palaiseau, France, 1986), p. 93

[89] Kim, Y.J., Gentle, K.W., Ritz, Ch.P., et. al., *Phys. Fluids* **3** 674 (1991).

[90] Catto, P.J., Myra, J.R., Wang, P.W., et. al., *Phys. Fluids B* **3** 2038 (1991).

[91] Rechester, A.B., and Stix, T.H., *Phys. Rev. Lett.* **36**, 587 (1976).

[92] Rosenbluth, M.N., Sagdeev, R.Z., Taylor, J.B., and Zaslavski, G.M., *Nucl. Fusion* **6** 297 (1966).

[93] Rechester, A.B., Rosenbluth, M.N., *Phys. Rev. Lett.* **40** 38 (1978).

[94] Mynick, H.E., and Strachan, J.D., *Phys. Fluids* **24**, 695 (1981).

[95] Zweben, S.J., Swain, D.W., and Fleischmann, H.H., *Nucl. Fusion* **18**, 1679 (1978).

[96] Barnes, C.W. and Strachan, J.D., *Phys. Fluids* **26** 2668 (1983).

[97] Catto, P.J., Myra, J.R., Wang, P.W., et. al., *Phys. Fluids B* **3** 2038 (1991).

[98] Nakamura, M., Minami, T., Hanada, K., et. al., *Nucl. Fus.* **31** 1485 (1991).

[99] Mantica, P., Vayakis, G., Hugill, J., et. al., *Nucl. Fus.* **31** 1649 (1991).

[100] Prater, R., private communication, November, 1991.

[101] Ohkawa, T., *General Atomics Company Report* GA-A13847 (1976).

[102] Miyamoto, K., Plasma Physics for Nuclear Fusion, MIT Press: Cambridge, Massachusetts (1980) pp. 224-6.

[103] Bickerton, R. J., Connor, J. W., and Taylor, J. B., *Nature Phys. Sci.* **229** 110 (1971)

[104] Lohr, J., Harvey, R. W., James, R. A., Et. al.,*Proc. 9th Topical Conf. Radio Frequency* Charleston (1991).

[105] Fidone, I., Giruzzi, G., Krivenski, V., et. al., *Nucl. Fusion* **27** 579 (1987).

[106] Shoucri, M., Shkarovsky, I., Fuchs, V., et. al., *Computer Phys. Comm.* **55** 253 (1989).

[107] Ando, A., Ogura, K., Tanaka, H., et. al., *Nucl. Fusion* **26** 107 (1986).

[108] Alikaev, V. V., Arsenev, Yu. A., Bobrovskii, A., et. al., *Sov. Phys. Tech. Phys.* **20** 322 (1975).

[109] Parail, V. V., and Pogutse, O. P., *Sov. J. Plasma Phys.* **2** 125 (1976)

[110] Parail, V. V. and Pogutse, O. P., *Nucl. Fusion* **18** 303 (1978).

[111] Luckhardt, S. C., et. al., *Phys. Fluids* **30** 2110 (1987).

[112]Golant, V. E., *Sov. Phys. Tech. Phys.* **16** 1980 (1972).

[113]Bers, A., *Proc. 3rd Topical Conf. on rf Plasma Heating,* Pasadena, Ca., Jan. 1978, pp. A1-1 to A1-10.

[114]Porkolab, M., in *Fusion* Ed. E. Teller, Academic Press (1981) Vol. 1, part B, p. 165.

[115]Bornatici, M., et. al., *Nucl. Fus.* **23** 1153 (1983).

[116]Porkolab, M., course notes, Spring 1988.

[117]Fuchs, V., Shoucri, M., Teichmann, J., and Bers, A. *Phys. Fluids* **31** 2221 (1988).